Computational Modelling of Structure and Dynamics in Lightweight Hydrides

Philippe Christoph Aeberhard

St. Catherine's College, University of Oxford

A thesis submitted to the Department of Chemistry of the University of Oxford for the degree of Doctor of Philosophy in Inorganic Chemistry.

Trinity Term 2012

All of the work described in this thesis is my own unless otherwise stated and has not been submitted previously for any other degree at this or any other university.

Philippe C Aeberhard, April 2012

Computational Modelling of Structure and Dynamics in Lightweight Hydrides

Philippe C Aeberhard, St. Catherine's College

A thesis submitted to the Department of Chemistry of the University of Oxford for the degree of Doctor of Philosophy in Inorganic Chemistry.

Trinity Term 2012

Abstract

Hydrogen storage in lightweight hydrides continues to attract significant interest as the lack of a safe and efficient storage of hydrogen remains the major technological barrier to the widespread use of hydrogen as a fuel. The metal borohydrides $Ca(BH_4)_2$ and $LiBH_4$ form the subject of this thesis; three aspects of considerable academic interest were investigated by density functional theory (DFT) and molecular dynamics (MD) modelling. (i) High-pressure crystal structures of $Ca(BH_4)_2$ were predicted from a structural analogy between metal borohydrides and isoelectronic metal oxides. The structural stability of hydrogen storage materials under high pressure is an important aspect, as high-pressure polymorphs may provide structures with better hydrogen desorption properties. The isoelectronic analogue of $Ca(BH_4)_2$ is TiO_2, and structural equivalents of $Ca(BH_4)_2$ in the baddeleyite, columbite and cotunnite structures of TiO_2 were found to be stable at elevated pressure. Thermodynamic stability was evaluated by computing the Gibbs energy with respect to pressure and temperature. The pressure-dependence of the Helmholtz energy was determined to described a third-order Birch-Murnaghan equation of state, and the harmonic approximation was used to compute the vibrational energy levels and the Helmholtz energy as a function of temperature. The proposed structures are consistent with reports of two hitherto unidentified high-pressure phases observed experimentally. (ii) The disordered structure of the high-temperature phase of $LiBH_4$ was studied by *ab initio* molecular dynamics (MD) at temperatures ranging from 200–535 K. It was found that the model emerging from analysis of the MD simulations properly accounts for dynamical disorder and fundamentally differs from the published experimental and theoretical structures. The validity of the MD model was corroborated by comparison of calculated pair distribution functions, vibrational spectra and a crystallographic model with neutron diffraction data; good agreement was found. A reassignment of the space group from $P6_3mc$ to $P6_3/mmc$ is proposed based on evidence for additional symmetry from MD simulations. (iii) Finally, a new MD-based method was developed to simulate fast ionic diffusion in $LiBH_4$. The colour diffusion algorithm—a nonequilibrium molecular dynamics method originally developed for the study of model fluids—was adapted and applied to self-diffusion of atoms in a solid for the first time. Calculated diffusion coefficients agreed very well with published measurements, and diffusion pathways that include collective particle effects were determined directly from the simulation results, thereby opening up a promising and efficient new method for the study of phenomena such as superionic conduction.

"Zwei Dinge sind zu unserer Arbeit nötig: Unermüdliche Ausdauer und die Bereitschaft, etwas, in das man viel Zeit und Arbeit gesteckt hat, wieder wegzuwerfen."

Albert Einstein

Acknowledgements

This DPhil thesis could not have been completed without the help and support of the following people and organisations, who are gratefully acknowledged.

First of all, my special thanks go to my supervisor Bill David for his guidance and support at every stage of this thesis. I would also like to extend my thanks to Keith Refson (Rutherford Appleton Laboratory) for his help and invaluable advice on all aspects of theoretical chemistry and computing throughout these nearly four years.

I am grateful to Chris Mundy, Shawn Kathmann, Greg Schenter and Garold Murdachaew (Pacific Northwest National Laboratory) for hosting me on a visit to the beautiful State of Washington and for teaching me all about molecular dynamics, Fortran programming and Seattle's coffee culture; Karl Travis (University of Sheffield) for helpful discussions and an initiation to nonequilibrium thermodynamics; Denis Evans and Stephen Williams (Australian National University) for hosting me in their beautiful city of Canberra and mentoring me with all aspects of nonequilibrium molecular dynamics; Timmy Ramirez-Cuesta (Rutherford Appleton Laboratory) for offering a pragmatic point of view on most things in life.

I would also like to thank Peter P Edwards and Martin O Jones for offering me the opportunity to work in this group, and Linda Webb for gently ruling the group with an iron hand.

Any casual visitor to the Inorganic Chemistry Laboratory knows that it tends to be a grey and melancholic place, which is why I am grateful to my wonderful colleagues:

Andrew Seel and Hung-Chun "Henry" Lai for their company at various conferences; Kate Ryan and David Royse for being great office mates with excellent humour; Liang Kong and Nazanin Rashidi-Alavijeh for keeping a hand on Henry and Andrew.

My research could not have been carried out without access to substantial high-performance computing resources: I thank Chris Mundy (Pacific Northwest National Laboratory) for giving me access to the National Energy Research Scientific Computing Centre; Stephen Williams (Australian National University) for sharing his resources at the Australian National Computing Infrastructure; the Oxford Supercomputing Centre; and the UK National Grid Service for access to SCARF.

Finally, I gratefully acknowledge the Engineering and Physical Sciences Research Council (EPSRC) and the Science and Technology Facilities Council (STFC) for providing the funding for my DPhil scholarship; St. Catherine's College for awarding me a Leathersellers' Company scholarship; Oxford University for providing a research exchange scholarship to the ANU; Pacific Northwest National Laboratory for partial funding of a visit to PNNL.

My final thanks go to Zhenmei Xi for her loving care and support and company in Canberra and Oxford.

Contents

CHAPTER 1

Introduction

"The Stone Age did not end for lack of stone."

Sheikh Ahmed Zaki Yamani

The use of hydrogen as a renewable and clean fuel forms the subject of this thesis, which thus has two aspects: the grander aspects of social and economic impact, and the cold, hard, scientific reality that stands in the way of this impact. Before the scope and research aims of this thesis are presented, therefore, the broader picture surrounding the systems studied shall be briefly summarised.

1.1 The hydrogen economy

There is much to be said about the fundamental role that hydrogen plays in the history of the universe. In addition to being the most abundant element in the universe and the fuel of the fusion reaction inside stars, hydrogen is also the principal element, by mass, of present-day hydrocarbon fuels. The idea of using hydrogen (H_2) as an energy carrier has been discussed many times since its discovery as an element. In his 1874 novel "L'île mystérieuse", the French science-fiction author Jules Vernes dreams of a future where

"hydrogen and oxygen will be used as an inexhaustible source of heat and light." He recognised that the chemical reaction:

$$H_2 + \tfrac{1}{2}\,O_2 \longrightarrow H_2O$$

not only releases a very substantial amount of energy (242 kJ of heat per mole of H_2), but also produces only water as the reaction product.

This clean combustion inspired the concept of using hydrogen as a replacement for petroleum in cars specifically, and as a mobile energy store in general. The combustion of hydrogen is not the only way to release its energy: by separating the oxidation reaction of hydrogen from the reduction of oxygen in a fuel cell, electricity can be generated directly and with a higher thermodynamic efficiency than through combustion. Fuel cells were invented in 1839 by Sir William Grove, and since then many different types of fuel cells have been developed using a range of fuels, from methanol and natural gas to hydrogen.

Practical interest in hydrogen fuel cell systems was and is mainly driven by the United States and Japanese governments, though other countries have launched national and international research programmes on hydrogen energy. Fuel cells had been explored as a "silent power source" for military applications, and early concepts for using hydrogen as an energy carrier revolved mainly around its use as a store for nuclear energy, for example in an article by Winsche *et al.* (1973). But the idea to use hydrogen and fuel cells as the basis of a more universal energy economy, and specifically to use it to power cars, gained a serious impetus in the West for the first time during the oil-crisis of 1973 (see, for example, Brewer, 1976). Petroleum prices soared due to political tensions between the US and the largest oil-producing countries, making the Western world painfully aware of the unfavourable geographical distribution of worldwide fossil fuel reserves.

The International Journal of Hydrogen Energy was established in 1976, marking one of the first international scientific collaborative efforts to advance the idea of the hydrogen economy; the first sentence of the first article of the first issue of this journal catches the zeitgeist (Marchetti, 1976): "The ruthless manoeuvring of the oilmen, and the panic

generated by skilful embargoes and great increases in oil prices has focused the attention of politicians, scientists and laymen on the problem of resources and scarcity." At that time, which was characterised by a general enthusiasm for the newly developed nuclear energy industry, hydrogen was seen as a replacement for natural gas and as a storage medium for the amply available nuclear electricity.

However, cheap fossil fuels returned after roughly a decade, and the initial enthusiasm for the hydrogen economy quickly faded when the vision of a future with hydrogen energy was clouded by a whole array of unsolved scientific and engineering problems. In 2003, the hydrogen energy project in the US was made a priority and long-term basic research programmes looking into overcoming the practical hurdles of the hydrogen economy were committed through the Department of Energy (DoE)—mainly for the same reason that caused its initial popularity during the oil-crisis: reduced dependence on imported fossil fuels. But this most recent surge of interest in the hydrogen economy also coincided with growing concerns about climate change, and thus hydrogen as a carbon-free energy carrier gained widespread popularity. A popular book about the hydrogen economy by Jeremy Rifkin described a future with hydrogen energy as the liberation of humanity from the reign of a handful of all-powerful oil-companies, with democratised and decentralised energy generation (Rifkin, 2002).

At the present time, ten years later, the dream evoked by Rifkin (2002) remains largely a dream, with many of the original promises replaced by the sobering results of recent research. The DoE identifies four industry segments of the hydrogen economy and corresponding targets for each of them; these are listed as follows (initiatives in other countries, with the exception of Japan, tend to follow DoE guidelines):

Production processes Hydrogen is an energy carrier and not an energy source; unlike fossil fuels, hydrogen cannot simply be extracted from the environment. At present, most hydrogen is produced from steam reforming of natural gas (thereby undermining the claim of a carbon-free fuel) and by the electrolysis of water. The latter process is still relatively inefficient and requires a high amount of electricity, which must be generated by other means. Photocatalytic splitting of water using sunlight

would ultimately be the optimal solution, but is at present at an embryonic stage.

Storage technologies As hydrogen is the lightest of gases, with a boiling point of 20 K at atmospheric pressure, storage presents a difficult problem especially for mobile applications. Pure hydrogen must either be compressed at room temperature to very high pressures (700 bar) or liquefied at 20 K. The former process expends a large amount of energy for the compression process and requires the development of robust storage tank materials; the latter process is equally energy-intensive and requires elaborate cryocooling mechanisms that are unsuitable for mobile applications. From a safety point of view, both forms are less than ideal. However, high-pressure storage is currently the adopted storage method for nearly all current and planned implementations of hydrogen energy in the short term. The storage of hydrogen in a solid medium would be safer and reduce the volume and pressure of the hydrogen tank; these storage materials are the subject of this thesis and shall be discussed in more depth in the next section.

Delivery Intimately linked with the previous two areas, the establishment of a hydrogen distribution infrastructure is crucial for the penetration of this technology.

Conversion technologies Hydrogen fuel cells are at present expensive and relatively short-lived, but current technology is already sufficiently advanced for early adoption and suitable for incremental optimisation.

In all of these areas, significant scientific breakthroughs are still required to make hydrogen energy suitable for, and competitive in, a mass market. The enthusiasm for the hydrogen economy is once more fading in the US: in 2009, the Secretary of Energy, Steven Chu, expressed his pessimism about a breakthrough in the near future in these four areas, saying in an interview with the magazine Technology Review that "if you need four miracles, that's unlikely: saints only need three miracles."

While hydrogen fuel cells are already being used in special segments or are currently being introduced in the time frame up to 2014 (forklifts, stationary backup power, fleets of buses in local transportation networks), the breakthrough into mainstream

transportation—hydrogen fuel cell cars—is the longest-term goal in the current strategy and, with the exception of Japan, is estimated not to take place before 2020; the main barrier is hydrogen storage. While no fundamental technological barriers exist for production, delivery and conversion, the principal drawback for mobile applications is the lack of a suitable mobile hydrogen storage option.

1.2 Hydrogen storage materials

As mentioned in the previous section, storage in pure elemental form, liquid or gaseous, is energy intensive for both liquefaction and compression processes—nevertheless, compressed gas storage at 700 bar is the only storage method currently employed in prototype hydrogen vehicles and other real systems, and is likely to be for a number of years to come. However, the latest "Hydrogen and Fuel Cell Program Plan" published by the DoE in 2011 formulates several targets for future hydrogen storage materials by 2017. Any hydrogen storage system must fulfil the following criteria:

- Storage capacity of at least 5.5% by weight and volumetric energy density of at least 1.3 kWh/L.
- Reversible storage materials that can be easily recharged on-board for vehicular applications at a refuelling rate of 1.67 kg/min.
- Materials must have low cost and low toxicity, and must be abundantly available.

The number of publications stored in the Chemical Abstract Services database under the keyword "hydrogen storage" increased exponentially until 2009 (Figure 1.1). The fact that the DoE targets have been revised over the past five years—earlier targets aimed at a storage capacity of 9% by weight by 2012, for example—indicates that no material reaching these targets has been identified to date despite intensive research programmes. A plethora of solid state storage options have been considered which can be categorised in many different ways; the overview that follows does not claim to be complete in any form, but storage options can broadly be grouped by the storage mechanism:

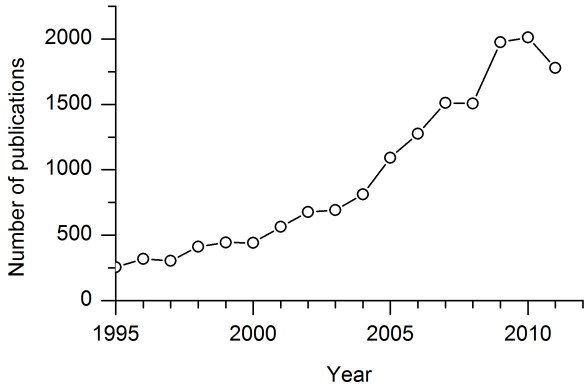

Figure 1.1: Number of abstracts deposited in the Chemical Abstracts Service database under the keyword "hydrogen storage" by publication year.

- Irreversible chemical storage in liquids or solids. One of the very first experiments any student of chemistry performs is the reaction of sodium or potassium metal with water, which evolves large amounts of hydrogen gas. Based on this principle (but without the violent inflammation of the evolved gas that usually follows the sodium in water experiment), mixtures of hydrides and organic or ionic liquids have been considered, but these types of system can only be regenerated off-board by a chemical restoration process (Staubitz *et al.*, 2010).

- Reversible storage by physisorption. Metal-organic frameworks, carbon nanotubes, graphite and zeolites are some of the materials considered for absorption of hydrogen under pressure. Because of the low binding enthalpy of hydrogen in such systems (Churchard *et al.*, 2011), no such material has been identified that stores more than a few weight percent of hydrogen at room temperature, although some success has been achieved at the boiling temperature of liquid nitrogen (79 K).

- Reversible storage in chemical hydrides. Hydrogen is stored in a solid through a thermally activated, reversible hydrogenation/dehydrogenation reaction; this is the approach considered in this thesis and shall be described in the following.

Chemical hydrogen storage is based on the principle that simple metallic hydrides form readily, reversibly and rapidly for some metals:

$$MH_2(s) \rightleftharpoons M(s) + H_2(g)$$

Reversible storage is the most important and the most difficult requirement; it sets the thermodynamic and kinetic limits of this storage reaction. In order to have thermodynamic reversibility under standard conditions (298 K and 1 bar of H_2 pressure), the standard free enthalpy of the reaction, $\Delta_r G^\circ$, must be zero:

$$\Delta_r G^\circ = \Delta_r H^\circ - T\Delta_r S^\circ = 0$$

In the above reaction all reactants are solids except for hydrogen which is a gas; the entropy of reaction therefore corresponds largely to the entropy of hydrogen because the difference in entropy between two solids is negligible compared to the entropy of a gas. Therefore, the entropy of reaction for any solid state storage material can be approximated by the standard entropy of H_2, which is $130.7\,\mathrm{J\,K^{-1}\,mol^{-1}}$. This means that at 298 K and 1 bar, the enthalpy of the storage reaction for an ideal hydrogen storage material should be:

$$\Delta_r H^\circ \approx +39 \text{ kJ/(mol } H_2)$$

For an ideal hydrogen storage material MH_2, the dehydrogenation reaction should therefore be endothermic and with roughly 39 kJ/(mol H_2) binding enthalpy for hydrogen. However, practical requirements demand that the reaction also be rapid at standard conditions, and even a thermodynamically ideal hydrogen storage system might desorb/absorb hydrogen painstakingly slowly. A storage material with an enthalpy significantly larger than the above will decompose at too high a temperature, and a material with a negative decomposition enthalpy cannot be reversible under any conditions, independent of its desorption/absorption kinetics. Thermodynamic screening of a material is therefore a convenient way of identifying hydrogen storage candidates, and the thermodynamics of a

material are best evaluated by modelling, as practical measurements of reaction enthalpies can be difficult and imprecise.

With hydrogen being the lightest of elements, the requirement for high weight capacity effectively restricts the bulk composition of any potential hydrogen storage material to the first two rows of the periodic table. (In terms of volumetric capacity, virtually all chemical hydrides fulfil target densities.) A brief overview of some candidate storage materials that have been widely studied is presented in the following paragraphs.

A seminal paper for hydrogen storage that cannot go uncited in any review of progress in hydrogen storage reports the discovery of reversible storage in sodium alanate ($NaAlH_4$) by Bogdanovic and Schwickardi (1997). The catalysing effect of $TiCl_3$ on the dehydrogenation of alanates, which had been known for several decades, was systematically studied, and it was found that the compound decomposed at 150°C and reabsorbed hydrogen at the same temperature in the presence of $TiCl_3$. However, each step took 5 h and therefore this reaction is too slow; the theoretical storage capacity of 5.6% was in practice found to be only 4.2% in the first dehydrogenation/hydrogenation cycle and dropped to 3.1% over 35 cycles (the authors reported this as being a consequence of a slowing down of the hydrogenation kinetics). The decomposition products are well known, and a detailed mechanism for decomposition was proposed from theoretical modelling by Gunaydin *et al.* (2008). Therefore, while the gravimetric storage capacity is rather low, it seems that an improvement of only one aspect, namely the catalyst to accelerate reaction kinetics, is needed to produce a viable "first-generation" solid hydrogen storage material. This has to date not happened.

A further seminal paper (Schlapbach and Züttel, 2001) highlighted that metal alloys such as $LaNi_5$ form hydrides at ambient conditions both rapidly and reversibly. In this class of materials, hydrogen is stored in atomic form in interstitials in the lattice of the alloy. Although $LaNi_5$ has a capacity of only around 2% by weight and is a rather expensive material, its kinetics and reversibility are to the present day unmatched by any other hydrogen storage material, and this has led to the further investigation of transition metal alloys by car makers.

Simple metal hydrides like LiH, MgH_2 or AlH_3 have a much higher weight capacity and are considerably cheaper than transition metal alloys, but the strongly ionic bonding character of H^- causes these materials to suffer from both unfavourable thermodynamics and kinetics (Grochala and Edwards, 2004). The thermodynamics of magnesium metal can in principle be tuned by elastic constraints (Baldi *et al.*, 2009), but no solution for the slow kinetics is known.

The class of complex metal hydrides involves complex anions with hydrogen bound to either B or N or Al. A large-scale thermodynamic screening project of metal borohydrides ($M(BH_4)_n$) was undertaken by Hummelshøj *et al.* (2009); light metal borohydrides are found to have a good storage capacity, and their desorption enthalpy is correlated with the cation electronegativity (Nakamori *et al.*, 2006). The alkali metal borohydrides turn out to be so stable that decomposition only starts at impracticably high temperatures. The alkaline-earth borohydrides have recently been reviewed by Rönnebro (2011); only $Mg(BH_4)_2$ and $Ca(BH_4)_2$ are of interest as $Be(BH_4)_2$ can be ruled out for any practical usage due to the high toxicity of beryllium, and barium borohydride is not known to exist but is too heavy. (Strontium borohydride is currently being investigated, but little is known about this compound.) Theoretical predictions of the dehydrogenation enthalpies of both $Mg(BH_4)_2$ and $Ca(BH_4)_2$ are conveniently close to the ideal value of 39 kJ/mol; kinetics, however, make it impossible to use these materials as is at the moment. Additionally, numerous decomposition studies of both these borohydrides have shown that the decomposition follows a complex reaction pathway involving the formation of many different intermediate and final products. Although reversibility has been proven, in principle, by rehydrogenating decomposition products under high H_2 pressure to reform the borohydrides, in practice no absorption/desorption cycle could be carried out due to slow kinetics and complex end product mixtures.

Nitrogen-based compounds include the amide $LiNH_2$ (Chen *et al.*, 2002), which decomposes in mixture with LiH, but has unfavourable thermodynamics: it decomposes at 230°C (Kojima and Kawai, 2005). Ammonia borane, NH_3BH_3 (Baitalow, 2002), decomposes in an exothermic reaction, therefore reversibility is excluded from the outset. Since

it is very cheap and decomposes at around 100°C, it is nevertheless an interesting candidate for single-use hydrogen storage (Staubitz *et al.*, 2010). Alkali metal substitution to form MNH_2BH_3 (Xiong *et al.*, 2008) results in cleaner decomposition products and largely eliminates the evolution of borazine, which is detrimental to fuel cells. Thus, hydrogen release of 10% by weight can be obtained at 91°C, but, again, decomposition is too slow.

Although individual review papers often conclude with the optimistic remark that much progress has been made in the development of reversible hydrogen storage, a survey of recent review papers leaves the author of this thesis in doubt whether progress is being made in the direction of solving the problem, or in the direction of realising that the classes (and combinations) of solid hydrogen storage materials examined heretofore provide no solution since the understanding of the core issue, catalysis and absorption/desorption reaction mechanisms, has not improved significantly since the first report of reversible hydrogen storage in sodium alanate. From an academic point of view, a large body of data has been accumulated on a diverse range of potential systems, and an equally diverse range of fundamental problems yet to be solved have been highlighted. From a practical point of view, the conclusion is that still no material fulfils the hydrogen storage targets and none seems to have significant advantages over titanium-doped $NaAlH_4$ and metal alloys such as $LaNi_5$.

The most fundamental unsolved problem is the issue of kinetics. Apart from the metal alloys, no system absorbs/desorbs hydrogen rapidly enough at moderate conditions. Although experimentation with $TiCl_3$ has led to increased reaction rates, a clear understanding of how the catalyst acts is still lacking and, as a consequence, it is not possible to systematically improve catalysis. Such an understanding can only be developed if the structure and dynamics of all involved materials are known at the atomic level. Solid state experimental data, for example from neutron or X-ray scattering techniques, can give valuable insight; however, they are not sufficient to form conclusions about all atomic processes, as each technique only gives an incomplete picture of the system. Rigorous modelling approaches must be combined with the experimental findings to produce a consistent and atomistic picture of the structure and dynamical characteristics of hydro-

gen storage materials.

This thesis focuses on the modelling of borohydrides, specifically $Ca(BH_4)_2$ and $LiBH_4$. The former is a high-capacity material with ideal thermodynamic properties, but its kinetics are dominated by complicated decomposition pathways and a variety of crystal structures of the starting material; the crystal polymorphism is of substantial academic interest and has been extensively studied in this thesis. $LiBH_4$ is thermodynamically too stable on its own to be useful, but its disordered structure makes it interesting in mixtures with, for example, MgH_2 (Bösenberg *et al.*, 2007).

1.3 *Deus ex machina*: materials modelling methods

Modelling methods can be broadly divided in two categories: interpolative and predictive (*ab initio*). Interpolative models are often based on observed relationships such as, for example, the apparent linear dependence of the volume of a solid on the temperature. By this model, which consists simply of the measured proportionality constant, it is possible to predict the volume expansion of a solid for a small temperature range, but while this is certainly useful in some fields, it does not establish a direct link between the structure of the material and the temperature nor does it explain the relationship between cause and effect. The corresponding predictive model describes the effect of the temperature on the atomic motion of the material and explains that the increasingly anharmonic vibrations at increased temperature lead to a macroscopic volume expansion.

This thesis is primarily concerned with materials modelling from first principles (*ab initio*). Quantum mechanics describes electrons and nuclei without approximation and is universally valid without any reference to empirical observations. The mathematical complication of quantum mechanical treatment of even the simplest systems[1] makes it impossible to apply quantum mechanical equations to chemical systems without introducing simplifications and approximations. The development of density functional theory (explained in Chapter 2) and the simultaneous development of more and more powerful

[1]From a chemist's point of view. The simplest systems from a physicist's point of view are naturally much simpler and exact solutions can be found with ease.

computers in the 1960s and 1970s finally made quantum chemistry useful for studying systems of practical interest, and the Nobel Prize in chemistry (not physics, remarkably) was awarded in 1998 for the development of density functional theory (Walter Kohn) and of computational quantum chemistry methods (John A Pople).

1.3.1 Electronic structure via density functional theory

Any computational treatment must always make a trade-off between accuracy and efficiency. Since computational time is a limited resource in practice, only a small subset of all possible chemical systems can ever be subjected to calculation, and it is therefore crucial to choose the modelling method based on the goals of the research and the available resources (both human and computer time). For the modelling of solid state materials, density functional theory (DFT) is the most widely used method. The importance of modelling has increased substantially in the field of chemistry over the past few years, and especially in the field of solid state and materials chemistry. Most publications of experimentally solved crystal structures contain DFT calculations of the proposed structure to confirm that it is physically meaningful because crystal structure determination methods do not take into account the interaction energies between atoms at all and subtle issues such as the location of hydrogen atoms can be ambiguous from, for example, X-ray powder diffraction measurements.

Many modelling methods exist that take a different approach to approximating the exact solution of the basic quantum mechanical equations, and some of them are undoubtedly more accurate than DFT, some of them less. In terms of absolute accuracy, quantum Monte Carlo methods (QMC) are probably among the best currently available methods and have the advantage of being conceptually intriguingly simple (for a recent review see Austin *et al.*, 2012). QMC finds an approximate solution to the fully correlated Schrödinger equation directly and can recover more than 90% of the correlation energy, thus making it the method of choice for systems with highly correlated electronic structures. This makes it one of the most accurate methods that are available; however, studies using QMC methods are extremely time-consuming. DFT is chosen in this thesis as the

best combination of versatility, accuracy and efficiency, as accuracy of the order of QMC methods is not required.

Currently used implementations of DFT for materials modelling are very efficient in terms of accuracy and system size that can be studied. The greatest drawbacks of DFT are its inability (i) to account properly for dispersion forces between molecules and (ii) to predict excited state properties, such as the band gap and conduction band structure of a semiconductor. Drawback (i) is due to the approximation that is most commonly used, which is based on local exchange-correlation functionals; however, DFT as a theory is exact, and more elaborate nonlocal functionals are being developed that address this drawback. The second drawback is inherent to the theoretical framework of DFT, but an extension of the DFT method, time-dependent DFT, exists that provides accurate predictions of excited state properties. However, both nonlocal functionals as well as time-dependent DFT are computationally very intensive and neutralise the computational efficiency as one of the main advantages of DFT. Since the hydrogen storage materials that are the subject of this thesis are densely packed ionic crystals and insulators with wide band gaps, these two drawbacks of using (time-independent) DFT with efficient local exchange-correlation functionals do not matter.

1.3.2 Molecular dynamics

DFT calculates with good accuracy the potential energy landscape with respect to the atomic positions, and with geometry optimisation algorithms it is possible to identify a stable structure as the local minimum of this potential energy landscape. To determine how the atomic nuclei move at finite temperature on this potential energy landscape, the molecular dynamics (MD) technique is used: the atomic motion is simulated by numerical integration of the equation of motion for each atomic nucleus in the system. Originally introduced for the simulation of Brownian motion of the particles of a simple (two-dimensional) model fluid by means of "fast electronic computors [sic]" (Alder and Wainwright, 1957), it can now be combined with DFT to model the thermal motion of the atoms in a real solid. The forces $\mathbf{F}_i$ acting on the nuclei are calculated from DFT rather than a simple model poten-

tial, such as the Lennard-Jones potential, and therefore the dynamics of the system are directly derived from the electronic structure of the material. From a modelling point of view, in hydrogen storage materials research, the interest is in the behaviour of the atomic nuclei which governs chemical reactions and structure, whereas the electronic structure is of secondary interest, unlike in semiconductor research for example.

In MD, the atomic nuclei are therefore treated as classical mass points, and the fact that nuclei are quantum particles is ignored completely. Quantum effects relevant to atomic nuclei include quantum tunnelling through potential energy barriers and the Heisenberg uncertainty principle stating that position and momentum cannot both be known to arbitrary precision, as the classical equation of motion suggests, both of which become less significant in the classical limit of high temperature and large particle mass. The consequence for MD results is that the trajectories obtained for light atoms, especially hydrogen, will contain systematic errors if the simulation is performed far from the classical limit; few structural properties of materials are significantly influenced by these effects, however.

MD simulations are *in principle* deterministic; the equations of motion predict the outcome at any time t without ambiguity, given initial conditions—if only they could be solved analytically in practice. In contrast, stochastic methods such as Monte Carlo simulations or Langevin dynamics inherently contain a random element, that is even if all the equations are solved analytically, it is impossible to predict an absolute outcome because of the involvement of random numbers in the algorithms, in agreement with the Heisenberg uncertainty principle. However, although MD simulations of condensed matter systems are in principle deterministic, the many-body equations of motion behave in a chaotic way, making them irreversible in practice. This can be expressed by the Lyapunov instability, which states that two identical systems described by identical equations of motion and starting from *almost* identical initial conditions lead to an exponential divergence of the outcomes of the two simulations:

$$\left|\mathbf{\Gamma}(t) - \mathbf{\Gamma}'(t)\right| \propto e^{\lambda t}$$

where $\mathbf{\Gamma}$ and $\mathbf{\Gamma}'$ are the positions of the two systems in phase space and λ is called the Lyapunov exponent. This is similar to computing predictions of the weather by meteorological simulations: because two simulations with minimally differing initial conditions—for example, a slightly different measurement of local air pressure—lead to two predictions that diverge exponentially with respect to time from each other, reliable forecasts[2] can only be made for a few days. This means that even though MD simulations are deterministic by nature, the outcome even for rather short times is somewhat arbitrary due to this instability: for example, if two simulations with identical initial conditions are performed on two different computer systems with different processor architectures, the tiny differences in numerical round-off error are sufficient to give rise to the Lyapunov instability.

How can MD simulations therefore lead to any valid results? The answer is that MD results must always be treated in the framework of (classical) statistical mechanics. The basic tenet of statistical mechanics is that the small inconsistencies that lead to the Lyapunov instability do not, in fact *must* not, matter for the results we want to obtain. This is true for all of physics and chemistry, both experimental and theoretical. Otherwise, there could be no such thing as a reproducible experiment, the concept that distinguishes the exact sciences from all others. To take a simple example, a measurement of the thermal conductivity of iron could not be reproduced, because in a subsequent experiment the initial conditions would not be the same: it is impossible to ensure that every single metal atom in the sample is in the same initial state (position and velocity) at the start of the measurement as they were in a previous measurement. In fact, a given set of experimental conditions for a macroscopic experiment has a very low probability of occurring more than once during the age of the universe. A fundamental principle of physics is that these small differences must not matter: our interest is in the measurement of a statistical quantity (in this case, the thermal conductivity), which is, for all practical matters, completely independent of the microscopic starting conditions.

The same principle holds for molecular dynamics. The precise values of the particle

[2]The definition of a reliable weather forecast clearly differs from country to country.

positions and momenta are secondary, as we are interested in computing statistical quantities; therefore, small imprecisions in, for example, integrating the equations of motion or in the calculation of forces are acceptable even though they lead to a completely different trajectory. The computed statistical quantities, however, will be the same within an error that depends on the scale of the simulation. Whereas in an experiment, samples of the order of 10^{23} atoms and time scales of seconds and beyond mean that statistical fluctuations are negligible, in MD the limit is typically 10^2–10^3 atoms and time scales of 10–100 ps.[3]

1.4 Scope and aim of this work

In this thesis, the DFT and MD modelling methods are applied to study structural aspects of $Ca(BH_4)_2$ and $LiBH_4$. From the point of view of hydrogen storage, $Ca(BH_4)_2$ has ideal thermodynamics and weight capacity, but its kinetics are poor. More importantly, its ability to adopt multiple crystal structures has not been fully explored. Significantly, $Ca(BH_4)_2$ appears generally to adopt similar structures to TiO_2; this structural analogy is explored by simulation as it has potential applicability to all group 1, 2 or 3 borohydrides. To understand the reaction kinetics of a material, its structural properties must first be known in detail. $LiBH_4$ is a crystalline but disordered material, and its disordered crystal structure is studied in detail by MD.

In Chapter 2, the fundamental theory underlying the modelling methods employed in this thesis is introduced in detail. The basic properties and principles of DFT are described and its potential and limitations presented. The effect of temperature must be included in any realistic modelling approach of materials, and so the basic relations of quantum and classical statistical mechanics are presented. The chapter ends by introducing the molecular dynamics method for the direct simulation of thermal motion.

Chapter 3 explains the analysis algorithms applied to obtain results from MD simula-

[3]This limit is due to the computational cost incurred by MD simulations: the computation of a single time step of a system of a few hundred atoms, using the DFT methodology described in this thesis, requires about 320 CPU-seconds on a present-day high-performance computing system; with a time step length of $\Delta t = 1$ fs, a single MD calculation of more than 10–100 ps is difficult to justify in practice.

tions that can be directly compared to experimental results. Algorithms to compute vibrational spectra, crystallographic displacement parameters and neutron scattering structure factors are presented.

In Chapter 4, high-pressure structures of $Ca(BH_4)_2$ are predicted that are derived from a structural analogy between metal borohydrides and isoelectronic metal oxides. The structural stability under high pressure is an important aspect, as high-pressure polymorphs may provide structures with better hydrogen desorption properties. Three new structures are predicted, their relative thermodynamic stabilities evaluated, and the results compared with recently published high-pressure experimental results.

We continue in Chapter 5 by investigating $LiBH_4$ at high temperature, when it becomes a disordered phase, in keeping with the other alkali metal borohydrides. As the disorder of this material is dynamic, the MD method is used to determine vibrational spectra and pair distribution functions and analyse the dynamics of the disorder quantitatively and at a range of temperatures between 200–535 K.

Finally, a new MD-based method is developed in Chapter 6 to simulate fast ionic diffusion in $LiBH_4$. The method is an adaptation of nonequilibrium molecular dynamics, originally developed for the study of fluids. It is shown that this methodology is suitable for modelling ionic diffusion in solids and for the determination of diffusion pathways; the potential of this method to simulate more general dynamic phenomena is also addressed.

Chapter 7, finally, summarises the work presented in this thesis and discusses opportunities for future research directions that follow from the work undertaken in this thesis.

CHAPTER 2

Theoretical basis

> "Gleichungen sind wichtiger für mich, weil die Politik für die Gegenwart ist,
> aber eine Gleichung etwas für die Ewigkeit."
>
> Albert Einstein

In this chapter, the fundamental theory underlying all modelling approaches used in this thesis is summarised, starting with density functional theory which is used to model the electronic structure and to calculate the total energy of a system, from which a number of other techniques are derived. The harmonic oscillator approximation to phonon modes is described without any treatment of anharmonic effects. To go beyond the harmonic approximation, the molecular dynamics technique is used in this thesis, which is described along with the relevant statistical mechanics relations.

The methods described in this chapter are implemented in the computational packages CASTEP (Clark *et al.*, 2005) and CP2K[1], which were used for almost all the calculations described in the following chapters.

[1] CP2K is a freely available suite of programmes for molecular dynamics simulations; it is available at: http://www.cp2k.org.

2.1 Density functional theory

Materials modelling requires the determination of the total energy of a system described as a collection of atomic nuclei and electrons, and therefore, because of the electrons, must be treated quantum mechanically. We summarise briefly the approach to the description of electrons by quantum mechanics; this is described in great detail in standard text books on electronic structure (e. g. Martin, 2004).

A molecular system of N atoms and N_e electrons is described by the Schrödinger equation, which for eigenstates Ψ_n is:

$$\hat{H}\Psi_n(\mathbf{r}_1, \ldots, \mathbf{r}_N, \mathbf{x}_1, \ldots, \mathbf{x}_{N_e}) = E_n\Psi_n(\mathbf{r}_1, \ldots, \mathbf{r}_N, \mathbf{x}_1, \ldots, \mathbf{x}_{N_e}) \tag{2.1}$$

where $\mathbf{x}_i$ are the coordinates of the electrons and $\mathbf{r}_I$ are the positions of the nuclei. The Hamiltonian operator, $\hat{H}$, describes the total energy in the system. In this thesis, no relativistic effects or external magnetic fields are considered, and the equation above therefore only includes the kinetic energy of all particles and the potential energy from the electrostatic interactions described by Coulomb's law. The Hamiltonian for a general chemical system is given by:

$$\hat{H} = -\frac{\hbar}{2m_e}\sum_i \nabla_i^2 - \sum_{i,I}\frac{Z_I e^2}{|\mathbf{x}_i - \mathbf{r}_I|} + \frac{1}{2}\sum_{i\neq j}\frac{e^2}{|\mathbf{x}_i - \mathbf{x}_j|} - \sum_I \frac{\hbar^2}{2m_I} + \frac{1}{2}\sum_{I\neq J}\frac{Z_I Z_J e^2}{|\mathbf{r}_I - \mathbf{r}_I|} \tag{2.2}$$

The index i is used to denote electrons, I to denote nuclei. The Schrödinger equation cannot be solved analytically for any system with more than one electron and one nucleus, the hydrogen atom is the only chemical system for which the above equation has a known analytical solution.

A number of approximations must be introduced in this analysis to be able to determine a solution. The first of these is the Born-Oppenheimer approximation (Born and Oppenheimer, 1927). Its basic premise is that in the Hamiltonian of Equation (2.2), the only term that can be considered as negligible is the kinetic energy of the nuclei: it is inversely proportional to m_I, the nuclear mass, which is at least 1800 times larger than m_e,

the electron mass. It can therefore be treated by perturbation theory and ignored in the above equation. As a result, the nuclear coordinates enter the equation only as constant parameters, and the Schrödinger equation is solved with zero nuclear kinetic energy; the Hamiltonian for the electrons is, in atomic units:

$$\hat{H} = \underbrace{-\frac{1}{2}\sum_i \nabla_i^2}_{\hat{K}_e} \underbrace{-\sum_{i,I} \frac{Z_I}{|\mathbf{r}_i - \mathbf{r}_I|}}_{\hat{V}_{ne}} + \underbrace{\frac{1}{2}\sum_{i\neq j} \frac{1}{|\mathbf{r}_i - \mathbf{r}_j|}}_{\hat{V}_{ee}} + \underbrace{\frac{1}{2}\sum_{I\neq J} \frac{Z_I Z_J}{|\mathbf{r}_I - \mathbf{r}_J|}}_{V_{nn}} \tag{2.3}$$

In this equation, the variables are the electronic coordinates, $\mathbf{x}_i$. The expectation value of any operator $\hat{O}$ for a wave function Ψ (not necessarily an eigenstate), in standard bra-ket notation, is given by:

$$\left\langle \hat{O} \right\rangle = \frac{\left\langle \Psi \left| \hat{O} \right| \Psi \right\rangle}{\left\langle \Psi | \Psi \right\rangle} \tag{2.4}$$

The expectation value of the total energy is the sum of the expectation values of the individual contributions to the total energy from Equation (2.3):

$$\left\langle \hat{H} \right\rangle = \left\langle \hat{T}_e \right\rangle + \left\langle \hat{V}_{ne} \right\rangle + \left\langle \hat{V}_{ee} \right\rangle + V_{nn} \tag{2.5}$$

The nucleus-electron interactions are given by:

$$\begin{aligned} \left\langle \hat{V}_{ne} \right\rangle &= -\frac{\left\langle \Psi \left| \sum_{i,I} \frac{Z_I}{|\mathbf{r}_i - \mathbf{r}_I|} \right| \Psi \right\rangle}{\left\langle \Psi | \Psi \right\rangle} \\ &= -\frac{N_e \int \mathrm{d}\mathbf{x} \sum_I \frac{Z_I}{|\mathbf{x} - \mathbf{r}_I|} \left(\int \mathrm{d}\mathbf{x}_2 \ldots \mathrm{d}\mathbf{x}_{N_e}\, \Psi^*(\mathbf{x}, \mathbf{x}_2, \ldots, \mathbf{x}_{N_e}) \Psi(\mathbf{x}, \mathbf{x}_2, \ldots \mathbf{x}_{N_e}) \right)}{\left\langle \Psi | \Psi \right\rangle} \end{aligned} \tag{2.6}$$

where Ψ^* is the complex-conjugate of Ψ. Because of the exclusion principle, the sum over all electrons reduces to multiplication by N_e and the order of integration does not matter. The nucleus-electron interactions can therefore be written in the form:

$$\left\langle \hat{V}_{ne} \right\rangle = \int \mathrm{d}\mathbf{x}\, n(\mathbf{x}) V_{\mathrm{ext}}(\mathbf{x}) \tag{2.7}$$

This defines the electron density as well as the external potential:

$$n(\mathbf{x}) = N_e \frac{\int \mathrm{d}\mathbf{x}_2 \ldots \mathrm{d}\mathbf{x}_{N_e}\, \Psi^*(\mathbf{x}, \mathbf{x}_2, \ldots, \mathbf{x}_{N_e}) \Psi(\mathbf{x}, \mathbf{x}_2, \ldots, \mathbf{x}_{N_e})}{\langle \Psi | \Psi \rangle} \tag{2.8}$$

$$V_{\mathrm{ext}}(\mathbf{x}) = -\sum_{I=1}^{N} \frac{Z_I}{|\mathbf{x} - \mathbf{r}_I|} \tag{2.9}$$

The nucleus-nucleus repulsion energy, V_{nn}, is a trivial additive constant in the Born-Oppenheimer approximation, and can be incorporated into $V_{\mathrm{ext}}(\mathbf{x})$. The electron-electron interaction is given by:

$$\begin{aligned} \left\langle \hat{V}_{ee} \right\rangle &= \frac{\left\langle \Psi \left| \frac{1}{2} \sum_{i \neq j} \frac{1}{|\mathbf{x}_i - \mathbf{x}_j|} \right| \Psi \right\rangle}{\langle \Psi | \Psi \rangle} \\ &= \frac{N_e(N_e - 1) \int \mathrm{d}\mathbf{x}\, \mathrm{d}\mathbf{x}' \frac{1}{|\mathbf{x} - \mathbf{x}'|} \left(\int \mathrm{d}\mathbf{x}_3 \ldots \mathrm{d}\mathbf{x}_{N_e}\, \Psi^*(\mathbf{x}, \mathbf{x}', \mathbf{x}_3, \ldots, \mathbf{x}_{N_e}) \Psi(\mathbf{x}, \mathbf{x}', \mathbf{x}_3, \ldots, \mathbf{x}_{N_e}) \right)}{2 \langle \Psi | \Psi \rangle} \end{aligned} \tag{2.10}$$

Again, the integration over all but two electron coordinates can be carried out to yield:

$$\left\langle \hat{V}_{ee} \right\rangle = \int \mathrm{d}\mathbf{x}\, \mathrm{d}\mathbf{x}' \, \frac{n_2(\mathbf{x}, \mathbf{x}')}{|\mathbf{x} - \mathbf{x}'|} \tag{2.11}$$

This defines the two-electron density matrix:

$$n_2(\mathbf{x}, \mathbf{x}') = \frac{N_e(N_e - 1)}{2} \frac{\int \mathrm{d}\mathbf{x}_3 \ldots \mathrm{d}\mathbf{x}_{N_e}\, \Psi^*(\mathbf{x}, \mathbf{x}', \mathbf{x}_3, \ldots, \mathbf{x}_{N_e}) \Psi(\mathbf{x}, \mathbf{x}', \mathbf{x}_3, \ldots, \mathbf{x}_{N_e})}{\langle \Psi | \Psi \rangle} \tag{2.12}$$

This is the probability of finding an electron at $\mathbf{x}$ if another electron is at $\mathbf{x}'$. An alternative expression for the electron-electron energy is based on the exchange-correlation hole, defined as:

$$h(\mathbf{x}, \mathbf{x}') = n_2(\mathbf{x}, \mathbf{x}') - n(\mathbf{x}) n(\mathbf{x}') \tag{2.13}$$

This function is the difference between the joint probability of finding electrons simultaneously at $\mathbf{x}$ and $\mathbf{x}'$ and the product of electron densities at $\mathbf{x}$ and $\mathbf{x}'$ and so is a measure of electron correlation. For very large separations of $\mathbf{x}$ and $\mathbf{x}'$, the joint proba-

bility approaches the product of one-electron densities and the exchange-correlation hole approaches zero. The electron-electron interaction energy is then:

$$\left\langle \hat{V}_{ee} \right\rangle = \underbrace{\int \mathrm{d}\mathbf{x}\,\mathrm{d}\mathbf{x}'\,\frac{n(\mathbf{x})n(\mathbf{x}')}{|\mathbf{x}-\mathbf{x}'|}}_{\langle \hat{V}_J \rangle} + \underbrace{\int \mathrm{d}\mathbf{x}\,\mathrm{d}\mathbf{x}'\,\frac{h(\mathbf{x},\mathbf{x}')}{|\mathbf{x}-\mathbf{x}'|}}_{\langle \hat{V}_{\mathrm{xc}} \rangle} \tag{2.14}$$

The first term of the sum is the classical Coulomb self-interaction energy of a charge density $n(\mathbf{x})$ and the second term is the exchange-correlation energy, defined as the difference between the exact, fully correlated electron-electron energy and the classical energy.

Inspection of the above equation shows that almost all terms can be expressed in terms of the electron density, except for the correlation energy and the kinetic energy. Is it possible to express the total energy entirely as a functional of the electron density, thereby replacing the $3N_e$-dimensional wave function by the 3-dimensional electron density function? In fact, it can be proven that it is, paving the way for density functional theory.

2.1.1 The Hohenberg and Kohn theorems

In a seminal paper, Hohenberg and Kohn (1964) proved that the electron density $n(\mathbf{x})$ can serve as the fundamental quantity to describe any system of N_e electrons moving in any given external potential $V_{\mathrm{ext}}(\mathbf{x})$. The basic content of the two theorems as well as their surprisingly simple proofs are presented here.

Theorem I (HKI) For any system of electrons with ground state density $n(\mathbf{x})$, moving in an external potential $V_{\mathrm{ext}}(\mathbf{x})$, the external potential is uniquely determined, to within an additive constant, by $n(\mathbf{x})$.

The proof works by demonstrating that the alternative to the theorem—namely that two different external potentials $V_{\mathrm{ext}}(\mathbf{x})$ and $V'_{\mathrm{ext}}(\mathbf{x})$ can lead to the same ground state density—is absurd. Given an external potential, the Hamiltonian is fully determined (to

within an additive constant):

$$\hat{H} = -\frac{1}{2}\sum_i \nabla_i^2 + \sum_i V_{\text{ext}}(\mathbf{x}_i) + \frac{1}{2}\sum_{i\neq j}\frac{1}{|\mathbf{x}_i - \mathbf{x}_j|} \tag{2.15}$$

The Hamiltonian, in turn, fully determines the ground state wave function, Ψ_0. The ground state electron density is determined from the ground state wave function by Equation (2.8). If the two potentials $V_{\text{ext}}(\mathbf{x})$ and $V'_{\text{ext}}(\mathbf{x})$ differ by more than just an additive constant, this leads to two different Hamiltonians $\hat{H}$ and $\hat{H}'$, which in turn must lead to two different ground state wave functions Ψ_0 and Ψ'_0. To prove HKI, it is now assumed that these two wave functions lead to the same ground state electron density n_0. We have:

$$\left\langle \Psi_0 \middle| \hat{H} \middle| \Psi_0 \right\rangle < \left\langle \Psi'_0 \middle| \hat{H} \middle| \Psi'_0 \right\rangle \tag{2.16}$$

This inequality stems from the variational principle: Ψ'_0 is not the ground state of $\hat{H}$ and the expectation value has its minimum for the true ground state wave function. However, $\hat{H}$ can be written as:

$$\hat{H} = \hat{H}' - \sum_i V'_{\text{ext}}(\mathbf{x}_i) + \sum_i V_{\text{ext}}(\mathbf{x}_i) \tag{2.17}$$

since only the external potentials are different. Therefore, the inequality is:

$$E_0 < E'_0 - \int \mathrm{d}\mathbf{x}\, n_0(\mathbf{x}) \left(V'_{\text{ext}}(\mathbf{x}) - V_{\text{ext}}(\mathbf{x})\right) \tag{2.18}$$

The argumentation for Equations (2.16)–(2.18) is repeated with exchanged primed and unprimed quantities, and we arrive at:

$$E'_0 < E_0 + \int \mathrm{d}\mathbf{x}\, n_0(\mathbf{x}) \left(V'_{\text{ext}}(\mathbf{x}) - V_{\text{ext}}(\mathbf{x})\right) \tag{2.19}$$

If the electron densities for both ground state wave functions are the same, as assumed, then addition of the two equations yields the inconsistent result:

$$E_0 + E'_0 < E_0 + E'_0 \tag{2.20}$$

Therefore, the initial assumption must be wrong, and no two potentials differing by more than an additive constant can lead to the same ground state electron density. The external potential uniquely defines the ground state density. It is worth adding here that the inequality in Equation (2.16) is only strictly true if the ground states are non-degenerate; for degenerate systems the argument can be extended with linear combinations of the ground state wave functions and the theorem remains valid.

A consequence of this theorem is that the ground state density alone determines *all* ground state properties of the system. This means that the ground state energy of a system of electrons in an external potential can be expressed as a functional that depends on the density alone:

$$E[n] = K[n] + E_{ee}[n] + \int \mathrm{d}\mathbf{x}\, V_{\mathrm{ext}}(\mathbf{x}) n(\mathbf{x}) + V_{nn} \tag{2.21}$$

Because the kinetic energy and the electron-electron interaction energy solely depend on the electron density and on no external variable, the functionals $K[n]$ and $E_{ee}[n]$ are universal, but their forms remain unknown; the first Hohenberg and Kohn theorem is merely an existence theorem. The second theorem provides a general method for determining the ground state density for any given external potential.

Theorem II (HKII) For a given external potential $V_{\mathrm{ext}}(\mathbf{x})$ and number of electrons $N_e = \int \mathrm{d}\mathbf{x}\, n_0(\mathbf{x})$ the correct ground state electron density $n_0(\mathbf{x})$ is the one that minimises the total energy functional, Equation (2.21).

The proof proceeds by demonstrating that for any density $n(\mathbf{x})$ that is not the ground state electron density, the total energy given by $E[n]$ is larger than $E[n_0]$. For a given external potential, the expectation value of the Hamiltonian is equal to the energy evaluated by the density functional for that wave function.

$$\frac{\left\langle \Psi_0 \left| \hat{H} \right| \Psi_0 \right\rangle}{\langle \Psi_0 | \Psi_0 \rangle} = E[n_0] = E_0 \tag{2.22}$$

This follows from HKI, since the ground state electron density n_0 uniquely determines

the external potential, which uniquely determines the Hamiltonian and its ground state wave function. Hence, the ground state energy can be evaluated either by the density functional or the expectation value of the Hamiltonian. If we consider a different density n' that integrates to the same number of electrons N_e, it follows from HKI that this density is the ground state density of a system with a different external potential and thus a different Hamiltonian, $\hat{H}'$. We then have:

$$E[n'] = \frac{\left\langle \Psi' \middle| \hat{H} \middle| \Psi' \right\rangle}{\langle \Psi' | \Psi' \rangle} > \frac{\left\langle \Psi_0 \middle| \hat{H} \middle| \Psi_0 \right\rangle}{\langle \Psi_0 | \Psi_0 \rangle} = E[n_0] \tag{2.23}$$

The inequality follows from the variational principle. This means that for a given external potential, the ground state electron density minimises the total energy functional, thereby establishing a variational principle for electron density. The true ground state density fulfils the condition:

$$\left(\frac{\mathrm{d}E[n]}{\mathrm{d}n} \right)_{n=n_0} = 0 \tag{2.24}$$

2.1.2 Kohn-Sham formulation of density functional theory

The Hohenberg and Kohn theorems are universally valid, not only for electron systems, but in fact for any system of particles whose interaction with some external potential is described by an expression of the same form as Equation (2.7). The basic content of the theorems is that a universal functional of the density exists, and that the true ground state is found by minimising the energy functional with respect to the density. The two main problems that prevent a practical application of these theorems to calculate the ground state properties are that the universal functional is not known exactly, and that no guidance for solving Equation (2.24) is given.

Density functional theory, as it is currently widely used for materials modelling, is almost always based on the formulation introduced by Kohn and Sham (1965). The starting point for the Kohn-Sham method is to express the electron density as the density of a hypothetical system of electrons that do not self-interact, but whose density is, by definition of this hypothetical system, identical to that of the fully interacting system.

This point will become clearer towards the end of this section. Formally, it means that each electron can be represented by a single wave function and the electron density is expressed as the sum of individual, uncorrelated electron densities:

$$n(\mathbf{x}) = \sum_{i=1}^{N_e} \psi_i^*(\mathbf{x})\psi_i(\mathbf{x}) \tag{2.25}$$

The Kohn-Sham orbitals ψ_i can be expressed as functionals of the density:

$$\psi_i(\mathbf{x}) = \frac{\mathrm{d}n}{\mathrm{d}\psi_i^*} \tag{2.26}$$

Equation (2.24) is then solved with the additional constraint that each of the individual electron wave functions be normalised to unity, leading to the constraint equation $g_i[n] = \langle \psi_i | \psi_i \rangle - 1$ for each wave function ψ_i. This is achieved by the method of Lagrange multipliers. The equation to be solved reads:

$$\frac{\mathrm{d}}{\mathrm{d}n}\left(E[n] - \sum_{i=1}^{N_e} \epsilon_i g_i[n]\right) = 0 \tag{2.27}$$

where ϵ_i are the Lagrange multipliers. Since the electron density is a simple functional of the Kohn-Sham orbitals, the minimum can equivalently be determined with respect to the Kohn-Sham orbitals by the chain rule:

$$\frac{\mathrm{d}}{\mathrm{d}n}\left(E[n] - \sum_{i=1}^{N_e} \epsilon_i g_i[n]\right)\frac{\mathrm{d}n}{\mathrm{d}\psi_i^*} = 0 \tag{2.28}$$

The energy functional is:

$$E[n] = K[n] + E_J[n] + E_{\mathrm{xc}}[n] + \int \mathrm{d}\mathbf{x}\, n(\mathbf{x})V_{\mathrm{ext}}(\mathbf{x}) + V_{nn} \tag{2.29}$$

The functional derivatives of each term in this sum can be derived separately.

The expression of the kinetic energy of a correlated electron density is unknown, but

is approximated as the sum of kinetic energies of the noninteracting electrons:

$$K_{\mathrm{KS}}[n] = \sum_{i=1}^{N_e} \left\langle \psi_i \left| -\frac{1}{2}\nabla_i^2 \right| \psi_i \right\rangle \tag{2.30}$$

Since this is not the true kinetic energy of the electron density, the exchange-correlation functional is formally redefined as:

$$E_{\mathrm{xc}}[n] = K[n] + E_{ee}[n] - (K_{\mathrm{KS}}[n] + E_J[n]) \tag{2.31}$$

The functional derivative of the kinetic energy reads:

$$\frac{\mathrm{d}K_{\mathrm{KS}}}{\mathrm{d}n}\frac{\mathrm{d}n}{\mathrm{d}\psi_i^*} = \frac{\mathrm{d}K_{\mathrm{KS}}}{\mathrm{d}\psi_i^*} = -\frac{1}{2}\nabla_i^2\psi_i \tag{2.32}$$

The Hartree interaction is simply:

$$\frac{\mathrm{d}E_J}{\mathrm{d}n} = \int \mathrm{d}\mathbf{x}' \, \frac{n(\mathbf{x}')}{|\mathbf{x}' - \mathbf{x}|} \equiv V_J(\mathbf{x}; n) \tag{2.33}$$

This defines the Hartree potential, where the notation $V_J(\mathbf{x}; n)$ means that it depends parametrically on the electron density n. The functional derivative of the interaction with the external potential is simply the external potential:

$$\frac{\mathrm{d}}{\mathrm{d}n}\left(\int \mathrm{d}\mathbf{x}\, n(\mathbf{x}) V_{\mathrm{ext}}(\mathbf{x})\right) = V_{\mathrm{ext}}(\mathbf{x}) \tag{2.34}$$

The only unknown term is the exchange-correlation functional. In analogy with the external and the Hartree potential, the exchange-correlation potential is introduced:

$$\frac{\mathrm{d}E_{\mathrm{xc}}}{\mathrm{d}n} \equiv V_{\mathrm{xc}}(\mathbf{x}; n) \tag{2.35}$$

The derivative of the Lagrangian constraints is:

$$\frac{\mathrm{d}}{\mathrm{d}\psi_i^*}\sum_{j=1}^{N_e} g_j = \psi_i \tag{2.36}$$

By inserting Equations (2.32)–(2.36) into Equation (2.28) we obtain:

$$-\frac{1}{2}\nabla_i^2\psi_i + (V_J + V_{\text{ext}} + V_{\text{xc}})\,\psi_i = \epsilon_i\psi_i \quad \forall i = 1 \dots N_e \tag{2.37}$$

This is similar to a one-particle Schrödinger equation:

$$\hat{H}_i^{\text{KS}}\psi_i = \epsilon_i\psi_i \tag{2.38}$$

with:

$$\hat{H}_i^{\text{KS}} = -\frac{1}{2}\nabla_i^2 + V_{\text{KS}}(\mathbf{x}; n) \tag{2.39}$$

The meaning of the initial assumption becomes now clear. The system is treated as a collection of noninteracting electrons that only interact with an effective potential $V_{\text{KS}} = V_J + V_{\text{ext}} + V_{\text{xc}}$. This effective potential does depend on the density implicitly, and therefore the system of equations needs to be solved self-consistently. How are the independent electron properties related to the true, fully interacting system? The answer resides solely in the exchange-correlation functional, which is the only unknown. The entire difficulty of the correlated many-body problem has been shifted into this one term, all other terms in Equation (2.29) are known analytically. Up to this point, density functional theory is exact (within the non-relativistic Born-Oppenheimer approximation).

2.1.3 Exchange-correlation functionals

As Equation (2.31) shows, the exchange-correlation functional contains all the "difficult" parts of the total energy: electron-electron correlation and a correction term for the kinetic energy. The exchange-correlation energy functional is written as:

$$E_{\text{xc}}[n] = \int \mathrm{d}\mathbf{x}\, n(\mathbf{x}) V_{\text{xc}}(\mathbf{x}; n) \tag{2.40}$$

If the mathematical form of this functional were known, DFT would be exact. The elegance of Kohn-Sham DFT is that even if exchange and correlation effects are not taken into

account, the Hartree energy, single-particle kinetic energy and interaction with the external potential typically account for more than 90% of the total energy in a system, and so if an approximation to the exchange-correlation energy can be found, close to 100% of the total energy can be recovered.

Unfortunately, it is very often exactly these very subtle correlation effects that are decisive for the properties of interest of a system. Determining energy differences between two systems can be compared to measuring the weight of the captain of a large ship by weighing the ship with and without the captain and then calculating the weight difference: even with a good relative precision of the measurement, the absolute error might still be larger than the quantity of interest.

Nevertheless, approximate expressions for the true exchange-correlation functional can be formulated. The earliest approximation for Kohn-Sham DFT was the local density approximation (LDA) that uses results from the uniform electron gas. The exact value of the exchange-correlation energy of a uniform electron gas of arbitrary density n_0 depends on the value of the density only and can be calculated numerically with great accuracy by using quantum Monte Carlo methods (briefly addressed in Section 1.3.1). The exchange-correlation energy of a uniform electron gas is then used in a system of varying density by the following approximate exchange-correlation potential:

$$V_{\mathrm{xc}}^{\mathrm{LDA}}(\mathbf{x}; n) = \frac{\epsilon\left(n(\mathbf{x})\right)}{n(\mathbf{x})} \tag{2.41}$$

where $\epsilon(n(\mathbf{x}))$ is the exchange-correlation energy of a uniform electron gas of density $n(\mathbf{x})$. In other words, the exchange-correlation potential at a certain point in space is treated as if the electron density in the system were uniform and equal to the electron density at this point. This simple approximation is able to produce remarkable results, but tends to overestimate bond strengths. An extension is the generalised gradient approximation (GGA), which includes dependence not only on the electron density, but its spatial gradients as well:

$$V_{\mathrm{xc}}^{\mathrm{GGA}}(\mathbf{x}) = f(\mathbf{x}, n(\mathbf{x}), \nabla n(\mathbf{x})) \tag{2.42}$$

Functionals of this form are local, that is they depend on only one location in space, as well as on the density and its derivatives at that location.

2.1.4 Bloch's theorem: periodic boundary conditions

This thesis is exclusively concerned with crystalline solids, which are inherently periodic systems. However, all condensed phases, including liquids, may be treated approximately as periodic systems by choosing a large enough periodic box (supercell) so that spurious self-interactions with periodic images are minimised. This also applies to disordered crystalline systems and point defects: the smallest periodically repeated unit must be large enough so that spurious spatial correlation is kept to a minimum. In this section, the lattice vectors, denoted by $\mathbf{T}$, refer to the translational symmetry of the supercell used in the simulations and not necessarily to the crystallographic lattice parameters of the system studied. A supercell might be constructed from an array of multiple crystallographic unit cells (referred to as primitive cells hereafter).

The translational symmetry implies that the external potential must be periodic since it is determined by the positions of the nuclei only, therefore the Hamiltonian and the electron density possess the same translational symmetry. Translational symmetry with respect to any lattice vector $\mathbf{T}$ is formally expressed by the translational operator $\hat{T}$:

$$\hat{T}\hat{H}(\mathbf{x}) = \hat{H}(\mathbf{x}+\mathbf{T}) = \hat{H}(\mathbf{x}) \tag{2.43}$$

$$\mathbf{T} = n_1\mathbf{a} + n_2\mathbf{b} + n_3\mathbf{c} \tag{2.44}$$

where $\mathbf{a}$, $\mathbf{b}$ and $\mathbf{c}$ are the primitive lattice vectors of the periodic box and n_1, n_2 and n_3 are any integer numbers. Because the translational operator leaves the Hamiltonian unchanged, the two operators commute and so the eigenfunctions of the Hamiltonian are at the same time eigenfunctions of all translational operators. Since all translational operators form a group, the eigenvalue must have an absolute value of unity. Any translational operator $\hat{T}$ can be expressed as a product of the primitive translations $\hat{T}_a$, $\hat{T}_b$, and $\hat{T}_c$. The

eigenvalue equations for the translational operators are:

$$\hat{T}\psi_i = \hat{T}_a^{n_1}\hat{T}_b^{n_2}\hat{T}_c^{n_3}\psi_i = t_a^{n_1}t_b^{n_2}t_c^{n_3}\psi_i \tag{2.45}$$

The eigenvalues t of the primitive translations are expressed as a complex phase:

$$t_a = e^{2\pi i k_1} \tag{2.46}$$

with k_1 unspecified at this point. We assume that the total system consists of $N_1 \times N_2 \times N_3$ supercells. The eigenvalue for $\mathbf{T} = 0$ must be equal to 1 as this corresponds to the identity operation, and the boundary conditions of the overall system dictate that the eigenvalue at the boundaries in each dimension must be the same. Therefore:

$$t_a^{N_1}t_b^{N_2}t_c^{N_3} = e^{2\pi i(k_1N_1+k_2N_2+k_3N_3)} = 1 \tag{2.47}$$

The sum in the exponential function must be equal to an integer number:

$$k_1N_1 + k_2N_2 + k_3N_3 = \mathbf{k}\cdot\mathbf{T} = m_1 + m_2 + m_3 \tag{2.48}$$

This defines the vector $\mathbf{k}$:

$$\mathbf{k} = \frac{m_1}{N_1}\mathbf{a}^* + \frac{m_2}{N_2}\mathbf{b}^* + \frac{m_3}{N_3}\mathbf{c}^* \tag{2.49}$$

where $\mathbf{a}^*$, $\mathbf{b}^*$ and $\mathbf{c}^*$ are the reciprocal lattice vectors. The Kohn-Sham orbitals in one supercell are therefore written as:

$$\psi_{i,\mathbf{k}}(\mathbf{x}) = e^{2\pi i\mathbf{k}\cdot\mathbf{x}}\, u_{i,\mathbf{k}}(\mathbf{x}) \tag{2.50}$$

$\mathbf{k}$ therefore takes the meaning of a quantum number and can be confined to the reciprocal unit cell as states with $\mathbf{k}' = \mathbf{G} + \mathbf{k}$, where $\mathbf{G}$ is a reciprocal lattice vector, are identical to

states with $\mathbf{k}$. The Kohn-Sham equations become:

$$\hat{H}^{\mathrm{KS}}_{i,\mathbf{k}}\, e^{2\pi i\mathbf{k}\cdot\mathbf{x}} u_{i,\mathbf{k}}(\mathbf{x}) = \epsilon_{i,\mathbf{k}}\, e^{2\pi i\mathbf{k}\cdot\mathbf{x}} u_{i,\mathbf{k}}(\mathbf{x}) \tag{2.51}$$

After left-multiplying by $e^{-2\pi i\mathbf{k}\cdot\mathbf{x}}$ we obtain, by making use of Equation (2.39):

$$-\frac{1}{2}(\nabla_i + i\mathbf{k})^2\, u_{i,\mathbf{k}}(\mathbf{x}) + V_{\mathrm{KS}}(\mathbf{x};n)\, u_{i,\mathbf{k}}(\mathbf{x}) = \epsilon_i\, u_{i,\mathbf{k}}(\mathbf{x}) \tag{2.52}$$

Therefore, instead of solving one Kohn-Sham equation for each electron in the overall system of $N_1 \times N_2 \times N_3$ supercells, one Kohn-Sham equation for each electron in one supercell is solved for each vector $\mathbf{k}$. The problem of an infinite number of electrons in a periodic crystal has been reduced to a problem of N_e electrons at an infinite number of $\mathbf{k}$-points within the reciprocal unit cell. However, it is found that the Bloch functions at $\mathbf{k}$-points that lie very close to each other are very similar. Therefore, $\mathbf{k}$-space can be sampled by a finite number of points and the Kohn-Sham equations are solved on a regular grid of $\mathbf{k}$-points.

2.1.5 Basis sets: plane waves

Because of Bloch's theorem, the Kohn-Sham equations can be Fourier transformed into reciprocal space. The Fourier transform of a periodic function, such as the Bloch functions, is:

$$u_{i,\mathbf{k}}(\mathbf{G}) = \sum_{\mathbf{T}} \int_{\Lambda} \mathrm{d}\mathbf{x}\, u_{i,\mathbf{k}}(\mathbf{x})\, e^{-2\pi i(\mathbf{x}+\mathbf{T})\cdot\mathbf{G}} = \left(\sum_{\mathbf{T}} e^{-2\pi i\mathbf{T}\cdot\mathbf{G}}\right) \int_{\Lambda} \mathrm{d}\mathbf{x}\, u_{i,\mathbf{k}}(\mathbf{x})\, e^{-2\pi i\mathbf{x}\cdot\mathbf{G}} \tag{2.53}$$

where Λ designates the supercell volume (the symbol V is not used here to avoid confusion with the notation for potentials). The Fourier transform is only nonzero at reciprocal lattice vectors $\mathbf{G} = g_1\mathbf{a}^* + g_2\mathbf{b}^* + g_3\mathbf{c}^*$. The same applies for the potential:

$$V_{\mathrm{KS}}(\mathbf{G};n) = \Lambda^{-1} \int_{\Lambda} \mathrm{d}\mathbf{x}\, V_{\mathrm{KS}}(\mathbf{x};n)\, e^{-2\pi i\mathbf{x}\cdot\mathbf{G}} \tag{2.54}$$

The kinetic energy operator is easily transformed into Fourier space by the basic properties of Fourier transforms. The Fourier transform of a product of two functions is equal to the convolution of the Fourier transforms of the two functions. Hence the Kohn-Sham equations in Fourier space are:

$$\frac{1}{2}(\mathbf{G}+\mathbf{k})^2 u_{i,\mathbf{k}}(\mathbf{G}) + \sum_{\mathbf{G}'} V_{\mathrm{KS}}(\mathbf{G}';n)\, u_{i,\mathbf{k}}(\mathbf{G}-\mathbf{G}') = \epsilon_i\, u_{i,\mathbf{k}}(\mathbf{G}) \tag{2.55}$$

To numerically solve these equations, the Bloch functions are expressed as a basis set expansion. For periodic systems, the basis set of plane waves is a natural choice, since the expansion coefficients are identical to the Fourier components.

$$u_{i,\mathbf{k}}(\mathbf{x}) = \sum_{\mathbf{G}}^{|\mathbf{G}|<G_{\max}} u_{i,\mathbf{k}}(\mathbf{G}) e^{2\pi i \mathbf{G}\cdot\mathbf{x}} \tag{2.56}$$

The set of plane waves is complete and orthonormal, but in practice only a finite number of plane waves can be considered, limited by a chosen maximum wave vector $G_{\max}$.

This transforms the Kohn-Sham equation into a matrix equation for the vector of plane wave expansion coefficients. Instead of finding the eigenfunctions, we now need to find the eigenvectors according to the equation:

$$\mathsf{H}^{\mathrm{KS}}_{i,\mathbf{k}}\, \mathbf{u}_{i,\mathbf{k}} = \epsilon_{i,\mathbf{k}}\, \mathbf{u}_{i,\mathbf{k}} \tag{2.57}$$

The Kohn-Sham matrix is given by:

$$\left(\mathsf{H}^{\mathrm{KS}}_{i,\mathbf{k}}\right)_{a,b} = \frac{1}{2}(\mathbf{G}_a+\mathbf{k})^2\, \delta_{\mathbf{G}_a,\mathbf{G}_b} + V(\mathbf{G}_a-\mathbf{G}_b;n) \tag{2.58}$$

where $\delta_{\mathbf{G}_a,\mathbf{G}_b}$ is the Kronecker delta and the entries of the component vector are given by:

$$\left(\mathbf{u}_{i,\mathbf{k}}\right)_a = u_{i,\mathbf{k}}(\mathbf{G}_a) \tag{2.59}$$

Each row/column of the Kohn-Sham matrix and each entry of the component vector

corresponds to a plane wave vector in the basis set. To solve Equation (2.57), the elements of the Kohn-Sham matrix must first be computed. For this, it is necessary to define the maximum dimensions of the matrix, that is, the maximum number of plane waves. Since the number of plane waves resulting from a maximum wave vector depends on the size of the cell, a varying cell size would imply a varying basis set quality. The number of plane waves included is therefore specified by a cut-off energy: since plane waves are the eigenfunctions of a free particle with only kinetic energy, the cut-off energy specifies the maximum kinetic energy of the plane waves that are to be included in the basis set. This parameter is independent of supercell size and is given by (in atomic units):

$$E_{\text{cut}} = \frac{1}{2} G_{\text{max}}^2 \tag{2.60}$$

Therefore, all plane waves $\mathbf{G}$ are included for which:

$$|\mathbf{G}| < \sqrt{2E_{\text{cut}}} \tag{2.61}$$

2.1.6 Dual basis sets: the Quickstep method

Plane waves are not the only basis functions that can be used; any complete, orthonormal set of functions can be used as a basis. The Kohn-Sham orbitals, Equation (2.25), can also be expanded in a set of Gaussian functions χ:

$$\psi_i(\mathbf{x}) = \sum_{\mu} p_{i,\mu} \chi_\mu(\mathbf{x}) \tag{2.62}$$

The functions $\chi_\mu(\mathbf{x})$ are typically atom-centred three-dimensional Gaussian functions. The density is expressed as:

$$n(\mathbf{x}) = \sum_{i}^{N_e} \sum_{\mu,\nu} p_{i,\mu} p_{i,\nu} \chi_\mu^*(\mathbf{x}) \chi_\nu(\mathbf{x}) \tag{2.63}$$

VandeVondele *et al.* (2005) introduced a method that uses a Gaussian and a plane wave basis set at the same time to achieve faster computation. A representation of the electron density $n_{\text{pw}}(\mathbf{x})$ in a plane wave basis is constructed such that $n_{\text{pw}}(\mathbf{x}) = n(\mathbf{x})$. The electron

density in the plane wave basis set is given by:

$$n_{\mathrm{pw}}(\mathbf{x}) = \sum_{\mathbf{G}}^{|\mathbf{G}<G_{\max}|} n_{\mathrm{pw}}(\mathbf{G}) e^{2\pi i \mathbf{G}\cdot\mathbf{x}} \tag{2.64}$$

and the plane wave expansion coefficients are given by the Fourier transform of the density expressed in the Gaussian basis:

$$n_{\mathrm{pw}}(\mathbf{G}) = \int \mathrm{d}\mathbf{x}\, n(\mathbf{x}) e^{-2\pi i \mathbf{G}\cdot\mathbf{x}} \tag{2.65}$$

The evaluation of the total energy functional then makes use of the Gaussian representation for the evaluation of the kinetic energy and of the interaction energy with the external potential. The plane wave representation is used to evaluate the electron-electron interaction energy.

$$\begin{aligned} E[n] = \sum\sum p_{i,\mu} p_{i,\nu} \left(\left\langle \chi_\mu \left| -\frac{1}{2}\nabla^2 \right| \chi_{nu} \right\rangle + \langle \chi_\mu \left| V_{\mathrm{ext}} \right| \chi_\nu \rangle \right) \\ + \int \mathrm{d}\mathbf{x}\, \mathrm{d}\mathbf{x}' \, \frac{n_{\mathrm{pw}}(\mathbf{x})\, n_{\mathrm{pw}}(\mathbf{x}')}{|\mathbf{x}-\mathbf{x}'|} + \int \mathrm{d}\mathbf{x}\, V_{\mathrm{xc}}(\mathbf{x})\, n_{\mathrm{pw}}(\mathbf{x}) + V_{nn} \end{aligned} \tag{2.66}$$

This is computationally very efficient if the external potential is represented by pseudopotentials, which will be discussed in the following section.

2.1.7 Pseudopotentials

Plane waves are the exact solutions of the homogeneous electron gas and therefore represent electrons that have a free electron character, such as the valence electrons of most systems, especially metals. Core electrons, in contrast, are highly localised around the nucleus and are therefore less well represented by plane waves: an extremely large number of plane waves are necessary for an accurate representation. Furthermore, since they are strongly bound to the nucleus, the total energy of the system is dominated by the energy of the core electrons and so most of the computational effort is needed to obtain accurate energies for the core electrons. But since their state and influence changes little between

different chemical environments, a "frozen-core" approximation is valid and they need not be treated with the full variational freedom of the valence electrons. By the pseudopotential approach, the core electrons are incorporated into the potential of the nuclei and only the valence electrons are described by Kohn-Sham orbitals.

Since core electrons are largely unaffected by the chemical environment, pseudopotentials are transferable: the same pseudopotential for a specific element can give accurate results in different chemical environments. Therefore, pseudopotentials can be developed by treating each element separately as an isolated atom. The accuracy of a pseudopotential is judged by comparing the resulting total energies (or forces, or other property of interest) to the result of an all-electron calculation, without pseudopotentials. The general method for generating a pseudopotential as well as the pseudopotential methods used in this thesis are described in the following paragraphs.

We consider an atom with nuclear charge Z and consequently Z electrons. The all-electron (AE) wave functions are the Kohn-Sham orbitals, solutions to Equation (2.37), and are labelled by quantum numbers n, l, m according to the Aufbau principle.

$$\psi^{\mathrm{AE}}_{n,l,m}(\mathbf{x}) = R^{\mathrm{AE}}_{nl}(x) Y^m_l(\phi,\theta) \tag{2.67}$$

Since the potential is radially symmetric, the atomic wave functions can be separated into the usual radial part, $R^{\mathrm{AE}}_{nl}(x)$, depending only on the distance $x = |\mathbf{x}|$ from the nucleus, and into the angular part which are the spherical harmonics $Y^m_l(\phi,\theta)$. For each electron, the Kohn-Sham equation has the form of a hydrogenic Schrödinger equation (SE):

$$\left(-\frac{1}{2}\nabla^2 + V^{\mathrm{AE}}_{\mathrm{KS}}(x; n^{\mathrm{AE}})\right) \psi^{\mathrm{AE}}_{n,l,m}(\mathbf{x}) = \epsilon^{\mathrm{AE}}_{n,l,m}\, \psi^{\mathrm{AE}}_{n,l,m}(\mathbf{x}) \tag{2.68}$$

where the potential $V^{\mathrm{AE}}_{\mathrm{KS}}(x; n^{\mathrm{AE}})$ is assumed to be spherical and is given by:

$$V^{\mathrm{AE}}_{\mathrm{KS}}(x) = -\frac{Z}{x} + V_J(x; n^{\mathrm{AE}}) + V_{\mathrm{xc}}(x; n^{\mathrm{AE}}) \tag{2.69}$$

The aim of the pseudopotential method is to replace the external potential by a pseu-

dopotential $V^{\mathrm{PP}}(x)$ so that the SE equations for the valence orbitals result in the same eigenvalues as the all-electron SE:

$$\left(-\frac{1}{2}\nabla^2 + V^{\mathrm{PP}}(x) + V_J(x; n^{\mathrm{PS}}) + V_{\mathrm{xc}}(x; n^{\mathrm{PS}})\right) \psi_j^{\mathrm{PS}}(\mathbf{x}) = \epsilon_j^{\mathrm{AE}} \psi_j^{\mathrm{PS}}(\mathbf{x}) \tag{2.70}$$

The (pseudo) valence electron density is given by:

$$n^{\mathrm{PS}}(\mathbf{x}) = \sum_{j=1}^{N_v} \left|\psi_j^{\mathrm{PS}}(\mathbf{x})\right|^2 \tag{2.71}$$

where j is an index running over all valence eigenfunctions only, and N_v is the number of valence electrons.

The atomic SE is separated into the angular and the radial equation. The angular equation does not depend on the potential and is therefore of no interest in this discussion as its solutions are the habitual spherical harmonics; the radial equation has the same form as in the case of the hydrogen atom:

$$\left(-\frac{1}{2}\frac{\mathrm{d}^2}{\mathrm{d}x^2} + \frac{l(l+1)}{2x^2} + V_{\mathrm{KS}}^{\mathrm{AE}}(x; n^{\mathrm{AE}})\right) x\, R_{nl}^{\mathrm{AE}}(x) = \epsilon_i^{\mathrm{AE}} R_{nl}^{\mathrm{AE}}(x) \tag{2.72}$$

The all-electron radial equations are solved numerically on a logarithmic radial grid to high precision, without the use of any basis set. With the radial wave functions known, the atomic SE is then inverted to solve it for the potential $V_{\mathrm{KS}}^{\mathrm{AE}}(x)$, which is then equated to the pseudopotential form:

$$\begin{aligned} V_{\mathrm{KS}}^{\mathrm{AE}}(x; n^{\mathrm{AE}}) = \epsilon_{i,l}^{\mathrm{AE}} - \frac{l(l+1)}{2x^2} + \frac{1}{2xR_{n,l}(x)}\frac{\mathrm{d}^2(xR_{n,l}(x))}{\mathrm{d}x^2} \\ = V_l^{\mathrm{PP}}(x) + V_J(x; n^{\mathrm{PS}}) + V_{\mathrm{xc}}(x; n^{\mathrm{PS}}) \end{aligned} \tag{2.73}$$

This equation defines the pseudopotential $V_l^{\mathrm{PP}}(x)$. The right-hand side in the above equation is called the screened potential, because it is equal to the nuclear potential screened by the Hartree and exchange-correlation potentials for the all-electron density; to obtain the pseudopotential, it must be unscreened with the Hartree and exchange-

correlation potentials for the valence electron density. The pseudopotential is dependent on the angular moment l in general. For the generation of a pseudopotential, the following considerations must be made:

- For which exchange-correlation functional should pseudopotentials be generated.
- For which electron configuration should the pseudopotential of the atom in question be generated. For example, for C, one could choose $1s^2 2s^2 2p^2$, or $1s^2 2s^1 2p^3$. This is important in order to assign the correct angular momentum l to each atomic orbital.
- Which electrons are included in the core, and which ones are valence electrons. For example, for C, the core electrons are usually $1s^2$, whereas for Li all electrons might need to be treated as valence electrons. Even in the latter case a pseudopotential can be generated.
- Which functional form for the pseudopotential should be chosen.

The first three points are application-dependent; for the last point, several pseudopotential schemes have been proposed.

The Hamann-Schlüter-Chiang (HSC) pseudopotential method (Hamann *et al.*, 1979) introduced the norm-conservation criterion that was important for almost all subsequent pseudopotential methods. The pseudopotential generation scheme depends on only one variable parameter: the cut-off radius r_{cl} for each angular momentum l. The all-electron potential is replaced by a pseudopotential $V^{\mathrm{HSC}}(x)$, and the wave functions for the valence electrons are replaced by pseudo wave functions $\psi^{\mathrm{PS}}(\mathbf{x})$ which satisfy the following criteria:

1. $\epsilon_j^{\mathrm{PS}} = \epsilon_j^{\mathrm{AE}}$ for the valence electrons.
2. The wave functions for the valence electrons agree beyond the cut-off: $\psi_j^{\mathrm{PS}}(x) = \psi_j^{\mathrm{AE}}(x) \quad \forall \quad x > r_{cl}$
3. Norm-conservation: $\int_0^r \mathrm{d}x\, \psi_j^{\mathrm{AE}}(x) = \int_0^r \mathrm{d}x\, \psi_j^{\mathrm{PS}}(x) \quad \forall \quad r > r_{cl}$
4. For $x \geq r_{cl}$, $L_l^{\mathrm{AE}}(x) = \frac{\mathrm{d}(\ln \psi_{j(l)}^{\mathrm{AE}}(x))}{\mathrm{d}x} = L_l^{\mathrm{PS}}(x)$ and $\frac{\mathrm{d}L_l^{\mathrm{AE}}(x)}{\mathrm{d}\epsilon} = \frac{\mathrm{d}L_l^{\mathrm{AE}}(x)}{\mathrm{d}\epsilon}$. This smoothness

and continuity criterion ensures a large degree of transferability of the pseudopotential.

The final atomic pseudopotential is written as:

$$V^{\mathrm{HSC}}(x) = \sum_{l,m} |Y_l^m\rangle \, V_l(x) \, \langle Y_l^m| \tag{2.74}$$

where the functional form of $V_l(x)$ contains adjustable constants that are fitted to satisfy the four criteria above and is angular momentum-dependent. The spherical harmonics projectors select the atomic character from any wave function (e. g. in a molecular or solid state calculation) and apply the correct angular momentum pseudopotential to it. However, these nonlocal projectors turn out to be quite inefficient in plane wave calculations.

Kleinman and Bylander (1982) proposed a transformation of a nonlocal pseudopotential into a semilocal form that is more efficient in calculations with plane waves. Parting from a pseudopotential of the HSC form, as in Equation (2.74), an arbitrarily chosen local potential function $V_L(x)$ is added and subtracted to obtain:

$$V^{\mathrm{KB}}(x) = V_L(x) + \sum_{l,m} |Y_l^m\rangle \, (V_l(x) - V_L(x)) \, \langle Y_l^m| = V_L(x) + V_{NL}(x) \tag{2.75}$$

The pseudopotential remains unchanged, but is now written in a local component (independent of angular momentum) and a nonlocal component $V_{NL}(x)$. A typical choice is to set the local potential equal to the highest angular momentum potential present in the atom, $V_L(x) = V_{l_{\max}}(x)$. The Kleinman-Bylander form of a pseudopotential is then written as:

$$V^{\mathrm{KB}}(x) = V_{l_{\max}}(x) + \sum_{l,m} |\beta_{l,m}\rangle \, B_{l,m} \, \langle \beta_{l,m}| \tag{2.76}$$

The projectors are strictly zero outside the core radius. The local potential is equal to the all-electron Coulomb potential outside the core radius. In the KB scheme, the projectors

and the constants $B_{l,m}$ are given by:

$$|\beta_{l,m}\rangle = \left|(V_l - V_{l_{\max}})\psi^{\mathrm{PS}}_{l,m}\right\rangle \tag{2.77}$$

$$B_{l,m} = \frac{1}{\left\langle \psi^{\mathrm{PS}}_{l,m} \left| V_l - V_{l_{\max}} \right| \psi^{\mathrm{PS}}_{l,m} \right\rangle} \tag{2.78}$$

where $\psi^{\mathrm{PS}}_{l,m}$ are the pseudo wave functions for which the original HSC pseudopotential was generated. The projector is zero outside the core region because $V_l(x) = V_{l_{\max}}(x)$ outside the core radius. It can be seen that this is equivalent to the original HSC pseudopotential if we apply this potential to any pseudo valence wave function $\psi^{\mathrm{PS}}_{l',m'}$:

$$V^{\mathrm{KB}} \left|\psi^{\mathrm{PS}}_{l',m'}\right\rangle = V_L \left|\psi^{\mathrm{PS}}_{l',m'}\right\rangle + \sum_{l,m} \frac{\left|(V_l - V_L)\psi^{\mathrm{PS}}_{l,m}\right\rangle \left\langle \psi^{\mathrm{PS}}_{l,m}(V_l - V_L)\right| \psi^{\mathrm{PS}}_{l',m'}\right\rangle}{\left\langle \psi^{\mathrm{PS}}_{l,m} \left| (V_l - V_L \right| \psi^{\mathrm{PS}}_{l,m} \right\rangle} \tag{2.79}$$

The second term in the numerator is:

$$\langle \psi_l (V_l - V_L) | \psi_{l'} \rangle = \langle Y^m_l | Y^m_{l'} \rangle \left\langle R^{\mathrm{PS}}_{nl} \left| V_l - V_L \right| R^{\mathrm{PS}}_{nl'} \right\rangle \tag{2.80}$$

This is zero if $l' \neq l$ and equal to the denominator if $l' = l$ and $m' = m$, and thus:

$$V^{\mathrm{KB}} \left|\psi^{\mathrm{PS}}_{l',m'}\right\rangle = V_{l'} \left|\psi^{\mathrm{PS}}_{l',m'}\right\rangle \tag{2.81}$$

For calculations with plane waves, three pseudopotential methods that are variations of the Kleinman-Bylander pseudopotential form are used in this thesis. The method by Goedecker *et al.* (1996) emphasises efficiency of integration in both real and Fourier space. The local and nonlocal potentials are written in a parametrised form that can be transformed analytically into Fourier space, reducing the computational effort for calculating the Kohn-Sham matrix elements with a plane wave basis set.

The optimised pseudopotentials by Rappe *et al.* (1990) take into account the special properties of plane wave basis sets and optimise the plane wave cut-off behaviour, so that calculations of quantities of interest are converged at as low a plane wave cut-off energy as

possible, as convergence in a solid is governed by the convergence of the pseudoatoms. The optimisation is implemented by requiring pseudopotentials to be continuous and smooth and by optimising the kinetic-energy convergence, to within a specific tolerance level in as small a basis as possible.

To achieve this, the kinetic energy in the high kinetic energy Fourier components of the pseudo wave function is minimised. If the kinetic energy of a pseudo wave function is distributed mainly among the low wave vector Fourier components, the kinetic energy will converge much faster with respect to cut-off energy. The Rappe scheme requires an additional optimisation parameter to be specified: the cut-off wave vector, G_c. The kinetic energy of the Fourier components with $G_j > G_c$ is minimised. The pseudopotential generation method replaces the all-electron wave function by a parametric pseudo wave function expanded in Bessel functions of the first kind (radial plane waves):

$$R_{nl}^{\mathrm{PS}}(x) = \begin{cases} \sum_{k=1}^{4} \alpha_k j_l(G_k x) + \sum_{p=1}^{n} \beta_p j_l(G_p x) & \forall \quad x \leq r_c \\ \sum_{k=1}^{4} \alpha_k j_l(G_k x) & \forall \quad x > r_c \end{cases} \tag{2.82}$$

The wave vectors G_k are chosen such that the pseudo wave function joins the all-electron wave function smoothly at $x = r_c$, and the wave vectors G_p are chosen such that $j_l(G_p r_c) = 0$. In a first step, the parameters α_k and β_p are optimised such that the kinetic energy of the wave function due to plane waves with a wave vector larger than G_c is minimised. This is achieved by minimising the following function:

$$p(\alpha_k, \beta_p) = -\frac{1}{2} \int \mathrm{d}\mathbf{x}\, \psi_{l,m}^{\mathrm{PS}*}(\mathbf{x}) \nabla^2 \psi_{l,m}^{\mathrm{PS}}(\mathbf{x}) - \frac{1}{2} \int_0^{G_C} \mathrm{d}G\, G^2 \psi_{l,m}^{\mathrm{PS}*}(G) \psi_{l,m}^{\mathrm{PS}}(G) + h(\alpha_k, \beta_p) \tag{2.83}$$

The first term is the total kinetic energy, the second term subtracts the kinetic energy due to plane waves up to wave vector G_C, and $h(\alpha, \beta)$ are Lagrangian constraints that ensure normalisation and smooth joining of the all-electron wave function at r_c (HSC criterion number 4 on page 39). From this wave function, the pseudopotential (in Kleinman-Bylander form) is generated by inverting the atomic SE.

Vanderbilt (1990) constructs ultrasoft pseudopotentials in nonlocal Kleinman-Bylander form by dropping the strict norm-conservation criterion. The starting point is a Kleinman-Bylander pseudopotential:

$$V^{\mathrm{USP}}(x) = V_L(x) + \sum_{i,j} \mathsf{B}_{ij} \left|\beta_i\right\rangle \left\langle\beta_j\right| \tag{2.84}$$

The projectors $|\beta_i\rangle$ and the matrix B are defined as:

$$\mathsf{B}_{ij} = \left\langle \psi_i^{\mathrm{PS}} \middle| \epsilon_i - \hat{T} - V_L \middle| \psi_j^{\mathrm{PS}} \right\rangle \tag{2.85}$$

$$\left|\beta_i\right\rangle = \sum_j \left(\mathsf{B}^{-1}\right)_{ji} \left(\epsilon_i - \hat{T} - V_L\right) \left|\psi_j^{\mathrm{PS}}\right\rangle \tag{2.86}$$

where ψ_i^{PS} are the pseudo wave functions solved for an eigenvalue ϵ_i. It is found that $\left(\hat{T} + V^{\mathrm{USP}}\right) \left|\psi_i^{\mathrm{PS}}\right\rangle = \epsilon_i \left|\psi_i^{\mathrm{PS}}\right\rangle$. The projectors are made ultrasoft by relaxing the norm-conserving criterion. The norm-conserving matrix Q is not required to be zero:

$$\mathsf{Q}_{ij} = \left\langle \psi_i^{\mathrm{AE}} \middle| \psi_j^{\mathrm{AE}} \right\rangle - \left\langle \psi_i^{\mathrm{PS}} \middle| \psi_j^{\mathrm{PS}} \right\rangle \tag{2.87}$$

The nonlocal potential is now redefined to obtain the ultrasoft pseudopotential:

$$V^{\mathrm{USP}}(x) = V_L(x) + \sum_{i,j} \mathsf{D}_{ij} \left|\beta_i\right\rangle \left\langle\beta_j\right| \tag{2.88}$$

with:

$$\mathsf{D}_{ij} = \mathsf{B}_{ij} + \epsilon_j \mathsf{Q}_{ij} \tag{2.89}$$

The relaxation of the norm-conservation means that an overlap operator must be introduced:

$$\hat{S} = 1 + \sum_{i,j} \mathsf{Q}_{ij} \left|\beta_i\right\rangle \left\langle\beta_j\right| \tag{2.90}$$

The eigenvalue equation modifies to:

$$\left(\hat{T} + \hat{V}^{\mathrm{USP}}\right) \left|\psi_i\right\rangle = \epsilon_i \hat{S} \left|\psi_i\right\rangle \tag{2.91}$$

and the habitual norm-conservation criterion is now modified to:

$$\left\langle \psi_i^{\mathrm{PS}} \middle| \hat{S} \middle| \psi_i^{\mathrm{PS}} \right\rangle = \left\langle \psi_i^{\mathrm{AE}} \middle| \psi_i^{\mathrm{AE}} \right\rangle \tag{2.92}$$

If $\mathsf{Q}_{ij} \neq 0$, B is not a Hermitian matrix, but D and Q nevertheless are, and therefore $\hat{S}$ and $\hat{H}$ are Hermitian operators. The only condition on the pseudopotential generation is that the all-electron and pseudo wave functions join up smoothly at the cut-off radius.

The lack of norm-conservation makes changes in the Kohn-Sham equations for a crystal system necessary. Denoting the Kohn-Sham orbitals of a general periodic system by $\phi_{n,\mathbf{k}}(\mathbf{x})$, they have to be normalised according to:

$$\langle \phi_{n,\mathbf{k}} | \, \hat{S} \, | \phi_{n',\mathbf{k}} \rangle = \delta_{nn'} \tag{2.93}$$

The other change is in the calculation of the charge density, which must be modified so as to include the so-called *augmentation charges* which correct for the lack of norm-conservation and ensure that the charge density integrates to N_v, the total number of (valence) electrons.

$$n^{\mathrm{PS}}(\mathbf{x}) = \sum_{n,\mathbf{k}} \phi^*_{n,\mathbf{r}}(\mathbf{x}) \phi_{n,\mathbf{k}}(\mathbf{x}) + \sum_{i,j} \rho_{ij} Q_{ij}(\mathbf{x}) \tag{2.94}$$

with:

$$\rho_{ij} = \sum_{n,\mathbf{k}} \langle \beta_i | \, \phi_{n,\mathbf{k}} \rangle \, \langle \phi_{n,\mathbf{k}} | \, \beta_j \rangle \tag{2.95}$$

$$Q_{ij}(\mathbf{x}) = \psi_i^{\mathrm{AE}*}(\mathbf{x}) \psi_j^{\mathrm{AE}}(\mathbf{x}) - \psi_i^{\mathrm{PS}*}(\mathbf{x}) \psi_i^{\mathrm{PS}}(\mathbf{x}) \tag{2.96}$$

$Q_{ij}(\mathbf{x})$ represents the augmentation charge density.

Ultrasoft pseudopotentials are the most efficient in plane wave calculations and are used wherever possible. Due to the complications arising from the augmentation charges in response calculations, the norm-conserving Rappe pseudopotentials are used instead, which are also very efficient with plane waves. The Goedecker pseudopotentials are less

efficient than the former two methods with plane waves as they are relatively hard and require a large basis set for accurate representations; however, their analytical simplicity and efficient Fourier transformation make them the first choice for methods that use Gaussian basis sets.

2.1.8 Geometry optimisation

For this thesis, the main interest is in modelling the atomic structure of a material, therefore the electronic structure is only indirectly relevant as it allows us to calculate the forces and force constants acting on the nuclei from first principles. As a consequence of the Born-Oppenheimer approximation, the positions of the nuclei enter the quantum mechanical treatment of the electrons only as constant parameters; the total energy evaluated from the Kohn-Sham energy functional therefore depends parametrically on the nuclear positions. The most stable atomic structure can be found by minimising this energy with respect to the nuclear positions since the most stable structure has the lowest energy, therefore in the equilibrium structure:

$$\frac{\partial E}{\partial \mathbf{r}_i} = -\mathbf{F}_i = 0 \tag{2.97}$$

for all atoms i, that is, all atomic forces must be zero in equilibrium.

Quantum mechanically, the forces are given by:

$$\mathbf{F}_i = -\left\langle \Psi_0 \left| \frac{\partial}{\partial \mathbf{r}_i} \hat{H} \right| \Psi_0 \right\rangle - \left\langle \frac{\partial}{\partial \mathbf{r}_i} \Psi_0 \left| \hat{H} \right| \Psi_0 \right\rangle - \left\langle \Psi_0 \left| \hat{H} \right| \frac{\partial}{\partial \mathbf{r}_i} \Psi_0 \right\rangle \tag{2.98}$$

Because of the variational principle, the ground state wave function is at an extremal point with respect to any parameter variation, and therefore the two last terms are zero, so the force is:

$$\mathbf{F}_i = \left\langle \Psi_0 \left| \frac{\partial}{\partial \mathbf{r}_i} \hat{H} \right| \Psi_0 \right\rangle \tag{2.99}$$

In density functional theory, taking density as the basic variable, the forces are given by

the gradient of the total energy functional:

$$\mathbf{F}_i = -\frac{\partial E[n_0]}{\partial \mathbf{r}_i} = -\int \mathrm{d}\mathbf{x}\, \frac{\partial V_{\mathrm{ext}}}{\partial \mathbf{r}_i} n_0(\mathbf{x}) - \int \mathrm{d}\mathbf{x}\, V_{\mathrm{ext}}(\mathbf{x}) \frac{\partial n_0}{\partial \mathbf{r}_i} - \frac{\partial V_{II}}{\partial \mathbf{r}_i} \tag{2.100}$$

Again, any derivative of the electron density with respect to nuclear coordinates is zero because of HKII. This is only true if the density n_0 is the exact ground state density; in the case of an approximation, these terms, which are called the Hellmann-Feynman forces, do not vanish and must be taken into account.

This can be generalised to the computation of any linear response. Thus, the stress tensor is given by:

$$\sigma_{i,j} = -\frac{E[n_0]}{\partial u_{i,j}} \tag{2.101}$$

where $u_{i,j}$ is the macroscopic strain, that is a deformation of the unit cell.

Determining an equilibrium structure requires the simultaneous numerical minimisation of Equation (2.100), and of Equation (2.101) if the cell shape and volume are to be minimised as well. These equations can be minimised by numerical minimisation methods if a starting set of nuclear coordinates (input structure) is given; numerical optimisation techniques applied to *ab initio* simulations are reviewed by Payne *et al.* (1992).

2.2 Lattice dynamics

In the previous section, the quantum mechanical method for determining the electronic ground state was described, which can be combined with minimisation techniques to find the equilibrium structure of a system. Invoking the Born-Oppenheimer approximation, the quantum mechanical problem of the nuclei can now be separately solved. The nuclei move in a Hamiltonian given by:

$$\left(-\sum_{i=1}^{N} \frac{\hbar^2}{2m_i} \nabla_i^2 + E(\mathbf{r}_i, \ldots, \mathbf{r}_N) \right) \Psi_n(\mathbf{r}_1, \ldots, \mathbf{r}_N) = E_n \Psi_n(\mathbf{r}_1, \ldots, \mathbf{r}_N) \tag{2.102}$$

where $E(\mathbf{r}_i, \ldots, \mathbf{r}_N)$ is the electronic ground state energy as a (parametric) function of the nuclear positions, according to the previous section.

For a system with N atoms that are all at their equilibrium position $\mathbf{r}_i^0$, the total energy can be expanded in a Taylor series with respect to the mass-weighted nuclear Cartesian coordinates $\mathbf{u}_i = \sqrt{m_i}\left(\mathbf{r}_i - \mathbf{r}_i^0\right)$:

$$E(\mathbf{u}_{1\ldots N}) = E_0 + \sum_i \left(\frac{\partial E}{\partial \mathbf{u}_i}\right) \cdot \mathbf{u}_i + \frac{1}{2}\sum_{i=1}^{N}\sum_{j=1}^{N}\left(\frac{\partial^2 E}{\partial \mathbf{u}_i \otimes \partial \mathbf{u}_j}\right)\mathbf{u}_i \cdot \mathbf{u}_j + \ldots \tag{2.103}$$

The ground state energy E_0 is a constant that will be ignored in the following; the first derivatives are by definition zero at equilibrium positions, and, in the harmonic approximation, all higher terms beyond the second derivatives are neglected. Thus the potential energy from the harmonic nuclear vibrations is given by:

$$E_{\mathrm{HA}}(\mathbf{u}_{1\ldots N}) = \frac{1}{2}\sum_{ij}\left(\frac{\partial^2 E}{\partial \mathbf{u}_i \otimes \partial \mathbf{u}_j}\right)\mathbf{u}_i \cdot \mathbf{u}_j = \frac{1}{2}\sum_{ij}\mathsf{k}_{ij}\mathbf{u}_i \cdot \mathbf{u}_j \tag{2.104}$$

k_{ij} are the force constant matrices and describe the force experienced by nucleus i if nucleus j is displaced (or vice versa).

The normal mode displacement vectors of this harmonic system can be determined if the force-constant matrix is known; computation of the full force constant matrix is addressed at the end of this section. The individual components of all $\mathbf{u}_i$ are combined linearly to form a new set of $3N$ vectors $\mathbf{Q}_i$:

$$\mathbf{Q}_i = Q_i \mathbf{c}_i \tag{2.105}$$

The linear expansion coefficient vectors $\mathbf{c}_i$ are chosen such that $\mathbf{c}_i \cdot \mathbf{c}_j = \delta_{ij}$. As a consequence, the force constant matrix k is transformed into a diagonal matrix λ and Equation (2.104) becomes:

$$E_{\mathrm{HA}}(\mathbf{Q}_i) = \frac{1}{2}\sum_i \lambda_i \mathbf{Q}_i^2 \tag{2.106}$$

This is achieved by finding the eigenvectors and eigenvalues of k, that is by solving the

following linear equation for each vector $\mathbf{c}_i$:

$$(\mathsf{k} - \lambda_i \mathsf{l})\mathbf{c}_i = 0 \tag{2.107}$$

With the normal mode force constants λ_i and the normal mode eigenvectors $\mathbf{c}_i$ known, the quantum harmonic oscillator problem becomes a sum of independent oscillators.

$$\hat{H} = \sum_{i=1}^{3N} \left(-\frac{1}{2}\hbar^2 \nabla_i^2 + \frac{1}{2}\lambda_i Q_i^2 \right) \tag{2.108}$$

Therefore, the wave function can be written as a product of wave functions depending on normal mode amplitude Q_i:

$$\Psi(\mathbf{r}_1, \ldots, \mathbf{r}_N) = \prod_i \Psi_i(Q_i) \tag{2.109}$$

Each normal mode therefore has the following Schrödinger equation:

$$\left(-\frac{1}{2}\hbar^2 \nabla_i^2 + \frac{1}{2}\lambda_i Q_i^2 \right) \Psi_{i,n}(\mathbf{Q}_i) = \epsilon_{i,n} \Psi_{i,n}(\mathbf{Q}_i) \tag{2.110}$$

The solutions are well known. The energy levels are given by:

$$\epsilon_{i,n} = \hbar\omega_i \left(n + \frac{1}{2} \right) \tag{2.111}$$

The mode frequency ω_i follows from the diagonalised force constant matrix:

$$\omega_i = \sqrt{\lambda_i} \tag{2.112}$$

In an infinite periodic crystal there are an infinite number of normal modes. In analogy with the Bloch theorem for electronic states, the periodicity of the force constant matrix is used:

$$\mathsf{k}_{i,j} = \mathsf{k}_{i+\mathbf{T},j+\mathbf{T}} \tag{2.113}$$

The meaning of this notation is that the force constant matrix of a pair of atoms i and j is the same as that of their periodic images at a lattice vector $\mathbf{T}$, denoted $i+\mathbf{T}$ and $j+\mathbf{T}$. In other words, the force constant only depends on the distance between atoms i and j. The total energy must not change when we translate the origin of the coordinate system by a lattice vector $\mathbf{T}$:

$$\frac{1}{2}\sum_{ij}\mathsf{k}_{ij}\mathbf{u}_i\mathbf{u}_j = \frac{1}{2}\sum_{ij}\mathsf{k}_{i+\mathbf{T},j+\mathbf{T}}\mathbf{u}_{i+\mathbf{T}}\mathbf{u}_{j+\mathbf{T}} = \frac{1}{2}\sum_{ij}\mathsf{k}_{i,j}\mathbf{u}_{i+\mathbf{T}}\mathbf{u}_{j+\mathbf{T}} \tag{2.114}$$

The displacement of nucleus i must therefore be related to that of its periodic image $i+\mathbf{T}$ by a complex phase:

$$\mathbf{u}_{i+\mathbf{T}} = \mathbf{u}_i e^{2\pi i\mathbf{q}\cdot\mathbf{T}} \tag{2.115}$$

The total energy of a periodic system with N atoms in the unit cell can be expressed as:

$$E = \int_{\Lambda^*}\mathrm{d}\mathbf{q}\sum_{\mathbf{T}}\sum_{i,j}^{N}\mathsf{k}_{i,j}\mathbf{u}_i\cdot\mathbf{u}_j e^{2\pi i\mathbf{q}\cdot\mathbf{T}} \tag{2.116}$$

For any given phonon wave vector $\mathbf{q}$, we can define the dynamical matrix for a pair of atoms i and j in the unit cell:

$$\mathsf{D}_{i,j}(\mathbf{q}) = \sum_{\mathbf{T}}\mathsf{k}_{i,j+\mathbf{T}}e^{2\pi i\mathbf{q}\cdot\mathbf{T}} \tag{2.117}$$

which is, formally, a Fourier series decomposition of the force constant matrix. Given this matrix at a phonon wave vector $\mathbf{q}$, it is diagonalised and $3N$ normal modes are obtained for each wave vector $\mathbf{q}$.

The force-constant matrix can either be calculated directly from the equation:

$$\mathsf{k}_{i,j} = \frac{1}{\sqrt{m_i m_j}}\begin{pmatrix}\frac{\partial^2 E}{\partial x_i\partial x_j} & \frac{\partial^2 E}{\partial x_i\partial y_j} & \frac{\partial^2 E}{\partial x_i\partial z_j}\\ \frac{\partial^2 E}{\partial y_i\partial x_j} & \frac{\partial^2 E}{\partial y_i\partial y_j} & \frac{\partial^2 E}{\partial y_i\partial z_j}\\ \frac{\partial^2 E}{\partial z_i\partial x_j} & \frac{\partial^2 E}{\partial z_i\partial y_j} & \frac{\partial^2 E}{\partial z_i\partial z_j}\end{pmatrix} \tag{2.118}$$

That is, for each atom pair i and j, the force constant matrix is the Hessian of the

energy. These second derivatives can either be evaluated numerically in the so-called finite displacements method: a supercell of primitive unit cells must be considered that is large enough so that the force constant of an atom with the most distant periodic image inside the supercell of all other primitive unit cell atoms decays to zero. The dynamical matrix at any phonon wave vector $\mathbf{q}$ can then be formed according to Equation (2.117) if the sum over (primitive) lattice vectors $\mathbf{T}$ converges inside the supercell. Alternatively, the dynamical matrix $\mathsf{D}(\mathbf{q})$ can be calculated explicitly at an arbitrary phonon wave vector by perturbation methods. A description of the perturbation theory would, however, digress too much from the main purpose of this thesis, and so we shall simply refer to a detailed description by Refson *et al.* (2006). By computing the dynamical matrix at a grid of phonon wave vectors, the real-space force constant matrix can be obtained by the inverse Fourier transform of Equation (2.117). These can then be Fourier transformed onto a much finer grid of phonon wave vectors.

2.3 Statistical mechanics

We summarise the essential results from statistical mechanics as described by Hill (1986), in preparation for our discussion of nonequilibrium statistical mechanics in Section 6.2.

Statistical mechanics provides the link between the microscopic description of a system on the atomic level and the macroscopic laws of classical thermodynamics. For the following discussion, a few essential results from classical thermodynamics are used which are stated without further derivation. The first principle of thermodynamics states that the internal energy, U, is a conserved quantity:

$$\mathrm{d}U = \mathrm{d}w + \mathrm{d}q \tag{2.119}$$

The second principle of thermodynamics defines the entropy:

$$\mathrm{d}S = \frac{\mathrm{d}q_{rev}}{T} \tag{2.120}$$

Furthermore, the auxiliary thermodynamic functions are defined as:

$$A = U - TS \tag{2.121}$$

$$H = U + pV \tag{2.122}$$

$$G = U + pV - TS \tag{2.123}$$

$$G = \mu N \tag{2.124}$$

$$pV = TS + \mu N - U \tag{2.125}$$

where A is the Helmholtz energy, H is the enthalpy, G is the Gibbs energy, μ is the chemical potential and pV is the grand potential. We only treat systems for which the volume V is the only external variable; hence, the work term is $\mathrm{d}w = -p\mathrm{d}V$. (Other external variables could be specified: for example, the surface area a when treating surfaces, and the surface tension σ would be the corresponding potential; the work term would be: $\mathrm{d}w = -p\mathrm{d}V - \sigma\mathrm{d}a$.) From this, the following thermodynamic identities follow for each set of three characteristic thermodynamic variables:

$$N, V, S: \quad \mathrm{d}U = -p\mathrm{d}V + T\mathrm{d}S + \mu\mathrm{d}N \tag{2.126}$$

$$N, V, T: \quad \mathrm{d}A = -p\mathrm{d}V - S\mathrm{d}T + \mu\mathrm{d}N \tag{2.127}$$

$$\mu, V, T: \quad \mathrm{d}(pV) = p\mathrm{d}V + S\mathrm{d}T + N\mathrm{d}\mu \tag{2.128}$$

$$N, V, U: \quad \mathrm{d}S = \frac{p}{T}\mathrm{d}V + \frac{1}{T}\mathrm{d}U - \frac{\mu}{T}\mathrm{d}N \tag{2.129}$$

2.3.1 The postulates of statistical mechanics

We now introduce the concept of a statistical mechanical ensemble, and the two postulates of statistical mechanics on which the subsequent derivation of statistical mechanical relations depends. These postulates have no formal proof, but are confirmed by experimental evidence.

A *thermodynamic system* of one component and with only one external variable (vo-

lume) is fully defined by three variables, of which at least one must be extensive. This system corresponds to the macroscopic system of interest in thermodynamic equilibrium. In a closed, isothermal system, for example, N, V and T are given and held constant.

The microscopic energy levels E_i of the system are given by the Schrödinger equation for the entire system:

$$\hat{H}\Psi_i = E_i\Psi_i \tag{2.130}$$

In general, each energy level i is degenerate and occurs g_i times. For non-degenerate levels E_i, we have $g_i = 1$. The energy levels in this most general form only depend on the number of particles and the volume:

$$E_i = f(N, V) \tag{2.131}$$

A *statistical ensemble* is a (mental) collection of $\mathcal{N}$ replicas of the system of interest. Macroscopically, the replicas are all identical as they all have the same values of the their state variables. On a microscopic level, however, each of the replicas may be in a different quantum state, as long as the quantum state is compatible with the state variables. $\mathcal{N}$ is a very large number and can be taken to approach infinity. In a statistical ensemble, the probability that a randomly selected replica is in quantum state i is designated by P_i.

The goal of statistical mechanics is to find an expression for P_i. In an ensemble of systems, at any given instant in time, the mechanical variables (variables that can be written as a function of the energy E_i) are in general different from replica to replica. Likewise, for a single replica, the mechanical variables fluctuate with time. We can define two ways of determining the average value of an arbitrary mechanical variable B:

$$\langle B\rangle_t = \lim_{t\to\infty} \frac{\int_0^t B(t')\mathrm{d}t'}{t} \tag{2.132}$$

$$\langle B\rangle_{\mathcal{N}} = \lim_{\mathcal{N}\to\infty} \frac{\sum_{k=1}^{\mathcal{N}} B_k}{\mathcal{N}} = \sum_{i=1}^{\infty} P_i B_i \tag{2.133}$$

The first expression is the time average and the second is called the ensemble average. The average, whichever way it is calculated, must be constant over time by definition, otherwise the system is not in equilibrium.

The first postulate of statistical mechanics states that in any ensemble of thermodynamic systems, the ensemble average of any mechanical quantity is equal to the time average. This is called the ergodic hypothesis and was first formulated by Ludwig Boltzmann:

$$\langle A \rangle_t = \langle A \rangle_{\mathcal{N}} = \langle A \rangle \tag{2.134}$$

In the following, angled brackets $\langle \ldots \rangle$ are used to designate a thermal average.

A consequence of this postulate is time-translational symmetry of equilibrium properties. An equilibrium property measured at a time t must be equal to the same property measured at a time $t + T$: $\langle B(t) \rangle = \langle B(t + T) \rangle$. This seemingly trivial result will have important consequences in classical statistical mechanics and in nonequilibrium molecular dynamics (Chapter 6).

The second postulate states that an isolated thermodynamic system (N, V, E constant) spends an equal amount of time in all accessible quantum states.

2.3.2 The canonical ensemble

The system of interest is a closed, isothermal system. Conceptually, we imagine a system enclosed by rigid walls that are permeable to energy exchange, but not to exchange of particles. The entire system is immersed in a heat bath at temperature T. The canonical ensemble is constructed by putting $\mathcal{N}$ replicas of the system in thermal contact with each other; the entire ensemble is surrounded by walls that do not allow any energy exchange, and the heat bath is removed. The entire ensemble is therefore at temperature T, and each replica is in a heat bath of the $\mathcal{N} - 1$ other replicas at temperature T. The entire ensemble itself is a supersystem that can be treated as an isolated system, with a constant number of particles $\mathcal{N}N$, constant volume $\mathcal{N}V$, and constant total energy E_{tot}. The total energy of the supersystem is given by:

$$E_{\text{tot}} = \mathcal{N} \langle E \rangle \tag{2.135}$$

where $\langle E \rangle$ is the average energy of the replicas.

At any instant in time, each replica is in one of the quantum states, that is the replicas are distributed over the possible quantum states; this distribution at an instant in time is defined by a set of numbers $\{n\} = n_1, n_2, \ldots, n_i, \ldots$, where n_i is the number of replicas that are in quantum state i. For each distribution, there are $\Omega_{\text{tot}}(\{n\})$ ways of achieving this distribution; the replicas are *identical but distinguishable*:

$$\Omega_{\text{tot}}(\{n\}) = \frac{\mathcal{N}!}{\prod_{i=1}^{\infty} n_i!} \tag{2.136}$$

The numerator is a consequence of the fact that each one of the $\mathcal{N}$ replicas can be assigned one of the quantum states of the distribution. The denominator comes from the fact that the order in which the replicas in the same quantum state are assigned does not distinguish one distribution from another. For each distribution $\{n\}$, we have the following conditions:

$$\sum_{i=1}^{\infty} n_i = \mathcal{N} \tag{2.137}$$

$$\sum_{i=1}^{\infty} n_i E_i = E_{\text{tot}} \tag{2.138}$$

We now turn to our central goal: to determine the probability P_i of finding a randomly chosen replica of the canonical ensemble in the quantum state E_i. By the first postulate, this is equivalent to determining the average number of systems $\langle n_i \rangle$ in the canonical ensemble that are in state E_i:

$$P_i = \frac{\langle n_i \rangle}{\mathcal{N}} \tag{2.139}$$

Each distribution $\{n\}$ represents a different quantum state of the supersystem. By the second postulate, each distribution $\{n\}$ therefore occurs with equal probability, and we determine $\langle n_i \rangle$ by averaging over all possible distributions $\{n\}$ that fulfil Equations (2.137) and (2.138).

$$\langle n_i \rangle = \frac{\sum_{\{n\}} \Omega_{\text{tot}}\left(\{n\}\right) n_i\left(\{n\}\right)}{\sum_{\{n\}} \Omega_{\text{tot}}\left(\{n\}\right)} \tag{2.140}$$

We solve the above equation by the maximum term method, which assumes that, since

$\mathcal{N} \to \infty$, only the term in the sums with the maximum value of $\Omega_{\text{tot}}(\{n\})$ is important; hence:

$$\langle n_i \rangle = \frac{\sum_{\{n\}} \Omega_{\text{tot}}\left(\{n\}\right) n_i\left(\{n\}\right)}{\sum_{\{n\}} \Omega_{\text{tot}}\left(\{n\}\right)} = \frac{\Omega_{\text{tot}}\left(\{n^{\max}\}\right) n_i\left(\{n^{\max}\}\right)}{\Omega_{\text{tot}}\left(\{n^{\max}\}\right)} \tag{2.141}$$

In other words, we need to determine the distribution $\{n^{\max}\}$ that maximises $\Omega_{\text{tot}}(\{n\})$.

As we must work with factorials, we use the Stirling approximation and determine instead the maximum of the logarithm of $\Omega_{\text{tot}}(\{n\})$, which is permissible as the logarithm is a monotonic function. The Stirling approximation states that:

$$\lim_{x\to\infty} \ln x! = x \ln x - x \tag{2.142}$$

The mathematical problem to solve is therefore a maximisation of $\ln \Omega_{\text{tot}}(\{n\})$ with respect to all n_i under the constraints of Equations (2.137) and (2.138). Using the method of Lagrange multipliers, the equation to solve is:

$$\frac{\partial}{\partial n_i}\left(\ln \Omega_{\text{tot}}(\{n\}) - \alpha \sum_{i=1}^{\infty} n_i - \beta \sum_{i=1}^{\infty} n_i E_i\right) = 0 \tag{2.143}$$

where α and β are the Lagrange multipliers to be determined. Using Stirling's approximation and Equation (2.136), we obtain:

$$P_i = \frac{n_i^{\max}}{\mathcal{N}} = e^{-\beta E_i} e^{-\alpha} \tag{2.144}$$

The multiplier α is determined by inserting the above result into Equation (2.137), which defines the canonical partition function Q:

$$e^{\alpha} = \sum_{i=1}^{\infty} e^{-\beta E_i(N,V)} = Q(N,V,T) \tag{2.145}$$

The probabilities P_i are therefore:

$$P_i = \frac{e^{-\beta E_i}}{Q(N,V,T)} \tag{2.146}$$

The multiplier β is linked to nonmechanical variables and is determined by the following argument. By definition of the ensemble average, the differential of the average energy is obtained by inserting Equation (2.146) for P_i:

$$\mathrm{d}\left\langle E\right\rangle = \mathrm{d}\left(\sum_{i=1}^{\infty} P_i E_i\right) = \sum_{i=1}^{\infty} P_i \mathrm{d}E_i - \frac{1}{\beta}\left(\mathrm{d}\left(\sum_{i=1}^{\infty} P_i \ln P_i\right) - \ln Q \sum_{i=1}^{\infty} \mathrm{d}P_i\right) \tag{2.147}$$

We can make the following substitutions:

$$\mathrm{d}E_i = \left(\frac{\partial E_i}{\partial V}\right)_N \mathrm{d}V = -p_i \mathrm{d}V \tag{2.148}$$

$$\sum_{i=1}^{\infty} P_i p_i = \left\langle p\right\rangle \tag{2.149}$$

$$\sum_{i=1}^{\infty} \mathrm{d}P_i = 0 \tag{2.150}$$

where the first substitution is from thermodynamic identities, Equation (2.126), and the third substitution follows from $\sum_i^{\infty} P_i = 1$. We obtain:

$$\mathrm{d}\left\langle E\right\rangle = -\left\langle p\right\rangle \mathrm{d}V - \frac{1}{\beta}\mathrm{d}\left(\sum_{i=1}^{\infty} P_i \ln P_i\right) \tag{2.151}$$

From thermodynamic identities, we have:

$$\mathrm{d}U = -p\mathrm{d}V + T\mathrm{d}S \tag{2.152}$$

As we can match statistical mechanical average energy and pressure with thermodynamic ones, we have the relation:

$$\mathrm{d}S = -\frac{1}{\beta T}\mathrm{d}\left(\sum_{i=1}^{\infty} P_i \ln P_i\right) \tag{2.153}$$

Since $\mathrm{d}S$ is an exact differential, so is the right-hand side:

$$\mathrm{d}S = \frac{\mathrm{d}f}{\mathrm{d}X}\mathrm{d}X = \mathrm{d}f(X) \quad \text{with } X = -\sum_{i=1}^{\infty} P_i \ln P_i \tag{2.154}$$

where $f(X)$ is an unknown function. Therefore:

$$\frac{\mathrm{d}f}{\mathrm{d}X} = \frac{1}{\beta T} \tag{2.155}$$

and:

$$S = f(X) \tag{2.156}$$

Second, to determine the functional form of $f(X)$, we note that the entropy is an additive quantity and determine whether X is additive, too, by considering a system AB that is made by joining two systems A and B through a heat-permeable wall. A and B can be any two closed systems at temperature T. We find that X is, in fact, additive ($X_{AB} = X_A + X_B$), and therefore:

$$S_{AB} = S_A + S_B = f(X_{AB}) = f(X_A + X_B) = f(X_A) + f(X_B) \tag{2.157}$$

By differentiating the last equality with respect to X_A and X_B, we find that f must be a linear function:

$$f(X) = k_B X \tag{2.158}$$

The constant k_B is at this point undetermined, but we notice that it is universal: it is independent of the nature of the system under consideration. This establishes the connection between β and T via Equation (2.155):

$$\beta = \frac{1}{k_B T} \tag{2.159}$$

Thus we arrive at the following, general expression for the entropy:

$$S = -k_B \sum_{i=1}^{\infty} P_i \ln P_i \tag{2.160}$$

In a canonical ensemble, the replicas are distributed over the quantum states as:

$$P_i = \frac{e^{-\frac{E_i(N,V)}{k_B T}}}{Q(N,V,T)} \quad ; \qquad Q(N,V,T) = \sum_{i=1}^{\infty} e^{-\frac{E_i(N,V)}{k_B T}} \tag{2.161}$$

Expressions for all thermodynamic functions in the canonical ensemble can now be derived using the general statistical mechanical formula for the entropy, Equation (2.160), and the expression for P_i for the canonical ensemble from Equation (2.161). This can be compared to the equations for the entropy that follow from the definition of the Helmholtz energy.

$$S = \frac{\langle E \rangle}{T} + k_B \ln Q(N,V,T) \tag{2.162}$$

$$S = \frac{U}{T} - \frac{A}{T} \tag{2.163}$$

From this comparison, we obtain the Helmholtz energy A, the characteristic function for the canonical ensemble with variables N, V, T, and all the other thermodynamic functions through differentiation of A.

$$A(N,V,T) = -k_B T \ln Q(N,V,T) \tag{2.164}$$

$$p(N,V,T) = k_B T \left(\frac{\partial \ln Q}{\partial V} \right)_{N,T} \tag{2.165}$$

$$S(N,V,T) = k_B T \left(\frac{\partial \ln Q}{\partial T} \right)_{N,V} + k_B \ln Q(N,V,T) \tag{2.166}$$

$$\mu(N,V,T) = -k_B T \left(\frac{\partial \ln Q}{\partial N} \right)_{V,T} \tag{2.167}$$

2.3.3 Canonical partition function of a harmonic oscillator

Considering a system of $3N$ harmonic oscillators according to Section 2.2, each energy level is given by the sum of the harmonic energies:

$$E_{\{n_k\}} = \sum_{k=1}^{3N} \hbar \omega_k (n_k + 1/2) \tag{2.168}$$

The partition function Q for a system of $3N$ harmonic oscillators is evaluated as:

$$Q(N,V,T) = \sum_{i=0}^{\infty} e^{-\frac{E_i}{k_B T}} = \prod_{k=1}^{3N} \left(\sum_{n_k=0}^{\infty} e^{-\frac{(n_k+1/2)\hbar\omega_i}{k_B T}} \right) \tag{2.169}$$

The infinite sum can be evaluated by a simple mathematical identity:

$$\sum_{n_k=0}^{\infty} e^{-\frac{(n_k+1/2)\hbar\omega_k}{k_B T}} = e^{-\frac{\hbar\omega_k}{2k_B T}} \sum_{n_k=0}^{\infty} \left(e^{-\frac{\hbar\omega_k}{k_B T}} \right)^{n_k} = \frac{e^{-\frac{\hbar\omega_k}{2k_B T}}}{1 - e^{-\frac{\hbar\omega_k}{k_B T}}} \equiv \frac{1}{2\sinh\left(\frac{\hbar\omega_k}{2k_B T}\right)} \tag{2.170}$$

With this result, the logarithm of the total partition function is thus:

$$\ln Q(N,V,T) = -\sum_{k=1}^{3N} \ln\left(2\sinh\left(\frac{\hbar\omega_k}{2k_B T}\right)\right) \tag{2.171}$$

For a periodic system, $N \to \infty$ and so we replace the sum over all vibrational modes with an integral over the density of states, $g(\omega)$:

$$\ln Q(N,V,T) = -\int_0^{\infty} \mathrm{d}\omega\, g(\omega)\, \ln\left(2\sinh\left(\frac{\hbar\omega}{2k_B T}\right)\right) \tag{2.172}$$

2.3.4 The microcanonical ensemble

The microcanonical ensemble is an ensemble of isolated systems with constant number of particles N, volume V and energy E, and can be seen as a degenerate canonical or grand canonical ensemble. Expressions can be derived by taking the results from the canonical ensemble and then selecting only the systems that have energy E. This energy is also the average energy and must correspond to one (or more in the case of degeneracy) of the quantum levels $E_i(N,V)$; the degeneracy of this quantum level is designated by $g(N,V,E)$. By the second postulate, the probability is the same for every quantum state, therefore:

$$P_i = \frac{1}{g(N,V,E)} \tag{2.173}$$

From the general expression for the entropy from the canonical ensemble, Equation (2.160), we obtain the expression for the entropy in the microcanonical ensemble:

$$S = -k_B \ln g(N, V, E) \tag{2.174}$$

$$\frac{1}{T} = k_B \left(\frac{\partial \ln g}{\partial E} \right)_{N,V} \tag{2.175}$$

$$p = k_B T \left(\frac{\partial \ln g}{\partial V} \right)_{E,N} \tag{2.176}$$

$$\mu = -k_B T \left(\frac{\partial \ln g}{\partial N} \right)_{V,E} \tag{2.177}$$

2.4 Classical statistical mechanics

Classical statistical mechanics (see, for example, Tolman, 1938) follows the same principles as statistical mechanics for quantum systems discussed in the previous section; the fundamental differences are:

- The energy of the classical system is not quantised in discrete levels E_i, but is given by the total classical energy, $H(\mathbf{p}, \mathbf{q})$, consisting of potential and kinetic energy as a function of the positions of all the particles, $\mathbf{q}$, and the momenta of the particles, $\mathbf{p}$, in the absence of any external field.

- The instantaneous state of the classical system is therefore not characterised by a discrete quantum state, but by the instantaneous values of all positions and momenta. This state can be described by $\mathbf{\Gamma} \equiv (\mathbf{p}, \mathbf{q})$. The space of all positions and momenta is called phase space and has $6N$ dimensions, and one particular state of the classical system is one point $\mathbf{\Gamma}$ in phase space.

- The probability of each quantum state being occupied, P_i, is replaced by a probability density function, $f(\mathbf{\Gamma})$. In equilibrium, the probability density function has a similar form to the quantum probabilities, for example in the canonical ensemble:

$$f_{NVT}(\mathbf{\Gamma}) = \frac{e^{-\frac{H(\mathbf{\Gamma})}{k_B T}}}{Q(N, V, T)} \tag{2.178}$$

An ensemble of $\mathcal{N}$ identical replicas of the classical system ($\mathcal{N} \to \infty$) is evenly distributed over *all* phase space points $\mathbf{\Gamma}$ that are consistent with the macroscopic state variables chosen for the ensemble, for example fixed number of particles, volume and total energy for the canonical ensemble. In the canonical partition function, the infinite sum over all quantum states is replaced by a phase-space integral over all positions and momenta, which is compactly noted as:

$$Q(N, V, T) = \frac{1}{N!} \int \mathrm{d}\mathbf{\Gamma}\, e^{-\frac{H(\mathbf{\Gamma})}{k_B T}} \tag{2.179}$$

The factor of $1/N!$ reflects the fact that classical particles follow neither Bose-Einstein nor Fermi-Dirac statistics as all particles as distinguishable even if they are identical. Rather, they follow Maxwell-Boltzmann statistics.

The evolution of one specific system through time, described by its trajectory $\mathbf{\Gamma}(t)$ through phase space, depends on the equation of motion for the system and can be simulated explicitly by the molecular dynamics technique (Section 2.5). Here, we are interested in the formulation of the general results that follow for an *ensemble* of systems that evolve in time. The ensemble of $\mathcal{N}$ systems can then be described by a distribution $f(\mathbf{\Gamma}, t)$, not necessarily equal to an equilibrium distribution. The evolution of this density function of systems in time is described by the Liouville equation and establishes the theoretical justification for molecular dynamics (as well as nonequilibrium dynamics, Chapter 6).

2.4.1 The Liouville equation[2]

This description follows Evans and Morriss (2008). In classical statistical mechanics, an individual system evolves in time according to its equation of motion. To describe the distribution of systems in the ensemble over phase space, we introduce the distribution function $f(\mathbf{\Gamma}, t)$. This function designates the number of systems per phase space volume

[2]The so-called Liouville equation was in fact not introduced by Liouville himself; rather, it was Ludwig Boltzmann who erroneously credited Liouville with this equation (Evans, personal communication).

element and normalises to unity:

$$\delta\mathcal{N} = f(\mathbf{\Gamma}, t)\delta\mathbf{\Gamma} \tag{2.180}$$

$$\int \mathrm{d}\mathbf{\Gamma}\, f(\mathbf{\Gamma}, t) = 1 \tag{2.181}$$

The function $f(\mathbf{\Gamma}, t)$ fulfils the following general conditions, independent of the details of the dynamics:

- $f(\mathbf{\Gamma}, t)$ is smooth, that is it has continuous partial derivatives with respect to all its arguments.
- The total number of systems is constant: $\int \mathrm{d}\mathbf{\Gamma}\, f(\mathbf{\Gamma}, t) = 1$ at all times t.
- $f(\mathbf{\Gamma}, t)$ evolves in time as individual systems flow through phase space; it eventually converges to an equilibrium (or steady-state in nonequilibrium dynamics) distribution function that is constant in time.

These properties lead to the Liouville equation, which is essentially a statement of the conservation of mass, that is the total probability sums to unity. The notation of a phase space point is expanded as a vector of the linear components:

$$\mathbf{\Gamma} = (q_1, q_2, \ldots, q_{3N}, p_1, p_2, \ldots, p_{3N}) \tag{2.182}$$

A volume element in phase space is given by:

$$\delta\mathbf{\Gamma} = \delta q_1 \delta q_2 \ldots \delta q_{3N} \delta p_1 \delta p_2 \ldots \delta p_{3N} \tag{2.183}$$

For each component, for example q_1, a mass balance equation can be written for systems that flow through the hypersurface perpendicular to that dimension and out again through

the hypersurface perpendicular to q_1 at point $q_1 + \delta q_1$:

$$\begin{aligned}\frac{\mathrm{d}}{\mathrm{d}t}\delta\mathcal{N}_{q_1} = (&f(q_1, q_2 \ldots, t)\, \dot{q}_1(q_1, q_2, \ldots, t) \\ &- f(q_1 + \delta q_1, q_2, \ldots, t)\, \dot{q}_1(q_1 + \delta q_1, q_2, \ldots, t))\, \delta q_2 \delta q_3 \ldots \delta p_{3N}\end{aligned} \tag{2.184}$$

This can be written as:

$$\begin{aligned}\frac{\mathrm{d}}{\mathrm{d}t}\delta\mathcal{N}_{q_1} &= -\left(f(q_1, q_2, \ldots, t)\frac{\partial \dot{q}_1}{\partial q_1} + \dot{q}_1\frac{\partial f}{\partial q_1} + \frac{\partial f}{\partial q_1}\frac{\partial \dot{q}_1}{\partial q_1}\delta q_1\right)\delta\mathbf{\Gamma} \\ &\approx -\left(f(q_1, q_2, \ldots, t)\frac{\partial \dot{q}_1}{\partial q_1} + \dot{q}_1\frac{\partial f}{\partial q_1}\right)\delta\mathbf{\Gamma}\end{aligned} \tag{2.185}$$

Summing the corresponding fluxes for all $6N$ dimensions, we obtain the total flux of systems through the volume element at $\mathbf{\Gamma}$:

$$\frac{\mathrm{d}}{\mathrm{d}t}\delta\mathcal{N} = -\sum_{i=1}^{3N}\left(f(q_1, q_2, \ldots, t)\left(\frac{\partial \dot{q}_i}{\partial q_i} + \frac{\partial \dot{p}_i}{\partial p_i}\right) + \dot{q}_i\frac{\partial f}{\partial q_i} + \dot{p}_i\frac{\partial f}{\partial p_i}\right)\delta\mathbf{\Gamma} \tag{2.186}$$

Comparing this equation to the definition of the distribution function, it is seen that the right-hand side is the time derivative of the distribution function at a fixed point $\mathbf{\Gamma}$. In compact vector notation, the above equation is written as:

$$\frac{\partial f}{\partial t} = -f(\mathbf{\Gamma}, t)\frac{\partial}{\partial \mathbf{\Gamma}}\cdot\dot{\mathbf{\Gamma}} - \dot{\mathbf{\Gamma}}\cdot\frac{\partial f}{\partial \mathbf{\Gamma}} = -\left(\frac{\partial}{\partial \mathbf{\Gamma}}\cdot\dot{\mathbf{\Gamma}} + \dot{\mathbf{\Gamma}}\cdot\frac{\partial}{\partial \mathbf{\Gamma}}\right)f(\mathbf{\Gamma}, t) \tag{2.187}$$

This defines the Liouvillean operator $i\mathcal{L}$.

$$i\mathcal{L} = \frac{\partial}{\partial \mathbf{\Gamma}}\cdot\dot{\mathbf{\Gamma}} + \dot{\mathbf{\Gamma}}\cdot\frac{\partial}{\partial \mathbf{\Gamma}} \tag{2.188}$$

The total time derivative is:

$$\frac{\mathrm{d}f}{\mathrm{d}t} = \frac{\partial f}{\partial t} + \frac{\partial f}{\partial \mathbf{\Gamma}}\cdot\frac{\partial \mathbf{\Gamma}}{\partial t} = \frac{\partial f}{\partial t} + \dot{\mathbf{\Gamma}}\cdot\frac{\partial f}{\partial \mathbf{\Gamma}} \tag{2.189}$$

Combining the above two equations, the Liouville equation in its most general form is obtained:

$$\frac{\mathrm{d}f}{\mathrm{d}t} = -f(\mathbf{\Gamma}, t)\frac{\partial}{\partial \mathbf{\Gamma}} \cdot \dot{\mathbf{\Gamma}} \tag{2.190}$$

If the dynamics that govern the time evolution of the system are derivable from a Hamiltonian (see below, Section 2.5.1), it is easy to see that:

$$\frac{\partial}{\partial \mathbf{\Gamma}} \cdot \dot{\mathbf{\Gamma}} = \sum_{i=1}^{N} \left(\frac{\partial}{\partial \mathbf{q}_i} \cdot \frac{\partial H}{\partial \mathbf{p}_i} - \frac{\partial}{\partial \mathbf{p}_i} \cdot \frac{\partial H}{\partial \mathbf{q}_i} \right) = 0 \tag{2.191}$$

For a system whose dynamics are derivable from a Hamiltonian, the Liouville equation is thus:

$$\frac{\mathrm{d}f}{\mathrm{d}t} = 0 \tag{2.192}$$

In the general case, the solution to the time evolution of the distribution function is given by the solution of the ordinary differential equation:

$$\frac{\partial f}{\partial t} = -i\mathcal{L}f(\mathbf{\Gamma}, t) \tag{2.193}$$

The solution defines the Liouvillean propagator:

$$f(\mathbf{\Gamma}, t) = e^{-i\mathcal{L}t} f(\mathbf{\Gamma}, 0) \tag{2.194}$$

$$e^{-i\mathcal{L}t} = \sum_{n=0}^{\infty} \frac{(-t)^n}{n!} (i\mathcal{L})^n \tag{2.195}$$

Using the canonical equilibrium distribution function from Equation (2.178), it is easy to see that the distribution function of an ensemble described by the classical canonical distribution function is independent of time, in accordance with the ergodic hypothesis.

2.5 *Ab initio* molecular dynamics

In molecular dynamics, the motion of the atoms in time is calculated numerically (Hoover, 1986). Atoms are treated as classical mass particles. The potential energy of a system of

atoms and the forces on the atoms, however, are calculated from DFT:

$$\mathbf{F}_i = -\frac{\partial E}{\partial \mathbf{r}_i} \tag{2.196}$$

The potential energy E and the forces are directly calculated from the electronic structure of the system using DFT as described in Section 2.1, but the details of the calculation of the forces and potential energy from a given set of atomic positions are irrelevant for the discussion of molecular dynamics.

2.5.1 The equation of motion: Newtonian, Lagrangian and Hamiltonian dynamics

Molecular dynamics involve the numerical integration of the Newtonian equation of motion for each atom i:

$$\mathbf{F}_i = m_i \frac{\mathrm{d}^2 \mathbf{r}_i}{\mathrm{d}t^2} = m_i \ddot{\mathbf{r}}_i \tag{2.197}$$

In equilibrium molecular dynamics, no external forces are assumed to be present and the system evolves in time according to the Newton equation of motion, where the force $\mathbf{F}_i$ on each particle is derived from the potential energy gradient. Therefore, the total energy is conserved and thus a constant of the motion.

The Lagrangian of a dynamical system is defined as the difference of kinetic and potential energy, expressed as functions of a set of coordinates $\mathbf{q}$ and their time derivatives $\dot{\mathbf{q}}$.

$$L(\mathbf{q}, \dot{\mathbf{q}}) = K(\dot{\mathbf{q}}) - U(\mathbf{q}) \tag{2.198}$$

The conjugate momentum $\mathbf{p}$ to a variable $\mathbf{q}$ is defined by:

$$\mathbf{p} = \frac{\partial L}{\partial \dot{\mathbf{q}}} \tag{2.199}$$

The Lagrangian equations of motion are derived from Hamilton's least-action principle: the path of motion between two points in space-time is such that the integral of L over

time (the action integral) is minimised with respect to $\mathbf{q}$ and $\dot{\mathbf{q}}$. This leads to the following general equation of motion:

$$\frac{\mathrm{d}}{\mathrm{d}t}\frac{\partial L}{\partial \dot{\mathbf{q}}} = \frac{\partial L}{\partial \mathbf{q}} \tag{2.200}$$

Rather than using generalised coordinates and their time derivatives, the Hamiltonian formulation of classical mechanics uses general coordinates and momenta. The Hamiltonian of a system is:

$$H = \dot{\mathbf{q}}\mathbf{p} - L(\mathbf{q}, \dot{\mathbf{q}}) \tag{2.201}$$

The equations of motion are therefore defined in the following way:

$$\dot{\mathbf{q}} = \frac{\partial H}{\partial \mathbf{p}} \tag{2.202}$$

$$\dot{\mathbf{p}} = -\frac{\partial H}{\partial \mathbf{q}} \tag{2.203}$$

In a general system consisting of N atoms in equilibrium without external forces and a potential that only depends on coordinates not velocities, the Hamiltonian corresponds to the total energy and is conserved:

$$H(\mathbf{r}_i, \mathbf{p}_i) = \sum_{i=1}^{N} \frac{\mathbf{p}_i^2}{2m_i} + U(\mathbf{r}_{1\ldots N}) \tag{2.204}$$

2.5.2 Numerical integration of the equations of motion: the velocity-Verlet algorithm

In a system of N interacting atoms, the many-body equations of motion can only be solved numerically because the forces, $\mathbf{F}_i$, depend on the positions of all the atoms in the system. To calculate the trajectory of a system, therefore, the positions and velocities are expanded in a Taylor series:

$$\mathbf{r}_i(\Delta t) = \mathbf{r}_i(0) + \Delta t\, \mathbf{v}_i(0) + \frac{\Delta t^2}{2}\frac{\mathbf{F}_i\left(\mathbf{r}(0)\right)}{m_i} + \mathcal{O}(\Delta t^3) \tag{2.205}$$

where $\mathbf{v}_i = \dot{\mathbf{r}}_i$. In the first step of the algorithm, the velocities at time $\Delta t/2$ are evaluated and used to calculate the positions at time Δt:

$$\mathbf{v}_i(\Delta t/2) = \mathbf{v}_i(0) + \frac{\mathbf{F}_i\left(\mathbf{r}_{1\ldots N}(0)\right)}{m_i}\frac{\Delta t}{2} \tag{2.206}$$

$$\mathbf{r}_i(\Delta t) = \mathbf{r}_i(0) + \mathbf{v}_i(\Delta t/2)\Delta t \tag{2.207}$$

The forces are then recalculated with the particles in the new positions, $\mathbf{F}_i\left(\mathbf{r}_{1\ldots N}(\Delta t)\right)$. These are then used to calculate the velocity at Δt:

$$\mathbf{v}_i(\Delta t) = \mathbf{v}_i(t\Delta t/2) + \frac{\mathbf{F}_i(\Delta t)}{m_i}\frac{\Delta t}{2} \tag{2.208}$$

Only one evaluation of the forces (usually the most time-consuming step) is required per time step Δt.

2.5.3 Microscopic connection to thermal parameters

The equations of motion above generate a trajectory of any desired length, and, by application of the ergodic hypothesis, we can calculate approximations to ensemble averages by simulation. But to be able to compute thermodynamic quantities such as temperature or pressure, they must be expressed as functions of the parameters of a microstate in a classical system, that is the positions and velocities.

For the temperature, there are two approaches. The only definition of the temperature used in this thesis is the ideal gas thermometer. In an ideal gas, the total energy is only kinetic energy, and the particles do not interact with each other. The average total kinetic energy is:

$$\langle K\rangle = \sum_{i=1}^{N}\frac{m_i}{2Q_i(N,V,T)}\int \mathrm{d}\mathbf{v}_i\,\mathbf{v}_i^2 e^{-\frac{m_i\mathbf{v}_i^2}{2k_BT}} = \frac{3N}{2}k_BT \tag{2.209}$$

The temperature of an ideal gas is therefore:

$$T = \frac{2}{3Nk_B}\langle K\rangle \tag{2.210}$$

It is important to note that, by its statistical mechanical definition, the temperature is an average quantity, and so for any molecular dynamics trajectory the temperature must be calculated as the time average over a trajectory; there is only one value for the temperature for a given system in equilibrium and it is constant in time. Nevertheless, it is convenient to define an instantaneous temperature $T(t)$, defined by inserting the instantaneous kinetic energy into the equation above, which is at any instant in time t:

$$K(t) = \sum_{i=1}^{N} \frac{1}{2} m_i \mathbf{v}_i^2(t) \tag{2.211}$$

The instantaneous temperature is a useful diagnostic quantity when performing molecular dynamics simulations, but it must be kept in mind that the only value that has physical meaning is the time average of the instantaneous temperature.

An alternative definition of temperature that does not rely on the ideal gas definition is the definition from thermodynamics:

$$T = \left(\frac{\partial U}{\partial S} \right)_{N,V} \tag{2.212}$$

For Hamiltonian systems, Rugh (1997) derived an expression of the temperature based on this form. However, the formula involves second derivatives of the Hamiltonian, Equation (2.2), and therefore the second derivative of the potential energy with respect to all nuclear coordinates must be calculated to evaluate the instantaneous temperature. This would require a full computation of the $3N \times 3N$ force constant matrix at each time step, which for *ab initio* molecular dynamics is intractable, and the ideal gas temperature definition is used throughout this thesis. Even though an inorganic solid bears little resemblance to an ideal gas from almost any point of view, its classical statistical mechanics only differ by the presence of the potential energy term. The equipartition principle demands that thermal energy, in equilibrium, is distributed evenly among all degrees of freedom, and therefore the relationship between kinetic energy and temperature must be exactly the same as in an ideal gas.

Formally, the molecular dynamics method integrating the Newtonian equation of motion conserves the total energy. Therefore, by integration of the equations of motion, the microcanonical ensemble is simulated, since the number of particles and the volume do not vary. Although all statistical ensembles result in the same average properties, it is often more convenient to specify a constant temperature rather than a constant total energy. To achieve this, the equations of motion must be modified by introducing constraints to control the temperature. These constraints are called thermostats, and in the following the two thermostat algorithms used in this thesis are described.

2.5.4 Nosé-Hoover thermostat

In order to simulate a system at constant temperature rather than constant energy, Nosé (1984a,b) proposes the introduction of an additional degree of freedom to simulate an extended system. The extended-system method was originally proposed by Andersen (1980) for the simulation of systems at constant pressure.

An additional degree of freedom, associated with the coordinate s, is introduced that represents the heat bath. In Nosé's formulation, the interaction between the heat bath and the simulated system is expressed through velocity scaling, defined by:

$$\dot{\mathbf{r}}' = s\dot{\mathbf{r}} \quad \Rightarrow \quad \frac{\mathrm{d}\mathbf{r}}{\mathrm{d}t'} = s\frac{\mathrm{d}\mathbf{r}}{\mathrm{d}t} \quad \Rightarrow \quad \mathrm{d}t = s\mathrm{d}t' \tag{2.213}$$

The primed quantity is the velocity in the real (physical) system, the unprimed quantity is the velocity in the extended system. The positions are identical in the real and the extended systems, but Equation (2.213) expresses a time scaling relationship between the two systems. The kinetic energy depends on the real velocity. The Lagrangian for the extended system, in extended-system coordinates, is thus postulated to be:

$$L_{\text{Nosé}}(\mathbf{r}_i, \dot{\mathbf{r}}_i, s, \dot{s}) = \sum_i \frac{m_i s^2 \dot{\mathbf{r}}_i^2}{2} - U(\mathbf{r}_{1\ldots N}) + \frac{M\dot{s}^2}{2} - gk_BT\ln s \tag{2.214}$$

The two additional terms are a kinetic energy term associated with the new variable s and

its (fictional) mass M, and the potential energy, with g a parameter to be determined such that canonical ensemble averages are generated. The momenta in the extended system are derived from the Lagrangian according to Equation (2.199) and are:

$$\mathbf{p}_i = m_i s^2 \dot{\mathbf{r}}_i \tag{2.215}$$

$$p_s = M\dot{s} \tag{2.216}$$

The Hamiltonian of the extended system is:

$$H_{\text{Nosé}}(\mathbf{r}_i, \mathbf{p}_i, s, p_s) = \sum_i \frac{\mathbf{p}_i^2}{2m_i s^2} + U(\mathbf{r}_{1\ldots N}) + \frac{p_s^2}{2M} + gk_BT \ln s \tag{2.217}$$

The momentum is substituted by the real system momentum, defined by:

$$\mathbf{p}_i' = \frac{\mathbf{p}_i}{s^2}, \quad \mathrm{d}\mathbf{p}' = \frac{\mathrm{d}\mathbf{p}}{s^{N_{df}}} \tag{2.218}$$

where N_{df} is the number of degrees of freedom in the system (if no other constraints are applied, usually $N_{df} = 3N$ for a system of N particles), and the compact notation $\mathrm{d}\mathbf{p} = \mathrm{d}\mathbf{p}_1 \ldots \mathrm{d}\mathbf{p}_N$ is used. The extended system Hamiltonian becomes:

$$H_{\text{Nosé}} = H' + \frac{p_s^2}{2M} + gk_BT \ln s \tag{2.219}$$

The Hamiltonian H' is the real system Hamiltonian because it has the form:

$$H' = \sum_i \frac{\mathbf{p}_i'^2}{2m_i} + U(\mathbf{r}_{1\ldots N}) \tag{2.220}$$

If we perform molecular dynamics using the equations of motion derived from the Nosé-Hamiltonian, the microcanonical ensemble of the extended system will be generated, where N, V and $E = H_{\text{Nosé}}$ are constant. The microcanonical partition function of the extended system is:

$$\Omega_{\text{Nosé}}(N, V, E) = \frac{1}{N!} \iiiint \mathrm{d}\mathbf{r}\, \mathrm{d}\mathbf{p}\, \mathrm{d}s\, \mathrm{d}p_s\, \delta(H_{\text{Nosé}} - E) \tag{2.221}$$

Writing this partition function in terms of the scaled momenta, from Equation (2.218), we obtain:

$$\Omega_{\text{Nosé}}(N,V,E) = \frac{1}{N!}\iiiint \mathrm{d}\mathbf{r}\,\mathrm{d}\mathbf{p}'\,\mathrm{d}s\,\mathrm{d}p_s\,s^{N_{df}}\,\delta\left(H' + \frac{p_s^2}{2M} + gk_BT\ln s - E\right) \tag{2.222}$$

We use the following property of the Dirac function of a function $h(s)$:

$$\delta\left(h(s)\right) = \frac{\delta(s-s_0)}{h'(s)} \tag{2.223}$$

where s_0 is the root of $h(s)$, and $h'(s)$ is the derivative of the function with respect to s. The root of the argument of the delta function in Equation (2.222) is:

$$s_0 = \exp\left(\frac{E - H' - \frac{p_s^2}{2M}}{gk_BT}\right) \tag{2.224}$$

and the derivative is:

$$\frac{\mathrm{d}}{\mathrm{d}s}\left(H' + \frac{p_s^2}{2M} + gk_BT\ln s - E\right) = \frac{gk_BT}{s} \tag{2.225}$$

The extended system partition function then reads:

$$\Omega_{\text{Nosé}}(N,V,E) = \frac{1}{N!}\iiiint \mathrm{d}\mathbf{r}\,\mathrm{d}\mathbf{p}'\,\mathrm{d}s\,\mathrm{d}p_s\,\frac{s^{N_{df}+1}}{gk_BT}\delta\left(s - \exp\left[\frac{E - H' - \frac{p_s^2}{2M}}{gk_BT}\right]\right) \tag{2.226}$$

The integration over s can be performed straightforwardly to give:

$$\Omega_{\text{Nosé}}(N,V,E) = \frac{1}{N!}\iiint \mathrm{d}\mathbf{r}\,\mathrm{d}\mathbf{p}'\,\mathrm{d}p_s\,\frac{1}{gk_BT}\exp\left(-\frac{(N_{df}+1)}{g}\frac{H' + \frac{p_s^2}{2M} - E}{k_BT}\right) \tag{2.227}$$

We now set $g = N_{df} + 1$ and factor out the integration over p_s:

$$\Omega_{\text{Nosé}}(N,V,E) = \frac{1}{(N_{df}+1)k_BT}\left[\int \mathrm{d}p_s\,e^{-\frac{p_s^2}{2Mk_BT}}\right]e^{\frac{E}{k_BT}}\left[\frac{1}{N!}\iint \mathrm{d}\mathbf{r}\,\mathrm{d}\mathbf{p}'\,e^{-\frac{H'}{k_BT}}\right] \tag{2.228}$$

The last term in square brackets can be identified with the canonical ensemble partition function for the Hamiltonian H'. The first term in square brackets is a Gaussian integral, which is generally solved as:

$$\int_{-\infty}^{+\infty} \mathrm{d}x\, a \exp\left(-\frac{(x-b)^2}{c^2}\right) = ac\sqrt{\pi} \tag{2.229}$$

Therefore, the microcanonical partition function of the extended system is directly proportional to the canonical partition function of the real system:

$$\Omega_{\text{Nosé}}(N,V,E) = \frac{1}{N_{df}+1}\sqrt{\frac{2\pi M}{k_B T}}\, e^{\frac{E}{k_B T}}\, Q'(N,V,T) \tag{2.230}$$

The classical canonical partition function $Q'(N,V,T)$ is given by:

$$Q'(N,V,T) = \frac{1}{N!}\iint \mathrm{d}\mathbf{r}\,\mathrm{d}\mathbf{p}'\, e^{-\frac{H'(\mathbf{r}_{1\ldots N},\mathbf{p}'_{1\ldots N})}{k_B T}} \tag{2.231}$$

The equations of motion for $\mathbf{p}$, $\mathbf{r}$, p_s, s, can be derived from the extended-system Hamiltonian, Equation (2.217). To obtain equations of motion in real-system time, the extended-system time is substituted by the real-system time according to Equation (2.213), and we obtain:

$$\dot{\mathbf{r}}'_i = \frac{\mathbf{p}_i}{m_i s} \tag{2.232}$$

$$\dot{\mathbf{p}}'_i = s\mathbf{F}_i(\mathbf{r}_{1\ldots N}) \tag{2.233}$$

$$\dot{s}' = s\frac{p_s}{M} \tag{2.234}$$

$$\dot{p_s}' = \sum_i \frac{\mathbf{p}_i^2}{m_i s^2} - (N_{df}+1)k_B T \tag{2.235}$$

To obtain the Nosé-Hoover equations of motion (Hoover, 1985), which are independent of s, Equation (2.232) is differentiated with respect to time:

$$\ddot{\mathbf{r}}'_i = \frac{\dot{\mathbf{p}}'_i m_i s - \mathbf{p}_i m_i \dot{s}'}{m_i^2 s^2} = \frac{\mathbf{F}_i(\mathbf{r}_{1\ldots N})}{m_i} - \dot{\mathbf{r}}'_i \frac{p_s}{M} \tag{2.236}$$

By setting $m_i\ddot{\mathbf{r}}_i = \dot{\mathbf{p}}'_i$, $m_i\dot{\mathbf{r}}_i = \mathbf{p}'_i$ and $\xi \equiv p_s/M$, Equations (2.232)–(2.236) can be combined to obtain the Nosé-Hoover equations of motion in real-system time:

$$\dot{\mathbf{r}}'_i = \frac{\mathbf{p}'_i}{m_i} \tag{2.237}$$

$$\dot{\mathbf{p}}'_i = \mathbf{F}_i(\mathbf{r}_{1\ldots N}) - \xi\mathbf{p}'_i \tag{2.238}$$

$$\dot{\xi} = \frac{1}{M}\left(\sum_i \frac{\mathbf{p}'^2_i}{m_i} - (N_{df}+1)k_BT\right) \tag{2.239}$$

The variable ξ is interpreted as a friction coefficient with its own equation of motion and couples the system to the heat bath at temperature T. These equations of motion can be integrated by using the velocity-Verlet algorithm described above. Only one parameter, namely the fictional mass M of the heat bath variable, must be chosen.

2.5.5 The Gaussian isokinetic thermostat

This thermostat is based on an alternative formulation of classical mechanics first described by Gauß (1826). The "principle of least constraint" was applied to formulate a thermostat for molecular dynamics by Evans *et al.* (1983). This thermostat does not produce a trajectory equivalent to the canonical ensemble as the Nosé-Hoover thermostat does, but an isokinetic ensemble, with a constant kinetic energy, is obtained. The equations of motion are derived from a constraint equation:

$$\dot{\mathbf{p}}_i = \mathbf{F}_i + \alpha\mathbf{p}_i \tag{2.240}$$

$$\dot{\mathbf{r}}_i = \frac{\mathbf{p}_i}{m_i} \tag{2.241}$$

$$\alpha = -\frac{\sum_i \frac{\mathbf{p}_i}{m_i}\cdot\mathbf{F}_i}{\sum_i \frac{\mathbf{p}_i^2}{m_i}} \tag{2.242}$$

These are very similar to the Nosé-Hoover equations of motion, but the thermostat coefficient α does not have its own equation of motion. Rather, the expression for α is derived by the condition that the kinetic temperature remains constant at the desired set value,

T_0, at all times:

$$\sum_{i=1}^{N} \frac{\mathbf{p}_i^2}{2m_i} = \frac{3N}{2} k_B T_0 \tag{2.243}$$

The constraint is obtained by differentiating this equation with respect to time:

$$\sum_{i=1}^{N} \frac{\mathbf{p}_i \cdot \dot{\mathbf{p}}_i}{m_i} = 0 \tag{2.244}$$

The equation of motion, Equation (2.240), is then inserted for $\dot{\mathbf{p}}_i$ to obtain:

$$\sum_{i=1}^{N} \frac{\mathbf{p}_i}{m_i} \cdot \mathbf{F}_i + \alpha \sum_{i=1}^{N} \frac{\mathbf{p}_i^2}{m_i} = 0 \tag{2.245}$$

Solving this for α, Equation (2.242) is obtained. It is notable that the set temperature T_0 does *not* enter the equations of motion at all; the Gaussian thermostat only keeps the temperature resulting from the initial momenta fixed.

It is a necessary condition for this thermostat that the centre of mass of the system is fixed in space and does not drift; the first reason is that the temperature is defined from the velocities (or momenta), as the temperature must be independent of whether the entire system is moving uniformly in one direction or stands still in space. The second reason is that the total acceleration must correspond to the total forces. From Equation (2.240), we have:

$$\sum_{i=1}^{N} \dot{\mathbf{p}}_i = \sum_{i=1}^{N} \mathbf{F}_i \quad \text{if and only if} \quad \sum_{i=1}^{N} \mathbf{p_i} = 0 \tag{2.246}$$

Therefore, the centre of mass velocity of the atoms subject to the thermostat algorithm must be zero.

CHAPTER 3

Analysis methods and algorithms

> "Another (very much consulted in this area) is a mere labyrinth of letters, but the next-to-last page says *Oh time thy pyramids*. This much is already known: for every sensible line of straightforward statement, there are leagues of senseless cacophonies, verbal jumbles and incoherences."
>
> Jorge Luis Borges, *The Library of Babel*

The previous chapter presented the physical models underlying the simulation techniques used in this thesis and the practical algorithms for performing these simulations. Molecular dynamics (MD) quickly generate vast amounts of data in the form of trajectories, consisting of the recorded positions of each atom in the system at each time step of the simulation, as well as other time-dependent data such as the instantaneous lattice parameters (in the case of variable-volume simulations) or the temperature. However, producing a molecular dynamics trajectory of a model system is in itself not a useful result: it is through the analysis of these raw data that insight is gained. From an MD trajectory, any physical property that can be expressed as a function of the coordinates and/or velocities of the atomic nuclei and of time can be extracted from MD data.

Whereas the computational techniques for generating MD data are fairly standardised

and, in general, shared by researchers in the field, few standard tools for the analysis of MD trajectories exist; this is likely to be a consequence of the individualities of each researcher's aims and interests. In this chapter, the general methods for the analysis of MD trajectories are described; all of the algorithms described in this chapter were implemented in computer codes.

3.1 Correlation functions and power spectra

The velocity autocorrelation function (VACF) of a system of N particles is defined as:

$$c(t,t') = \left\langle N^{-1} \sum_{i=1}^{N} \mathbf{v}_i(t) \cdot \mathbf{v}_i(t') \right\rangle \tag{3.1}$$

where $\mathbf{v}_i(t)$ is the instantaneous velocity of particle i at time t. The average is a thermal average and therefore the VACF is an equilibrium property. As such, time-translational symmetry applies: $c(t,t') = c(t+T,t'+T)$, where T is an arbitrary length of time, and so:

$$c(t,t') = c(0,t'-t) = \left\langle N^{-1} \sum_{i=1}^{N} \mathbf{v}_i(0) \cdot \mathbf{v}_i(t'-t) \right\rangle \tag{3.2}$$

The VACF only depends on the time difference, $t'-t$. Replacing $\tau = t'-t$, we obtain:

$$c(\tau) = \left\langle N^{-1} \sum_{i=1}^{N} \mathbf{v}_i(0) \cdot \mathbf{v}_i(\tau) \right\rangle \tag{3.3}$$

The thermal average is evaluated as a time average, which means averaging over all time origins:

$$c(\tau) = c_0^{-1} \int_{-\infty}^{+\infty} \mathrm{d}s \, N^{-1} \sum_{i=1}^{N} \mathbf{v}_i(s) \cdot \mathbf{v}_i(s+\tau) \tag{3.4}$$

$$c_0 = \int_{-\infty}^{+\infty} \mathrm{d}s \tag{3.5}$$

The normalised VACF is given by:

$$C(\tau) = \frac{c(\tau)}{c(0)} \tag{3.6}$$

For a finite MD trajectory of n time steps of a system of N atoms, the VACF is evaluated as:

$$c(\tau_k) = \frac{1}{n-k} \sum_{a=1}^{n-k} \left(N^{-1} \sum_{i=1}^{N} \mathbf{v}_i(t_a) \cdot \mathbf{v}_i(t_{a+k}) \right) \tag{3.7}$$

where the subscripts a and k designate the discrete time steps of the MD trajectory: $t_k = k\Delta t$, where Δt is the time step used to integrate the equations of motion.

The main interest of computing the VACF is to calculate its power spectrum (Fourier transform), which will give the frequency spectrum of vibrational motion present in the system:

$$P(\omega) = \int_0^\infty \mathrm{d}\tau \, e^{-i\omega t} \, C(\tau) \tag{3.8}$$

To demonstrate this, the VACF of a single classical harmonic oscillator of frequency ω_0 is calculated, the velocity of which is described by:

$$v(t) = v_0 \cos(\omega_0 t) \tag{3.9}$$

Inserting this form of the velocity into Equation (3.3) leads to:

$$c(\tau) = \left\langle v_0^2 \cos(\omega_0 \tau) \right\rangle = \left\langle v_0^2 \right\rangle \cos(\omega_0 \tau) \tag{3.10}$$

$$c(0) = \left\langle v_0^2 \right\rangle \tag{3.11}$$

The power spectrum of this normalised VACF is a single peak at frequency ω_0:

$$P(\omega) = \int_0^\infty \mathrm{d}\tau \, \cos(\omega_0 \tau) e^{-i\omega t} = \sqrt{\frac{\pi}{2}} \delta(\omega - \omega_0) \tag{3.12}$$

The same analysis can be applied to the angular velocity autocorrelation function (AACF). For a system of N rotating bodies (e. g. molecules), the AACF is defined as:

$$c_\theta(\tau) = \left\langle N^{-1} \sum_{i=1}^{N} \boldsymbol{\omega}_i(0) \cdot \boldsymbol{\omega}_i(\tau) \right\rangle \tag{3.13}$$

where $\boldsymbol{\omega}_i(\tau)$ is the angular velocity of molecule i. This is a subset of the VACF and its power spectrum will give a subset of the vibrational spectrum. Since the AACF only captures rotational motion, the power spectrum represents a spectrum of librational modes. These are the only ways in which the correlation functions are used in the work of this thesis. Kleinhesselink and Wolfsberg (1992) give an in-depth discussion of the calculation of autocorrelation functions in MD, including the factors affecting the accuracy of the computed results.

Cross-correlation functions are a more general application of correlation functions. In this thesis, the angular velocity cross-correlation function shall be used. It is defined as:

$$c_x(\tau) = \left\langle N_{\alpha\beta}^{-1} \sum_{\{\alpha\beta\}}^{N_{\alpha\beta}} \boldsymbol{\omega}_\alpha(0) \cdot \boldsymbol{\omega}_\beta(\tau) \right\rangle$$

This cross-correlates the angular velocities of a pair of molecules α, β, whose relationship can be defined at will, for instance nearest-neighbour molecules. The sum in the above equation is then taken over all pairs α, β found in the system. Unlike the autocorrelation function, the cross-correlation function does not have time-inversion symmetry and needs to be defined for positive as well as negative τ. From an MD trajectory, the cross-correlation is evaluated according to the following equation:

$$c(\tau_k) = \frac{1}{n - |k|} \sum_{a=\max(0,-k)}^{\min(n,n-k)} N_{\alpha\beta}^{-1} \sum_{\{\alpha\beta\}}^{N_{\alpha\beta}} \boldsymbol{\omega}_\alpha(t_a) \cdot \boldsymbol{\omega}_\beta(t_{a+k}) \tag{3.14}$$

3.2 Debye-Waller factors

The Debye-Waller factor is the Fourier transform of the probability density of a harmonically vibrating nucleus. The probability that a nucleus is found at a displacement $\mathbf{u}$ (in Cartesian coordinates) from its equilibrium position is:

$$P(\mathbf{u}) = C \exp\left(-\frac{1}{2}\mathbf{u} \cdot \mathsf{V}^{-1}\mathbf{u}\right) \tag{3.15}$$

with

$$\mathsf{V}_{ij} = \langle u_i u_j \rangle \tag{3.16}$$

where the average is a time average. We now express $\mathbf{u}$ in a different basis (noting that all vectors are row vectors):

$$\mathbf{u} = \mathbf{\Delta} \begin{pmatrix} a^*\mathbf{a} \\ b^*\mathbf{b} \\ c^*\mathbf{c} \end{pmatrix} \tag{3.17}$$

where a^* is the length of the reciprocal lattice vector $\mathbf{a}^*$ and $\mathbf{a}^* \cdot \mathbf{a} = 1$. The components of $\mathbf{\Delta}$ have dimension Å. The probability is then expressed as:

$$P(\mathbf{\Delta}) = C \exp\left(-\frac{1}{2}\mathbf{\Delta} \cdot \mathsf{U}^{-1}\mathbf{\Delta}\right) \tag{3.18}$$

with U correspondingly expressed in the new basis:

$$\mathsf{U}_{ij} = \langle \Delta_i \Delta_j \rangle \tag{3.19}$$

The elements of the symmetric matrix U are the anisotropic displacement factors and have dimension Å^2. If the simplified model of isotropic displacement is used, the matrix U reduces to:

$$\mathsf{U}_{ij} = U_{\text{iso}} \quad \text{if } i = j \tag{3.20}$$

$$\mathsf{U}_{ij} = 0 \quad \text{if } i \neq j \tag{3.21}$$

From MD simulations, the anisotropic displacement factors can be calculated directly according to Equation (3.19). Alternatively, the probability distribution in space can be computed by determining the atomic probability density according to:

$$P_{\mathrm{MD}}(\mathbf{r}) = \frac{1}{n}\sum_{k=1}^{n}\delta(\mathbf{r}-\mathbf{r_k}) \tag{3.22}$$

where $\mathbf{r}_k$ is the position of the atom at time step k in a trajectory of n time steps, and then fitting the obtained density to the functional form of Equation (3.18).

3.2.1 Centre of mass drift correction

In equilibrium MD, with no external forces, the centre of mass of the system must have a constant velocity, which is set to zero through the choice of initial velocities of the system and the centre of mass should remain fixed. However, due to numerical round-off errors in the integration of the equations of motion, small numerical errors accumulate and result in a small, erratic drift of the centre of mass. This small drift needs to be corrected for before analyses involving the positions of the atoms are conducted, such as the computation of Debye-Waller factors; it is not necessary to correct for the centre of mass drift if only the velocities of the atoms enter the analysis, for example in the computation of the VACF, as the effect of the drift on the velocities is negligible. The corrected positions $\mathbf{r}_i$ are obtained from the trajectory positions $\mathbf{r}'_i$ and particle masses m_i by:

$$\mathbf{r}_i(t) = \mathbf{r'}_i(t) - \frac{\sum_{p=1}^{N} m_p \mathbf{r}'_p(t)}{\sum_{q=1}^{N} m_q} \tag{3.23}$$

3.3 Analysis of molecular orientation by quaternions

A rigid object in three-dimensional space is completely specified in a coordinate system x, y, z by fixing three different points of the object in space, which results, in general, in six degrees of freedom: three Cartesian coordinates are required to fix an arbitrary reference point of the object in space; a further two are necessary to describe the position of the second point with reference to the first, and one more parameter is required to

fix the third point. Therefore, the position and orientation of a rigid object in space is completely described by three positional parameters (e. g. the position of its centre of mass) and by three orientation parameters. Orientational and positional degrees of freedom can be treated separately. For a very general discussion, this rigid object can be taken to be a coordinate system XYZ, which we call the rotating frame, whose position and orientation in the absolute coordinate system xyz is determined by the three coordinates of the origin of XYZ and by three orientational parameters determining the orientation. The position and orientation of any arbitrary rigid object can thus be defined by one constant set of coordinates specified in XYZ and the six degrees of freedom that define the position and orientation of XYZ in xyz.

Traditionally, the most popular choice for orientational parameters are the so-called Euler angles (Euler, 1776). The angles ϕ, θ, χ define the orientation of the rotating frame with respect to the absolute frame: ϕ is the angle between the x-axis and the Xz-plane; θ is the angle between the X- and z-axes; χ is the angle between the Y-axis and the Xz-planes. Hence, values of $\phi = 0$, $\theta = \chi = \pi/2$ correspond to an unrotated reference frame and the axes of XYZ coincide with those of xyz. If we take as an example an H_2O molecule with fixed bond lengths and H-O-H bond angle, we need three Cartesian coordinates to fix the O atom, two angles to fix the orientation of one of the H atoms with respect to the O atom, and one further angle to fix the rotation of the other H atom with respect to the O-H bond. Thus, vector $\mathbf{r} = r\hat{\mathbf{X}}$ in a rotating frame that is rotated by the Euler angles ϕ, θ becomes $\mathbf{u} = (x, y, z)$ in the laboratory frame, defined by:

$$x = r \sin\theta \cos\phi \tag{3.24}$$

$$y = r \sin\theta \sin\phi \tag{3.25}$$

$$z = r \cos\theta \tag{3.26}$$

Expressed in words, the angle ϕ describes the angle that the projection of $\mathbf{r}$ into the xy-plane forms with the positive x-axis, measured counter-clockwise, and varies from 0 to 2π; θ describes the angle between $\mathbf{r}$ and the positive z-axis and varies from 0 to π. Explicitly,

the Euler angles ϕ and θ are calculated from $\mathbf{u}$ as:

$$\phi = \begin{cases} \arccos \frac{x}{u \sin\left(\arccos \frac{z}{u}\right)} & \text{if } y \geq 0 \\ 2\pi - \arccos \frac{x}{u \sin\left(\arccos \frac{z}{u}\right)} & \text{if } y < 0 \end{cases} \tag{3.27}$$

$$\theta = \arccos \frac{z}{u} \tag{3.28}$$

The slightly complicated definition with two separate cases for ϕ arises from the fact that the arccos function takes values in the interval $[0, \pi]$. The coordinates (ϕ, θ, r) are also known as the spherical coordinates of the point $\mathbf{u}$.

In principle, any orientation of an object can be defined by the three Euler angles, and according to Euler's theorem, any two orientations of a rigid object are related by one single rotation. The problem arises when $\theta = 0$, at which point the angles ϕ and χ become dependent on each other since the axes from which these angles are defined become collinear. This becomes obvious from Equation (3.27): if $z = r$, then $x, y \to 0$ and the argument of the arccos function goes towards $\frac{0}{0}$ and ϕ is undefined. The angular equation of motion has no solution at this point, a problem known as gimbal-lock (and a crucial problem to be avoided in aerospace engineering). This singularity of the Euler angle space has led to the search for an alternative formulation of orientation space.

3.3.1 Quaternions

The idea of using four parameters instead of three to describe the three-dimensional orientation space was first introduced by Leonhard Euler himself (Euler, 1776), but the term *quaternion* and the presentation of the algebraic rules for quaternion multiplication is attributed to Hamilton (1844).

A quaternion is defined as a complex number with three different imaginary parts rather than only one:

$$q = s + v_1 \mathrm{i} + v_2 \mathrm{j} + v_3 \mathrm{k} \tag{3.29}$$

The multiplication of the imaginary axes i, j, k is non-commutative and is defined by the following equations:

$$\mathrm{i}^2 = \mathrm{j}^2 = \mathrm{k}^2 = -1 \tag{3.30}$$

$$\mathrm{ij} = \mathrm{k}, \qquad \mathrm{jk} = \mathrm{i}, \qquad \mathrm{ki} = \mathrm{j} \tag{3.31}$$

$$\mathrm{ji} = -\mathrm{k}, \qquad \mathrm{kj} = -\mathrm{i}, \qquad \mathrm{ik} = -\mathrm{j} \tag{3.32}$$

In what follows, we use the following notation:

$$q = (s, \mathbf{v}) \tag{3.33}$$

where s denotes the real part of the quaternion, and $\mathbf{v} = (v_1, v_2, v_3)$ is a vector in $\mathbb{R}^3$ whose components are the coefficients of the imaginary parts from Equation (3.29).

The result of a multiplication of two quaternions $q_1 = (s, \mathbf{v})$ and $q_2 = (t, \mathbf{w})$ follows from Equations (3.30)–(3.32):

$$\begin{aligned} q_1 q_2 =& st - v_1 w_1 - v_2 w_2 - v_3 w_3 \\ &+ (s w_1 + t v_1 + v_2 w_3 - v_3 w_2)\mathrm{i} \\ &+ (s w_2 + t v_2 + v_3 w_1 - v_1 w_3)\mathrm{j} \\ &+ (s w_3 + t v_3 + v_1 w_2 - v_2 w_1)\mathrm{k} \end{aligned} \tag{3.34}$$

An interesting little known side-note is that the definition of the cross-product of three-dimensional vectors historically arises from the rules of quaternion multiplication; if two quaternions with their real parts equal to zero are multiplied, the result is:

$$\begin{aligned} (0, \mathbf{v})(0, \mathbf{w}) &= (v_2 w_3 - v_3 w_2)\mathrm{i} \\ &+ (v_3 w_1 - v_1 w_3)\mathrm{j} \\ &+ (v_1 w_2 - v_2 w_1)\mathrm{k} \\ &\equiv (0, \mathbf{v} \times \mathbf{w}) \end{aligned} \tag{3.35}$$

In compact notation, therefore, the multiplication of two quaternions is:

$$q_1 q_2 = (s, \mathbf{v})(t, \mathbf{w}) = (st - \mathbf{v} \cdot \mathbf{w}, s\mathbf{w} + t\mathbf{v} + \mathbf{v} \times \mathbf{w}) \tag{3.36}$$

Hamilton defines the following properties and operations of a quaternion $q = (s, \mathbf{v})$. The modulus, or norm, of a quaternion is:

$$|q| = \sqrt{s^2 + v_1^2 + v_2^2 + v_3^2} \tag{3.37}$$

A unit quaternion is any quaternion q for which $|q| = 1$. The identity quaternion, I, follows from the usual definition of the neutral element of any algebra that $qI = Iq = q$:

$$I = (1, \mathbf{0}) \tag{3.38}$$

which is easily verified using Equation (3.36). Similarly, the inverse quaternion q^{-1} is defined from the definition that $qq^{-1} = I$:

$$q^{-1} = \frac{(s, -\mathbf{v})}{|q|} \tag{3.39}$$

In analogy with complex numbers in algebra, the conjugate quaternion is defined as:

$$q^* = (s, -\mathbf{v}) \tag{3.40}$$

and we have:

$$|q|^2 = qq^* \tag{3.41}$$

3.3.2 Application of quaternions to describe orientations

It is also attributable to Hamilton (1847) that quaternions can be used to represent orientations. As stated by Euler's theorem, any two orientations of a rigid object are related by one single rotation that is defined by an axis $\hat{\mathbf{u}}$ and an angle of rotation α; $\hat{\mathbf{u}}$ is a unit vector in $\mathbb{R}^3$ and α takes values between 0 and 2π. This means that a rotation by

α around $\hat{\mathbf{u}}$ is indistinguishable from a rotation by $-\alpha$ around $-\hat{\mathbf{u}}$. By specifying a rotation axis and an angle, we define four parameters for a rotation, meaning that there is a redundancy, expressed in the condition (or convention) that $|\hat{\mathbf{u}}| = 1$. This redundancy could be eliminated by demanding that $|\hat{\mathbf{u}}| = \alpha$, reducing the number of parameters to three. However, this would give rise to a singularity in the case of a rotation by zero angle around any axis, which would invariably be described by the same vector of zero length for which no inverse is defined.

Hamilton shows that if we define a unit quaternion as

$$q = (s, \mathbf{v}) = (\cos(\alpha/2), \sin(\alpha/2)\hat{\mathbf{u}}) \tag{3.42}$$

and write a position vector $\mathbf{r}$ in quaternion form:

$$r = (0, \mathbf{r}) \tag{3.43}$$

then the quaternion r', defined by:

$$r' = qrq^{-1} = (0, \mathbf{r}') \tag{3.44}$$

represents the rotation of vector $\mathbf{r}$ by angle α around axis $\hat{\mathbf{u}}$; the rotation is clockwise when viewed along $\hat{\mathbf{u}}$. Quaternions defined in this way are unit quaternions:

$$|q| = 1 \tag{3.45}$$

In the quaternion representation, a rotation by zero angle is always represented by the identity quaternion I, which is its own inverse. Thus, all singularities are removed.

Explicitly, the rotated vector $\mathbf{r}'$ is given by:

$$\begin{aligned}\mathbf{r}' = \cos^2(\alpha/2)\mathbf{r} + 2\cos(\alpha/2)\sin(\alpha/2)\hat{\mathbf{u}} \times \mathbf{r} \\ + \sin^2(\alpha/2)(\hat{\mathbf{u}} \cdot \mathbf{r})\hat{\mathbf{u}} - \sin^2(\alpha/2)(\hat{\mathbf{u}} \times \mathbf{r}) \times \hat{\mathbf{u}}\end{aligned} \tag{3.46}$$

From this expression, it can be found (with some tedious but straightforward linear algebra) that the operation in Equation (3.44) can also be represented by a matrix operation on $\mathbf{r}$:

$$\mathbf{r}' = \mathsf{R}\mathbf{r} = \begin{pmatrix} s^2 + v_1^2 - v_2^2 - v_3^2 & 2v_1v_2 + 2sv_3 & 2v_1v_3 - 2sv_2 \\ 2v_1v_2 - 2sv_3 & s^2 - v_1^2 + v_2^2 - v_3^2 & 2v_2v_3 + 2sv_1 \\ 2v_1v_3 + 2sv_2 & 2v_2v_3 - 2sv_1 & s^2 - v_1^2 - v_2^2 + v_3^2 \end{pmatrix} \mathbf{r} \tag{3.47}$$

It is clear that by representing rotations by the four parameters of a quaternion rather than the three Euler angles, rotation operations become much simpler both from a notational point of view as well as from a computational point of view: the evaluation of the rotation matrix R above from a given quaternion $(s, \mathbf{v})$ involves only multiplication and addition operations and no evaluation of trigonometric functions. This, as well as the elimination of the gimbal-lock singularity of Euler angles and its compact, clean and rigorous notation, makes quaternions the clear favourite choice over Euler angles for representing orientation space in analysis algorithms.

3.3.3 Superposition of two molecules

In the analysis of molecular dynamics trajectories, the problem can often arise of having to superpose two identical molecules (identical composition and connectivity of atoms) which may be slightly distorted versions of each other, for means of comparison. This reduces to the problem of identifying the rotation (in the form of a quaternion) and the displacement (in the form of a displacement vector) that superpose one molecule onto the other, which are separate problems. In the specific case of this thesis, the problem is to approximate a vibrating BH_4^- anion by a reference BH_4^- anion in an ideal tetrahedral geometry. As the vibrating anion will in each instantaneous conformation be slightly distorted from ideal tetrahedral geometry, a quaternion needs to be determined that rotates the reference tetrahedral anion into as close a match of the deformed anion as possible. This procedure is described by Kearsley (1989).

Since all atoms are distinguishable, the problem reduces to rotating one ordered set

of N vectors $\mathbf{x}_i = (x_i, y_i, z_i)$ into another set $\mathbf{x'}_i = (x'_i, y'_i, z'_i)$ by a quaternion q to be determined. The prerequisite for this is that both sets have their centroids on the origin:

$$\frac{1}{N}\sum_{i=1}^{N}\mathbf{x}_i = \frac{1}{N}\sum_{i=1}^{N}\mathbf{x}'_i = \mathbf{0} \tag{3.48}$$

which is easily achieved by shifting each set by their centroid vector. The quaternions e_i are the residual quaternions between the rotated and the target vector set:

$$e_i = (0, \mathbf{x}'_\mathbf{i}) - q(0, \mathbf{x}_i)q^{-1} \tag{3.49}$$

Since the norm of a quaternion is unchanged when multiplied by a unit quaternion, e is right-multiplied by q to yield:

$$e_i q = (0, \mathbf{x'}_i)q - q(0, \mathbf{x}_i) \tag{3.50}$$

The penalty function that is minimised is thus the sum of the norms of $e_i q$. The Lagrange multiplier method is used to constrain the norm of q to unity; the penalty function is therefore:

$$\epsilon(q) = \sum_{i=1}^{N} w_i \left|(0, \mathbf{x'}_i)q - q(0, \mathbf{x}_i)\right|^2 + \lambda(1 - |q|^2) \tag{3.51}$$

where w_i are weighting factors that can be arbitrarily chosen (here, all $w_i = 1$) and λ is the Lagrange multiplier. Performing the quaternion multiplication results in:

$$\begin{aligned}\epsilon(s, v_1, v_2, v_3) = \sum_{i=1}^{N} w_i \Big[&\big(v_1(x_i - x'_i) + v_2(y_i - y'_i) + v_3(z_i - z'_i)\big)^2 \\ &+ \big(s(x'_i - x_i) - v_3(y'_i + y_i) + v_2(z'_i + z_i)\big)^2 \\ &+ \big(s(y'_i - y_i) - v_1(z'_i + z_i) + v_3(x'_i + x_i)\big)^2 \\ &+ \big(s(z'_i - z_i) - v_2(x'_i + x_i) + v_1(y'_i + y_i)\big)^2\Big] \\ &+ \lambda(1 - s^2 - v_1^2 - v_2^2 - v_3^2)\end{aligned} \tag{3.52}$$

To find the minimum of this function with respect to the quaternion parameters, the

equation is differentiated with respect to each parameter, resulting in a system of four equations that can be written in matrix form in the following way:

$$\mathsf{M}\begin{pmatrix} s \\ v_1 \\ v_2 \\ v_3 \end{pmatrix} = \lambda \begin{pmatrix} s \\ v_1 \\ v_2 \\ v_3 \end{pmatrix} \tag{3.53}$$

with the matrix M given by:

$$\mathsf{M} = \sum_{i=1}^{N} w_i \begin{pmatrix} \left(a_i^2 + b_i^2 + c_i^2\right) & (B_i c_i - C_i b_i) & (C_i a_i - A_i c_i) & (A_i b_i - B_i a_i) \\ (B_i c_i - C_i b_i) & \left(a_i^2 + B_i^2 + C_i^2\right) & (a_i b_i - A_i B_i) & (a_i c_i - A_i C_i) \\ (C_i a_i - A_i c_i) & (a_i b_i - A_i B_i) & \left(A_i^2 + B_i^2 + C_i^2\right) & (b_i c_i - B_i C_i) \\ (A_i b_i - B_i a_i) & (a_i c_i - A_i C_i) & (b_i c_i - B_i C_i) & \left(A_i^2 + B_i^2 + c_i^2\right) \end{pmatrix} \tag{3.54}$$

where $a_i = x_i' - x_i$, $b_i = y_i' - y_i$, $c_i = z_i' - z_i$ and $A_i = x_i' + x_i$, $B_i = y_i' + y_i$, $C_i = z_i' + z_i$. This is a symmetric, Hermitian matrix. The problem reduces to finding the eigenvalues and eigenvectors; four eigenvalues will be found with $0 \leq \lambda_1 \leq \lambda_2 \leq \lambda_3 \leq \lambda_4$; the eigenvector corresponding to the smallest eigenvalue λ_1 is the quaternion that minimises Equation (3.52).

3.3.4 Generation of random orientations

In certain situations, it may be necessary to generate a set of molecules that are randomly oriented in space, with a random distribution that is isotropic; in other situations it is desirable to choose a rotation axis randomly. It is not sufficient to trivially choose Euler angles from a uniformly distributed random number set, nor is it correct to generate the four components of a quaternion by uniform random number generation. This is because, for a grid of Euler angles ϕ_i, θ_i with constant spacings $\Delta\phi, \Delta\theta$, there will be a higher density of grid points near the poles of the unit sphere. The problem reduces to uniformly sampling the surface of a sphere in three or four dimensions. Marsaglia (1972) provides a

recipe with mathematical proofs for achieving this. To generate a point on the surface of a three-dimensional sphere, one generates two random numbers x_1 and x_2 from uniform distributions in $[-1; 1]$. One then forms:

$$y_1 = x_1^2 + x_2^2 < 1 \tag{3.55}$$

The numbers x_1, x_2 are rejected and new ones drawn until this condition is satisfied; on average this requires $8/\pi$ random numbers to be determined until a suitable pair is found. The following unit vector randomly samples the surface of the unit sphere:

$$\hat{\mathbf{r}} = \left(2x_1\sqrt{1-y_1},\, 2x_2\sqrt{1-y_1},\, 1-2y_1\right) \tag{3.56}$$

To extend this algorithm to four dimensions, an additional pair of random numbers x_3 and x_4 is formed until the condition is satisfied:

$$y_2 = x_3^2 + x_4^2 < 1 \tag{3.57}$$

The quaternion is formed as:

$$q = \left(x_1,\, x_2,\, x_3\sqrt{\frac{1-y_1}{y_2}},\, x_4\sqrt{\frac{1-y_1}{y_2}}\right) \tag{3.58}$$

The mathematical proof for uniform sampling shall not be repeated here, but is elegantly and succinctly presented by Marsaglia (1972). Isotropic rotational diffusion is modelled by a random rotational walk with a constant step angle and a rotational axis that is at each step determined by Equation (3.56).

3.3.5 Calculation of the angular velocity of a molecule

For an object that rotates around a constant axis with a constant angular velocity $\boldsymbol{\omega}$, the change in the quaternion q that describes its orientation is given by the following equation:

$$\dot{q} = (0, \boldsymbol{\omega}/2)q \tag{3.59}$$

This is right-multiplied by q^{-1} to give:

$$(0, \boldsymbol{\omega}) = 2\dot{q}q^{-1} \tag{3.60}$$

From an MD trajectory, the time-evolution of the quaternion is easily evaluated numerically at time step t_i using finite differences:

$$\dot{q}(t_i) \approx \frac{q(t_i) - q(t_{i-1})}{\Delta t} \tag{3.61}$$

Given the orientation of a molecule at two consecutive time steps $i-1$ and i, the angular velocity is calculated by:

$$(0, \boldsymbol{\omega}) = 2\frac{q(t_i) - q(t_{i-1})}{\Delta t} q^{-1}(t_i) \tag{3.62}$$

3.4 Neutron scattering

Neutron scattering is a very versatile technique for the study of condensed matter structure and dynamics. Because neutrons are scattered by nuclei and not electrons, there is a very close similarity between neutron scattering cross sections and the equations of molecular dynamics. The two techniques strongly complement one another.

In the most general definition of a neutron scattering experiment, a flux $\mathbf{j}_0$ of neutrons characterised by a wave vector $\mathbf{k}_0$ and energy ϵ_0 is scattered by the sample. Since neutrons are small and light particles, they can be treated as a plane wave, $\exp(i\mathbf{k}_0 \cdot \mathbf{r})$; the energy is the kinetic energy of the neutron and equal to $\epsilon_0 = \hbar^2 k_0^2 / 2m_n$. The total number of scattered neutrons arriving per second in any direction on a surface enclosing the sample is given by $I_1 = |\mathbf{j}_0| \, \sigma_c$, where σ_c is defined as the total scattering cross-section. The motivation of a neutron scattering experiment is to measure exactly where and with what energy the neutrons arrive; through modern detector arrays, it is possible to measure a

substantial proportion of the complete differential scattering cross-section. We are interested in the number of neutrons per second arriving at an angle θ from the incident beam, at $\mathbf{Q} = \mathbf{k}_0 - \mathbf{k}_1$, into a solid angle element $\mathrm{d}\Omega$ having energies between ϵ_1 and $\epsilon_1 + \mathrm{d}\epsilon_1$, with $\hbar\omega = \epsilon_0 - \epsilon_1$:

$$\mathrm{d}I_1 = |\mathbf{j}_0| \left(\frac{\mathrm{d}^2\sigma_c}{\mathrm{d}\Omega\, \mathrm{d}\epsilon_1} \right)_{\theta,\epsilon_1} \mathrm{d}\Omega\, \mathrm{d}\epsilon_1 \tag{3.63}$$

Hempelmann (2000) and Dove (2002) offer an elegant derivation of the differential scattering cross-section from the above equation based on an accurate treatment by quantum mechanics and perturbation theory, which shall be very briefly summarised here to illustrate the close relationship between the neutron scattering factor and the information contained in an MD trajectory. The result of this treatment is the following expression of the differential scattering cross-section:

$$\left(\frac{\mathrm{d}^2\sigma_c}{\mathrm{d}\Omega\, \mathrm{d}\epsilon_1} \right) = \frac{k_1}{k_0} \frac{1}{2\pi\hbar} \int_{-\infty}^{+\infty} \mathrm{d}t \sum_{i=1}^{N} \sum_{j=1}^{N} b_i b_j \left\langle e^{-i\mathbf{Q}\cdot\mathbf{r}_i(0)} e^{i\mathbf{Q}\cdot\mathbf{r}_j(t)} \right\rangle e^{i\omega t} \tag{3.64}$$

This results from the quantum mechanical treatment of a very general scattering process. The term in the average can be written as:

$$e^{-i\mathbf{Q}\cdot\mathbf{r}_i(0)} e^{i\mathbf{Q}\cdot\mathbf{r}_j(t)} = \int \mathrm{d}r\, \delta(r - r_i(0)) e^{-i\mathbf{Q}\cdot\mathbf{r}} \int \mathrm{d}r\, \delta(r - r_j(t)) e^{i\mathbf{Q}\cdot\mathbf{r}} = \rho_i(-\mathbf{Q}, 0)\rho_j(\mathbf{Q}, t) \tag{3.65}$$

This is the spatial Fourier transform of the atomic density, which is expressed by Dirac functions:

$$\rho_i(\mathbf{Q}, t) = e^{i\mathbf{Q}\cdot\mathbf{r}_i(t)} \tag{3.66}$$

$$\rho_i(\mathbf{r}, t) = \delta(\mathbf{r} - \mathbf{r}_i(t)) \tag{3.67}$$

which defines the intermediate structure factor:

$$F(\mathbf{Q}, t) = \frac{1}{N} \sum_{i,j} \langle b_i b_j \rangle \langle \rho_i(-\mathbf{Q}, 0)\rho_j(\mathbf{Q}, t) \rangle \tag{3.68}$$

The dynamical structure factor is defined as:

$$S(\mathbf{Q},\omega) = \int \mathrm{d}t\, F(\mathbf{Q},t)\, e^{i\omega t}) \tag{3.69}$$

With this definition we have:

$$\rho_i(\mathbf{Q},t) = e^{i\mathbf{Q}\cdot\mathbf{r}_i(t)} \tag{3.70}$$

$$F(\mathbf{Q},t) = \frac{1}{N}\sum_{i,j} \langle b_i b_j\rangle \,\langle \rho_i(-\mathbf{Q},0)\rho_j(\mathbf{Q},t)\rangle \tag{3.71}$$

$$S(\mathbf{Q},\omega) = \frac{1}{N}\sum_{i,j} \langle b_i b_j\rangle \int \mathrm{d}t\ \langle \rho_i(-\mathbf{Q},0)\rho_j(\mathbf{Q},t)\rangle\ e^{i\omega t} \tag{3.72}$$

The average $\langle b_i b_j\rangle$ can mathematically be replaced by $\langle b_i b_j\rangle - \langle b_i\rangle\langle b_j\rangle + \langle b_i\rangle\langle b_j\rangle$ without changing anything, allowing the separation of coherent and incoherent scattering. The first (incoherent) part, $\langle b_i b_j\rangle - \langle b_i\rangle\langle b_j\rangle$, is different from zero only if there is a correlation between the scattering lengths at atom sites i and j, which is only the case if either $i = j$ or if i and j are pure isotopes with only one value for the scattering length; in the latter case the incoherent contribution vanishes. Therefore, the incoherent part reduces to $\left\langle b_i^2\right\rangle - \langle b_i\rangle^2$.

The intermediate structure factor can thus be written as:

$$F(\mathbf{Q},t) = F_{\mathrm{coh}}(\mathbf{Q},t) + F_{\mathrm{incoh}}(\mathbf{Q},t) \tag{3.73}$$

$$F_{\mathrm{coh}}(\mathbf{Q},t) = \frac{1}{N}\sum_{i,j} \langle b_i\rangle\langle b_j\rangle \left\langle e^{i\mathbf{Q}\cdot[\mathbf{r}_i(t)-r_j(0)]}\right\rangle \tag{3.74}$$

$$F_{\mathrm{incoh}}(\mathbf{Q},t) = \frac{1}{N}\sum_{i} \left(\left\langle b_i^2\right\rangle - \langle b_i\rangle^2\right) \left\langle e^{i\mathbf{Q}\cdot[\mathbf{r}_i(t)-\mathbf{r}_i(0)]}\right\rangle \tag{3.75}$$

The structure factor is defined as:

$$S(\mathbf{Q}) = \int_{-\infty}^{+\infty} \mathrm{d}\omega\, S(\mathbf{Q},\omega) = \int \mathrm{d}t\, F(\mathbf{Q},t) \int_{-\infty}^{+\infty} \mathrm{d}\omega\, e^{i\omega t} = F(\mathbf{Q},0) \tag{3.76}$$

Furthermore, the spatial Fourier transform of the intermediate scattering factor yields the

correlation function $G(\mathbf{r}, t)$ (Keen, 2001).

$$G(\mathbf{r}, t) = \frac{1}{8\pi^3} \int \mathrm{d}\mathbf{Q}\, F(\mathbf{Q}, t) e^{-i\mathbf{Q}\cdot\mathbf{r}} \tag{3.77}$$

Using Equation (3.71), this becomes:

$$G(\mathbf{r}, t) = N^{-1} \sum_{i,j} \langle b_i b_j \rangle \int \mathrm{d}\mathbf{r}' \, \left\langle \delta(\mathbf{r}' - \mathbf{r}_i(0)) \delta(\mathbf{r}' + \mathbf{r} - \mathbf{r}_j(t)) \right\rangle \tag{3.78}$$

Here we are only interested in $t = 0$, which allows us to integrate the above equation:

$$G(\mathbf{r}, 0) = N^{-1} \sum_{i,j} \langle b_i b_j \rangle \left\langle \delta(\mathbf{r} + \mathbf{r}_i(0) - \mathbf{r}_j(0)) \right\rangle \tag{3.79}$$

This can also be written as:

$$G(\mathbf{r}, 0) = \delta(\mathbf{r}) \sum_i \frac{\langle b_i^2 \rangle}{N} + N^{-1} \sum_{i \neq j} \langle b_i b_j \rangle \left\langle \delta(\mathbf{r} + \mathbf{r}_i(0) - \mathbf{r}_j(t)) \right\rangle \tag{3.80}$$

The second term above is set equal to $\rho g(\mathbf{r})$, defining the radial distribution function:

$$g(\mathbf{r}) \equiv (\rho N)^{-1} \sum_{i \neq j} \langle b_i b_j \rangle \left\langle \delta(\mathbf{r} + \mathbf{r}_i(0) - \mathbf{r}_j(0)) \right\rangle \tag{3.81}$$

Through the relation with the structure factor, Equation (3.76), we can write this as:

$$g(\mathbf{r}) = 1 + \rho^{-1} \int \mathrm{d}\mathbf{Q} \left(S(\mathbf{Q}) - \frac{\sum \langle b_i^2 \rangle}{N} \right) e^{-i\mathbf{Q}\cdot\mathbf{r}} \tag{3.82}$$

Since in practice most measurements are made on powdered samples rather than single crystals, the resolution with respect to the direction of $\mathbf{Q}$ vanishes, and only the magnitude Q can be controlled. The relative orientations of $\mathbf{Q}$ and any vector inside the crystal must be averaged over all orientations. The powder averages of the above equations are:

$$\frac{1}{4\pi} \int_0^{2\pi} \int_0^{\pi} e^{iQr\cos\theta} \sin\theta \, \mathrm{d}\theta \, \mathrm{d}\phi = \frac{1}{4\pi} \int_0^{2\pi} \int_1^{-1} e^{iQrx} \mathrm{d}x \, \mathrm{d}\phi = \frac{\sin(Qr)}{Qr} \tag{3.83}$$

On all other terms the powder average has no effect, except for the replacement of the vectors by their absolute values. The volume element d$\mathbf{r}$ is replaced by $4\pi r^2 \mathrm{d}r$, and d$\mathbf{Q}$ by $4\pi Q^2 \mathrm{d}Q$. Thus we have:

$$g(r) = 1 + 4\pi\rho^{-1} \int \mathrm{d}Q \left(S(Q) - \frac{\sum \langle b_i^2 \rangle}{N} \right) \frac{Q \sin(Qr)}{Qr} \tag{3.84}$$

The explicit expression for the pair distribution function from Equation (3.81) becomes:

$$g(r) = (\rho N)^{-1} \sum_{i \neq j} \langle b_i b_j \rangle \langle \delta(r - |\mathbf{r}_i(0) - \mathbf{r}_j(0)|) \rangle \tag{3.85}$$

The pair distribution function (PDF) can be measured from total scattering as well as calculated directly from MD simulations according to Equation (3.85). A few comments about the practical computation of the PDF shall be made. First, a maximum value r_{cut} up to which the PDF is to be computed, must be defined. Second, a bin size, Δr, must be defined. Numerically, the PDF is therefore computed for a number $s = r_{\mathrm{cut}}/\Delta r$ of bins. The average of Equation (3.85) is evaluated as a time average over an MD trajectory:

$$g(r) = \left(\int_0^\infty \mathrm{d}t \right)^{-1} (\rho N)^{-1} \sum_{i \neq j} \langle b_i b_j \rangle \int_0^\infty \mathrm{d}t \, \delta(r - |\mathbf{r}_i(t) - \mathbf{r}_j(t)|) \tag{3.86}$$

Replacing the time integral by a sum over n time steps, we obtain:

$$g(r_m) = \frac{2}{n} (\rho N)^{-1} \sum_{i=1}^{N-1} \sum_{j=i+1}^{N} \langle b_i b_j \rangle \sum_{k=1}^{n} \int_{r_{m-1}}^{r_m} \mathrm{d}r \, \delta(r - |\mathbf{r}_i(t_k) - \mathbf{r}_j(t_k)|) \tag{3.87}$$

CHAPTER 4

Calcium borohydride structure prediction

> "There are known knowns ... there are known unknowns ... But there are also unknown unknowns."
>
> Donald Rumsfeld, US Secretary of Defence in 2003

In this chapter, hypothetical structures of the hydrogen storage material calcium borohydride, $Ca(BH_4)_2$, under elevated pressure (up to 60 GPa) are proposed based on an *ab initio* crystal structure prediction. Among the metal borohydrides, calcium and magnesium borohydride are the most promising for hydrogen storage applications because of their weight capacity and thermodynamic properties, as well as practical reasons such as safety and cost. Though crystalline beryllium borohydride exists, it is highly toxic even in the smallest quantities and therefore not suitable to make up the bulk of a commercial hydrogen storage material. Furthermore, both magnesium and calcium are abundantly and cheaply available elements, whereas other di- or trivalent borohydrides (e. g. $Y(BH_4)_3$, $Zr(BH_4)_4$) are both too expensive and of too low weight capacity to be considered as a bulk hydrogen storage material for large-scale use (Bird and Churchill, 1967; Sato *et al.*, 2008).

The thermal decomposition with hydrogen release occurs in the solid state, but the

mechanisms are not straightforward for either $Ca(BH_4)_2$ or $Mg(BH_4)_2$. A number of pathways are imaginable leading to different decomposition products. In one of the first theoretical studies on potential decomposition pathways of pure $Ca(BH_4)_2$ (Miwa *et al.*, 2006), the enthalpy of decomposition into the elements was predicted to be 75.5 kJ/(mol H_2), meaning that this reaction is thermodynamically highly unfavourable and would occur only at very high temperatures. The same authors also considered decomposition into $CaB_6 + 2\,CaH_2$ and calculated a decomposition enthalpy of 32 kJ/(mol H_2), which is in the favourable range for thermal decomposition as explained in Chapter 1. Other theoretical studies of possible reaction pathways have been performed (Wolverton *et al.*, 2008; Ozolins *et al.*, 2009; Zhang *et al.*, 2010) and numerous possible end products were considered, most notably $CaB_{12}H_{12} + 5\,CaH_2$. Decomposition products of reaction composites that increase the relative stability of the decomposition products, such as $Ca(BH_4)_2 + MgH_2$, were also considered. Decomposition enthalpies were consistently found in the range 30–40 kJ/(mol H_2), and thus $Ca(BH_4)_2$ is predicted to have very favourable thermodynamics for thermal decomposition.

Yet in practice it has been found that decomposition is not governed by thermodynamics but kinetics: all reported experimental decomposition temperatures are substantially above the thermodynamic decomposition temperature of around 100°C. Kim *et al.* (2008) reported decomposition of pure $Ca(BH_4)_2$ to occur at a temperature of 380°C. Determining the structures of the end products of thermal decomposition has proved to be extremely difficult: in an X-ray diffraction study of thermal decomposition by Riktor *et al.* (2007), no CaB_6 nor any other known phase containing boron was detected in the diffraction pattern of the decomposition products, only an "unknown phase". It was found that the decomposition products depended on the heating rate and the final temperature of the desorption reaction, as well as the presence of additives such as $TiCl_3$. A method of synthesising $Ca(BH_4)_2$ reported by Rönnebro and Majzoub (2007) proved the reversibility of the hydrogen desorption reaction: the synthesis proceeded by hydrogenation of

the assumed decomposition products CaB_6 and CaH_2.

$$CaB_6 + 2\,CaH_2 \xrightarrow[\text{2) 350 bar } H_2,\ 400^\circ C]{\text{1) ball milling, pelletisation}} 3\,Ca(BH_4)_2 \tag{4.1}$$

It was noted that the above reaction did not proceed unless 5–10% in weight of a dopant was added, acting as a catalyst; the successful dopants were $TiCl_3$ and $TiCl_3$ + Pd, but no rationale for the choice of these dopants was given nor is their mode of action known. Reliable experimental results for the decomposition enthalpy cannot be found in the literature. To clearly understand decomposition pathways and thermodynamics, the crystal structures of the material must first be known.

$Ca(BH_4)_2$ displays a rich polymorphism: several solid phases are known that are theoretically predicted to be of similar thermodynamical stability, explaining their coexistence under ambient conditions. The phase of the material seems to depend on the synthesis method. Miwa *et al.* (2006) synthesised and solved the crystal structure of the α-phase of $Ca(BH_4)_2$ for the first time through laboratory X-ray diffraction and presented a solution in space group *Fddd*. Their synthesis method consisted of heating in vacuum a $Ca(BH_4)_2 \cdot 2\,THF$ adduct (which is commercially available) at 433 K for 1 hour. In another experimental study, Riktor *et al.* (2007) synthesised $Ca(BH_4)_2$ using the wet chemical method—previously introduced by Chłopek *et al.* (2007) to synthesise $Mg(BH_4)_2$—to produce a mixture of two $Ca(BH_4)_2$ phases by the reaction:

$$CaH_2 + 2\,Et_3N \cdot BH_3 \longrightarrow Ca(BH_4)_2 + 2\,Et_3N \tag{4.2}$$

Neither of the two phases in the obtained mixture was the previously reported α-phase, and they were termed β- and γ-phases. They performed a synchrotron X-ray crystallographic study with *in situ* heating of the material and shed the first light on the complex phase diagram of $Ca(BH_4)_2$. They noted that the γ-phase gradually transformed into the β-phase without decomposition and that the γ-phase transformed into an additional phase of the material, termed the δ-phase; none of the newly identified phases of $Ca(BH_4)_2$

was crystallographically solved. A solution of the β-phase crystal structure was found by neutron powder diffraction measurements by Buchter *et al.* (2008b), who used the reactive hydride composites synthesis method proposed by Barkhordarian *et al.* (2007) to synthesise a sample consisting mainly of the β-phase. The reactive hydride composite method (Barkhordarian *et al.*, 2007) uses MgB_2 as a source of more reactive boron than its elemental form to produce borohydrides of Ca, Li or Na:

$$CaH_2 + MgB_2 \xrightarrow{H_2\,(350\text{ bar})} Ca(BH_4)_2 + MgH_2 \tag{4.3}$$

Later, using the wet chemical method from Reaction (4.2), a solution of the γ-phase crystal structure was found, again by neutron powder diffraction (Buchter *et al.*, 2009). The crystallographic refinement from neutron powder diffraction resulted in space group $P4_2/m$ for the β-phase and $Pbca$ for the γ-phase. All original structure determination papers for the α, β and γ phases (Miwa *et al.*, 2006; Buchter *et al.*, 2008b, 2009) each include a computational determination of the thermodynamical and dynamical stability of the phase, and the predicted ground state geometry.

These crystal structures are not entirely without controversy, however. Filinchuk *et al.* (2009b) revisited and revised the published crystal structures with "high-quality *in situ* synchrotron diffraction" studies to propose alternative structures of this high-hydrogen content material. The revised structure of the α-phase was reported to have symmetry $F2dd$, with the argument that this slightly lower symmetry led to a refined structure with nearly undistorted BH_4 tetrahedra and larger minimum H-H separation between neighbouring anions, making for a physically more reasonable structure. The β-phase was revised to be in $P\bar{4}$ symmetry. Though the authors clearly demonstrated that the revised structure resulted in a better fit than the previous $P4_2/m$ model, it is questionable whether an X-ray technique is able to provide significantly more reliable data than neutron diffraction, given that 8 out of 11 atoms in the sample are hydrogen atoms. It can only be concluded that diffraction studies of one and the same material do not lead to unambiguous solutions of the crystal structure, and the $Fddd$ vs $F2dd$ and $P4_2/m$ vs $P\bar{4}$ structures must

be seen as alternatives—a synchrotron X-ray diffraction study by Noritake *et al.* (2010), for example, reconfirmed the first reported crystal structures (*Fddd*, $P4_2/m$, and *Pbca*). An additional result from the study by Filinchuk *et al.* (2009b) was the observation of a second-order phase transition of the α-phase at 495 K into a tetragonal $I\bar{4}2d$ structure termed α'.

As a consequence of this polymorphism, many theoretical studies have attempted to predict other solid phases as well as phase stabilities with respect to temperature and pressure. Shortly after the resolution of the α-phase, a DFT structure prediction attempt was published by Vajeeston *et al.* (2007), where the method of database searching was used: 28 structure types with molecular formula $A(XY_4)_2$ from the Inorganic Crystal Structure Database (ICSD) were tested as starting points for structures with $Ca(BH_4)_2$ chemistry, and the energetic stabilities of the resulting structure types were determined by equation of states fitting. Among the structures, the *Fddd* structure of the α-phase did turn out to be the energetically most favourable one. Majzoub and Rönnebro (2009) performed a random crystal structure search to identify other possible phases and compute their thermodynamic stabilities as a function of temperature and pressure, based on the total harmonic free energy. They also pointed out that experimental crystal structure solving methods produce structures by fitting a parametrised structure model to the experimentally observed diffraction data, but do not take into account any form of atom-atom interaction physics, and therefore the obtained structures must be checked by DFT computation whether they are physically reasonable; a good example is the structural solution of a model with strongly distorted BH_4 units for the low-temperature phase of $LiBH_4$ (see Chapter 5), for which there is clearly no physical justification, and was corrected in later experimental structures.

Phase transitions in $Ca(BH_4)_2$ with respect to temperature were studied experimentally by Riktor *et al.* (2007), who found that the phase transition from γ to β occurred slowly and gradually in the temperature range 40–290°C. The transition from γ to δ occurred completely at 290–330°C. The material finally decomposed at 330–380°C where the β-phase decomposed; decomposition of the δ-phase occurred at 400–480°C. While all

phases that are observed at ambient pressure and varying temperature are known (with the exception of the δ-phase), phase transitions with respect to pressure are not well studied. Two experimental high-pressure studies have been published: George *et al.* (2009a) report on *in situ* synchrotron X-ray diffraction experiments of a mixture of α- and β-$Ca(BH_4)_2$ compressed in a diamond anvil cell up to 25 GPa (1 GPa corresponds to 10 kbar). Upon compression, the β-phase transformed into a "disordered" phase above 10.2 GPa, but did not transform back upon decompression; consequently, the β-phase is not the ground state. In an *in situ* Raman/IR study by Liu *et al.* (2010) of the compression of a phase-pure sample of α-$Ca(BH_4)_2$ (termed phase I) in a diamond anvil cell up to 10 GPa, three additional phases were identified (phases II–IV). Phase II was formed at 2.3 GPa, which transformed into phase III at 3.9 GPa; it was speculated that phase II might be an intermediate phase in the transition to phase III. Phase IV formed at 6.6 GPa. However, none of the crystal structures of the new phases could be determined.

In this chapter, a crystal structure prediction of $Ca(BH_4)_2$ structures at high pressure (up to 60 GPa) is presented, exploiting an observed structural similarity between TiO_2 and $Ca(BH_4)_2$ phases. The work by Majzoub and Rönnebro (2009) did analyse thermodynamic stability as a function of pressure, but the predicted structures were taken from a prediction at zero pressure. Here, structures directly generated at high pressure shall be considered.

4.1 Crystal structure prediction methods

The reliable prediction of stable crystal structures of a compound of known composition by purely theoretical and computational methods is an unsolved problem which, if solved, would present a major advance in the predictive power of theoretical methods. Its significance might be compared to the problem of predicting protein folding patterns in biochemistry, or indeed the attempt to predict stock market or consumer behaviour in the field of economics. In all fields, various prediction algorithms of differing degrees of creativity (and success) have proliferated, but none that can claim universal success has emerged in any of these fields.

The underlying problem of crystal structure prediction is a global $3N$-dimensional minimisation problem, where N is the number of atoms in the unit cell:

$$G(\mathbf{r}^0_{1\ldots N}) = \min_{\{\mathbf{r}_i\}} G(\mathbf{r}_{1\ldots N}) \tag{4.4}$$

$G(\mathbf{r}_{1\ldots N})$ is the Gibbs energy hypersurface. For a given geometry $\{\mathbf{r}_{1\ldots N}\}$, the Gibbs energy can be approximately evaluated by the methods discussed in Chapter 2. Since all three spatial coordinates of each atom can, in principle, vary independently, the free enthalpy is a function in a $3N$-dimensional configuration space and the correct crystal structure is the global Gibbs energy minimum in this configuration space. The form of the Gibbs energy hypersurface in configuration space is not known analytically, and therefore no mathematical method exists for determining the global minimum on this hypersurface. The geometry optimisation algorithms mentioned in Section 2.1.8 are only able to determine the nearest local minimum given a starting point on the hypersurface (input structure). To find the global minimum, the entirety of configuration space would need to be sampled, which is in practice impossible. Consider a simple system of 4 atoms in a fixed unit cell. If each of the 12 dimensions of this configuration space is sampled by 10 sampling points, which would be rather coarse, then a total of 10^{12} sampling points in configuration space would have to be evaluated: an absurdly resource-intense task for the determination of a rather simple system. The computational time needed to evaluate any one point on this hypersurface is the limiting factor for systematic searches.

Effective crystal structure prediction methods are developed by restricting configuration space by empirical rules that impose constraints—a typical example is to restrict atom-atom distances to reasonable ranges: in general, no structure needs to be considered where any atom-atom distance is shorter than a certain minimum value. The problem is therefore generally split into two parts: the first, the generation of "reasonable" starting structures, often with the help of random sampling techniques, where the definition of "reasonable" is what leads to so many different competing methods. Since only a very limited subpart of the full configuration space can ever be searched by any crystal struc-

ture prediction attempt, picking the best pockets of configuration space is the art in this field. The second part is the accurate evaluation of the relative energetic stability of the selected starting structures, which is generally done by high-level DFT computation.

The most straightforward way to obtain starting structures is by direct random sampling, with a minimum of constraints imposed. This method has been proposed by Pickard and Needs (2009) and is argued to be the most unbiased method for identifying stable structures. Their method uses unbiased random number generation to generate the positions of atoms, and/or rigid molecular units, and the unit cell vectors of a given system, with relatively few and straightforward constraints imposed. The number and type of atoms per unit cell is fixed, as is the space group symmetry; furthermore, generated structures with a unit cell volume and minimum atom-atom distances falling outside a specified range are rejected. The accepted random structures are then directly subjected to geometry optimisation, and after a number of cycles it is expected that a much smaller number of stable structures are identified. In this way, only a restricted subset of all possible structures can be identified.

The precise evaluation of the Gibbs energy by DFT is the most time-consuming step; however, a high level of accuracy is not needed if the structure is subsequently discarded in the course of the structure search. Another method consists in the generation of a set of candidate structures by a much simpler and thus faster, but less accurate computational method. In this way, considerably more random structures than in the previously described method can be screened and their energy evaluated according to the simplified energy functional. Only the generated structures that fall in a narrow range of energies are then subjected to full geometry optimisation by DFT. The prototype electrostatic ground state method (PEGS) by Majzoub and Ozolins (2008) performs random structure searches evaluating the energy by a simple energy functional that computes the Coulomb energy of anions and cations. A Monte Carlo algorithm generates a range of energetically favourable starting structures, whose geometry is subsequently optimised by accurate DFT calculations. It might be pointed out that in the original presentation of the PEGS algorithm, the random sampling of the Euler angles for generating random orientations of complex

Table 4.1: Comparison of structural properties of borohydrides and their isoelectronic metal oxide equivalents. Lithium borohydride data from Filinchuk *et al.* (2008b); alkaline-earth oxide data from Gerlach (1922); TiO_2 data from Baur (1961) and Howard *et al.* (1991); $Mg(BH_4)_2$ data from Filinchuk *et al.* (2009a); $Ca(BH_4)_2$ data from Miwa *et al.* (2006); Buchter *et al.* (2008b, 2009). $LiBH_4$ ($Fm\bar{3}m$) is a high-pressure structure, the reported volume is V_0 from an equation of state fit.

Borohydride	Space group	Volume	Isoelectronic oxide	Space group	Volume	V_1/V_2
$LiBH_4$	$Fm\bar{3}m$	47.3	BeO	$Fm\bar{3}m$	13.67	3.460
	$P6_3mc$	56.9385		$P6_3mc$	13.865	4.107
$NaBH_4$	$Fm\bar{3}m$	57.6075	MgO	$Fm\bar{3}m$	18.67	3.0986
KBH_4	$Fm\bar{3}m$	76.14	CaO	$Fm\bar{3}m$	27.27	2.792
$Mg(BH_4)_2$	$P6_122$	114.68	SiO_2			
	$Fddd$	117.87				
$Ca(BH_4)_2$	$I4_1/amd$	108.27	TiO_2	$I4_1/amd$	34.07	3.178
	$P4_2/m$	105.35		$P4_2/mnm$	31.21	3.376
	$Pbca$	102.83		$Pbca$	32.17	3.196

anions does not sample orientation space isotropically, as addressed in Section 3.3.4.

The method by Neumann (2008) operates in a similar way, but is aimed at molecular rather than ionic crystals. Since the packing of molecular crystals is strongly dependent on dispersion forces, a parametrised force field is constructed for each type of molecular crystal first. This force field, rather than a simple electrostatic energy functional, is then used when generating candidate structures for subsequent DFT optimisation.

Suitable starting structures can also be found from known, existing structures of a similar type. Isostructural pairs are commonly used in experimental crystallography to help solving crystal structures from diffraction data. The crystal structure of a new compound is solved by taking as a starting point the known crystal structure of a "similar" compound, that is a compound with the same general formula. With the advent of consolidated structural databases such as the Cambridge Crystal Structural Database or the Inorganic Crystal Structure Database (ICSD), it has become convenient to computationally analyse vast numbers of initial structures in this way. For example, the polymorph II of TiO_2 was solved by creating an initial model based on columbite ($PbCl_2$) as the limited data obtained from diffraction did not allow for a rigorous crystal structure solving method (Simons and Dachille, 1967). Similarly, much later, another polymorph of TiO_2 was hypothesised to adopt the cotunnite structure of ZrO_2 based on the reasoning that cotunnite has an extremely high bulk modulus for an oxide, similar to the unknown

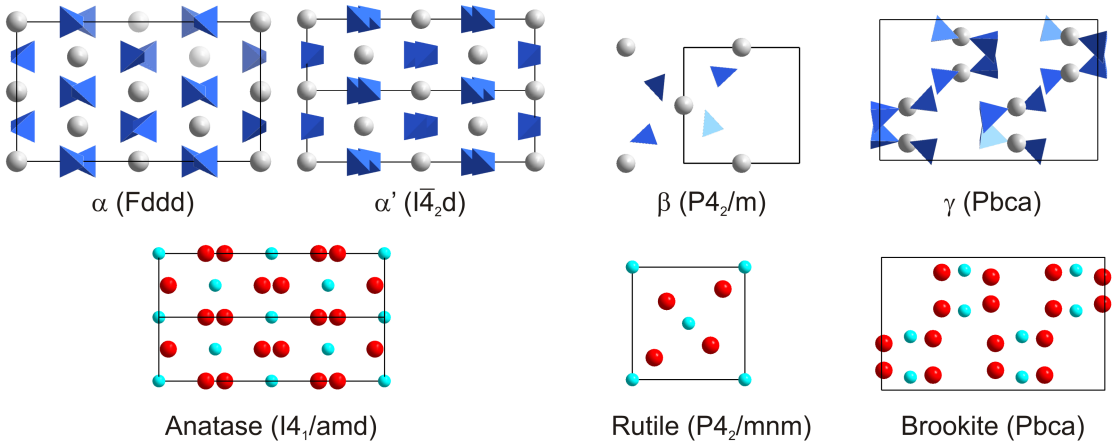

Figure 4.1: Ambient-pressure polymorphs of TiO_2 (bottom) compared to the known structures of $Ca(BH_4)_2$ (top). Blue spheres: Ti atoms; red spheres: O atoms; grey spheres: Ca atoms; blue tetrahedra: BH_4 units.

high-pressure phase of TiO_2; this assumption was tested computationally, and the predicted structure was subsequently found experimentally (Dubrovinsky *et al.*, 2001). In this chapter, we make use of the same principle to predict high-pressure crystal structures of $Ca(BH_4)_2$ based on the high-pressure polymorphs of TiO_2.

4.1.1 Structural analogy between oxides and borohydrides

Table 4.1 shows the structural similarity between metal oxides and borohydrides. The alkali metal borohydrides have rock-salt structures, as do the alkaline earth oxides. A notable exception is the case of $LiBH_4$, isoelectronic with BeO, which both adopt very similar hexagonal structures under normal conditions; they both exist in the rock-salt phase as well, but only at elevated pressure. $Mg(BH_4)_2$, which is isoelectronic with SiO_2, is peculiar in that its molar volume is much larger than that of $Ca(BH_4)_2$, even though the inverse trend is observed when going down in the periodic table for the alkali borohydrides. $Mg(BH_4)_2$ forms very large unit cells ($Z = 30$ and 64 for the $P6_122$ and $Fddd$ structures, respectively) and the structures can be described as open frameworks formed by edge and corner-sharing tetrahedra, with Mg at their centres and BH_4 at the vertices. SiO_2 is known to be able to adopt a vast number of zeolitic structures. In the case of $Ca(BH_4)_2$, the known polymorphs all have corresponding TiO_2 structures, as shown in Figure 4.1.

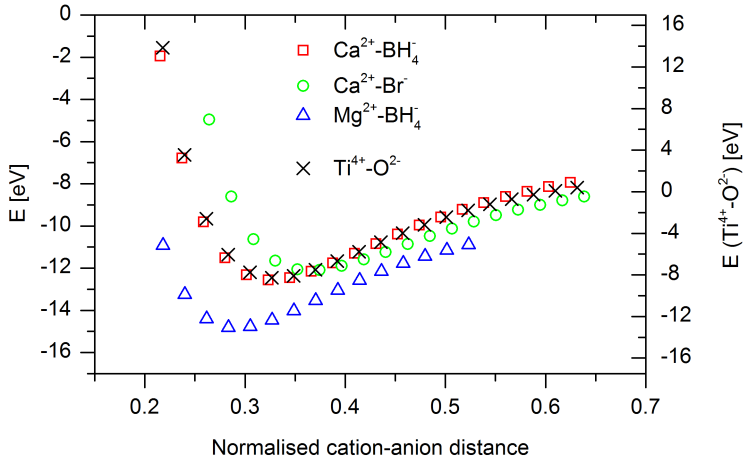

Figure 4.2: Binding energies for gas-phase ion pairs of compounds that exist in the rutile structure. The energy was calculated using the Gaussian03 programme (Frisch *et al.*, 2003). The cation-anion distance was divided by the lattice parameter a of each material.

TiO_2 has also three more structures under high pressure, and these structures are taken as templates to predict high-pressure structures for $Ca(BH_4)_2$.

Is there a physical principle underlying this structural similarity? If we are to use the high-pressure polymorphs for structure prediction, it is legitimate to scrutinise whether any causal relation exists for this similarity or whether it is pure coincidence. For example, $CaBr_2$ has a rutile structure as well, and has been used previously by Nakamori *et al.* (2006) to predict the β-phase of $Ca(BH_4)_2$, but since only two polymorphs are known for $CaBr_2$, its structure cannot be used to extrapolate on the polymorphism of $Ca(BH_4)_2$. Three factors suggest that a fundamental similarity is present between $Ca(BH_4)_2$ and TiO_2. The first is, as mentioned, the fact that the two are isoelectronic and both strongly ionic crystals. The Ca^{2+} and Ti^{4+} cations have the same electronic configuration, and the BH_4^- anion is isoelectronic with O^{2-}, though the borohydride anion is a molecular entity rather than an atomic anion.

The second factor is a similar ratio of cation-anion distance to cationic radius. In TiO_2, the ratio of ionic radius of Ti^{4+} to the average Ti-O distance is 0.31, whereas in $Ca(BH_4)_2$ the corresponding ratio of Ca^{2+} ionic radius to average Ca-B distance is 0.34. In $CaBr_2$, this ratio is closer to 0.40. This leads to a similar binding curve between cations and anions. In Figure 4.2, the binding potential between cations and anions was calculated

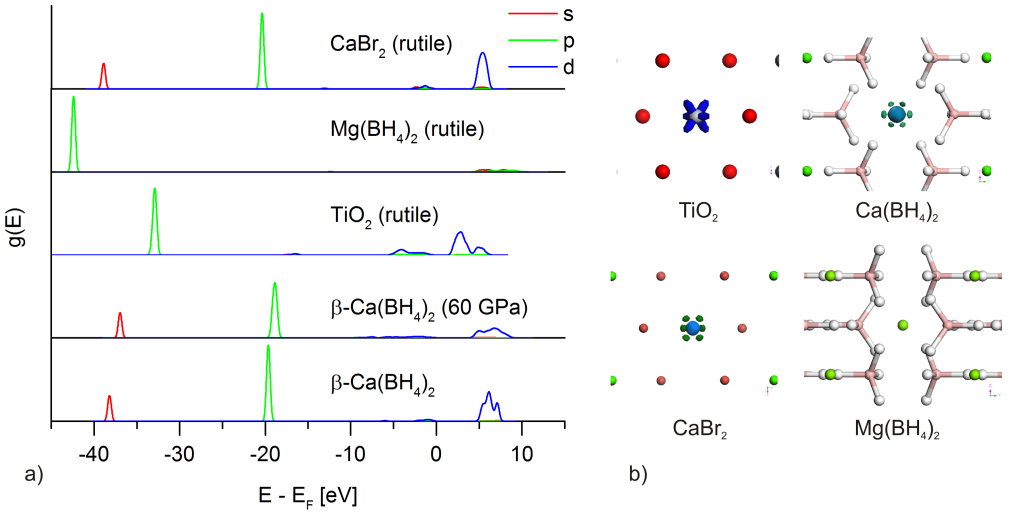

Figure 4.3: a) Electron density of states for various rutile structured crystals, projected on the metal cations and decomposed into angular momentum contributions; b) isosurface plots of density difference.

for four different compounds that all have the rutile structure; the cation-anion distance is given in fractional coordinates of the corresponding crystal. Apart from a different scaling factor of the energy that accounts for the different oxidation states in alkaline-earth metal compounds compared to TiO_2, the energy curves for $Ca(BH_4)_2$ and TiO_2 are very similar, and thus it is reasonable to expect that similar structures are forming not only at ambient pressure, but also at high pressure. From Table 4.1, it is seen that the volume of the $Ca(BH_4)_2$ polymorphs is consistently 3.25 times higher than the volume of TiO_2; in linear dimension, this factor corresponds to 1.48, reflected in the difference in average bond lengths in the two compounds.

The third factor concerns the electronic structure of the cations. From a qualitative and hand-waving point of view, it is noted that, as the electronic configurations are the same for both Ca^{2+} and Ti^{4+}, they both have empty d-orbitals in relatively low energy able to accept electron density. This ability to involve the highly directional d-orbitals in cation-anion bonding fundamentally shapes the crystal structures the compounds are likely to adopt. Figure 4.3 shows the electronic density of states (eDOS) by angular momentum projected on the metal atoms for four rutile-structured materials. It is seen that the calcium-based compounds all have an empty band of d-electrons, albeit at a

higher energy than TiO_2. This d-character in the empty orbitals is entirely absent in $Mg(BH_4)_2$, but equally present in $CaBr_2$. Why $CaBr_2$ does not serve as a better model despite the cation having the same favourable electronic properties (since it is the same cation) is explained by the previous point, namely that the anion binds to the cation with a different equilibrium distance.

For these three reasons, and the general observation of isoelectronic oxides being isostructural with borohydrides, it is hypothesised that TiO_2 is isostructural with $Ca(BH_4)_2$ at all pressures, and so under high pressure the same structures are adopted. This is the working assumption for the thermodynamic stability calculation that follows.

4.2 Computational method

Density functional theory (DFT, see Section 2.1) was used to optimise the geometry of all input structures and to calculate the electronic ground state energy. The phonon density of states was computed in the harmonic approximation to calculate the Helmholtz energy contribution of the nuclear vibrations. A pure plane-wave basis set and Vanderbilt ultrasoft pseudopotentials were used for optimal accuracy and efficiency. All computations were performed using the CASTEP code (Clark *et al.*, 2005).

The functional for exchange and correlation used in all calculations was the Perdew-Burke-Ernzerhof (PBE) functional (Perdew *et al.*, 1996). The reason for this choice is that PBE is a good general functional for solid-state calculations. While it does not excel in all classes of solids and for all properties, it has the advantage of being a pure *ab initio* functional (it is parameter-free) and has been found to provide good results for phase transition pressures as well as total energy. A number of comparative studies exist comparing the PBE functional with various other functionals for their performance on total energies and lattice parameters (Zupan *et al.*, 1998; Haas *et al.*, 2009). PBE also gives among the best predictions for molecular systems, being free from drastic overbinding or underbinding (Haas *et al.*, 2010): an important factor because of the presence of BH_4 units in the systems studied here. A general feature of PBE for most types of solids

is a slight overestimation of lattice parameters due to underbinding. As with all local functionals, dispersion forces are not well accounted for; however, the presence of dispersion forces in a relatively close-packed material like $Ca(BH_4)_2$ is assumed to make a negligible contribution to the total energy, and will be subject to a large degree of error cancellation when calculating energy differences. PBE was also found to give the most accurate energy differences between different phases of solid Si, SiO_2 and Fe (Zupan *et al.*, 1998).

Ground-state geometries and energies were determined by minimising the total electronic energy, as explained in Section 2.1.8. The geometry optimisation algorithm varies the atomic positions until the forces on all atoms are lower than a specified threshold, which was chosen to be 0.05 eV/Å. Furthermore, the unit cell was relaxed by simultaneously minimising the cell stress; the threshold was 0.1 GPa. The geometry optimisation preserves the space group symmetry of the starting structure, reducing the number of degrees of freedom in the optimisation. This means that no lower-symmetry structures than the starting structures can be obtained, though higher symmetry could in principle be found.

The phonon modes were calculated in the harmonic approximation, with the dynamical matrix computed using density functional perturbation theory. For the phonon calculations, norm-conserving pseudopotentials were used rather than ultrasoft pseudopotentials. The reason for using two sets of pseudopotentials is to achieve an optimal balance between computational efficiency and accuracy, as a large number of calculations were carried out. Ultrasoft pseudopotentials provide similar accuracy as high-quality norm-conserving pseudopotentials, but allow for a computationally more efficient optimisation of the geometry and evaluation of the total electronic energy. For computing dynamical matrices by the density functional perturbation method, however, ultrasoft pseudopotentials necessitate a treatment that is significantly more involved, and in fact the CASTEP code does not have this capability. It is far more efficient to compute phonon frequencies using norm-conserving pseudopotentials. Although other codes do exist that are capable of evaluating phonon frequencies using ultrasoft pseudopotentials, it was deemed more simple to switch pseudopotentials rather than switch codes. Before performing a phonon frequency cal-

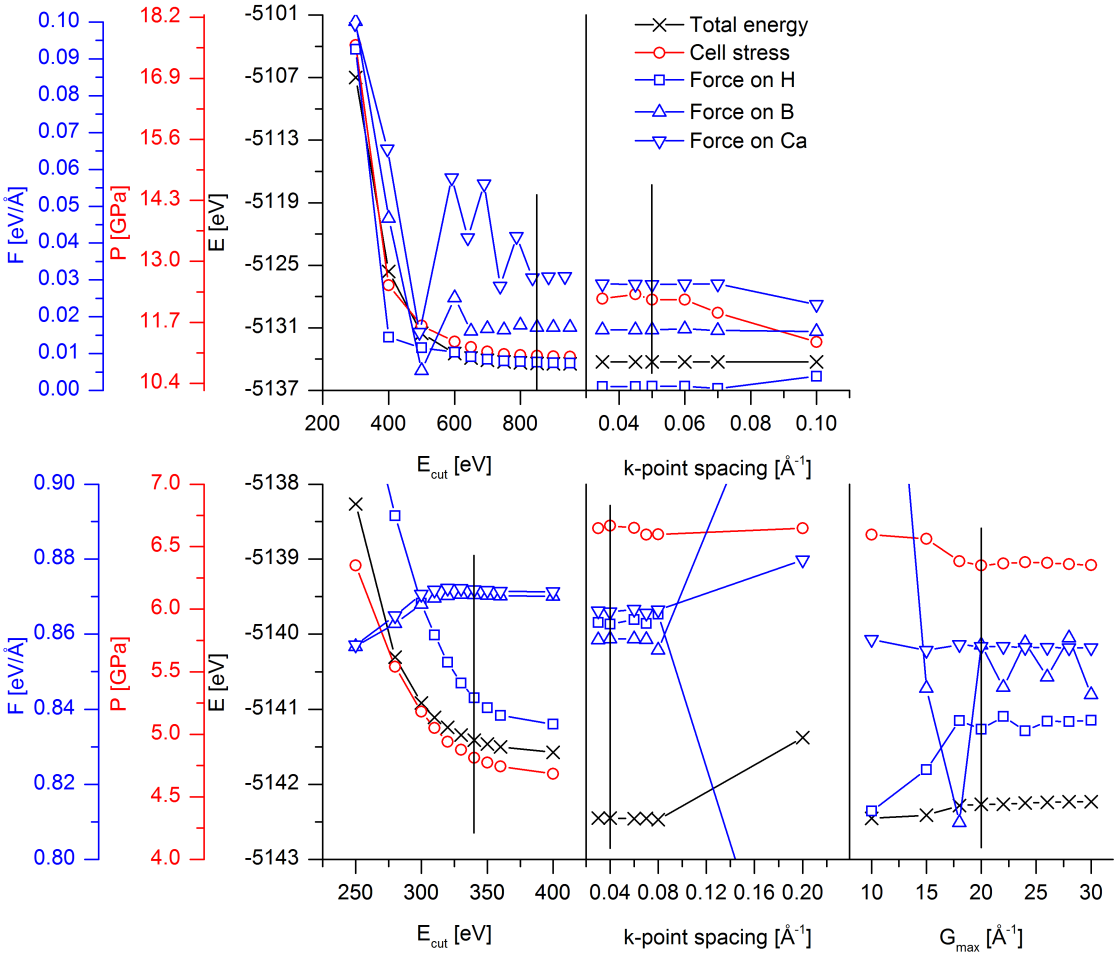

Figure 4.4: Convergence testing with norm-conserving (top) and ultrasoft pseudopotentials (bottom) with respect to plane wave cut-off energy (left), **k**-point grid spacing (middle) and maximum Fourier grid component (right, only for ultrasoft pseudopotentials). The convergence behaviour of the total energy, cell stress and force on each element are plotted. The selected value for each parameter is indicated by a black, vertical line.

culation, ultrasoft pseudopotentials were replaced by norm-conserving potentials and the geometry reoptimised—with a fixed unit cell—to an atomic force threshold of 0.01 eV/Å. The lower threshold was necessary because phonon frequency calculation require a highly optimised ground state. The reoptimised geometries differed minimally from the geometries optimised with ultrasoft pseudopotentials. The phonon **q**-point grid was taken to be the same as the electronic **k**-point grid and was then interpolated onto a much finer grid through Fourier interpolation to obtain a phonon density of states, $g(\omega)$.

The main parameters affecting the accuracy are the plane wave cut-off energy, E_{cut}, the

maximum Fourier component of the inverse-space density matrix, $G_{\max}$, and the **k**-point sampling grid. In a series of single-point calculations of the (unoptimised) β-$Ca(BH_4)_2$ structure, each of these parameters was varied in turn while the other two were kept fixed, and the total energy, cell stress and forces on the atoms were calculated. Their variations against the varied parameter are shown in Figure 4.4 with the chosen parameters indicated. The chosen values result in a variation in the forces of less than 0.001 eV/Å. Convergence in the energy does not need to be very precise, because the similar dependence of the total energy on the cut-off energy for all phases means that errors in energy differences tend to cancel out; this is not the case with the forces.

4.3 Generation and optimisation of predicted structures

To arrive at a predicted structure, input structures were generated from the crystal structures of TiO_2 in the cotunnite, baddeleyite and columbite structures. The TiO_2 lattice parameters were expanded by a factor of 1.48, calcium atoms were placed on titanium sites, and boron atoms on oxygen sites. Hydrogen atoms were arranged in a regular tetrahedron around each boron site with an initial B-H bond length of 1.20 Å. In baddeleyite and columbite, the boron atoms are on general positions with no site symmetry, and the initial orientation of the BH_4 units are not constrained by symmetry. In cotunnite on the other hand, the BH_4 units are on sites with site symmetry *.m.* and so only two different orientations of the tetrahedron are possible. Since the starting structure influences the optimised structure because only the nearest local minimum is found, a number of input structures for baddeleyite and columbite with randomly chosen BH_4 orientations were generated for geometry optimisation. In effect, a very restricted form of the random structure searching method by Pickard and Needs (2009), explained above, was performed; for baddeleyite and columbite, 10 different input structures were generated for each by randomly choosing an orientation quaternion (Section 3.3.4) for the BH_4 unit, and the lowest energy orientation was chosen. In each case, the 10 random input structures led to three or four distinct minimised structures. In cotunnite, the only two possibilities were

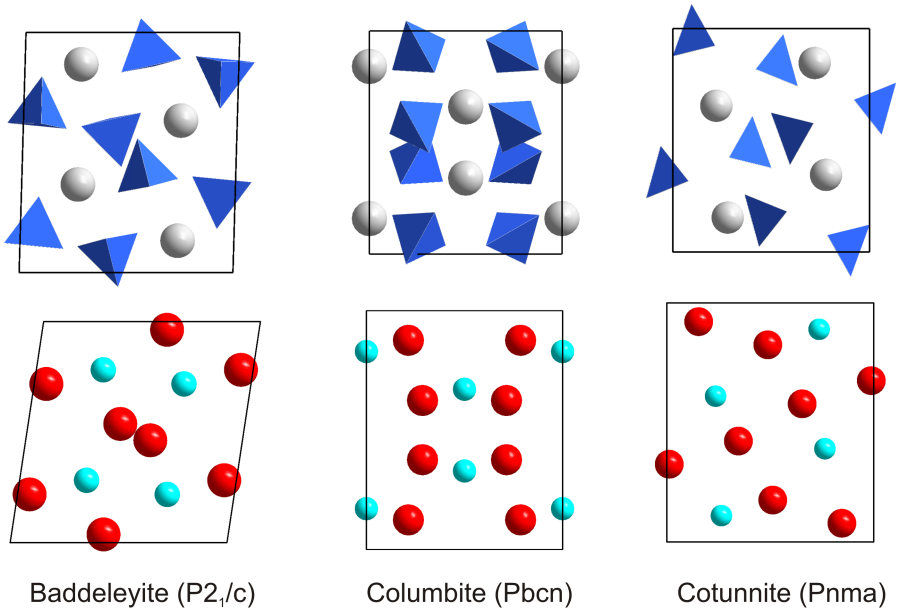

Figure 4.5: Bottom row: the known crystal structures of high-pressure TiO_2 polymorphs from the literature; top row: predicted and optimised high-pressure $Ca(BH_4)_2$ structural analogues.

tested and the lower energy one chosen.

As these structures are expected to be high-pressure structures, it is not surprising that geometry optimisations at first failed if the unit cell was relaxed to zero stress. An external pressure had to be imposed, and all structures were optimised at a nominal external stress of 60 GPa where stable structures were obtained. Figure 4.5 shows the resulting structures, crystallographic parameters are given in Table 4.2. It can be seen that they remain very similar to the TiO_2 template structures, with the exception of the monoclinic baddeleyite structure: the cell angle β is very close to 90°. Subsequent phonon calculation of all structures produced phonon spectra with no imaginary frequency modes, suggesting that all structures are dynamically stable.

4.4 Phase equilibria

Having established the structural stability of all phases, it remains to be determined how thermodynamically stable they are with respect to each other. Here we are interested in isothermal phase stabilities with respect to variations in pressure, that is isothermal

Table 4.2: Structural parameters of the predicted high-pressure phases of $Ca(BH_4)_2$.

Baddeleyite, space group $P2_1/c$ (No. 14)			
$a = 7.0201$ Å, $b = 6.3637$ Å, $c = 7.9061$ Å, $\beta = 91.6407°$			
Atom *(Wyckoff pos.)*	x	y	z
Ca ($4e$)	0.73680	0.51920	0.36710
B ($4e$)	0.57860	0.24040	0.59090
B ($4e$)	0.07290	0.19840	0.83530
H ($4e$)	0.40130	0.92160	0.85830
H ($4e$)	0.46440	0.73590	0.05950
H ($4e$)	0.26890	0.65270	0.89030
H ($4e$)	0.54910	0.65490	0.83380
H ($4e$)	0.07510	0.78070	0.62340
H ($4e$)	0.79630	0.79890	0.59890
H ($4e$)	0.91640	0.51490	0.62120
H ($4e$)	0.91830	0.69010	0.81820
Columbite, space group *Pbcn* (No. 60)			
$a = 6.1909$ Å, $b = 7.1905$ Å, $c = 6.4862$ Å			
Atom *(Wyckoff pos.)*	x	y	z
Ca (4c)	1/2	0.34060	3/4
B ($8d$)	0.73990	0.09110	0.54960
H ($8d$)	0.66090	0.81250	0.91710
H ($8d$)	0.38270	0.32410	0.36240
H ($8d$)	0.10400	0.46120	0.33310
H ($8d$)	0.19010	0.95440	0.03440
Cotunnite, space group *Pnma* (No. 62)			
$a = 6.9124$ Å, $b = 3.6695$ Å, $c = 7.8723$ Å			
Atom *(Wyckoff pos.)*	x	y	z
Ca ($4c$)	0.27890	1/4	0.15450
B ($4c$)	0.50270	1/4	0.83560
B ($4c$)	0.13070	3/4	0.96510
H ($4c$)	0.90470	1/4	0.88990
H ($4c$)	0.43810	3/4	0.02400
H ($4c$)	0.99830	3/4	0.87620
H ($4c$)	0.86440	3/4	0.24130
H ($8d$)	0.21520	0.01310	0.92330
H ($8d$)	0.92030	0.52300	0.68190

phase transition pressures. Temperatures considered are 0 K and 298 K. Thermodynamic stability is determined by the Gibbs energy (free enthalpy), $G = A + pV$, and the thermodynamically most stable phase is determined by calculating the relative Gibbs energies at any temperature and pressure.

A thermodynamic equation of state (EOS) links one state variable to the others by an analytic expression which is specific for the type of system. Thermodynamically, the state of a system is completely defined by specifying $2 + n$ variables where n is the number of chemical components, and of which at least 1 must be an extensive variable. For example, specifying volume, density and temperature of a one-component system completely defines its thermodynamic state, meaning there are in principle three degrees of freedom. An example of an EOS is the ideal gas equation, which is a full pVT-relationship, establishing a relationship between pressure, volume and temperature and thereby removing one degree of freedom. Only two variables can be independently specified, and the third one is determined by the EOS. If, for example, the temperature is fixed then an isothermal pV-relationship results.

For solids, naturally a different equation of state is necessary. The Birch-Murnaghan equation of state (Murnaghan, 1944; Birch, 1947) relates the pressure to the volume of an ideal harmonic solid. In the original formulation by Murnaghan (1944), the equation of state arises from Hooke's law, but assuming that the elastic constants depend linearly on stress (pressure). From classical thermodynamics, the variable linking pressure and volume is the bulk modulus, B, itself a function of pressure:

$$-V\left(\frac{\partial p}{\partial V}\right)_T = B \tag{4.5}$$

The Murnaghan equation of state simply assumes that the dependence on pressure is linear:

$$B = B_0 + pB_0' \tag{4.6}$$

Here, B_0 and B_0' are the bulk modulus at zero pressure and the pressure derivative of the bulk modulus at zero pressure, respectively. If this form is inserted back into Equation (4.5)

and the equation integrated with respect to volume, we obtain an analytical expression for the pressure as a function of volume which depends on the two constant parameters B_0 and B_0'.

$$p(V) = \frac{B_0}{B_0'}\left[\left(\frac{V_0}{V}\right)^{B_0'} - 1\right] \tag{4.7}$$

Birch (1947) improved the description subsequently by deriving a general formula for the dependence of the free energy on the strain in cubic crystals and, by generalising to isotropic media where the strain becomes proportional to the volume, the dependence of pressure on the volume is found to be:

$$p(V) = \frac{3B_0}{2}\left(\left(\frac{V_0}{V}\right)^{7/3} - \left(\frac{V_0}{V}\right)^{5/3}\right)\left(1 + \frac{3}{4}(B_0' - 4)\left[\left(\frac{V_0}{V}\right)^{2/3} - 1\right]\right) \tag{4.8}$$

This EOS establishes a relationship between two state variables; to determine the coefficients B_0 and B_0' one therefore needs to fit this functional form to a series of measured or calculated p, V value pairs of the system of interest. Since the calculation of the stress using DFT is imprecise, the Birch-Murnaghan EOS, Equation (4.8), is converted into an expression of Helmholtz energy versus volume by the following thermodynamic relation:

$$\left(\frac{\partial A}{\partial V}\right)_T = -p \tag{4.9}$$

Equation (4.8) is therefore integrated with respect to volume to yield the following relationship:

$$A(V) = A_0 + \frac{9V_0B_0}{16}\left[\left(\left(\frac{V_0}{V}\right)^{2/3} - 1\right)^3 B_0' + \left(\left(\frac{V_0}{V}\right)^{2/3} - 1\right)^2\left(6 - 4\left(\frac{V_0}{V}\right)^{2/3}\right)\right] \tag{4.10}$$

with the same meanings of the parameters B_0 and B_0'.

Computationally, the Helmholtz energy is given by

$$A = A_{\text{pot}} + A_{\text{vib}} \tag{4.11}$$

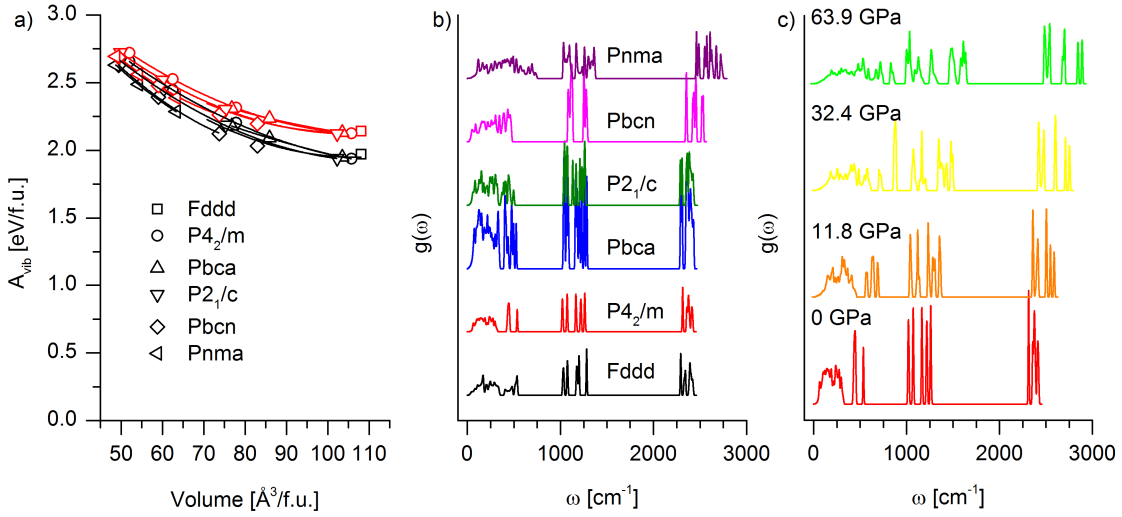

Figure 4.6: a) Vibrational contribution to the Helmholtz energy for each phase, calculated from the phonon density of states at 0 K (black) and at 298 K (red); symbols: calculated values; lines: quadratic interpolation; b) phonon density of states for each phase; c) effect of pressure on the phonon density of states of the β-phase.

The individual contributions to the Helmholtz energy can be computed by DFT in the quasi-harmonic approximation. A_{pot} is the static total energy of the structure and given directly by DFT. Since $Ca(BH_4)_2$ is an insulator with a large band gap, thermal excitations are negligible at 298 K and this term is considered constant with respect to temperature. A_{vib} is the energy of the phonon modes and depends on temperature as well as volume.

To compute the DFT energy, A_{pot}, as a function of volume, a hydrostatic pressure is applied on the structure and its geometry and lattice optimised under pressure. The volume of the cell results indirectly from this calculation. For each phase, including the ambient-pressure α-, β- and γ-phases, a series of 10 structures at external pressures ranging from 0 to 60 GPa was geometry-optimised and the resulting volumes and energies for each phase calculated.

The phonon density of states (PDOS), $g_V(\omega)$, depends on the volume V only and thus must be calculated varying the volumes of each phase. However, since a full phonon density of states calculation is computationally extremely expensive, it was only possible to compute the vibrational energy for 3 or 4 different volumes for each phase. We note that the vibrational Helmholtz energy varies only slowly with volume and that it is very

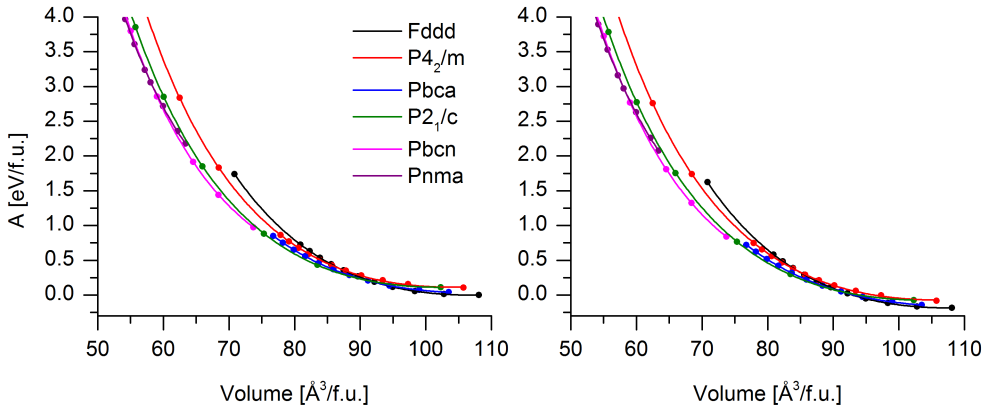

Figure 4.7: Calculated Helmholtz energy as a function of volume (symbols) and fitted Birch-Murnaghan equation of state (lines) for each phase; left: 0 K, right: 298 K.

similar between phases, and thus it was estimated that the vibrational energy can be interpolated quadratically. The α-phase shows a soft mode at pressures as low as 1 GPa, and so the vibrational energy could not be calculated for this phase at multiple volumes. The vibrational contributions are summarised for two temperatures, 0 K and 298 K, in Figure 4.6.

The temperature dependence of the energetic and entropic contributions of the nuclear vibrations cannot be ignored, and thus the dependence of A_{vib} on temperature as well as volume must be taken into account. The vibrational Helmholtz energy at temperature T is given by:

$$A_{\text{vib}} = -k_B T \ln Q(N, V, T) \tag{4.12}$$

The partition function $Q(V, T)$ is given by Equation (2.172) in Chapter 2 (page 58):

$$\ln Q(N, V, T) = -\int_0^\infty \mathrm{d}\omega \, g_V(\omega) \, \ln\left(2 \sinh\left(\frac{\hbar\omega}{2k_B T}\right)\right) \tag{4.13}$$

where $g_V(\omega)$ is the PDOS of the system at volume V, normalised to $3N$. We thus calculate the Helmholtz energy from the computed PDOS as:

$$A_{\text{vib}} = k_B T \int_0^\infty \mathrm{d}\omega \, g_V(\omega) \, \ln\left(2 \sinh\left(\frac{\hbar\omega}{2k_B T}\right)\right) \tag{4.14}$$

The integral is evaluated numerically, given the PDOS, $g_V(\omega)$, from the phonon mode

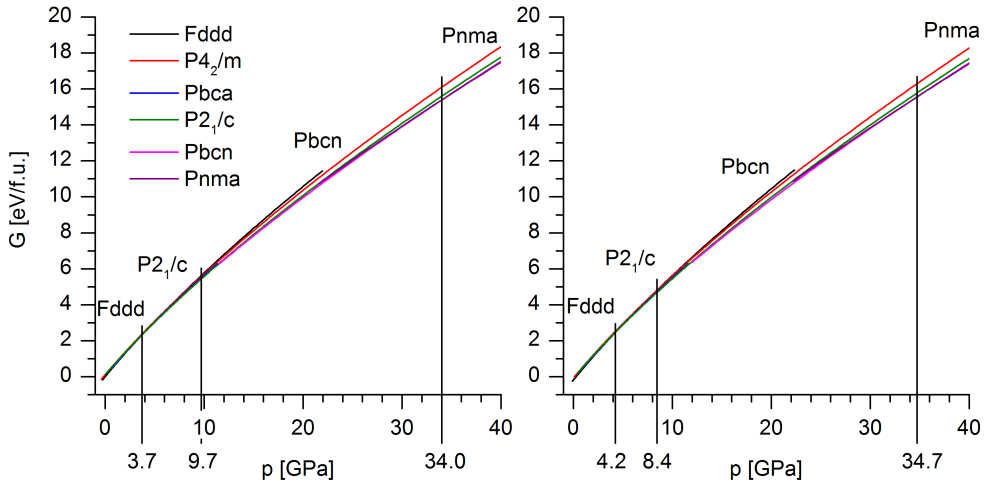

Figure 4.8: Computed Gibbs energy versus pressure for all phases at 0 K (left) and at 298 K (right); the thermodynamically most stable phases are indicated for each pressure interval. The zero of the energy scale has been set to A_0 of the α-phase at 0 K.

calculation.

Equation (4.10) was fitted to each set of energy-volume data by nonlinear least-squares fitting to determine the parameters B_0 and B_0'. The final EOS fits are shown in Figure 4.7 and fitting parameters are summarised in Table 4.3. A partial phase diagram at constant temperature is shown in Figure 4.8, where the Gibbs energy ($G = A + pV$) is plotted versus pressure at constant temperature. The thermodynamically most stable phase at each pressure is the one with the lowest Gibbs energy.

Phase transitions occur where the Gibbs function of the most stable phase crosses that of another phase which then becomes the lowest energy phase. At a constant temperature, the phase transition happens at a pressure p where the Gibbs energies of two phases become equal:

$$A_1(V_1) + pV_1 = A_2(V_2) + pV_2 \tag{4.15}$$

This is the equation of the common tangent to the EOS curves for the two phases, $A_1(V_1)$ and $A_2(V_2)$, since the pressure is in turn the negative slope of the EOS and must be equal for both phases.

$$p = -\left(\frac{\partial A_1}{\partial V}\right)_{T,V=V_1} = -\left(\frac{\partial A_2}{\partial V}\right)_{T,V=V_2} \tag{4.16}$$

Solution of Equations (4.15)–(4.16) gives the phase transition pressure p (as well as V_1

Table 4.3: Parameters of the third-order Birch-Murnaghan equation of state for all phases from a nonlinear least squares fit to computed free energies.

		0 K		
Phase	B_0 [GPa]	B_0'	V_0 [Å^3/f.u.]	A_0 [eV/f.u.]
α	23.41(6)	4.002(9)	106.80(2)	0 (def)
β	22.9(6)	4.00(4)	103.9(3)	+0.114(4)
γ	17.3(4)	3.98(8)	107.5(2)	+0.0317(10)
Baddeleyite	21.2(5)	3.97(3)	102.2(3)	+0.112(4)
Columbite	25.9(4)	3.969(17)	95.8(3)	+0.341(7)
Cotunnite	38(16)	3.8(5)	87(6)	+1.0(2)
		298 K		
Phase	B_0 [GPa]	B_0'	V_0 [Å^3/f.u.]	A_0 [eV/f.u.]
α	23.29(6)	3.961(9)	107.60(2)	-0.184892(17)
β	20.8(6)	4.06(5)	106.2(4)	-0.071(6)
γ	15.3(4)	4.09(9)	110.1(2)	-0.163(1)
Baddeleyite	19.7(5)	4.00(4)	104.2(4)	-0.074(5)
Columbite	24.2(4)	3.989(18)	97.7(3)	+0.133(8)
Cotunnite	35(16)	3.8(5)	89(7)	+0.8(3)

and V_2).

As has been repeatedly found experimentally, we find that the α-phase is the thermodynamic ground state, while the β and γ-phases are metastable at all pressures at room temperature. The latter two phases do not become the thermodynamic ground state at any pressure at room temperature; instead, the α-phase transforms directly into the baddeleyite phase. All curves are extremely close to each other, with a maximum spread of values of less than 0.3 eV/f.u., corresponding to about 29 kJ/mol. Therefore, all these phases would be expected to be able to coexist, if they exist at all, as is the case with the ambient pressure phases.

4.5 Conclusion

In this chapter, the complex phase diagram of solid $Ca(BH_4)_2$ has been examined as a function of pressure. The phase stability with respect to pressure of experimentally confirmed as well as predicted structures was determined by means of DFT calculations of a thermodynamic equation of state for each phase. Input structures for the predicted phases were generated by extending an observed structural analogy between TiO_2 and $Ca(BH_4)_2$

at ambient pressure to high pressure. The resulting structures are both dynamically stable and similar in free enthalpy to existing phases.

An equation of state was calculated by fitting the third-order Birch-Murnaghan equation of state to series of energy values at varying volumes; the fits obtained were excellent (with the exception of the cotunnite phase) both at zero temperature and at room temperature (298 K), as the uncertainties given in Table 4.3 show. The Helmholtz energies were calculated by the harmonic approximation, with atomic vibrations treated as perfectly harmonic at any temperature. By this method, the full phase diagram can be calculated at any pressure and temperature, though the limitation of the harmonic crystal approximation for calculating accurate Gibbs energies using DFT at any temperature and pressure must be kept in mind.

As was seen, the Gibbs enthalpy dependence on pressure is extremely similar for all polymorphs of a material, and thus a minimal change in the relative energy of one phase with respect to another will result in a huge shift of the predicted phase transition pressure. For example, the inclusion of anharmonic effects, or a small change in the interpolation scheme for the vibrational energies, is expected to considerably shift phase transition pressures.

Independent of thermodynamic considerations, though, is whether a given structure is dynamically stable at all or not. All of the predicted high-pressure phases had stable structures under high pressure, as evidenced by the absence of imaginary phonon frequencies. Geometry optimisation at zero pressure, on the other hand, led to structures with imaginary phonon frequencies, or to no convergence of the geometry optimisation at all. These instabilities—or soft modes—might point to the existence of displacive phase transitions of these phases, which unfortunately have to remain unexplored in this work.

It is correctly predicted that the α-phase is the ground state at ambient pressure at both 0 K and at room temperature, and that the β- and γ-phases are metastable at room temperature. In common with the high-pressure *in situ* Raman/IR study by Liu *et al.* (2010), we find two phase transitions in the range 0–10 GPa. In our prediction, two phase transitions are postulated at room temperature at 4.2 GPa and 8.4 GPa, with

multiple phases of very similar stability around the phase transition at 4.2 GPa. Given these predictions, it could be hypothesised that the baddeleyite ($P2_1/c$) and columbite ($Pbcn$) phases correspond to the observed phases III and IV.

This method does not predict which structure a given material will transform into as the pressure is increased; rather, a given set of (hypothetical or real) structures is taken and their relative thermodynamic stabilities are determined. The meaning of a predicted phase transition pressure is therefore: if both phases do exist in the pressure range and temperature in question, then the free enthalpy difference will be zero at that pressure and one will transform into the other. The prediction cannot ascertain whether the predicted phase can ever be observed experimentally or whether the phase transition will actually occur as predicted: numerous similar theoretical predictions with respect to temperature and pressure of known and hypothetical phases (e. g. Majzoub and Rönnebro, 2009) have so far turned out to be absent in experiment. An alternative method would be direct simulation of a phase transition at given conditions, without *a priori* knowledge of the target phase, but this would necessitate a molecular dynamics approach which would be a formidable computational task; furthermore, only displacive phase transition are likely to be captured.

A currently unanswered question is whether the phases predicted in this chapter can be observed by experiment or whether they remain purely hypothetical. Arguments for their real existence are to be found in the structural comparison with TiO_2, where there are the same formal electronic configurations, similar ionic radius ratios, and the presence of low-lying empty d-bands on the metal cation. However, none of these observed similarities lead to the necessary conclusion that the structures must be identical, and experimental high-pressure crystal structure determination will have the last word. The purpose of this work is not to propose a new, general crystal structure prediction method; rather, an observed qualitative analogy between two materials was explored for the prediction of structures in the very specific case of the hydrogen storage material, $Ca(BH_4)_2$.

CHAPTER 5

Dynamical disorder in lithium borohydride

"Do not let the lack of data get in the way of producing scientific results."

ANONYMOUS

After an initial flurry of interest in the 1950s as a candidate rocket fuel, lithium borohydride ($LiBH_4$) has been a focus of hydrogen storage research over the past decade because of its attractive 18.5% by weight hydrogen storage capacity. $LiBH_4$ in itself is not a viable hydrogen storage material because of its high decomposition temperature and complex decomposition products. It has, however, been studied as a component of both $Li_4BN_3H_{10}$ and Li_2BNH_6 (Chater *et al.*, 2006, 2007), two significant "one-shot" hydrogen stores with practical decomposition temperatures. $LiBH_4$ also readily absorbs ammonia (Johnson *et al.*, 2009) and has potential as an ammonia storage material. Its principal interest, however, centres on the recent discovery of superionic behaviour and it is this property and the associated atomic structural and dynamical processes which form the body of work in this chapter.

Two solid phases of $LiBH_4$ are known at atmospheric pressure: these are an orthorhombic low-temperature phase (space group *Pnma*), termed LT hereafter, which undergoes a

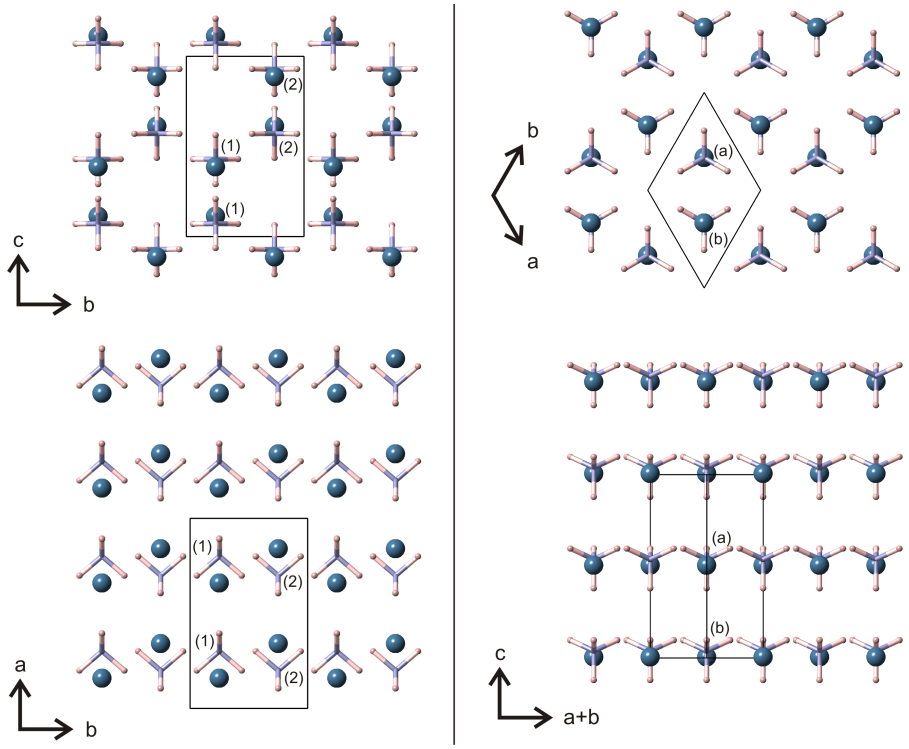

Figure 5.1: Crystal structures of $LiBH_4$ according to Filinchuk *et al.* (2008a); left: LT phase at 298 K, right: HT phase at 473 K. The labels (1) and (2) designate BH_4 units related by the *a* glide plane; (a) and (b) denote the two layers in the HT phase related by the 6_3 screw axis.

first-order phase transition at around 380 K into a high-temperature phase (HT phase), which has been established to be hexagonal, but otherwise there is significant controversy surrounding the details of its crystal structure. The currently accepted space group is $P6_3mc$, first assigned by Soulié *et al.* (2002) and most recently reaffirmed by Filinchuk *et al.* (2008a) by synchrotron X-ray diffraction experiments on both single-crystal and powder samples. Theoretical results, however, suggest an instability in this structure (Miwa *et al.*, 2004; Łodziana and Vegge, 2004) and have cast doubt on its correctness.

The transition from the LT to the HT phase involves a subtle change in the arrangement of the lithium and borohydride units, but both polymorphs are structurally similar: they consist of hexagonal layers of $LiBH_4$, stacked in the *a*-direction in LT and the *c*-direction in HT, which are more ordered in LT, and more symmetric in HT (Figure 5.1). The experimental crystal structures suggest that both phases are very ordered with no partial site occupancies; in the HT phase, the BH_4 units have a well defined orientation with one

of their B-H bonds pointing along the *c*-axis of the crystal structure.

The assumption of an ordered structure has been called into question, and a disordered, centrosymmetric structure has been proposed on the basis of experimental findings that include second harmonic generation analysis (David, personal communication) that strongly suggest the existence of a centre of symmetry and a disordered structure better described in space group $P6_3/mmc$. However, the nature of the disorder (in both LT and HT) on the atomic scale is not well understood and a crystallographic analysis only yields information about the average structure. In this chapter, a detailed theoretical analysis from *ab initio* molecular dynamics (MD) calculations is presented to support the new proposed $P6_3/mmc$ symmetry of the HT phase. The ground state structures of both the LT and HT phase lithium borohydride are thoroughly investigated and a detailed atomistic description of the disorder and dynamical processes in the crystal is presented.

5.1 History of structural studies

The first crystal structure study was performed by Harris and Meibohm (1947), who found the space group for the LT phase to be $Pnma$; its lattice constants were determined, but no atomic positions were reported. It was not until 2002 that the crystal structures of both the LT and the HT phases were solved from X-ray powder diffraction data (Soulié *et al.*, 2002), and in 2008 two further polymorphs under high pressure were identified and their crystal structures solved (Filinchuk *et al.*, 2008b). The first crystal structure determination concluded that the HT phase is in $P6_3mc$ symmetry, although the authors already pointed out that $P6_3/mmc$ was an alternative consistent with the systematic absences in the diffraction pattern (Soulié *et al.*, 2002). Based on the subsequent Rietveld refinement, $P6_3mc$ was concluded to be the correct one, ruling out the other possible space groups and thereby disordered structures. The only model found from structure solution included ordered positions and the possibility of partial occupancies was neglected. The first published crystal structures for the LT phase (Harris and Meibohm, 1947; Soulié *et al.*, 2002) reported heavily deformed BH_4 units, but this was corrected in subsequent

diffraction studies. No other model for the HT phase than the simple ordered model with $P6_3mc$ symmetry has since been considered.

Theoretical studies of solid $LiBH_4$ soon followed: in 2004, the optimised geometries and phonon frequencies of the experimental crystal structures were determined from density functional theory (DFT) calculations (Miwa *et al.*, 2004; Łodziana and Vegge, 2004). These calculations found that many of the phonon modes of the $P6_3mc$ structure associated with BH_4 libration had imaginary frequencies (soft modes), pointing out a structural instability. An imaginary frequency mode indicates that the atom positions are not in fact the lowest-energy configuration, as a small displacement of the atoms into the immediate vicinity leads to a lowering of the energy and thus the force constant for the mode is negative (the vibrational frequency is calculated as the square root of the force constant). This type of anomaly is often present in structures at the point of a phase transition, or in disordered structures. However, the authors of these theoretical studies chose to be very cautious and, unable to accommodate their theoretical findings at the zero-temperature level with the experimental results, concluded that "finite temperature effects are probably crucial" for an adequate description of the HT phase. Other theoretical studies (Kang *et al.*, 2005; Zarkevich and Johnson, 2008; Tekin *et al.*, 2010) aimed at predicting alternative crystal structures for the HT phase and produced various results that were energetically more stable than the $P6_3mc$ structure and more or less consistent with the observed X-ray diffraction pattern.

In what unfortunately degenerated into a feud between experimentalists and theoreticians, experimental crystallographers responded to the calling into question of their experimental findings. In a recent synchrotron X-ray diffraction study that presented the first single-crystal structure determination of the HT phase (Filinchuk *et al.*, 2008a), it was proclaimed that "proof of the $P6_3mc$ structure" had been provided, and alternative structures predicted by theoretical calculation were "confidently rejected". Despite this bold statement, two important facts were not addressed: the first, that even with single crystals and high-quality synchrotron radiation, X-ray diffraction remains a relatively imprecise tool for the accurate determination of hydrogen positions and fundamentally different mo-

dels need not necessarily influence the quality of a refinement decisively, making it difficult to judge the quality of one model against another; and the second, that the model chosen by the authors only allowed four hydrogen positions with full occupancy and displacement factors to be determined and thus did not possess the flexibility to describe a disordered structure. The unusually large displacement factors they obtained as a consequence were vaguely explained by dynamical disorder being present.

Neutron diffraction techniques hold more promise for locating hydrogen atoms because of the large neutron scattering cross section of the hydrogen isotopes. The first neutron powder diffraction study was performed by Hartman *et al.* (2007), who reconfirmed undistorted tetrahedra for the LT phase. The HT phase was not solved anew, but the old $P6_3mc$ model was refined, and for the first time reliable hydrogen positions could be determined. The refined structure immediately pointed out a problem: the anisotropic displacement parameters (ADPs) for hydrogen turned out to be so large that a simple harmonic structure seemed implausible. At this point, it became impossible to ignore the disorder, as the ADPs suggest that the hydrogen atoms spend as much time on their nominal equilibrium positions as they do in the vicinity of the nearest-neighbour hydrogen atom. Both the shape of the ADPs and the imaginary frequency phonon modes suggested fast rotational motion of the BH_4 units.

Meanwhile, theoreticians seemed unimpressed by the reaffirmation of the $P6_3mc$ structure and, driven mainly by the argument of lattice instability, continued to propose new theoretical structures from random search strategies not based on experimental evidence (Tekin *et al.*, 2010). The study by Łodziana and Vegge (2004, 2006) also presented a mini-simulated annealing study of $LiBH_4$ and they reported some new possible space groups, none of which have been found experimentally.

Attempts to describe the rotational behaviour of the BH_4 units began as early as 2002 (Gomes *et al.*, 2002), when it was concluded from Raman spectroscopy line broadening that dynamical disorder seems to be present for the borohydride units. In a subsequent study by the same authors (Hagemann *et al.*, 2004), a vague model describing two different reorientational jump mechanisms resulted in two energy barriers (5 and 60 kJ/mol) and

provided a better fit than a model with only one barrier, though the authors conceded that the meaning of the calculated barriers was not clear. A similar direction was pursued in a temperature-dependent NMR study (Skripov *et al.*, 2008) of the LT phase, where it was found that the reorientation of the BH_4 units was most likely a superposition of two separate processes with distinct activation energies (0.182 eV and 0.251 eV); it was concluded that the two reorientation processes were "probably" rotations about the C_2 and C_3 axes. In a combined theoretical and experimental approach to the study of dynamical disorder, inelastic neutron scattering experiments were performed by Buchter *et al.* (2008a) that revealed a dependence on energy of the measured phonon density of states that was of higher than quadratic order, characteristic of disordered systems and glasses. The rotational energy landscape was also elucidated by DFT calculations, and the authors found indications that the structure is in a well defined geometry in the LT phase and in an unstable one in HT, stabilised only by entropy. Remhof *et al.* (2010) measured BH_4 reorientational dynamics of alkali borohydrides using quasi-elastic neutron scattering (QENS) and tested a number of reorientational models. They found that reorientational jumps of 90° around the tetrahedron C_2 axis were the predominant phenomenon in the HT phase, which is analogous to the reorientational dynamics of NH_4^+ in solid ammonia halides. For the LT phase, they found that a model assuming jumps of 120° around the C_3 axis was the predominant process; only these two models were considered. The models reproduce the elastic incoherent structure factors (EISFs) which were measured directly by QENS, but the usefulness of EISF fitting may be questioned as it is, on the one hand, extremely difficult to judge the quality of a fit, and on the other hand, a systematic way of improving the fit does not exist as EISF fitting is entirely model based and offers little flexibility in terms of adjustable parameters. Martelli *et al.* (2011) also performed QENS experiments on $LiBH_4$/LiI solutions and found that the rotational motion increased with the presence of iodine. In another neutron scattering study of the disorder, Callear *et al.* (2010) measured the neutron pair distribution function (PDF) at varying temperatures and showed that while the BH_4 units kept their ideal tetrahedral geometry, the absence of features in the PDF could not be merely explained by large-amplitude librations of the

BH_4 units, but more rotational disorder was implied.

While all studies agreed that no precise orientation for the BH_4 units in the HT phase can be defined and that there are frequent reorientations in the LT phase, a detailed picture of dynamics is still lacking. It was all but missed that a molecular dynamics study by Ikeshoji *et al.* (2009) finally suggested that lithium does not occupy one harmonic position, but is distributed over two split positions. The consequence of this finding is a centrosymmetric structure, ruled out by synchrotron diffraction experiments on the grounds that a value of $\left|E * E^{-1}\right| = 0.756$ suggests absence of centrosymmetry (Filinchuk *et al.*, 2008a), but recent measurements of the nonlinear optical properties of $LiBH_4$ by second-harmonic generation (David, personal communication) strongly suggest the presence of a centre of inversion.

In this chapter, we perform MD simulation of $LiBH_4$ at several temperatures and present analyses that rationalise all previous findings that contradict the $P6_3mc$ structure and, by combining this information with all available experimental data, provide evidence for a centrosymmetric $P6_3/mmc$ structure. It shall be noted here that lithium ion mobility and disorder has also been of considerable interest, but this will be left to Chapter 6 for an in-depth discussion.

5.2 Computational details

Born-Oppenheimer MD simulations were performed using periodic boundary conditions and the equations of motion were integrated by a velocity-Verlet algorithm as described in Section 2.5. The forces acting on the atomic nuclei are at each time step evaluated by a full DFT calculation of the energy and forces. To increase the efficiency of the DFT calculation, the QUICKSTEP method was used, which relies on a dual basis set consisting of a plane-wave basis and a Gaussian basis. The main parameters for the calculation that have to be chosen are the time step for the integration of the equations of motion and the basis sets for the DFT calculation. The computational package CP2K was used for all MD calculations.

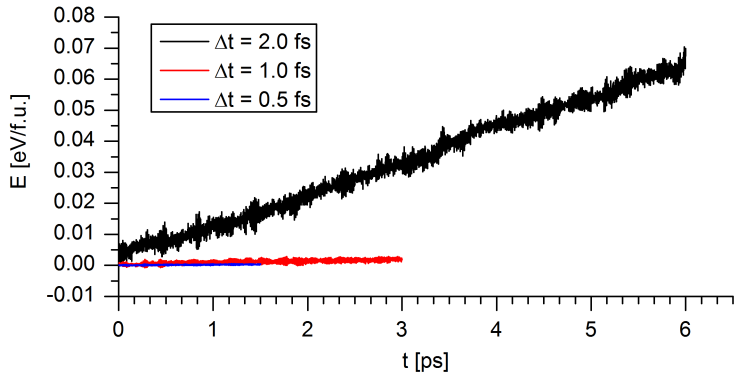

Figure 5.2: Drift of the total energy with different time steps in the simulation of the HT phase at 535 K in the NVE ensemble.

The choice of time step of an MD calculation depends on the nature of the simulated system and on the integrator algorithm (see Section 2.5.2). Too large a time step will result in an inaccurate trajectory, and while the exact following of the correct trajectory is irrelevant (see discussion in Section 1.3), an inaccurate trajectory will result in a drift in the conserved quantity. This drift results in the wrong ensemble being sampled, leading to physically less meaningful statistics. As a rule of thumb, to achieve accurate conservation of energy with the velocity-Verlet algorithm, the fastest oscillatory movement needs to be sampled by a minimum of about 10-15 time steps. The fastest oscillations in molecular systems are usually the stretching modes of vibrating bonds; for $LiBH_4$, this is the B-H vibration with a frequency of 2300 cm^{-1}. This translates into an oscillation time of about 15 fs, and so the optimal time step is estimated at around 1 fs. A series of short MD simulations in the microcanonical (NVE) ensemble starting from the same phase point with different time steps were performed and the drift of the total energy was determined (Figure 5.2). Using a time step of 1.0 fs results in a steady energy drift of less than 1 meV per ps per formula unit, and insignificantly less drift than with a time step of 0.5 fs, so 1.0 fs was chosen as the time step for all MD simulations of $LiBH_4$.

The details of the DFT calculation are as follows. As in the case of $Ca(BH_4)_2$ (Chapter 4) and for the same reasons, the PBE functional was used as a good general solid-state functional. The plane wave cut-off energy was chosen at 280 Ry. The short-range double-zeta Gaussian basis set for all elements developed by VandeVondele and Hutter (2007) was

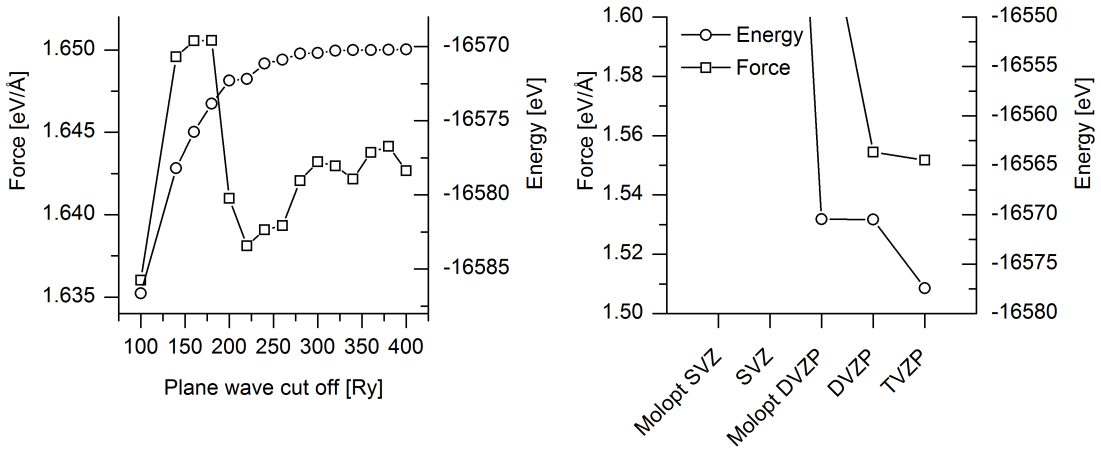

Figure 5.3: Basis set convergence testing. Variation of the force on an arbitrarily chosen boron nucleus and of the total energy with respect to plane-wave cut-off and Gaussian basis set quality.

used as it is well-tested with the PBE functional and offers the best performance versus accuracy for condensed systems. A convergence test of the atomic forces for a randomly chosen time step during an MD run (Figure 5.3) showed that the chosen basis set had reasonably converged. The Goedecker-Tetter-Hutter pseudopotentials were used (Goedecker *et al.*, 1996).

The supercell was chosen to contain 288 atoms (48 formula units), leading to a supercell of about $1\,\mathrm{nm}^3$ volume. The lattice parameters at the corresponding temperatures were taken from the literature (Filinchuk *et al.*, 2008a), as lattice parameters determined from synchrotron X-ray diffraction are the most precise and DFT is not very good at predicting lattice parameters due to underestimation of nonbonded interactions in DFT with the PBE functional. The supercells were constructed according to $S = MP$, where P and S are matrices of Cartesian row-vectors of the primitive cell axes and the supercell axes, respectively. The transformation matrix M is given by:

$$M_{\mathrm{LT}} = \begin{pmatrix} 2 & 0 & 0 \\ 0 & 3 & 0 \\ 0 & 0 & 2 \end{pmatrix}; M_{\mathrm{HT}} = \begin{pmatrix} 3 & 3 & 0 \\ -2 & 2 & 0 \\ 0 & 0 & 2 \end{pmatrix}$$

for the LT and HT supercells; both result in a supercell containing 48 formula units. The

Table 5.1: MD simulations of $LiBH_4$ performed with the CP2K code. The lattice parameters at each temperatures are according to Filinchuk *et al.* (2008a).

T_0 [K]	Lattice parameters [Å]	Trajectory
200	$a = 7.14959$, $b = 4.42819$, $c = 6.74184$	NVT (50 ps)
298	$a = 7.17713$, $b = 4.43598$, $c = 6.80344$	NVT (52 ps)
373	$a = 7.21377$, $b = 4.43317$, $c = 6.88368$	NVT (34 ps)
380	$a = 4.2667$, $c = 6.9223$	NVK (3 ps), NVT (20 ps)
473	$a = 4.29303$, $c = 6.98183$	NVT (21 ps)
535	$a = 4.3228$, $c = 7.0368$	NVK (1 ps), NVT (20 ps)
535	$a = 7.21377$, $b = 4.43317$, $c = 6.88368$	NVT (18 ps), NPT (20 ps)

supercell axes x, y, z are aligned with the cell vectors $\mathbf{a}, \mathbf{b}, \mathbf{c}$ in the LT phase; in the HT phase the supercell axes x, y, z are aligned with the directions $\mathbf{a}+\mathbf{b}, \mathbf{a}-\mathbf{b}, \mathbf{c}$ of the primitive cell. No symmetry constraints were imposed in any simulations described in this chapter.

All MD simulations were carried out in the canonical (NVT) and the isobaric-isothermal (NPT) ensembles. An overview of the computations performed is presented in Table 5.1. To control the kinetic temperature in the system, the Nosé-Hoover thermostat was used, more precisely a Nosé-Hoover chain of length 3 (Martyna *et al.*, 1992). As explained in Section 2.5.4, the Nosé-Hoover thermostat results in a trajectory in the canonical ensemble. For controlling the pressure, an anisotropic Nosé-Hoover barostat was used (Martyna *et al.*, 1994).

5.3 Time-averaged crystal structure

We first focus on the average structural properties of $LiBH_4$. By the ergodic hypothesis, time-averaged phase variables are equivalent to ensemble-averaged values provided that the system is in thermal equilibrium. Experimental measurements almost always measure averages (except for highly specialised techniques with sub-picosecond resolution, none of which have been applied to the study of the present system), and so the average structural properties calculated from MD data are directly comparable to experimental results. We shall compare the average crystal structure and pair-distribution function to their measured equivalents from neutron scattering experiments.

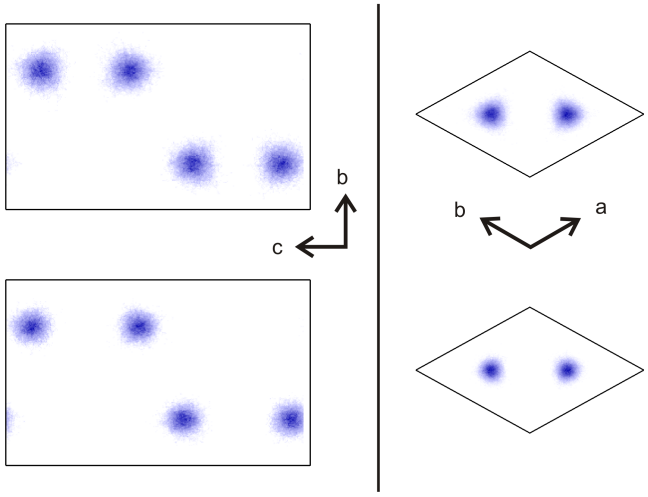

Figure 5.4: Comparison of atom positions in the horizontal plane for lithium atoms (top) and boron atoms (bottom) at similar temperatures (HT: 380 K; LT: 373 K). The intensity of the blue colour indicates the probability density of the atoms.

5.3.1 Li and B sublattices

The time-averaged lithium and boron positions are determined by projecting the simulation supercell back into the primitive orthorhombic or hexagonal cell for the LT and HT trajectories, respectively, in order to obtain a spatial average over all individual unit cells contained in the supercell. The positions are time-averaged by computing a two-dimensional histogram of the b, c coordinates of the Li and B atoms for the LT phase (a and b coordinates for HT) over the equilibrated part of each trajectory; these histograms are shown in Figure 5.4 and represent the atomic position distribution in the crystallographic unit cell, time-averaged and space-averaged.

From the distributions in Figure 5.4, it emerges that both species have their average coordinates in the horizontal plane centred on the crystallographic positions, and their variations around that equilibrium position are described by harmonic vibration; no disorder is present for either phase. The lithium atoms are seen to be more mobile than the boron atoms, as they are smeared out more, especially in the HT phase. Indications for high ionic mobility can be seen in occasional attempted excursions of the lithium atoms away from the average position, but no jump away from the site was observed over the whole duration of the trajectories. Therefore, the lithium and boron positions in the horizontal

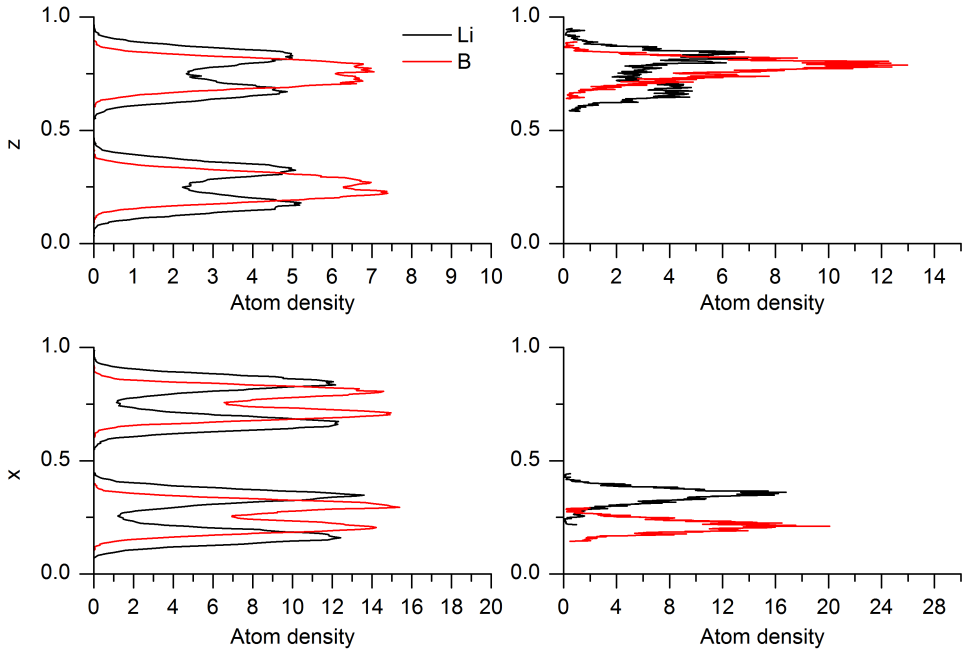

Figure 5.5: The vertical coordinate distribution of the lithium atoms for the HT phase at 380 K (top two panels) and the LT phase at 373 K (bottom two panels). In each case, the left graphs show all lithium atoms in the simulation box averaged; the right graphs show the distribution for one randomly chosen lithium and boron atom.

plane are well described by simple displacement factors.

In the vertical direction, Figure 5.5 shows a discrepancy with the $P6_3mc$ crystallographic models for the HT phase (shown in Figure 5.1). According to this model, only two positions in the vertical direction for the lithium atoms would be expected; instead, we find four. In agreement with Ikeshoji *et al.* (2009), we find that the two crystallographic sites of lithium are split in the vertical direction and the atomic distributions of lithium and boron in the vertical direction in the HT phase is similar in the LT phase, in which there are clearly four distinct crystallographic sites for both lithium and boron. The lithium and boron atoms are dynamically disordered over two sites, though the split sites of the latter are closer together. The dynamic nature of this disorder can be shown by computing the atomic distribution for one single lithium and boron atom in the simulation box, which shows the same position split, indicating rapid hopping between the two sites; this is discussed further in Section 5.4.2. In contrast, the time-averaged position for one lithium atom for the LT phase only shows one position with a Gaussian distribution, as

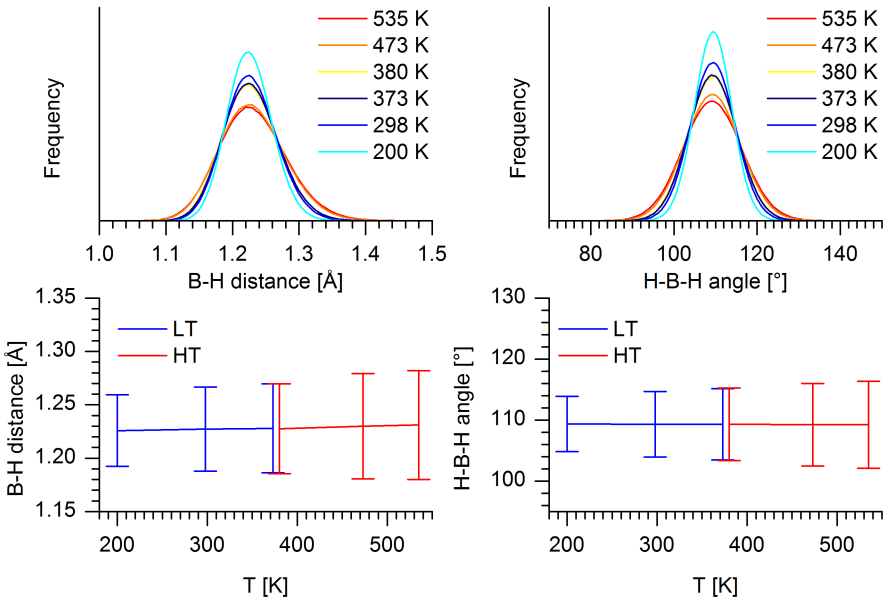

Figure 5.6: Top: H-B-H bond angle and B-H bond length distributions at the simulated temperatures. Bottom: temperature dependence of the mean and standard deviation of the bond angles and bond length, obtained from Gaussian fitting of the bond angle and bond length distributions.

expected for an ordered system. We notice that the distributions of both elements are symmetric with respect to a horizontal mirror plane at $z = 0.25$ and $z = 0.5$.

5.3.2 Borohydride geometry and orientation

The B-H bond is a very stable bond and no dissociations are detected at any temperature in our MD simulations; $LiBH_4$ is reported to decompose only at a temperature of 653 K, higher than the melting point (Züttel *et al.*, 2003). To determine the time-averaged positions of the hydrogen atoms, the geometry and orientations of the BH_4 units are investigated. The BH_4 units are, on average, perfectly tetrahedrally shaped, with no persistent deformations, as shown by the distributions of B-H bond lengths and H-B-H bond angles (Figure 5.6). The bond angles are centred at the perfect tetrahedron angle α, given by:

$$\alpha = 2 \arcsin\left(\sqrt{\frac{2}{3}}\right) \approx 109.47^\circ \tag{5.1}$$

Only the width of the distribution (connected to the H-B-H bending-mode amplitudes) increases with temperature in both phases, showing that this mode is very harmonic. The

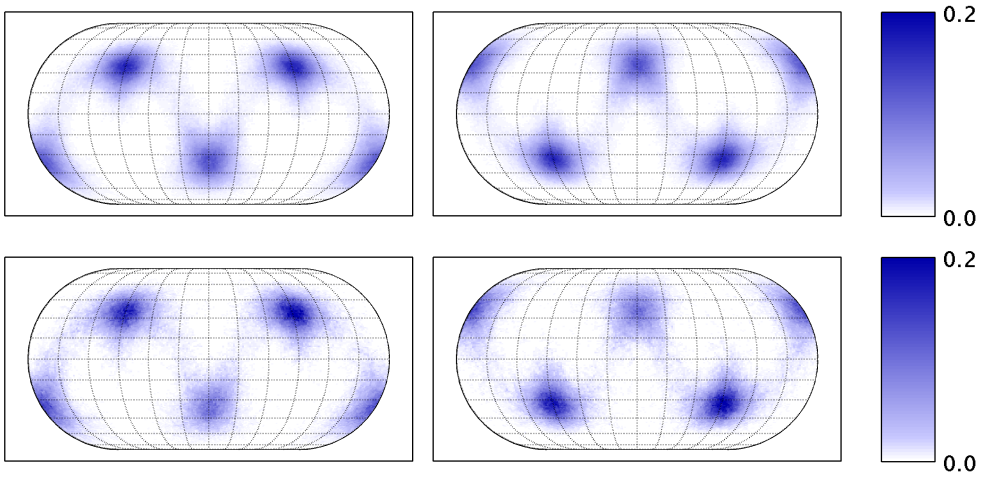

Figure 5.7: Hydrogen distributions in the LT phase at 373 K. Top: distribution for all hydrogen atoms in the supercell; bottom: distribution for a single hydrogen atom in the supercell. The ϕ-axis is horizontal, the θ-axis is vertical.

anharmonicity results in an increasing average bond length with temperature.

As the BH_4 units can be regarded as perfect tetrahedra on average, their average orientations in the crystal remain to be addressed for which the following procedure is followed. The hydrogen atom positions of each BH_4 unit are projected on the unit sphere centred on the boron atom. The hydrogen atom distributions on the unit sphere are then represented in terms of the spherical coordinates θ and ϕ, where θ is the angle with the vertical axis and ϕ is the angle in the horizontal plane with the positive y-axis (LT phase) or x-axis (HT phase). Since there are two differently oriented BH_4 units in each phase, separate distributions for each type are computed. The distributions are graphically represented by making use of geographical map projection techniques to represent the distribution in an area preserving projection; for this we use the Eckert IV projection. The distributions are shown as hydrogen density per solid angle, $\rho(\theta, \phi) = \mathrm{d}N(\theta, \phi)/\mathrm{d}\Omega$, with the infinitesimal solid angle element $\mathrm{d}S$ at ϕ, θ given by $\mathrm{d}S = \sin\theta\,\mathrm{d}\theta\,\mathrm{d}\phi$. The resulting density plots are shown in Figures 5.7 and 5.8 and are shown both for the spatial average over all BH_4 units, and for one single H atom in the whole supercell.

In the LT phase, the hydrogen distributions in Figure 5.7 shows that only one orientation of the tetrahedron is adopted, in agreement with the crystal structure. The distri-

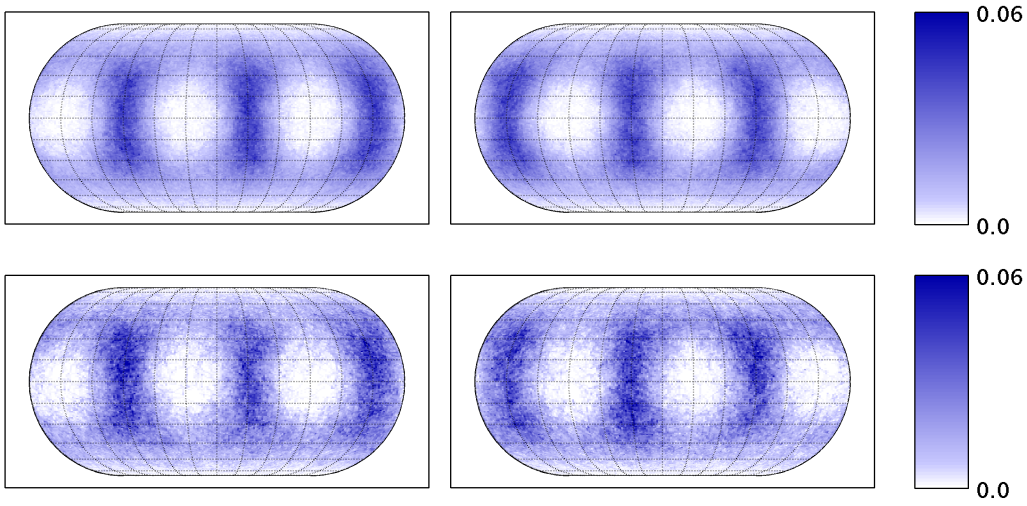

Figure 5.8: Hydrogen distributions in the HT phase at 380 K for all hydrogen atoms (top) compared to the distribution of one single hydrogen atom (bottom).

bution for one single H atom is qualitatively the same, meaning that each hydrogen atom occupies all four tetrahedral positions with equal probability, and therefore the tetrahedra are rapidly reorienting by rotational jumps. If no reorientational jumps were possible, this plot would only show one single spot as the hydrogen atom considered would remain in this position during the entire trajectory. As only one orientation of the tetrahedron is allowed, this means that the BH_4 unit undergoes reorientational jumps around the proper rotations of the tetrahedral symmetry group (C_2 and C_3 axes). This is in agreement with the deep energy minima calculated by Buchter *et al.* (2008a) from static DFT calculations.

In the HT phase, the hydrogen distributions in Figure 5.8 show a completely different picture: in contrast with the LT phase, no single tetrahedron orientation stands out; the average orientation is smeared out over large domains of ϕ and θ values. The favourable regions for the hydrogen atoms are three broad bands in the vertical direction (along θ), at regular ϕ intervals of 120°, showing three-fold symmetry along the c-axis. Each of these bands is symmetric with respect to the horizontal plane. This pattern suggests a high degree of dynamical disorder in the orientation of the BH_4 units. Two additional symmetry elements that are not part of the local tetrahedral site symmetry must be present to give rise to this pattern: a vertical C_3 axis, parallel to the crystal 6_3 screw axis, and a horizontal

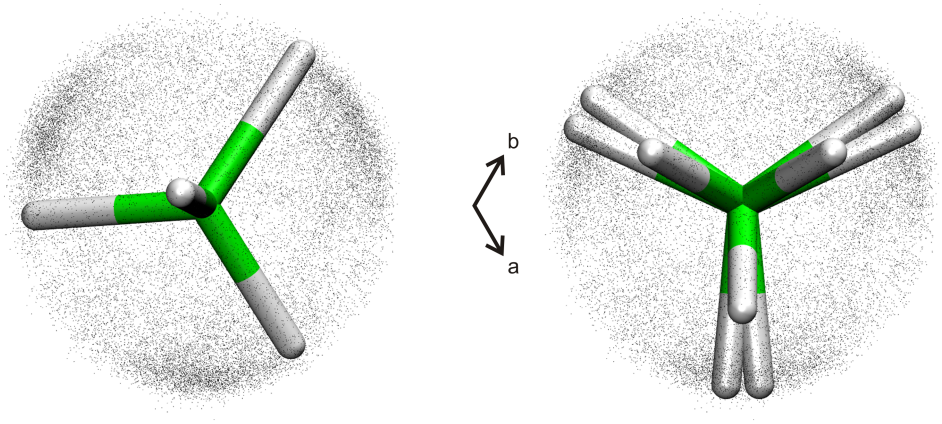

Figure 5.9: Proposed model for HT orientations, viewed along the vertical (c) axis. Left: one snapshot during the MD trajectory; right: fixed-orientation model, each hydrogen position shown has an occupancy of 1/3.

mirror plane passing through the origin (i.e. the boron atom). Figure 5.9 shows a minimal arrangement of orientations of the BH_4 unit in its site that possesses the external symmetry elements of the hydrogen distribution—the vertical C_3 axis and the horizontal mirror plane—in addition to the symmetry elements of the tetrahedron; each depicted hydrogen position has an occupancy of 1/3. In this model the BH_4 performs reorientational jumps between these orientations. The presence of the additional horizontal mirror plane—found for the hydrogen positions as well as for the lithium and boron positions, as described above (Figure 5.5)—changes the space group of the structure from $P6_3mc$ to $P6_3/mmc$.

5.3.3 Comparison of time-averaged positions to neutron scattering data

The results from this section can be compared to results from neutron scattering experiments. All neutron scattering experiments described in this section were carried out by Dr Sam Callear and Prof Bill David on the General Materials diffractometer (GEM) at the ISIS spallation neutron source.

The neutron pair distribution function (PDF) was calculated from the trajectory according to the procedure described in Section 3.4. The PDF has been measured from neutron total scattering on GEM (Callear *et al.*, 2010) for the isotopomer $LiBD_4$, and so the neutron scattering length for deuterium was used for the calculated PDF, even though

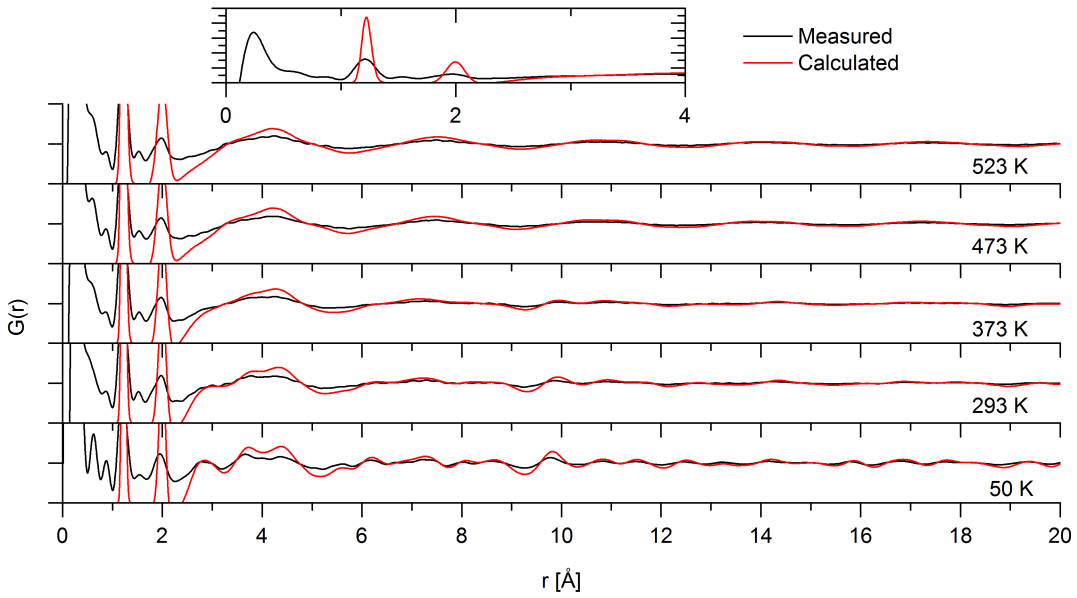

Figure 5.10: Measured (black) and calculated (red) neutron pair distribution functions.

the dynamics were performed with the natural isotopic abundance masses. Both at short and long distances the calculated PDF agrees well with the experimentally measured PDF; the comparison is shown in Figure 5.10. Two peaks stand out at short distance that represent the B-D and D-D distances, which are in the same ratio as the edge length to the centre-vertex distance of a tetrahedron:

$$d_{\text{D-D}} = \sqrt{\frac{8}{3}}\, d_{\text{B-D}} \tag{5.2}$$

This shows that the BH_4 units are in undistorted tetrahedral shape.

The findings from this section can be combined to form a model of a $P6_3/mmc$ structure that can be used in a Rietveld refinement. To represent the hydrogen distribution from Figure 5.8, which varies almost continuously, hydrogen positions are arranged spherically around the boron atoms at a distance $r = 1.230\,\text{Å}$, with hydrogen atoms spaced by $\Delta\theta = \Delta\phi = 15°$, and their occupancy given by an occupancy function $f_{\text{occ}}(\theta, \phi)$ that reproduces the pattern of Figure 5.8 with fittable parameters. Any smooth, positive definite function on the surface of a sphere can be decomposed in the set of the real-valued

spherical harmonics $Y_l^m(\phi,\theta)$, which form a complete orthonormal set:

$$Y_l^m(\phi,\theta) = N_l^m P_l^m(\cos\theta)\cos(m\phi), \quad l = 0\ldots l_{\max}, \quad m = 0\ldots l \tag{5.3}$$

where $P_l^m(x)$ are the associated Legendre polynomials. The normalisation constants N_l^m are such that orthonormality is preserved:

$$\int_0^{\pi}\int_0^{2\pi} Y_l^m(\theta,\phi)Y_{l'}^{m'}(\theta,\phi)\,\sin\theta\,\mathrm{d}\theta\,\mathrm{d}\phi = \delta_{l,l'}\delta_{m,m'} \tag{5.4}$$

The occupancy function $f_{\mathrm{occ}}(\theta,\phi)$ is constructed from spherical harmonics with $l_{\max} = 6$. The model function is given by:

$$f_{\mathrm{occ}}(\theta,\phi) = \sum_{l=0}^{l_{\max}}\sum_{m=0}^{l} c_l^m Y_l^m(\theta,\phi+\phi_0) \tag{5.5}$$

Because of the vertical threefold axis and the horizontal mirror plane present in $P6_3/mmc$, only spherical harmonics functions with the proper symmetry need to be considered, that is only Y_l^m with $m = 0,3,6,9,\ldots$ and $l-m = 0,2,4,6,\ldots$ are included in the expansion. The occupancy of each hydrogen position is given by $f_{\mathrm{occ}}(\theta,\phi)\Delta\Omega$ where $\Delta\Omega$ is the finite solid angle per hydrogen position; in this model, 182 positions are given on the sphere, and so $\Delta\Omega = 4\pi/182$. The coefficients c_l^m are adjustable parameters and determined by Rietveld refinement. The coefficients are normalised such that the solid-angle integral of the occupancy function is 4:

$$\int_0^{\pi}\int_0^{2\pi} f_{\mathrm{occ}}(\theta,\phi)\,\sin\theta\,\mathrm{d}\theta\,\mathrm{d}\phi = 4 \tag{5.6}$$

These coefficients are summarised in Table 5.2. The result of the fitting model is shown in Figure 5.11. The neutron data were collected by Dr Sam Callear and the Rietveld refinement was performed by Prof Bill David.

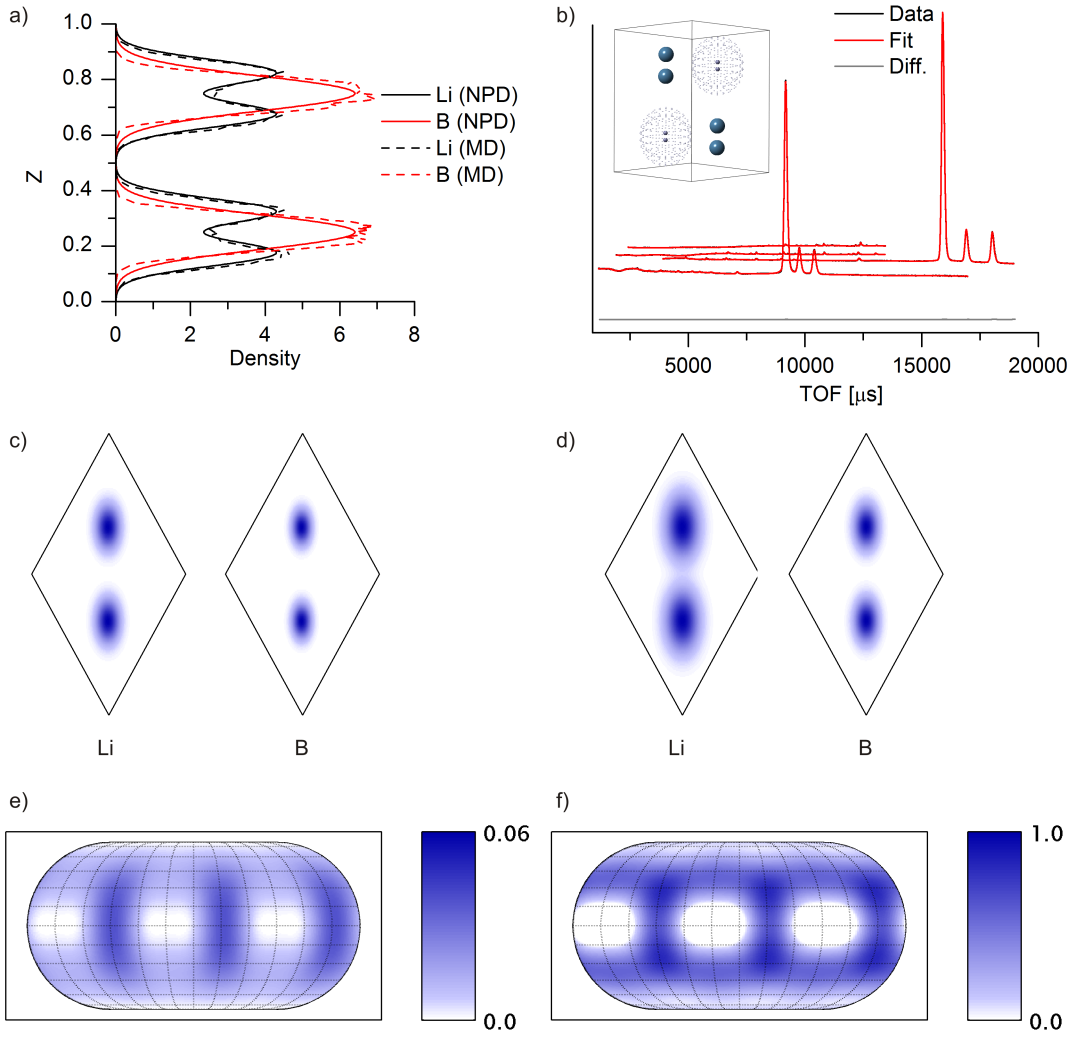

Figure 5.11: MD structure compared to the neutron powder diffraction (NPD) structure for the HT phase at 473 K. a) Distribution of Li and B z-coordinates; b) NPD pattern and Rietveld fit; c) and d) Li and B xy-coordinate distributions from MD and from Rietveld refinement, respectively; e) and f) hydrogen distribution around B represented by spherical harmonics expansion from MD and Rietveld refinement, respectively.

Table 5.2: Fitted parameters for a crystallographic model of the HT phase at 473 K in space group $P6_3/mmc$, comparing Rietveld (NPD) results to MD results.

		x	y	z	u_{11} [Å^2]	u_{33} [Å^2]
Li	MD	0.3333(5)	0.6667(8)	0.1753(4)	0.06644(15)	0.1037(15)
	NPD	1/3	2/3	0.1751(7)	0.131(2)	0.105(9)
B	MD	0.3333(4)	0.6667(7)	0.2132(2)	0.04272(10)	0.0604(10)
	NPD	1/3	2/3	0.2282(11)	0.0670(6)	0.163(3)

H positions	c_0^0	c_2^0	c_3^3	c_4^0	c_5^3	c_6^0	c_6^6	$d_{\text{B-H}}$ [Å]
MD	0.05118(5)	-0.01086(4)	0.03080(5)	-0.00849(3)	-0.00185(5)	0.00319(4)	0.00873(5)	1.23000(5)
NPD	0.038955	-0.00102(16)	0.02064(10)	-0.0108(2)	-0.0036(3)	0.0027(5)	-0.0001(3)	1.230(2)

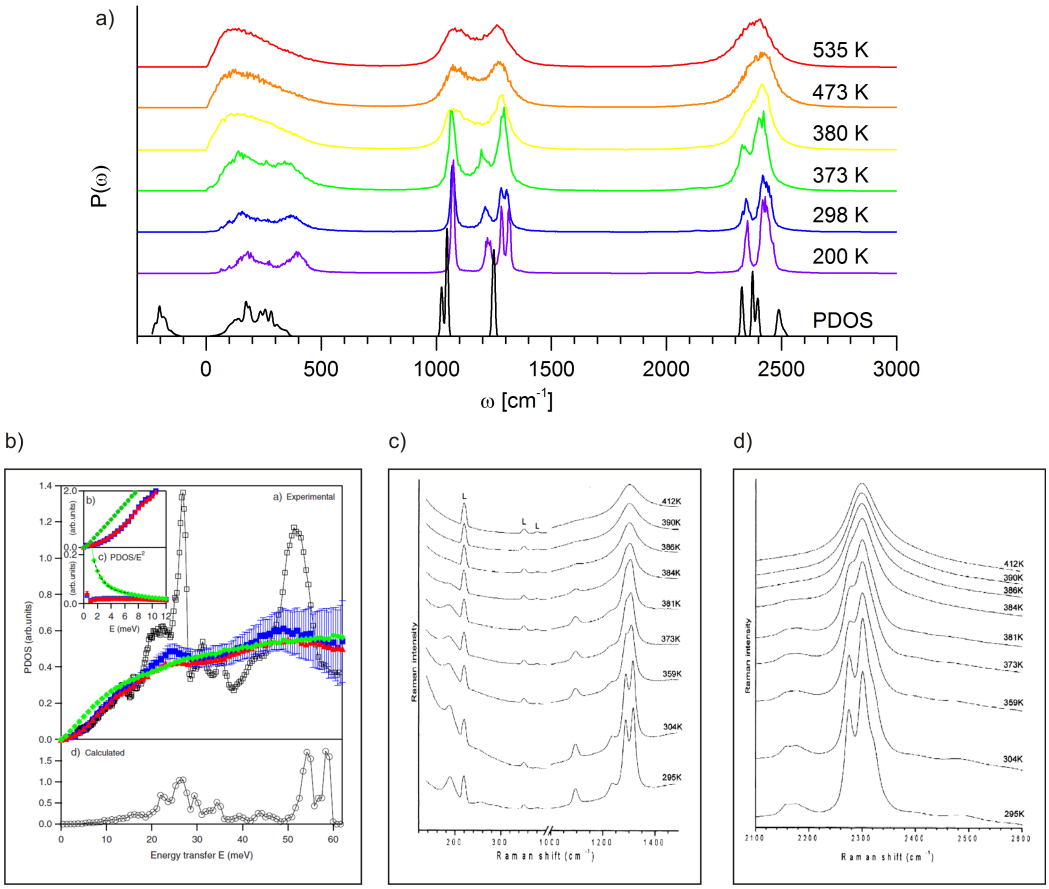

Figure 5.12: a) Power spectra obtained from the VACF calculated for each MD trajectory. PDOS is the phonon density of states from a phonon mode calculation of the optimised $P6_3mc$ structure; b) INS spectrum. Reprinted with permission from Buchter *et al.* (2008a), copyright (2008) by the American Physical Society. c) and d) Raman spectra. Reprinted from Gomes *et al.* (2002) with permission from Elsevier.

5.4 Dynamical disorder mechanisms

In the previous section, we compared time-averaged data extracted from the MD trajectories with the experimentally measured powder diffraction pattern and pair-distribution function and found good agreement, therefore corroborating the MD model as an accurate representation of the disordered HT phase. In this section, the dynamical aspects of the structure and the disorder are addressed, notably the vibrational spectrum and BH_4 rotational diffusion and jump model. This will be compared with NMR, quasi-elastic neutron scattering (QENS) and IR/Raman spectroscopy data published in the literature.

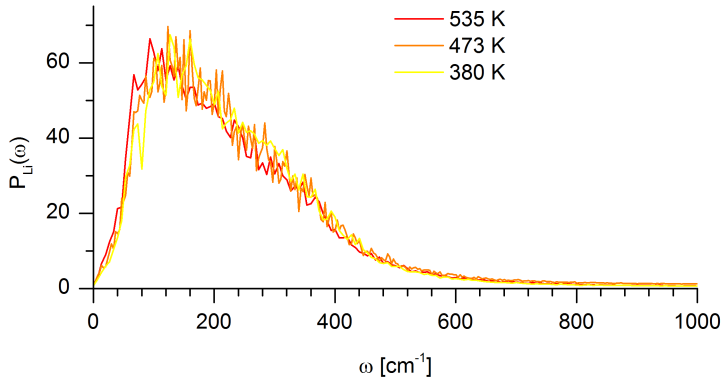

Figure 5.13: VAC power spectrum in the HT phase calculated for lithium atoms only.

5.4.1 Vibrational spectrum

The vibrational spectrum can be calculated from the velocity autocorrelation function (VACF); the power spectrum of the VACF is a representation of the vibrational spectrum, as was discussed in detail in Section 3.1. The power spectra are shown in Figure 5.12, and can be compared to the Raman spectra measured by Gomes *et al.* (2002). The split peak at 1300 cm^{-1} in the LT phase is well reproduced in the power spectrum, and coalesces into one peak at the phase transition temperature, in keeping with the measured Raman spectrum. Likewise, the sharp peak at 1100 cm^{-1} disappears in the Raman spectrum at the phase transition; in the power spectrum this peaks becomes a very broad feature above the phase transition temperature since the power spectrum does not take into account any selection rules. This good match between the calculated vibrational spectrum and the measured Raman spectrum shows that the dynamical properties are represented better by the MD structure than by phonon frequency calculation from the $P6_3mc$ DFT model, also shown in Figure 5.12.

5.4.2 Li motion

The partial VACF power spectrum for lithium atoms only (Figure 5.13) shows no lithium diffusion on the time scale accessible to these MD simulations; no diffusional jumps are recorded at any temperature, even though lithium borohydride is known to be a superionic conductor (Matsuo *et al.*, 2009). This shows the limits of standard, equilibrium MD for

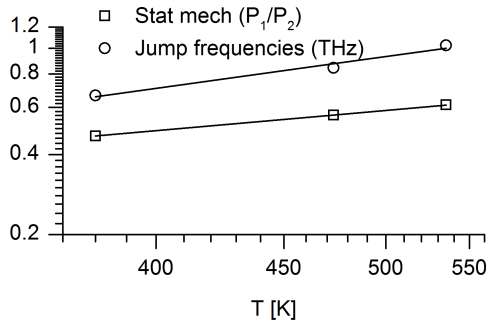

Figure 5.14: Arrhenius plot of the calculated Li jump frequency and of the statistical mechanical probability ratio.

tackling slow processes and forms the subject of Chapter 6.

The vibration of the lithium atom in its site has a very low frequency. The jump frequency from one split site to the next was determined by the following simple analysis: whenever a lithium atom crosses the plane of boron atoms by more than 0.5 Å a jump event is recorded. The jump frequencies thus calculated depend on temperature by a simple Arrhenius model (Figure 5.14); parameters are: $A = 2.8(1.2)\,\mathrm{THz}$, $E_A = 47(7)\,\mathrm{meV}$. In terms of wavenumbers, the attempt frequency corresponds to $\omega = 93\,\mathrm{cm}^{-1}$ which corresponds to the onset of the high intensity, broad feature in the lithium VACF power spectrum. Another method of determining a value for the energy barrier for lithium jumps is by statistical mechanical analysis of the atomic distributions (Figure 5.5). In the canonical ensemble, the probability of finding the system at $\mathbf{\Gamma}_1$ and the probability of finding it at $\mathbf{\Gamma}_2$ are related to the energy difference between $\mathbf{\Gamma}_1$ and $\mathbf{\Gamma}_2$. These two phase points are taken to be the equilibrium split positions and the mid-point; since only the z-coordinate is considered, this corresponds to integration over all other degrees of freedom. The relation between the values of the distribution at $\mathbf{\Gamma}_1$ and $\mathbf{\Gamma}_2$ and the free energy at these points is:

$$\frac{f(\mathbf{\Gamma}_1)}{f(\mathbf{\Gamma}_2)} = \exp\left(-\frac{E_1 - E_2}{k_B T}\right) \tag{5.7}$$

By this method, an energy difference of $E_1 - E_2 = 30.2(4)\,\mathrm{meV}$ is obtained. Results from these two analyses of lithium split-site jump motion are summarised in Table 5.3. The lower estimate from the statistical mechanical estimate takes into account lithium atoms

Table 5.3: Lithium split-site jumping frequencies for the HT phase.

T [K]	Frequency [THz]	Mean dwell time [ps]	$f(\mathbf{\Gamma}_1)/f(\mathbf{\Gamma}_2)$
380	0.6655	1.5027	2.1291
473	0.8443	1.1843	1.7806
535	1.0244	0.9762	1.6292
E_A [meV]	47(7)		30.2(4)
A [THz]	2.8(1.2)	0.3580	-

approaching the barrier and then returning to their original site, without completing the jump. This number agrees well with the barrier of 20 meV obtained by Ikeshoji *et al.* (2009), which was calculated from only one run at one temperature and not from an Arrhenius fit over multiple temperatures.

5.4.3 BH_4 reorientational dynamics by free diffusion and by jumps

We established in Section 5.3.2 that the BH_4 units are rapidly reorienting in both the LT and HT phases. In the LT phase, reorientational movement consists of jumps that preserve the original orientation, that is jumps around the proper rotations of the tetrahedron, which are 6 C_2 and 8 C_3 operations. In the HT phase, in addition to the proper tetrahedral rotations, we must also consider reorientational jumps by the two vertical C_3 operations introduced by the crystal symmetry 6_3 screw axis as no unique tetrahedral orientation is preserved. In this section, we consider a rotational jump diffusion model and a continuous rotational diffusion model to describe the disordered structure of the BH_4 units.

To analyse the rotational motion, all H-B-H bending and B-H stretching vibrational motions of the BH_4 units were projected out from the MD trajectories. Since it was found that the BH_4 units are on average perfect tetrahedra, we fitted the BH_4 units at each time step to the closest rigid tetrahedral BH_4 unit with fixed B-H bond length set to the average bond length found above. The algorithm described in Section 3.3.3 was used to fit the BH_4 units, which may be deformed due to vibrational motion, into an ideal tetrahedral shape at each time step. As a result, each BH_4 may be represented by a quaternion describing the instantaneous rotational orientation of the fitted ideal, rigid tetrahedron, reducing the trajectory to a trajectory of 48 quaternions describing the rotational motion of the BH_4

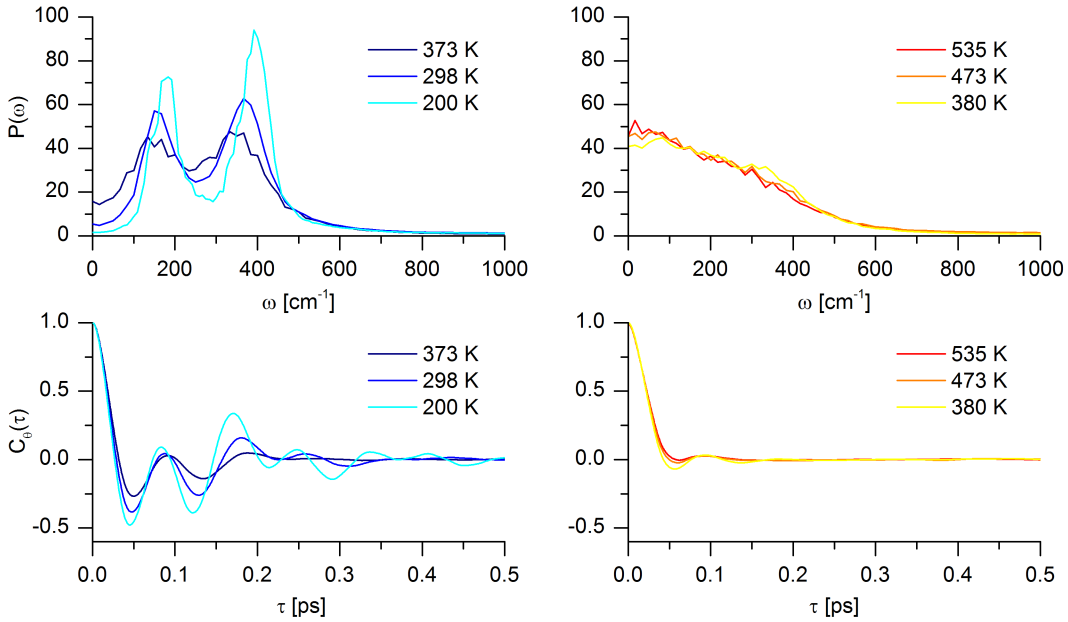

Figure 5.15: AACF (bottom) and power spectra (top) for the LT (left) and HT (right) phases at different temperatures.

units. This made the subsequent analyses described below much simpler.

The angular velocity autocorrelation function (AACF) and its power spectrum were calculated (Section 3.1) to determine the modes of vibrational motion. Analogous to the power spectrum of the velocity autocorrelation function, which is a spectrum of atom vibrational frequencies, the power spectrum of the AACF represents the frequencies of rigid-body rotational vibrations (librations) of the BH_4 units. Since rigid-body librations do not involve any change of dipole moment or polarisability, these modes are forbidden in both IR and Raman spectroscopy, but inelastic neutron scattering (INS) is expected to capture this motion. Figure 5.15 shows the AACF power spectra for the LT and HT phases at all temperatures considered.

In the LT phase at 200 K, there is nearly no rotational diffusion component, and the intensity of the power spectrum at zero frequency is at the baseline level. Already at 298 K, the zero-frequency intensity increases. This is in line with QENS measurements by Remhof *et al.* (2010), where no elastic line broadening was observed up to a temperature of 200 K. Two peaks are present in the spectra of the LT phase, indicating two librational modes at 192 and 392 cm^{-1}. An anharmonic effect can be seen as well, as the peak position shifts to

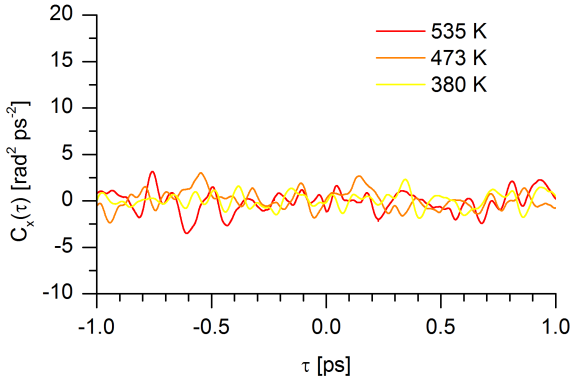

Figure 5.16: Angular cross-correlation function of nearest-neighbour BH_4 units in the HT phase.

Table 5.4: Rotational diffusion constants and Arrhenius parameters for BH_4 units calculated from the AACFs.

T [K]	D_θ [rad^2/s]	T [K]	D_θ [rad^2/s]	$D_{\theta\perp}$ [rad^2/s]	$D_{\theta\parallel}$ [rad^2/s]
200	0.029×10^{12}	380	1.616×10^{12}	1.118×10^{12}	0.498×10^{12}
298	0.162×10^{12}	473	2.223×10^{12}	1.489×10^{12}	0.617×10^{12}
373	0.608×10^{12}	535	2.602×10^{12}	1.768×10^{12}	0.834×10^{12}
E_A [eV]	0.11(2)	E_A [eV]	0.0538(6)	0.051(3)	0.055(17)
A [rad^2/s]	$14(2)\times10^{12}$	A [rad^2/s]	$8.3(1.0)\times10^{12}$	$5.3(1.0)\times10^{12}$	$2.5(1.2)\times10^{12}$

lower frequencies with increasing temperature. The INS spectrum measured by Buchter *et al.* (2008a) shows two features in the LT phase at 25 K at 217 and 411 cm^{-1} that give way to a broad, featureless curve after transition into the HT phase. The power spectrum of the AACF for the HT phase at all temperatures shows that there are hardly any vibrational components; a non-zero intensity at zero frequency indicates diffusive motion. The AACF at short times shows that for HT there is still some vibrational component present.

We establish that the rotational motions of the BH_4 units are independent and uncorrelated with the rotational motions of their nearest-neighbour units by plotting the angular velocity cross-correlation function (ACCF) between nearest-neighbour BH_4 units. The ACCFs for the HT phase are shown in Figure 5.16 and show that no spatial cross-correlation is present at any temperature.

The rotational diffusion can be quantified by calculating the rotational diffusion coefficient from the AACF. Results are shown in Table 5.4. The rotational diffusion constant for the HT phase is comparable to that of ammonium ions in aqueous solution at room

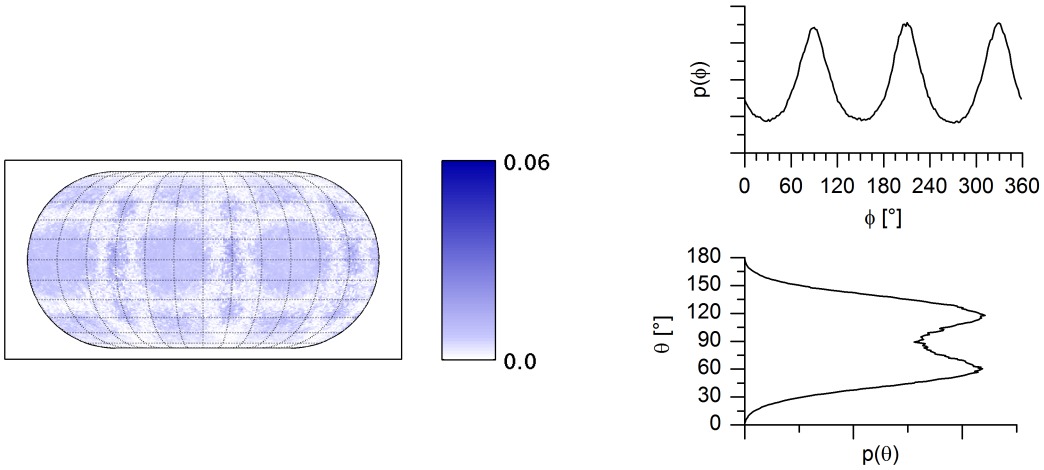

Figure 5.17: Left: static angular correlation given by Equation (5.9), right: plots of $p(\theta) = \int_0^{2\pi} \mathrm{d}\phi \, \sin\theta \, P(\theta, \phi)$ and $p(\phi) = \int_0^{\pi} \mathrm{d}\theta \, P(\theta, \phi)$.

temperature (Chang and Dang, 2003). This high mobility supports the large amount of disorder highlighted in the previous section. The diffusion coefficients are analysed by the Arrhenius equation:

$$D_\theta = A \exp\left(-\frac{E_a}{k_B T}\right) \tag{5.8}$$

The two librational modes in the LT phase can be attributed to jump rotations around the C_2 and the C_3 axes, respectively, and represent a jump model for reorientation; this will be discussed further below, when the jump model is addressed. In the HT phase, however, mainly diffusive motion is observed, and before attempting to rationalise this with a jump model, the diffusive motion model is explored further. The hydrogen distributions show a decorrelation of the rotation around the vertical axis and of the rotation around any axis in the horizontal plane; this is clear if we plot $\Delta P(\theta, \phi)$, which is given by:

$$\Delta P(\theta, \phi) = P(\theta, \phi) - \int_0^{\pi} \mathrm{d}\theta P(\theta, \phi) \int_0^{2\pi} \mathrm{d}\phi \sin\theta P(\theta, \phi) \tag{5.9}$$

This is represented in Figure 5.17, where it is clear that $\Delta P(\theta, \phi)$ is close to zero at any θ, ϕ. Therefore, we may treat rotation around the principal axis separately from rotation around any axis perpendicular to the principal axis. The AACF for the two separate components of the rotation are shown in Figure 5.18. More diffusive nature is observed

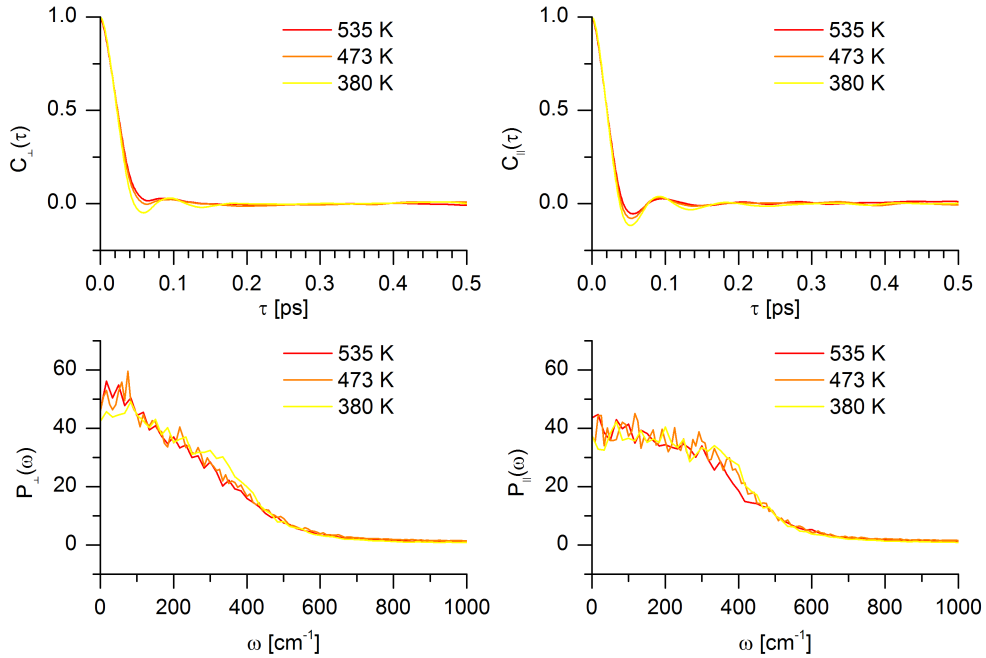

Figure 5.18: AACFs of BH_4 rotation around a rotation axis parallel to the vertical axis ($c_{||}(\tau)$) and around axes perpendicular to the vertical axis ($c_{\perp}(\tau)$) in the HT phase.

around the horizontal axes than around the vertical axis. This indicates that the BH_4 units perform rotational jumps around the vertical C_3 axis, and undergo restricted rotational diffusion around axes that lie in the horizontal plane.

In order to model the rotational diffusion in the LT phase by a jump model, all reorientations must solely be quantified by the proper rotations of the tetrahedron, since these are the only rotations a rigid body can physically perform. These are 8 C_3 rotations (axes aligned along the B-H bonds) and 6 C_2 operations (axes bisecting the H-B-H angles). All rotational motion is attempted to be described in terms of reorientational events by one of these operations. As with the diffusive model, we ignore all bending and stretching vibration by fitting the BH_4 units to perfect tetrahedra and consider the trajectory of quaternions that describe the rotation of the BH_4 units with respect to the initial orientation, which is taken as a reference. We follow the procedure of Pawley and Dove (1985) for the determination of a reorientational event using a quaternion formalism.

The symmetry rotations are represented by a set of quaternions:

$$q_s = (\cos(\alpha_s/2), \sin(\alpha_s/2)\hat{\mathbf{v}}_s) \tag{5.10}$$

where α_s is the rotation angle and either 120° or 180°, and $\hat{\mathbf{v}}_s$ is the axis of rotation. When the quaternion of the trajectory approaches one of these symmetry operations, a rotation event is registered. The condition for detecting a reorientation event s is expressed as:

$$q_i(t)q_s^{-1} \cdot I > \gamma_s q_i(t) \cdot I \tag{5.11}$$

where $q_i(t)$ is the quaternion describing the orientation of BH_4 unit i at time t, q_s is symmetry operation s and the dot product indicates four-dimensional dot-product formation with the unit quaternion I. Whenever this condition is true, a rotation event with respect to operation s is registered and $q_i(t)$ for all subsequent time steps replaced by $q_i(t)q_s^{-1}$. The coefficient γ_s corrects for the fact that some symmetry operation fulfil Equation (5.11) before other symmetry operations, which will then never be observed. Pawley and Dove (1985) show that for random isotropic diffusion of a tetrahedron, C_3 rotation events will always be recorded before C_2 rotation events if $\gamma_s = 1$ for all symmetry events, hence C_2 jumps will never be counted in isotropic diffusion. To determine γ_3 at which an equal rate of C_2 and C_3 reorientations is detected for completely random, isotropic rotational diffusion, we calibrated our analysis algorithm using a rotational random walk following the procedure described in Section 3.3.4 and found a value of $\gamma_3 = 1.24$.

The reorientational jump rates as a function of temperature are shown in Figure 5.19 and Arrhenius parameters are reported in Table 5.5 for each type of reorientational jump. From these values, we can calculate a diffusion coefficient according to:

$$D_{\theta,\mathrm{LT}} = \frac{1}{6}\frac{\mathrm{d}\left\langle\theta^2\right\rangle}{\mathrm{d}t} = \frac{1}{6}\left(\frac{4\pi^2}{9}f_{C3} + \pi^2 f_{C2}\right) \tag{5.12}$$

$$D_{\theta,\mathrm{HT}} = \frac{1}{6}\frac{\mathrm{d}\left\langle\theta^2\right\rangle}{\mathrm{d}t} = \frac{1}{6}\left(\frac{4\pi^2}{9}(f_{C3} + f_{C3'}) + \pi^2 f_{C2}\right) \tag{5.13}$$

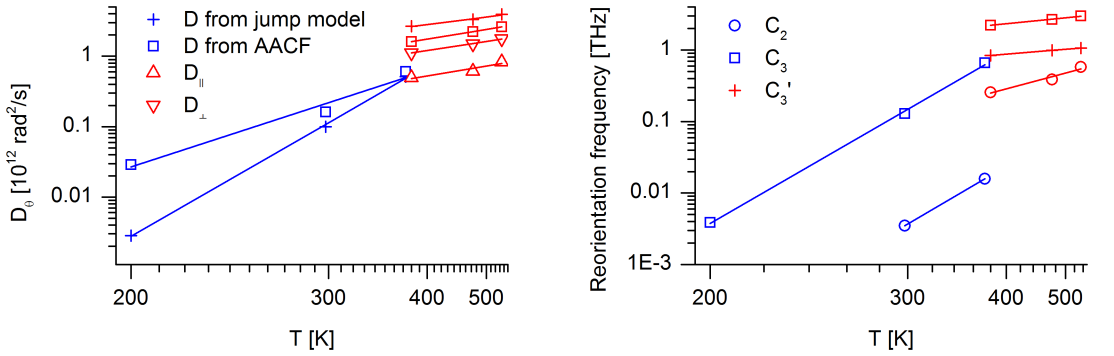

Figure 5.19: Arrhenius plots of the diffusion coefficients calculated according to Equations (5.12) and (5.13), and of the individual reorientational jump frequencies for tetrahedral C_2 and C_3 rotations and for external C_3' rotation in the HT phase,

Table 5.5: Arrhenius parameters for the rotational jumping model.

	D, rad^2/s		C_2 frequency, THz		C_3 frequency, THz		Crystal C_3'	
	E_A [eV]	A [rad^2/s]	E_A [eV]	A [THz]	E_A [eV]	A [THz]	E_A [eV]	A [THz]
LT	0.192(5)	191.9(1.2)×10^{12}	0.2	6.6	0.190(6)	230.8(1.3)512		
HT	0.042(6)	9.5(1.2)×10^{12}	0.087(17)	3.6(1.6)	0.032(3)	5.9(1.1)	0.0270(6)	1.9(1.0)

for the LT and HT phase, respectively, where f_{C3} is the reorientation frequency around the C_3 axes, and f_{C2} is the reorientation frequency around the C_2 axes. For HT, where we consider an additional C_3 axis parallel to the crystallographic c-axis, frequency $f_{C3'}$ is included accordingly. According to QENS measurements (Remhof *et al.*, 2010), the activation energy for the residence time is 0.18 eV, matching very closely the activation energy calculated for either reorientation mode and for the overall diffusion coefficient.

5.5 Simulation of the phase transition

The structural differences between the LT and HT phases are rather subtle, and we investigated whether an increase in temperature in the LT phase in an MD simulation leads to a transition into the hexagonal phase on the MD time scale, with and without allowing the lattice parameters to relax.

The LT trajectory at 373 K was continued by setting the thermostat temperature to 535 K in the canonical ensemble, with fixed volume. After equilibration at this temperature, the rotational diffusion coefficient of the BH_4 units was found to be very similar

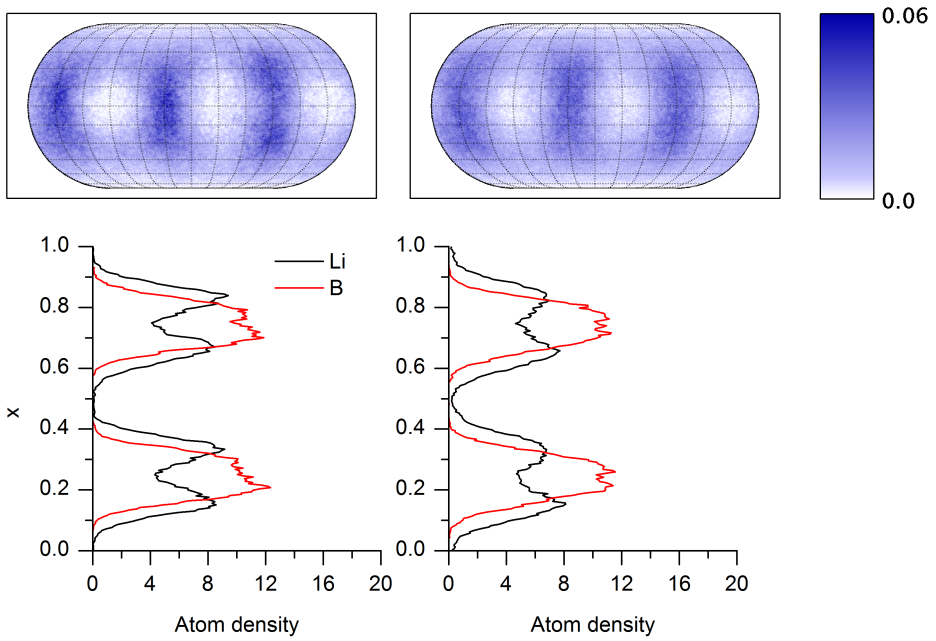

Figure 5.20: Z-histogram and rotational orientations a) during NVT trajectory at 535 K, b) during NPT trajectory at the same temperature.

to the HT phase at 535 K. The z-coordinate distribution of boron and lithium shows the same pattern as for the HT phase, that is split positions with dynamical disordering (Figure 5.20). This rearrangement of B and Li atoms enables more rotation for the BH_4 groups. The orientational distribution of the hydrogen atoms looks similar to the HT phase, and the symmetry of the cell has changed: BH_4 groups symmetry-related by the a-glide plane in the LT phase become related by a three-fold rotation similar to the HT phase, although the three-fold symmetry is not fully established because of the constrained lattice.

The NVT simulation was continued by changing from constant volume to constant pressure, with the supercell free to vary anisotropically. After a very short time, the supercell dilates and can equally well be described as a supercell composed of hexagonal primitive cells. The evolution of the cell parameters, decomposed in primitive hexagonal parameters, is shown in Figure 5.21. Figure 5.20 also shows that the hydrogen distribution becomes identical to the HT phase after a short NPT simulation.

The relaxed supercell parameters are summarised in Table 5.6 and are slightly larger

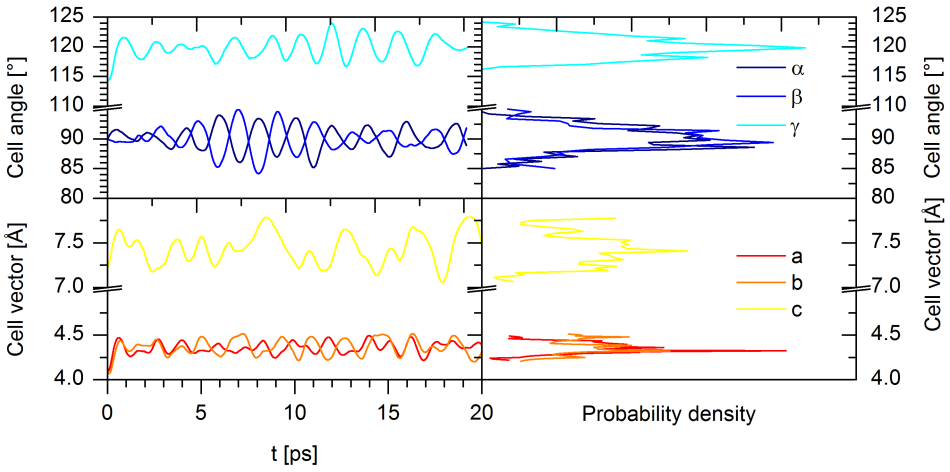

Figure 5.21: Left: evolution of the supercell in the NPT simulation at 535 K, reduced to the primitive hexagonal lattice. Right: histogram of cell parameters over the NPT trajectory.

Table 5.6: Lattice parameters of hexagonal cell obtained from NPT simulation at 535 K compared to experimental lattice parameters according to Filinchuk *et al.* (2008a).

	a [Å]	b[Å]	c[Å]	α (°)	β(°)	γ(°)
MD	4.3580(8)	4.3686(12)	7.434(2)	90.06(3)	89.95(3)	119.84(2)
Exp.	4.3228	4.3228	7.0368	90	90	120

than experimental values, as is typical for DFT. The a and b parameters are overestimated by 0.5 to 1.0%, but the c parameter is overestimated by as much as 6%; a reason might be dispersion interactions between the horizontal layers of the structure, which are badly accounted for in DFT in general and thus the binding in the c-direction is underestimated.

5.6 Conclusion

Canonical MD simulations of the LT and HT phases of $LiBH_4$ were performed at three different temperatures for each phase. This allowed us not only to study the crystal structure at each temperature, but also to examine the temperature dependence of various dynamical properties such as the vibrational spectrum and the rotational diffusion constants for the BH_4 units. In contrast to experimental crystal structure determination, MD simulations do not impose any symmetry constraints on the structure other than the supercell translational symmetry, and so trajectory analysis allows the average crystal structure to be determined from first principles.

The MD simulations use accurate DFT calculations for the determination of the atomic forces, but follow classical dynamics. Quantum rotational jumps of the BH_4 units, due to the light hydrogen atoms, could influence the reorientational frequencies and lead to an underestimate of the frequency values. Possible size effects of the finite supercell size on the rotational diffusion remain unexplored in this study, but the absence of rotational cross-correlation between nearest-neighbours suggests that they are negligible.

The reorientational dynamics of the BH_4 units have been found to consist of tetrahedral C_3 and C_2 rotational jumps in the LT phase, and rotational frequencies for both processes were obtained. The rotational frequencies show Arrhenius behaviour, and the calculated activation energies coincide very well with the ones measured using QENS by Remhof *et al.* (2010).

The results strongly indicate that the symmetry of the HT phase is $P6_3/mmc$, the main features being that the BH_4 units have no preferential orientation and that the lithium and boron positions are split, indicating the presence of a horizontal mirror plane. This symmetry was obtained by analysing MD trajectories that were generated without any symmetry constraints and with the experimental $P6_3mc$ structure as the starting point, indicating that the entropy effects, much cited in previously published tentative explanations of the disorder, actually lead to an increase in symmetry and that the $P6_3mc$ structure is not stable. Even an isothermal-isobaric MD simulation, starting from the LT structure with a flexible lattice will spontaneously make a transition into a $P6_3/mmc$ structure above the experimental phase transition temperature. A null measurement of a second harmonic generation signal in both LT and HT phases (David, personal communication) indicates that the crystal possesses a centre of inversion in both phases. The time-averaged structure extracted from trajectory analysis and subsequently used as a starting structure for Rietveld refinement resulted in a better fit to neutron powder diffraction data than the old $P6_3mc$ model. The combination of experimental and theoretical results presented in this chapter overwhelmingly supports the proposition that the correct space group symmetry of the HT phase is $P6_3/mmc$.

CHAPTER 6

Nonequilibrium molecular dynamics for solid-state diffusion

"Prediction is very difficult, especially about the future."

Niels Bohr

The molecular dynamics (MD) technique presented in Chapter 2 simulates a system at thermodynamic equilibrium, and is a very powerful method for the structural study of anharmonic and dynamically disordered systems at variable temperature. This was illustrated extensively in the previous chapter in the discussion of dynamical disorder in $LiBH_4$. In this chapter, we are interested in another dynamical property of $LiBH_4$ that escapes simulation by MD, namely its solid state lithium ion conductivity.

Hexagonal lithium borohydride has been found experimentally to have one of the highest lithium ion conductivity values measured of any material. In conductivity measurements and ^{7}Li-NMR experiments, Matsuo *et al.* (2007) found that the conductivity is ionic and not electronic and that the lithium ion conductivity exceeded $0.14\,\mathrm{S\,cm^{-1}}$ at 535 K in the high-temperature hexagonal phase. This conclusion was drawn from comparison

of direct measurements of the electric conductivity with the analysis of lithium mobility by ^{7}Li-NMR spectroscopy: the conductivity value from the impedance measurement was matched by the conductivity calculated from the measured lithium self-diffusion coefficient from ^{7}Li-NMR using the Nernst-Einstein equation (discussed below), proving that the electric conductivity is caused by the high lithium mobility. Pure $LiBH_4$ only adopts the superionic hexagonal structure above 110°C, which clearly would limit its potential application at room temperature or lower, but the hexagonal phase has been successfully stabilised at lower temperatures by forming solid solutions with LiCl (Miyazaki *et al.*, 2011).

High ionic mobility plays a significant role in many hydrogen storage materials. It has been found that ionic diffusion is an important mechanism in the decomposition of $NaAlH_4$, which is governed by transport from the bulk to the surface where decomposition occurs (Gunaydin *et al.*, 2008). Ionic conductivity is also important for materials used in components of other energy systems, such as fuel cell membranes or solid battery electrolytes.

In this chapter, a nonequilibrium molecular dynamics method is developed and applied to model the ionic diffusion in pure $LiBH_4$ at 535 K. The reason for using a nonequilibrium method is that ion site jumps, which are the elementary processes of ionic diffusion, are rare events.

6.1 Theoretical treatment of solid state diffusion

It is possible to calculate the rate of a process by transition state theory, which involves computing the activation energy of a reaction. However, this requires that the initial state and the transition states (saddle points on the potential energy surface) are known (Maronsson *et al.*, 2012), and presumes that no other activation barriers other than the one(s) considered are involved in the reaction. It is therefore a very approximate treatment that does not take into account collective particle effects, and the assumed initial and final states may be incomplete or incorrect. The MD technique lends itself best to the simulation

of dynamical processes as collective atomic motion is simulated directly, without any prior knowledge of the simulated process.

Diffusion is macroscopically described by Fick's Law, which is expressed in the form:

$$\mathbf{J}(\mathbf{r},t) = -D\,\nabla c(\mathbf{r},t) \tag{6.1}$$

where $\mathbf{J}$ is the particle flux (number of particles per area per second), D is the diffusion coefficient and ∇c is the concentration gradient of the species. This equation *defines* the transport diffusion coefficient D. To simulate diffusion by MD, a microscopic expression for the diffusion coefficient must be derived.

6.1.1 The Sutherland-Einstein equation for diffusion

If an infinitesimal volume element $\mathrm{d}\mathbf{r} = \mathrm{d}x\,\mathrm{d}y\,\mathrm{d}z$ located at $\mathbf{r}$ is considered, the change of the number of particles with time within this element is given by the influx minus the outflux of particles in each Cartesian direction:

$$\frac{\mathrm{d}N_x}{\mathrm{d}t} = J_x(x)\,\mathrm{d}y\,\mathrm{d}z - J_x(x+\mathrm{d}x)\,\mathrm{d}y\,\mathrm{d}z = \left(\frac{\partial}{\partial x}J_x\right)\mathrm{d}x\,\mathrm{d}y\,\mathrm{d}z \tag{6.2}$$

$$\frac{\mathrm{d}N_y}{\mathrm{d}t} = J_y(y)\,\mathrm{d}x\,\mathrm{d}z - J_y(y+\mathrm{d}y)\,\mathrm{d}x\,\mathrm{d}z = \left(\frac{\partial}{\partial y}J_y\right)\mathrm{d}x\,\mathrm{d}y\,\mathrm{d}z \tag{6.3}$$

$$\frac{\mathrm{d}N_z}{\mathrm{d}t} = J_z(z)\,\mathrm{d}x\,\mathrm{d}y - J_z(z+\mathrm{d}z)\,\mathrm{d}x\,\mathrm{d}y = \left(\frac{\partial}{\partial z}J_z\right)\mathrm{d}x\,\mathrm{d}y\,\mathrm{d}z \tag{6.4}$$

The sum of these equations results in the principle of mass conservation:

$$\frac{\partial c(\mathbf{r},t)}{\partial t} = -\nabla\cdot\mathbf{J}(\mathbf{r},t) \tag{6.5}$$

since $c(\mathbf{r},t) = (\mathrm{d}N_x + \mathrm{d}N_y + \mathrm{d}N_z)/\mathrm{d}x\,\mathrm{d}y\,\mathrm{d}z$. If we combine this equation with Fick's law, Equation (6.1), we obtain a partial differential equation for the concentration:

$$\frac{\partial c(\mathbf{r},t)}{\partial t} - D\nabla^2 c(\mathbf{r},t) = 0 \tag{6.6}$$

The Sutherland-Einstein equation (Sutherland, 1905; Einstein, 1905) is obtained by interpreting $c(\mathbf{r}, t)\,\mathrm{d}\mathbf{r}$ as the probability at time t of finding a particle in a volume $\mathrm{d}\mathbf{r}$ at $\mathbf{r}$. The probability density $c(\mathbf{r}, t)$ changes over time, but at all times t integrates to unity over all space:

$$\int \mathrm{d}\mathbf{r}\, c(\mathbf{r}, t) = 1 \tag{6.7}$$

With this interpretation, the initial condition is taken to be a Dirac function, $c(\mathbf{r}, 0) = \delta(\mathbf{r})$, that is to say the particle is known to be at $\mathbf{r} = 0$ at time zero. This suggests that the solution to Equation (6.6) is a Gaussian distribution with a time-dependent variance of the form $c(\mathbf{r}, t) = \left(2\pi\sigma^2(t)\right)^{-d/2} \exp\left(-r^2/2\sigma^2(t)\right)$. The solution is given by:

$$c(\mathbf{r}, t) = \frac{1}{(4\pi D t)^{d/2}} e^{-\frac{|\mathbf{r}|^2}{4DDt}} \tag{6.8}$$

where d is the dimensionality of $\mathbf{r}$.

The microscopic expression is obtained from the mean-squared displacement (MSD) of the particle, that is the average squared displacement at time t of the particle from its position at time zero. Microscopically, this is defined as:

$$\left\langle r^2(t) \right\rangle = \frac{1}{N} \sum_{i=1}^{N} |\mathbf{r}_i(t) - \mathbf{r}_i(0)|^2 \tag{6.9}$$

By this expression the MSD can be computed directly from an MD trajectory. However, given the probability distribution $c(\mathbf{r}, t)$ of the particle, the MSD is also equal to the second moment of this probability distribution:

$$\left\langle r^2(t) \right\rangle = \int \mathrm{d}\mathbf{r}\, r^2 c(\mathbf{r}, t) = 2dDt \tag{6.10}$$

which follows since $c(\mathbf{r}, t)$ is a Gaussian function. Taking the time derivative of both sides of this equation, the Sutherland-Einstein formula is obtained:

$$D = \frac{1}{2d} \frac{\mathrm{d}\left\langle r^2(t) \right\rangle}{\mathrm{d}t} \tag{6.11}$$

By computing the MSD as a function of time from an MD simulation according to Equation (6.9), D can be directly calculated by the Sutherland-Einstein formula as the average time derivative of the MSD.

6.1.2 Green-Kubo formalism for diffusion

The Green-Kubo formula for diffusion is obtained from the Sutherland-Einstein formula, Equation (6.11), by inserting the microscopic expression for the MSD, Equation (6.9), but replacing the particle position by the integral of the velocity:

$$\mathbf{r}_i(t) - \mathbf{r}_i(0) = \int_0^t \mathrm{d}s\, \mathbf{v}_i(s) \tag{6.12}$$

Equation (6.9) then reads:

$$\left\langle r^2(t) \right\rangle = \left\langle \left(\int_0^t \mathrm{d}s\, \mathbf{v}(s) \right) \cdot \left(\int_0^t \mathrm{d}s'\, \mathbf{v}(s') \right) \right\rangle \tag{6.13}$$

The product of integrals can be written as:

$$\int_0^t \mathrm{d}s \int_0^t \mathrm{d}s'\, \left\langle \mathbf{v}(s) \cdot \mathbf{v}(s') \right\rangle = \int_0^t \mathrm{d}s \int_0^s \mathrm{d}s'\, \left\langle \mathbf{v}(s) \cdot \mathbf{v}(s') \right\rangle + \int_0^t \mathrm{d}s \int_s^t \mathrm{d}s'\, \left\langle \mathbf{v}(s) \cdot \mathbf{v}(s') \right\rangle \tag{6.14}$$

The integrand in the last expression is the velocity autocorrelation function, and is an equilibrium property. We take advantage of the time-reversal symmetry and the time-translational symmetry of equilibrium properties and make the following variable substitution:

$$u = t - s \;\rightarrow s = t - u,\; \mathrm{d}s = -\mathrm{d}u$$

$$u' = t - s' \rightarrow s' = t - u', \mathrm{d}s' = -\mathrm{d}u'$$

Equation (6.14) becomes:

$$\int_t^0 \mathrm{d}u \int_t^{t-u} \mathrm{d}u' \left\langle \mathbf{v}(t-u) \cdot \mathbf{v}(t-u') \right\rangle + \int_t^0 \mathrm{d}u \int_{t-u}^0 \mathrm{d}u' \left\langle \mathbf{v}(t-u) \cdot \mathbf{v}(t-u') \right\rangle \quad (6.15)$$

Time-translational symmetry ($f(u) = f(t+u)$) and time-reversal symmetry ($f(u) = f(-u)$) of equilibrium properties allow us to rewrite the expression above as:

$$\left\langle r^2(t) \right\rangle = 2 \int_0^t \mathrm{d}u \int_0^u \mathrm{d}u' \left\langle \mathbf{v}(u) \cdot \mathbf{v}(u') \right\rangle \quad (6.16)$$

We make another variable substitution:

$$\tau = u' - u \rightarrow \mathrm{d}u' = \mathrm{d}\tau$$

and, taking advantage of time-reversal and time-translational symmetry, obtain:

$$\left\langle r^2(t) \right\rangle = 2 \int_0^t \mathrm{d}u \int_0^u \mathrm{d}\tau \left\langle \mathbf{v}(0) \cdot \mathbf{v}(\tau) \right\rangle \quad (6.17)$$

The time derivative of this expression is simply:

$$\frac{\mathrm{d} \left\langle r^2(t) \right\rangle}{\mathrm{d}t} = 2 \int_0^t \mathrm{d}\tau \left\langle \mathbf{v}(0) \cdot \mathbf{v}(\tau) \right\rangle \quad (6.18)$$

Inserting the above expression into the Sutherland-Einstein formula (equation (6.11)), we obtain the Green-Kubo relation for the diffusion coefficient:

$$D = \frac{1}{d} \int_0^\infty \mathrm{d}\tau \left\langle \mathbf{v}(0) \cdot \mathbf{v}(\tau) \right\rangle \quad (6.19)$$

We have thus two formalisms to calculate the diffusion coefficient from an MD trajectory. The Green-Kubo formalism is more general, and similar relations exist for transport coefficients for phenomena other than diffusion, but it should be noted that both formalisms are equivalent.

6.1.3 Treatment of rare events in molecular dynamics

Ionic diffusion in solids is generally orders of magnitude slower than in fluids even for the most highly conductive solids. Moreover, ionic diffusion proceeds by discrete ion jumps from site to site rather than continuous diffusion as in fluids. These basic events of ionic diffusion in crystalline solids are therefore rare events on the MD time scale. The time step for the integration of the equations of motion in an MD simulation is determined by the most rapid process, whereas the time scale of the phenomenon of interest might be considerably larger. In $LiBH_4$, the most rapid atomic motion is the stretching vibration of B-H bonds with a frequency of about $2300\,cm^{-1}$, meaning that the time scale for this process is about 15 fs for one oscillation (Section 5.4.1). By contrast, diffusion at 535 K occurs by lithium jumps with a frequency that Matsuo *et al.* (2007) measured to be one jump in 200 ps per lithium atom. The time scales of the time step determining process and of the process of interest differ by a factor of 10^4, and this time scale mismatch makes the MD computation a stiff problem: a vast number of time steps, of the order of 10^5, would need to be computed to observe at least one occurrence of the event. This is an unreasonably large computational effort given the expected outcome of observing one event. The limits of equilibrium MD for calculating diffusion coefficients using the Sutherland-Einstein or Green-Kubo formulas become apparent when applied to lithium borohydride at 535 K: the results from a 20 ps equilibrium MD trajectory are shown in Figure 6.1 and compared to results for liquid argon, modelled by an analytical Lennard-Jones interatomic potential. Even though $LiBH_4$ has a high experimental ionic conductivity at this temperature, for a typical trajectory of 20 ps the MSD of the lithium atoms has zero average slope since all lithium atoms simply vibrate around their lattice positions and do not move away; in contrast, liquid argon shows a steady rise of the MSD versus time. Similarly, the velocity autocorrelation function (VACF) for liquid argon converges to zero rather quickly due to the random motions decorrelating the velocities over long times, and by integrating the VACF over a sufficiently long but finite time period, the diffusion coefficient can be determined accurately. For $LiBH_4$, however, the VACF

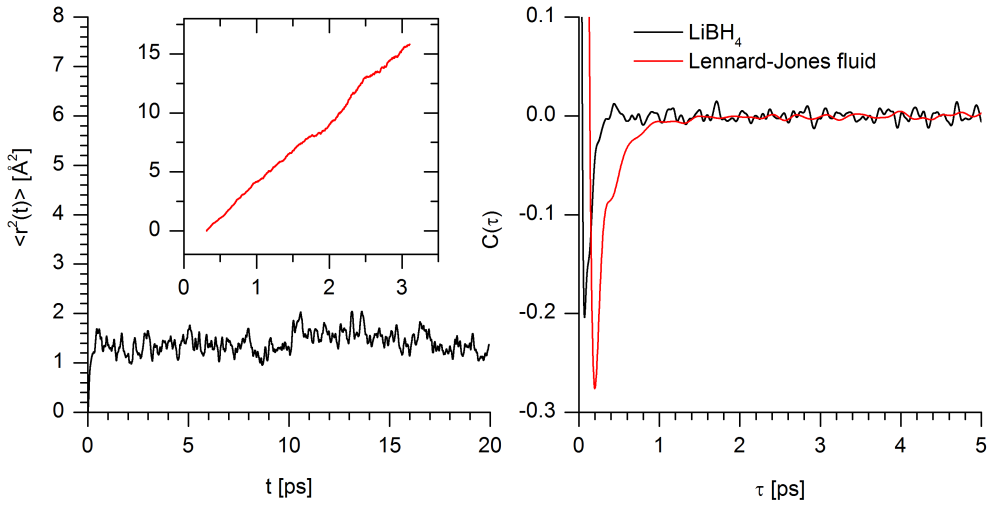

Figure 6.1: Left: MSD for $LiBH_4$ at 535 K, calculated from an equilibrium MD trajectory (NVT ensemble, Nosé-Hoover thermostat) of 20 ps. The inset shows the MSD for liquid argon, modelled by a Lennard-Jones potential. Right: VACF of $LiBH_4$ from the same equilibrium MD trajectory (black line) and VACF of liquid argon (red line).

contains all the vibrational components of the lithium atoms as discussed in Section 3.1 and oscillates around zero for very long times; to accurately evaluate the Green-Kubo formula the VACF would have to be integrated over a very long time interval and be sampled with high accuracy.

A simple guideline for MD is that events with an activation energy E_A larger than the thermal energy, k_BT, are rare events and will occur on a much longer time scale than is accessible by MD simulation, assuming the rate of the event can be described by an Arrhenius equation:

$$k = k_0 \exp\left(-\frac{E_A}{k_BT}\right) \tag{6.20}$$

The Arrhenius prefactor k_0 is typically of the order of molecular vibrations, so if E_A is of the same order as the thermal energy, the rate constant will be of the same order of magnitude as k_0 and the reaction will be readily observed in MD simulation. In order to simulate rare events by molecular dynamics, a scheme to accelerate the rare events must be introduced to increase the frequency of these events while keeping the distorting influence on the physics of the event to a minimum. The following approaches have previously been taken to reduce the time scale mismatch in MD simulations of rare events:

- Performing the simulation at high temperature. From Equation (6.20), increasing the thermal energy k_BT relative to the activation energy E_A will make the described event less rare. The disadvantage of this method is that the simulated system does not necessarily correspond to the system of interest. Farrell *et al.* (2009) applied this method to $Li_4BN_3H_{10}$, which is another highly conductive solid material. The necessary increase in temperature to observe diffusion in MD was so high that the system melted and the liquid state was simulated rather than the solid state. Increasing the temperature not only changes the kinetics of the process of interest but affects the entire system, often in an irregular fashion. The physical description of what is observed at high temperature is not easily extrapolated to the temperature range of interest.

- Selective heating of the mobile atoms. In contrast to the previous method, in this method the kinetic energy is not uniformly distributed among all the atoms in the system, but is concentrated in the lithium atoms by maintaining a velocity distribution that does not correspond to the equilibrium distribution. The justification for this method is that the event of a lithium atom hopping into an adjacent site is made possible by the natural, but rather rare, fluctuations of the kinetic energy of the lithium atoms so that the energy is sufficient to cross an activation barrier. Boulfelfel *et al.* (2011) applied this method to lithium diffusion in $LiFePO_4$, where fluctuations are induced artificially at regular intervals during the simulation. The advantage is that the framework of immobile atoms is not affected by the temperature increase, but the disadvantage of this *ad hoc* method is that no accurate description of the artificial fluctuations exists and so quantitative results (diffusion coefficients, activation barriers) cannot be obtained. The method is useful for mechanism and pathway discovery. It should be noted that selective heating can be realised in experiment: energy may be pumped into a specific vibrational mode by laser irradiation, effectively leading to an increased temperature in a certain degree of freedom and breaking equipartition temporarily; the heat will quickly dissipate

into the entire system, however.

- Reduce the mismatch of time scales by rescaling the atomic masses. In this method, named mass tensor molecular dynamics (Tsuchida, 2011), it is taken advantage of the fact that structural ensemble averages, such as the radial distribution function or free energies, do not depend on the atomic masses. The motion of the fastest atomic vibrations are slowed down by increasing the atom mass, or, conversely, the slowest motions are accelerated by reducing the masses of the heavier atoms. However, dynamical quantities such as diffusion coefficients or vibrational spectra cannot be obtained, as the motion of the system becomes unphysical due to the altered atomic masses. Again, extrapolation of the altered system back onto the realistic system with the real atomic masses is not straightforward.

- The metadynamics simulation technique (Laio and Parrinello, 2002), which is based on a method named hyperdynamics by Voter (1997), modifies the standard dynamics of MD simulations and its main purpose is to uncover the minimum energy path of a specific event. Different variants of metadynamics exist (Laio and Gervasio, 2008), but the common feature is the assumption that the pathway of the event can be described in the coordinate space of a small number of collective variables, which need to be defined in advance. A collective variable can be any function of the instantaneous atom positions $\mathbf{r}_i$; for example, the progress of a reaction might be described by the evolution of a bond length and of a bond angle. In equilibrium MD, the system will be trapped in a small stable region of the collective variable space; the metadynamics algorithm makes the system escape this stable region across the lowest energy barrier in the space of the collective variables by periodically adding a repulsive Gaussian-shaped potential energy term at the collective variable values that the system has visited most often. These repulsive potentials force the system away from its most stable configuration until the stable region is "filled up" by repulsive potential terms and the system can cross an energy barrier into the nearest neighbouring stable region. This technique is mostly applied to reaction mechanisms

in small organic molecules in the gas phase, but it has also been applied to elucidate the diffusion pathway of Si_x species on Si(100) surfaces (Ceriotti *et al.*, 2009). The main disadvantage of this method is that it requires preliminary knowledge of the phenomenon under study and that a multitude of parameters have to be chosen, such as the height and width of the Gaussian potentials as well as the frequency of their creation. The choice of collective variables—which has been called a "black art" rather than a science—requires the infamous "chemical intuition", and there is no guarantee that the chosen collective variable subspace spans the relevant areas of phase space sufficiently to describe the reaction.

To address the specific case of lithium ion diffusion in hexagonal lithium borohydride, an MD study was performed by Ikeshoji *et al.* (2011), where the technique of mass-scaling, discussed above, was used to reduce the mismatch in time scales of lithium and B-H motion. By additionally using linear scaling techniques for increasing the efficiency of the density functional theory force calculation step, the authors were able to increase the overall efficiency of the simulation by a factor of 5. However, as stated above, mass-scaled simulations lead to unphysical results for dynamical properties, and although some lithium motion was observed, it must be seen as a qualitative study. A method based on nonequilibrium thermodynamics is now proposed for application to solid ion conductors.

6.2 Nonequilibrium thermodynamics and simulation

By the definition of thermodynamic equilibrium, the state variables of a system do not depend on position or on time and so all gradients are zero in equilibrium. Transport phenomena, such as diffusion or heat flow, are by their nature nonequilibrium processes as they manifest themselves macroscopically by the presence of gradients in the system: Fick's law for diffusion or Fourier's law for heat conduction are linear relations between the gradient of concentration and particle flux or the temperature gradient and heat flux. The vast majority of experiments are performed under nonequilibrium conditions. It is therefore natural to seek a theoretical description of the nonequilibrium state and base

modelling methods on it.

An authoritative treatment on the basics of nonequilibrium thermodynamics can be found in the textbook by de Groot and Mazur (1984), here only a few points relevant to diffusion are presented. In a thermodynamic system away from equilibrium, the state variables are not constant in space or time. The *local equilibrium postulate* states that if the system is sufficiently close to thermodynamic equilibrium, then the usual thermodynamic relations still hold locally, such as the first principle:

$$T\mathrm{d}S = \mathrm{d}U + p\mathrm{d}V + \mu\mathrm{d}N \tag{6.21}$$

The first principle has been rearranged to group all conserved quantities on the right-hand side. Equation (6.5) is the mass conservation principle and describes the conservation of N; an analogous equation can be written for U since the total energy is conserved. The evolution of the volume for a mass element is described by an equation of motion involving the pressure p. Entropy, on the other hand, is not a conserved quantity in a nonequilibrium system, but increases monotonically by the second law of thermodynamics. The conservation equation for entropy therefore contains a source term which describes entropy production. The entropy source term is generally written in the form:

$$\frac{\partial S(\mathbf{r},t)}{\partial t} = \sum_{\alpha} \mathbf{J}_\alpha \cdot \mathbf{X}_\alpha \geq 0 \tag{6.22}$$

where $\mathbf{J}_\alpha$ and $\mathbf{X}_\alpha$ are thermodynamic fluxes and conjugate thermodynamic forces. By the definition of the equilibrium state, the entropy production term becomes zero when all thermodynamic forces are zero; in equilibrium, all fluxes are zero as well. This leads to a dependence of the thermodynamic fluxes of the forces, which can be seen as a Taylor expansion truncated after the linear term:

$$\mathbf{J}_i = \sum_j L_{ij}\mathbf{X}_j \tag{6.23}$$

Considering a system where there is only a concentration gradient present, the previous

equation can be identified with Fick's law for diffusion. Therefore, in Fick's law, the diffusion coefficient is equal to the *linear* expansion coefficient L_{ij}. It is worth keeping in mind that the above linear relation was derived under the assumption that the local equilibrium postulate holds. The phenomenological transport equations—which were derived before the advent of nonequilibrium thermodynamics—are linear relationships in the local equilibrium approximation.

In nonequilibrium molecular dynamics (NEMD), transport phenomena are simulated directly. The MD model is modified by artificially introducing a thermodynamic force $\mathbf{X}$ to shift the system away from equilibrium and induce transport processes, thereby directly calculating transport coefficients as the ratio of induced flux to inducing field. NEMD simulations mimic an experiment and so the methods for generating the force $\mathbf{X}$ and measuring the flux $\mathbf{J}$ are specific to the transport phenomenon studied.

Historically, one of the first NEMD calculations was performed by Ashurst and Hoover (1973), who studied shear viscosity of liquid argon by performing a molecular dynamics simulation that imitates a shear flow measurement. In the Couette model, shear flow is induced by placing the fluid between two infinite parallel solid planes that move at a constant relative speed and thus generate a constant shear stress rate on the fluid. The NEMD simulation imposes the shear stress rate by moving boundary conditions: one plane of the simulation box is given a constant speed with respect to the opposite plane of the box. The shear viscosity is directly calculated from the measured shear flow rate. A similar method using inhomogeneous boundary conditions was also devised for the measurement of thermal conductivity: Ciccotti and Tenenbaum (1980) simulated a Lennard-Jones fluid in a large box with two opposing walls acting as thermal reservoirs. As an atom collides with the wall, it is reflected from the wall with a new velocity that is randomly chosen from an equilibrium velocity distribution corresponding to the temperature of the reservoir. The opposite wall acts in the same way but has a different temperature and thus a temperature gradient is created by the opposing walls.

To implement an analogous method for the diffusion of particles (atoms or molecules), a gradient in concentration or chemical potential has to be set up in the system. In analogy

with the temperature gradient method, this can be achieved by opposite walls of the supercell acting as particle reservoirs at constant chemical potential. In the dual control volume grand canonical molecular dynamics method (DCV-GCMD), Heffelfinger and Swol (1994) implemented small volume slices at opposite walls that act as particle reservoirs at constant chemical potential. However, this method is cumbersome and computationally very demanding as even larger systems need to be set up to obtain appreciable control volumes and a large enough region between the two control volumes. A different method is gradient relaxation molecular dynamics (GRMD), presented by Maginn *et al.* (1993) for calculating the diffusivity of methane inside a porous silica framework. Two separate systems at different concentrations are equilibrated by regular equilibrium MD and are subsequently brought into contact by joining both systems to form a super-system. A discontinuous concentration jump is present at the interface between the two subsystems, and by continuing regular molecular dynamics, this gradient is then relaxed. In keeping with the other early NEMD methods, this method mimics an experiment (for example, an uptake rate measurement) as closely as possible.

Imposing nonequilibrium boundary conditions has severe disadvantages: the different boundary conditions break the periodicity of the system and periodic boundary conditions cannot be applied; the system is inhomogeneous. The results are therefore strongly size-dependent. To ensure that the local equilibrium postulate is valid, the gradient needs to be relatively small, which necessitates systems that are much larger than for regular equilibrium MD.

A significant advance in NEMD techniques was the development of homogeneous algorithms, termed synthetic NEMD. Explicit gradients in the system are replaced by an external field that imitates the effect of the gradient. Homogeneous algorithms were developed for shear viscosity (Evans, 1979), thermal conductivity (Evans, 1982), and for self-diffusion (Evans *et al.*, 1983). These developments are summarised by Evans and Morriss (1984, 2008). Synthetic NEMD methods do not recreate experimental conditions (such as gradients in temperature or shear stress) in simulations explicitly, but rather introduce an external field, $\mathbf{F}_e$, that mimics the effect of a real gradient by introducing

it into the equations of motion for all particles. The method is therefore homogeneous because the external field acts on all particles in the system and so fully periodic boundary conditions can be applied as in equilibrium MD. The system needs to be no larger than for a similar study using equilibrium MD methods. The effect of the external field is described by linear response theory and is thus exact. The action of the field on the system is designed so as to obtain the desired response. In the case of mass diffusion, the effect of the concentration gradient is simulated directly by allowing the external field to exert a force on the diffusing particles that is proportional to $c_i\mathbf{F}_e$, where c_i is called the colour charge of particle i and can be chosen at will. The action of the field is analogous to the action of an electric field on an electric charge; the term "colour charge" is used rather than electric charge to stress the fact that both the external field and the colour charges are entirely fictitious. In the absence of an external field, the colour charges have no influence on the interactions between particles and the system behaves according to equilibrium dynamics. A nonzero external field will induce a response of the system, and this response is described in the framework of isothermal response theory (Morriss and Evans, 1985); thus the theory is exact.

NEMD studies in the past have mostly focussed on liquids or gases since transport phenomena are of interest predominantly in the fields of chemical engineering and fluid dynamics. Comparatively simple models have been used to model the interactions between particles of the fluid, such as the Lennard-Jones potential which bears resemblance to liquid argon. Here we propose to apply the colour diffusion algorithm for the first time to a solid modelled by a full *ab initio* interaction potential.

6.2.1 Linear response theory

In this section, the derivation of the linear response to an artificial external field is briefly presented according to Morriss and Evans (1985). The external perturbation is defined as an external field, $\mathbf{F}_e(t)$, with which the particles of the system interact. The field considered here is constant in space but can, in general, vary with time. The interaction of the particles with the field is defined by a set of coupling coefficients, so the equations

of motion that govern the dynamics of a nonequilibrium system under the influence of an external field are the following:

$$\dot{\mathbf{q}}_i = \frac{\mathbf{p}_i}{m_i} + \mathsf{C}_i \mathbf{F}_e(t) \tag{6.24}$$

$$\dot{\mathbf{p}}_i = \mathbf{F}_i + \mathsf{D}_i \mathbf{F}_e(t) \tag{6.25}$$

Equations (6.24) and (6.25) do not include any thermostat, but since heating is quadratic to the external field, the linear response is not influenced by this effect. The matrices C_i and D_i determine how the system interacts with the external field. This set of equations cannot, in general, be derived from any Hamiltonian. The external field produces heat by performing work on the system. The total energy content of the system is the sum of potential and kinetic energy:

$$H_0 = \sum_{i=1}^{N} \frac{\mathbf{p}_i^2}{2m_i} + E(\{\mathbf{q}\}) \tag{6.26}$$

If the external field is zero and in the absence of any thermostat, this is a constant of the motion (Newtonian dynamics); however, with a nonzero field, the internal energy increases at a rate that can be calculated by taking the time derivative of H_0, using the equations of motion above to obtain:

$$\dot{H}_0 = \sum_{i=1}^{N} \left[\frac{\mathsf{D}_i \mathbf{p}_i}{m_i} - \mathsf{C}_i \mathbf{F}_i \right] \cdot \mathbf{F}_e(t) \equiv -\mathbf{J}(\mathbf{\Gamma}) \cdot \mathbf{F}_e(t) \tag{6.27}$$

This equation defines the *dissipative flux*, $\mathbf{J}(\mathbf{\Gamma})$:

$$\mathbf{J}(\mathbf{\Gamma}) \equiv \sum_{i=1}^{N} \left(-\frac{\mathsf{D}_i \mathbf{p}_i}{m_i} + \mathsf{C}_i \mathbf{F}_i \right) \tag{6.28}$$

We now consider the response of an arbitrary phase variable, $B(\mathbf{\Gamma})$, to the perturbation by $\mathbf{F}_e(t)$. As has been discussed in Section 2.4, a phase variable can be calculated from a

distribution function f (not necessarily an equilibrium distribution) as:

$$\langle B(t)\rangle = \int \mathrm{d}\mathbf{\Gamma}\, B(\mathbf{\Gamma}) f(\mathbf{\Gamma}, t) \tag{6.29}$$

The response of $B(\mathbf{\Gamma})$ can be determined if the distribution function in the nonequilibrium situation is known. To derive an expression for f, we return to the most general law of the distribution, the Liouville equation. The distribution function evolves in time according to the Liouville equation:

$$\frac{\partial}{\partial t} f(\mathbf{\Gamma}, t) = -i\mathcal{L} f(\mathbf{\Gamma}, t) \tag{6.30}$$

The distribution function is then decomposed into an equilibrium part (of any ensemble) and a nonequilibrium part.

$$\frac{\partial}{\partial t} \left(f_0(\mathbf{\Gamma}) + \Delta f(\mathbf{\Gamma}, t)\right) = -\left(i\mathcal{L}_0 + i\Delta\mathcal{L}(t)\right)\left(f_0(\mathbf{\Gamma}) + \Delta f(\mathbf{\Gamma}, t)\right) \tag{6.31}$$

We assume that at time $t = 0$, the external field is zero and the system is in the equilibrium distribution f_0, which may be from the canonical or isokinetic ensemble. The equilibrium Liouville operator $i\mathcal{L}_0$, when acting on f_0, does not change the latter; the propagator preserves the equilibrium distribution and the term $i\mathcal{L}_0 f_0$ is eliminated along with the time derivative of f_0 from the left-hand side. The cross-term $i\Delta\mathcal{L}(t)\Delta f(\mathbf{\Gamma}, t)$ is of second order in the perturbation, and is here ignored; we only consider the *linear* behaviour of the system. We are left with:

$$\frac{\partial}{\partial t}\Delta f(\mathbf{\Gamma}, t) + i\mathcal{L}_0 \Delta f(\mathbf{\Gamma}, t) = -i\Delta\mathcal{L}(t) f_0(\mathbf{\Gamma}) \tag{6.32}$$

This is a first-order non-homogeneous differential equation for Δf, whose formal solution is:

$$\Delta f(\mathbf{\Gamma}, t) = -\int_0^t \mathrm{d}s\, e^{-i\mathcal{L}_0(t-s)} i\Delta\mathcal{L}(s) f_0(\mathbf{\Gamma}) \tag{6.33}$$

The function $i\Delta\mathcal{L}(s)f_0(\mathbf{\Gamma})$ can be related to the dissipative flux; to derive it, we must explicitly assume an ensemble. If we take the canonical ensemble:

$$f_0(\mathbf{\Gamma}) \to f_{NVT}(\mathbf{\Gamma}) = \frac{e^{-\frac{H_0(\mathbf{\Gamma})}{k_B T}}}{Q(N,V,T)} \tag{6.34}$$

then the Liouville operator, Equation (2.188), applied to f_{NVT} gives:

$$i\mathcal{L}f_{NVT}(\mathbf{\Gamma}) = \dot{\mathbf{\Gamma}} \cdot \frac{\partial}{\partial \mathbf{\Gamma}} f_{NVT}(\mathbf{\Gamma}) = -\frac{\dot{H}_0}{k_B T} f_{NVT}(\mathbf{\Gamma}) = \frac{\mathbf{J}(\mathbf{\Gamma}) \cdot \mathbf{F}_e(t)}{k_B T} f_{NVT}(\mathbf{\Gamma}) \tag{6.35}$$

Combining Equations (6.35) and (6.33), an expression for the nonequilibrium distribution function is obtained, with the boundary condition $f(\mathbf{\Gamma}, 0) = f_{NVT}(\mathbf{\Gamma})$. The response is, therefore, according to Equation (6.27):

$$\langle B(t) \rangle = \langle B(0) \rangle_{NVT} + \frac{1}{k_B T} \int_0^t \mathrm{d}s\, \mathbf{F}_e(s) \cdot \left(\int \mathrm{d}\mathbf{\Gamma}\, B(\mathbf{\Gamma}, t-s)\, \mathbf{J}(\mathbf{\Gamma}, 0)\, f_{NVT}(\mathbf{\Gamma}) \right) \tag{6.36}$$

It should be noted that the left-hand side is an ensemble average over the nonequilibrium system at time t if the system was in a canonical distribution at time $t = 0$, whereas the ensemble average on the right-hand side is over an equilibrium ensemble without external field (here the canonical ensemble):

$$\langle B(t) \rangle = \langle B(0) \rangle_{NVT} + \frac{1}{k_B T} \int_0^t \mathrm{d}s\, \langle B(t-s)\, \mathbf{J}(0) \rangle_{NVT} \cdot \mathbf{F}_e(s) \tag{6.37}$$

This defines the response of phase variable B to a perturbation that is described by an external field and its dissipative flux.

6.3 The colour-field algorithm for diffusion in solids

From this general result, Evans *et al.* (1983) devised an algorithm called the colour field algorithm that links the response of the system to the self-diffusion coefficient. In the original work, the algorithm was applied to an isotropic liquid, and it has been applied to the diffusion of methane molecules inside a porous silica framework (Maginn *et al.*, 1993).

Here the algorithm is applied to the highly mobile lithium ions in the superionic conductor $LiBH_4$ at 535 K, under the assumption that the lithium atoms behave in an analogous way to the particles of a fluid inside the rigid and passive framework of the BH_4^- anions. This assumption is based on the experimental result that translational diffusion of BH_4 units in solid $LiBH_4$ is found to be at least two orders of magnitude slower than for the lithium atoms (Martelli *et al.*, 2010). Here the colour diffusion algorithm is implemented in the framework of *ab initio* MD rather than a simple analytical force field to take into account the fully correlated potential energy surface calculated by density functional theory for maximum accuracy. The external field $\mathbf{F}_e$ is chosen to interact solely with the lithium atoms and to have no effect on the motion of the other atoms in the system. The effect is analogous to the interaction with an electric field: the field interacts with the charge to exert a force on a particle. We assign colour charges of $c_i = \pm 1.0$ to lithium atoms, with half of the atoms assigned a positive charge and the other half of the lithium atoms assigned a negative charge, and $c_i = 0$ to all other atoms. The response that is considered is the colour flux, analogous to an electric current density. The linear response according to Equation (6.37) derived above is explicitly developed in the following paragraphs and the link to the self-diffusion coefficient of the lithium atoms in solid $LiBH_4$ established.

The coupling parameters C_i and D_i that define the interaction of the external field with the system are defined as follows:

$$\mathsf{C}_i \to 0 \tag{6.38}$$

$$\mathsf{D}_i \to c_i \tag{6.39}$$

The colour charges c_i are zero for all atoms in the system except for lithium atoms, for which $c_i = 1$ for half of them and $c_i = -1$ for the other half. The dissipative flux is thus given by:

$$\mathbf{J}(\mathbf{\Gamma}) = -\sum_{i=1}^{N} c_i \frac{\mathbf{p}_i}{m_i} \tag{6.40}$$

The response that we consider is the colour flux J_c in the direction of the external field and

so is a scalar quantity; analogous to the electric current density, this quantity is defined as the amount of colour charge flowing through an area perpendicular to the external field direction:

$$J_c(t) = \frac{1}{V} \sum_{i=1}^{N} c_i v_i(t) \tag{6.41}$$

where $v_i(t) = \mathbf{v}_i(t) \cdot \mathbf{F}_e \left|\mathbf{F}_e\right|^{-1}$ is the component of the velocity of atom i collinear with $\mathbf{F}_e$. It is clear that the equilibrium average of this quantity is zero because of total momentum conservation. With these definitions, Equation (6.37) is written:

$$\langle J_c(t) \rangle = \frac{V}{k_B T} \int_0^t \mathrm{d}s \, \langle J_c(t-s) \, J_c(0) \rangle_{NVT} \, F_e \tag{6.42}$$

It is important to note that the canonical average on the right-hand side of this equation, denoted $\langle \ldots \rangle_{NVT}$, is calculated from field-free dynamics. The autocorrelation of the colour flux is now written in terms of the velocities using Equation (6.41):

$$\langle J_c(t-s) \cdot J_c(0) \rangle_{NVT} = \frac{1}{V^2} \sum_{i=1}^{N} \sum_{j=1}^{N} c_i c_j \, \langle v_i(t-s) \, v_j(0) \rangle_{NVT} \tag{6.43}$$

In the thermodynamic limit, the cross-correlation terms cancel out and we are left with:

$$\langle J_c(t-s) \, J_c(0) \rangle_{NVT} = \frac{1}{V^2} \sum_{i=1}^{N} c_i^2 \, \langle v_i(t-s) \, v_i(0) \rangle_{NVT} \tag{6.44}$$

Inserting this back into Equation (6.42), we find:

$$\langle J_c(t) \rangle = \frac{1}{k_B T V} \sum_{i=1}^{N} c_i^2 \int_0^t \mathrm{d}s \, \langle v_i(t-s) \, v_i(0) \rangle_{NVT} \, F_e \tag{6.45}$$

This equation relates the average response at time t induced by a nonzero field to the integral of the velocity autocorrelation function in equilibrium. Since $c_i^2 = 1$ for all particles of interest, the sum is equal to the total number N_c of charged particles:

$$\sum_{i=1}^{N} c_i^2 \int_0^t \mathrm{d}s \, \langle v_i(t-s) \, v_i(0) \rangle_{NVT} = N_c \int_0^t \mathrm{d}s \, \langle v(t-s) \, v(0) \rangle_{NVT} \tag{6.46}$$

Because the canonical averages in this equation are calculated from field-free (equilibrium) dynamics, the velocity autocorrelation function can be replaced by the Green-Kubo expression for the diffusion coefficient, Equation (6.19), by letting the simulation time t go to infinity; $d = 1$ since all vector quantities are projected into one dimension. Thus:

$$D = \frac{k_B T}{\rho_c} \lim_{t\to\infty} \lim_{F_e\to 0} \frac{\langle J_c(t)\rangle}{F_e} \tag{6.47}$$

where $\rho_c = N_c/V$. $J_c(t)$ is the colour flux measured at a time t of one system which was in thermodynamic equilibrium at time $t = 0$. The ensemble average is the average of a large number of such simulations each after a time t, starting from all possible configurations in the equilibrium distribution. In the long-time limit, the colour flux diverges unless the system is in a steady-state, which can only be achieved by applying a thermostat to extract the heat dissipated by the external field. The above relation is still valid if a thermostat is applied to the molecular dynamics; this was first proved by Morriss and Evans (1985).

6.3.1 Implementation of the algorithm

The equations of motion used in equilibrium MD simulations must be modified to perform NEMD with a constant colour field. The thermostat used for all NEMD simulations is the Gaussian isokinetic thermostat, and so the equations of motion for $LiBH_4$ are:

$$\dot{\mathbf{q}}_i = \frac{\mathbf{p}_i}{m_i} \tag{6.48}$$

$$\dot{\mathbf{p}}_i = \begin{cases} \mathbf{F}_i + \alpha\mathbf{p}_i + \mathbf{F}_c & \forall i \in \{\mathrm{B,\ H}\} \\ \mathbf{F}_i + c_i\mathbf{F}_e & \forall i \in \{\mathrm{Li}\} \end{cases} \tag{6.49}$$

where α couples the system to the Gaussian thermostat and $\mathbf{F}_e$ is a constraint force:

$$\alpha = -\frac{\sum_{i\in\{\mathrm{B,\ H}\}} \frac{\mathbf{p}_i\cdot(\mathbf{F}_i+\mathbf{F}_c)}{m_i}}{\sum_{i\in\{\mathrm{B,\ H}\}} \frac{\mathbf{p}_i^2}{m_i}} \tag{6.50}$$

$$\mathbf{F}_c = -\frac{1}{N_{\mathrm{B,\ H}}} \sum_{i\in\{\mathrm{B,\ H}\}} \mathbf{F}_i \tag{6.51}$$

The main difference from equilibrium MD is that the lithium atoms are excluded from the thermostat. The constraint force $\mathbf{F}_c$ keeps the centre of mass of the atoms subjected to the thermostat fixed in space and notably counteracts any forces exerted on the borohydrides by the moving lithium atoms (which are completely unconstrained), as well as any numerical drift. This is a necessary condition for the Gaussian isokinetic thermostat (see Section 2.5.5).

The reason for excluding the lithium atoms from the thermostat is that all thermodynamic quantities have to be calculated from Galilean invariants, that is quantities that are identical in a moving as well as a resting reference frame. Therefore only the *peculiar* velocities of all atoms must be included in the definition of the kinetic temperature. The external field in the isothermal colour diffusion algorithm induces a streaming velocity of the colour charged species: the centre of mass of all atoms of the species is not fixed but moves in the direction of the external field. Thermostat algorithms remove kinetic energy isotropically whereas the external field injects kinetic energy in one Cartesian direction specifically, and so equipartition between all three degrees of freedom of each particle is no longer given, and the total kinetic energy would accumulate in the degree of freedom parallel to the external field. To cope with this problem, one possibility would be to only thermostat the degrees of freedom perpendicular to the external field (Evans *et al.*, 1983), another is to subtract the streaming velocity of the species and thermostat only the peculiar velocities. The latter approach requires the computation of the streaming velocity, which is difficult to achieve accurately in a small system. For this reason, we choose not to thermostat the mobile species (lithium atoms) at all. The Gaussian thermostat is therefore only coupled to the boron and hydrogen atoms, which do not interact with the external field, and the lithium atoms move freely without any thermostat coupling. The temperature of the lithium atoms is indirectly controlled by heat exchange through collisions with the boron and hydrogen atoms. As the temperature has no effect on the linear response, this simple scheme will produce exactly the same results as the system with all atoms coupled to the thermostat. Figure 6.2 shows the evolution of the temperature of lattice atoms and mobile atoms over the course of a simulation according to the equations

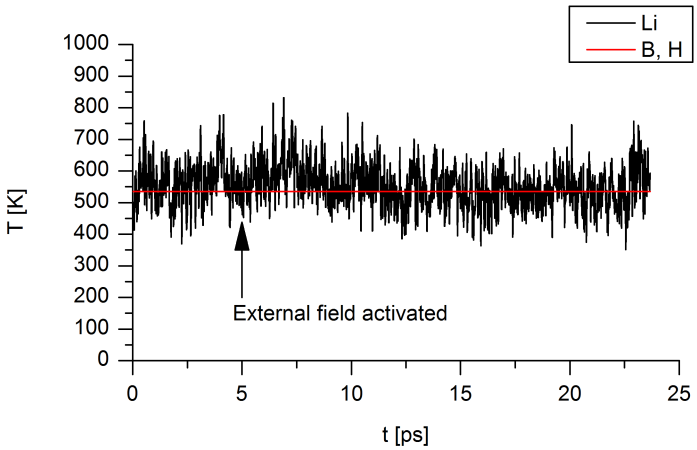

Figure 6.2: The instantaneous kinetic temperatures of the mobile lithium atoms (black) and of the immobile BH_4 units (red) from an NEMD simulation of $LiBH_4$ at 535 K where the external field was switched on after 5 ps.

of motion, Equations (6.48)–(6.51), where the external field $\mathbf{F}_e$ is switched on at time $t = 5\,\text{ps}$. The temperature difference increases quadratically with the field strength, and so provides a measure of nonlinearity.

$$\Delta T_{\text{Li-B}} \propto |\mathbf{F}_e|^2 \tag{6.52}$$

As can be seen from Figure 6.2, the temperature fluctuates around the thermostat temperature.

These modifications were implemented in the CP2K code, which is freely available under the GNU public license and can therefore be modified at will. The force calculations were computed by DFT, exactly in the same way as in the MD calculations of $LiBH_4$ presented in Chapter 5. It is worth noting, though, that the underlying MD implementation does not play a role for the NEMD algorithm to work and it may be implemented into any existing computational package performing MD simulations of solids. Modifications required involve the thermostat algorithm (to exclude the mobile ions) and the addition of the colour force, but—importantly—the integrator scheme can be left unchanged.

In practice, the steady-state average colour flux is calculated from one NEMD run as

the time average of the steady-state colour flux:

$$\langle J_c \rangle = \lim_{t\to\infty} \langle J_c(t) \rangle = \lim_{t_s\to\infty} \frac{1}{t_s} \int_0^{t_s} \mathrm{d}t\, J_c(t) \tag{6.53}$$

By equation (6.41) this leads to:

$$\langle J_c \rangle = \lim_{t_s\to\infty} \frac{1}{t_s V} \sum_{i=1}^{N} c_i \left(\mathbf{r}_i(t_s) - \mathbf{r}_i(0) \right) \tag{6.54}$$

The average can then be estimated from a linear fit to a plot of $\frac{1}{V} \sum_{i=1}^{N} c_i \left(\mathbf{r}_i(t_s) - \mathbf{r}_i(0) \right)$ against time t. The slope of this plot corresponds to the average calculated according to Equation (6.54).

Finally, it is interesting to note the correspondence of the colour flux with an electric current density. The electric current density is given by:

$$\mathbf{J} = \sigma \mathbf{E} \tag{6.55}$$

where $\mathbf{E}$ is the applied electric field, measured in $\mathrm{V\,cm^{-1}}$. The value of the conductivity is thus given by the division of a current density by the applied electric field:

$$\sigma = \frac{J}{E} \tag{6.56}$$

In ionic conductors, where the mobile ions are the only charge carriers for electric currents, the conductivity and the diffusion coefficient of the mobile ions are related by the generalised Nernst-Einstein equation:

$$\sigma = \frac{(Ze)^2 \rho_c}{k_B T} D = (Ze)^2 \lim_{F_e\to 0} \frac{\langle J_c \rangle}{F_e} \tag{6.57}$$

The first equality is the Nernst-Einstein equation, the second equality is obtained by inserting Equation (6.47) for the diffusion coefficient. The ionic conductivity is therefore proportional to the ratio of colour flux and colour field, similar as in Equation (6.56).

The units of colour conductivity are converted into electrical conductivity as follows. With the flux (current density) given in $\mathrm{A\,cm^{-2}}$ and the electric field given in $\mathrm{V\,cm^{-1}}$, the resulting unit for the conductivity is $\mathrm{S\,cm^{-1}}$.

$$[\sigma] = \frac{\mathrm{S}}{\mathrm{cm}} = \frac{\mathrm{C}^2}{\mathrm{J\ s\ cm}} \tag{6.58}$$

In our simulation units, the unit of colour flux by colour field is:

$$\left[\frac{J_c}{F_e}\right] = \frac{1}{\mathrm{eV\ ps\ \AA}} \tag{6.59}$$

Because the colour charges of all charged particles are ± 1 without unit, the ratio of colour flux and field needs to be multiplied by $(Ze)^2$, which for lithium ions is e^2 with e the elementary charge in Coulomb. The conversion factor between simulation and physical units is thus:

$$1\frac{1}{\mathrm{eV\ ps\ \AA}} \longrightarrow 16.02176565\frac{\mathrm{S}}{\mathrm{cm}} \tag{6.60}$$

As the measured conductivity of $LiBH_4$ at 535 K is about $0.1\,\mathrm{S\,cm^{-1}}$, we expect to obtain a colour conductivity of the order of $6{\times}10^{-3}\,(\mathrm{eV\ ps\ \AA})^{-1}$.

It is again emphasised that the term *colour* charge is used to make a clear distinction with the electric charge, despite the parallel with ionic conductivity just outlined. Even though we are mimicking ionic conduction through a solid, we refrain from calling the field an electric field since that would imply an effect on the electronic structure of the solid and complicate the DFT treatment.

6.4 Results for $LiBH_4$

The colour diffusion algorithm described in the previous section was applied to pure (defect-free) $LiBH_4$ at 535 K to determine the diffusion constant and the diffusion mechanism. Since $LiBH_4$ is a hexagonal crystal, a different diffusion constant is expected according to the direction in which the field is applied. Two series of NEMD calculations

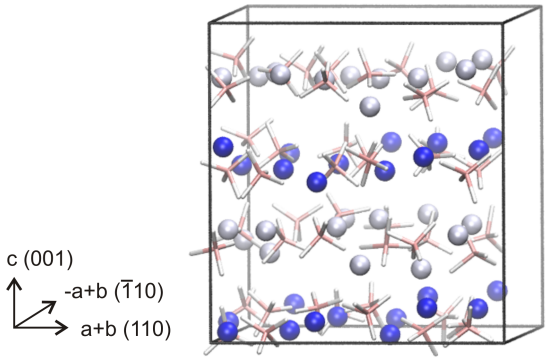

Figure 6.3: Configuration of the system used in these simulations. Light spheres: lithium atoms with colour charge +1, dark spheres: lithium atoms with colour charge −1.

were performed: one with the field in the (110) direction (in the hexagonal plane), and one with the field in the (001) direction (perpendicular to the hexagonal plane).

6.4.1 Computational details

A supercell of 288 atoms (48 formula units) was used; the orthorhombic simulation box had dimensions 12.9685 Å × 14.9747 Å × 14.0736 Å and a volume of 2733.08 Å^3. The lithium atoms were assigned a colour charge of ±1, half the atoms were given +1, the other half −1, all other atoms carried zero colour charge. The overall colour charge of the system was zero.

Calculations were carried out using exactly the same computational parameters as for equilibrium MD of $LiBH_4$ (Chapter 5). Although some success might be achieved by parametrising the force field, thus substantially decreasing the computational cost, the development itself of such a force field including testing and benchmarking is very time-consuming, its guaranteed applicability is limited only to the reference system, and the accuracy is decreased. For this reason, we rely on *ab initio* methods (DFT) as a generally applicable method of force calculation for any system. The system was equilibrated at zero external field with the Gaussian isokinetic thermostat for 10 ps. Figure 6.3 shows the configuration of the system after this equilibration period. All NEMD computations were started from the same configuration.

Since *ab initio* molecular dynamics calculations are computationally very demanding,

it is worth estimating the behaviour of the expected error. In order to use Equation (6.54) to compute an average value for the flux, the simulation needs to be run for a certain amount of time t_s, which is limited by the computing resources available. The error in the average flux is directly proportional to the error in the displacement of the mobile ions, which in the linear regime is proportional to the square root of time:

$$\sigma(\Delta x) \propto \sqrt{t_s} \tag{6.61}$$

Conversely, the absolute displacement is proportional to the product of field strength and simulation time.

$$\Delta x \propto F_e t_s \tag{6.62}$$

We aim for a constant relative error of the average flux:

$$\frac{\sigma(\Delta x)}{\Delta x} \propto \frac{\sqrt{t_s}}{F_e t_s} = \text{constant} \tag{6.63}$$

To keep a constant uncertainty in the response, the simulation time as a function of field strength therefore varies as:

$$t_s \propto \frac{1}{F_e^2} \tag{6.64}$$

If the field is reduced by a factor of two, the simulated time should be increased by a factor of four to get the same relative error of the average flux.

6.4.2 Linearity of the response

Figure 6.4 summarises the calculations that were performed at different directions and strengths of the external field. This series of calculations served to identify the linear response domain of the system. In the linear regime the value of the conductivity is expected to remain constant with increasing field strength. It should be noted, though, that the average response values were computed from rather short NEMD trajectories, and so the error margin is expected to be large.

Nevertheless, it is obvious that the response is not linear at field strengths above

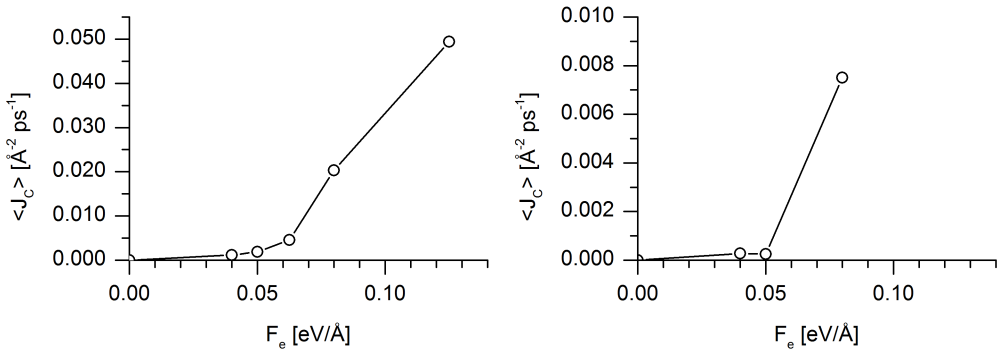

Figure 6.4: The response of the system to the colour field in the (110) direction (left) and in the (001) direction (right) against varying strengths of the external field.

$6.0{\times}10^{-2}\,\mathrm{eV/Å}$. Inspection of the trajectory showed in fact that the force exerted by the external field on the lithium atoms was so strong that they were moving in free flight through the lattice. The regular site-hopping mechanism was not followed. This behaviour is unphysical as it is fundamentally different from the mechanism at zero field, thus the response is not expected to be linear. All results obtained with fields larger than $6.0{\times}10^{-2}\,\mathrm{eV/Å}$ include nonlinear effects, whose treatment is not within the scope or goals of this work.

A field strength of $F_e = 5.0 \times 10^{-2}\,\mathrm{eV/Å}$ is chosen to be the highest external field for which a linear response can be assumed. As the response of the system is weak, a long NEMD run at this field strength was performed and a more precise result for the diffusion coefficient obtained.

6.4.3 Calculation of the diffusion coefficient

Figure 6.5 shows the integrated dissipative flux over time as well as a linear fit according to Equation (6.54). The integrated energy dissipation is, according to Equation (6.27):

$$H_0(t) - H_0(0) = \int_0^t J_c(t) V F_e = F_e \sum_{i=1}^{N} c_i \Delta r_i(t) \tag{6.65}$$

Plotting the integrated energy dissipation against time shows two things. First, similar to the Sutherland-Einstein equation, diffusion is shown by the displacement of atoms versus time; in the present case it is not the mean *squared* displacement, but the total linear

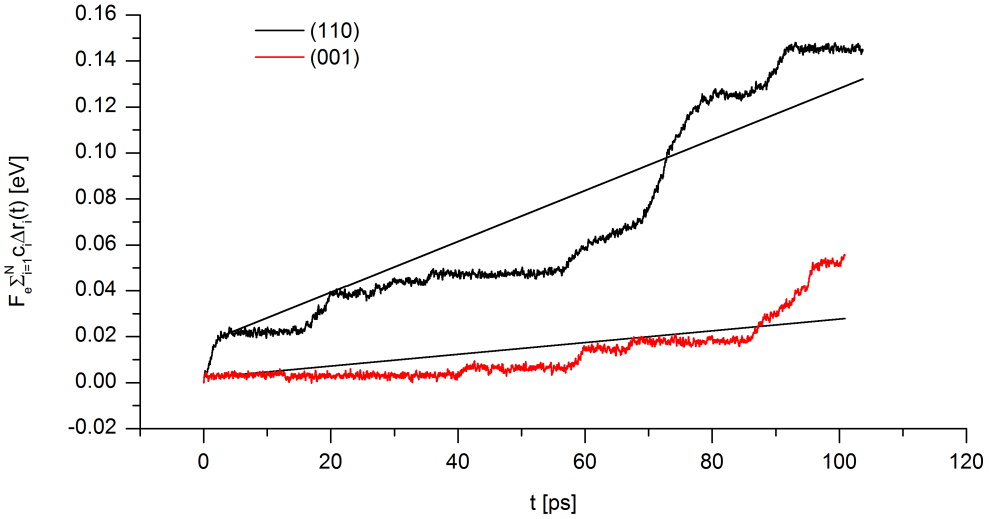

Figure 6.5: The integrated dissipative flux of a long NEMD run with an external field strength of 5.0×10^{-2} eV/Å. The average response is determined from the slope of a linear fit without intercept to the steady state (after $t = 3.5$ ps) .

Table 6.1: Ionic conductivity and lithium self-diffusion coefficient at 535 K determined from the colour flux of one long trajectory for each direction of the external field. Experimental values are according to Matsuo *et al.* (2007).

F_e direction	(110)	(001)	Exp.
t_s [ps]	100.0	100.0	
σ [S/cm]	0.355	0.082	0.139
D [cm^2/s]	5.82×10^{-6}	1.34×10^{-6}	2.28×10^{-6}

displacement. This displacement evolves as a series of discrete jumps separated by time intervals with no increase, characteristic for diffusion *via* site jumps. Second, it is clear from Equation (6.54) that the slope of the energy dissipation is equal to $VF_e \langle J_c \rangle$. A straight line without intercept was fitted to the data, ignoring the first 3.5 ps to allow for establishment of the steady state, to determine $\langle J_c \rangle$. Ionic conductivity and lithium diffusion coefficients are determined by Equations (6.47) and (6.57) and are summarised in Table 6.1.

The conductivity value in the (110) direction is, as expected, much larger than in the (001) direction. In the (110) direction ions are moving in the hexagonal plane, whereas in the (001) direction hexagonal planes must be crossed. The experimental value of the conductivity to compare with at 535 K is 0.14 S cm^{-1} for a powder sample (Matsuo *et al.*, 2007). This value lies between the computed values for the two directions, showing

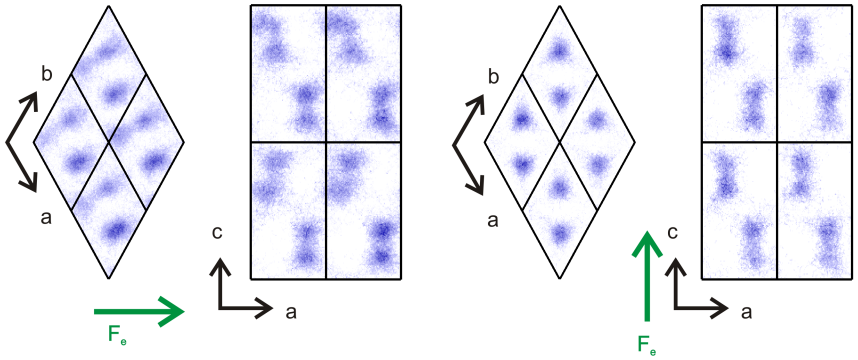

Figure 6.6: The average lithium atom densities viewed along the *c*- and *b*-axes from the long NEMD run with the field in the (110) direction (two images on the left) and in the (001) direction (two images on the right).

excellent agreement.

The error of the linear response is estimated to be less than 10%, as an increase of the field by only 20% results in a consistently higher response (Figure 6.4). Taking into account that subsequently the simulation time was increased fivefold, and since the relative error of a linear response decreases proportionally to the square root of simulation time, we estimate the error of this method to be 10%. However, this does not take into account other systematic errors stemming from the MD method itself.

6.4.4 Diffusion mechanism

The NEMD trajectory of a run in the linear regime, at a field strength of $5.0\times10^{-2}\,\mathrm{eV/Å}$, is analysed to elucidate the site-hopping mechanism of the lithium ions. The first analysis is of the sites in the crystal where the lithium atoms spend most of their time. To this end, a plot of the average lithium atom densities over the entire steady-state is drawn in Figure 6.6. The original simulation cell was projected into a smaller array of $2 \times 2 \times 2$ hexagonal cells for more convenient visualisation. As expected, most of the lithium density is centred on the crystallographic lattice sites, but with a slight displacement in the positive or negative (110)-direction due to polarisation by the colour field. Some lithium density is clearly present in the empty hexagonal vacancies situated at $(0, 0, 0)$ in the primitive cell. This suggests, as has previously been discussed by Ikeshoji *et al.* (2011), that lithium

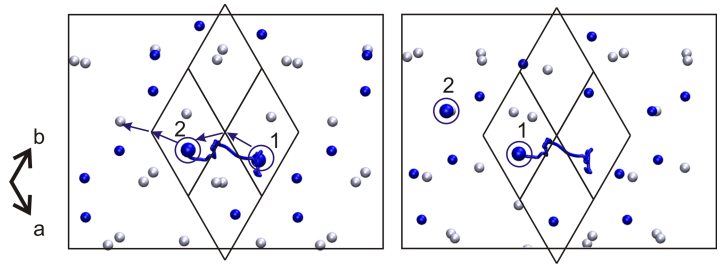

Figure 6.7: The mechanism of one hopping event, viewed along the *c*-axis; the pathway of atom 1 is traced by a blue line. Atom 1 first jumps into an interstitial site. As atom 2 jumps into an interstitial site, atom 1 jumps into the lattice site vacated by atom 2.

atoms occupy these sites as they diffuse through the solid. Thus we can identify the same metastable state for the lithium atoms as Ikeshoji *et al.* (2011). By contrast, in the case of the field along the (001) direction, the polarisation of the equilibrium lattice sites is along the (001)-axis as expected, but any density in the hexagonal vacancies is absent.

Following the trajectory of a single lithium atom as it diffuses, we gain insight into the diffusion pathway (Figure 6.7). It is found that the lithium atoms invariably move from their lattice site into an interstitial site, and from there to a neighbouring empty lattice site.

6.5 Conclusion

In this chapter, the colour field NEMD method was applied for simulating ionic diffusion in a solid superionic conductor. Nonequilibrium simulation methods have previously been mostly applied to study model liquids or plastic phases, because fluid dynamics have principally motivated the development of NEMD methods. This is the first time that this method has been applied to a crystalline solid and it is shown that the method works for highly mobile ions that are able to jump from site to site in a crystalline lattice.

Ion self-diffusion is accelerated by mimicking the effect of a concentration gradient through an artificial external field. Because the external field is spatially homogeneous the requirements for system size are comparable to equilibrium MD. In comparison to equilibrium MD-based methods, which manipulate the parameters of the simulation such as temperature or the mass of the atoms to accelerate the time scale of these rare events,

one additional parameter is introduced, the external field. This parameter is completely independent of temperature or the atomic masses, and the NEMD method can be applied at any temperature and quantitative data can be obtained. It is thus possible to study the temperature dependence of transport phenomena by NEMD, though this was not undertaken in this thesis. Through linear response theory, the effect of the external field can be linked to the Green-Kubo relationships that describe transport processes as equilibrium correlation functions, thereby establishing an exact link with the transport coefficient—provided the system is in the linear regime.

Results obtained for the diffusion coefficient are in agreement with experimental results, and are far better than other MD methods which typically obtain at best results in the same order of magnitude. Conductivities of $0.35\,\mathrm{S\,cm^{-1}}$ and $0.08\,\mathrm{S\,cm^{-1}}$ were obtained for diffusion in the (110) and (001) direction in the crystal, respectively. Conductivity is significantly higher in the hexagonal plane than for movement perpendicular to these planes. The experimentally measured conductivity to compare with is $0.139\,\mathrm{S\,cm^{-1}}$ at 535 K, measured by Matsuo *et al.* (2007), which lies between the values for the two principal directions. In an anisotropic environment like crystalline $LiBH_4$, the diffusion coefficient is dependent on the direction of diffusion. In practice this does not play a role unless single crystal or thin film samples are used, but in NEMD the diffusion direction can be chosen by applying the external field in a specific direction.

The method works on the premise that the system under the perturbation of the external field is in the linear regime. The main difficulty, as has been identified here, is that solid ion conductors—even such fast conductors as lithium borohydride at an elevated temperature of 535 K—still have comparatively large barriers for ion diffusion, in which case the linear regime becomes narrow. The effect of the external field is to reduce the time between events. In equilibrium (zero-field) the time between successive jumps means that jumps are uncorrelated and can be seen as a Markov chain (Hempelmann, 2000, chapter 4). In the linear regime, the external field reduces the time between successive jumps, but still leaves enough time for the events to be uncorrelated; nonlinear effects arise in part from the correlation of successive jumps.

The movement of lithium ions through a crystal has much in common with the problem of glassy systems. In both cases, it seems that "avalanches" of events occur at arbitrary intervals, and the interval has a high chance of being much larger than the observation time that we have available. Hence, one solution is to perform a large number of runs over a certain fixed simulation time t_s, and to look at the distribution of results (in this case, the displacement of atoms); this should be a Gaussian in the linear regime (Williams and Evans, 2006). However, due to the highly computationally intensive nature of *ab initio* molecular dynamics, it is not possible to undertake the required number of runs for this approach.

The main sources of error in evaluating the average steady-state colour flux according to Equation (6.54) are the nonlinearity of the response and sufficient run time to evaluate the average. These two are related: if the external field is too strong, nonlinear effects will start to become non-negligible and the linear response equation produces wrong results. On the other hand, with a stronger field more ion hopping events will occur for a given simulation time and the time-average of the response will have less uncertainty. Conversely, a weak external field ensures that the response is linear and the linear response expression for the diffusion coefficient will be more exact; however, a much longer run time is needed to gather a sufficient number of ion hopping events. The external field is therefore the parameter that tunes the frequency of the rare events. In contrast to methods where the event frequency is tuned by selective heating or mass scaling, the colour field algorithm is a controlled approximation that can be systematically improved by tuning the external field and the simulation run time.

Though the colour field algorithm is homogeneous and removes the awkward size effects of explicit gradient simulations, finite size effects still play an important role in the modelling of diffusion. Since conduction depends on lattice sites becoming available into which another lithium atom is then drawn, thereby starting a chain, the collective motion is important for the diffusion mechanism and a large enough system should be simulated to avoid correlation effects between nearest periodic images.

As the generated NEMD trajectories follow realistic dynamics, this represents a viable

approach for mechanism discovery in solid state diffusion. Unlike in metadynamics simulations or transition state theory treatments, no *a priori* knowledge of the diffusion mechanism is required and only one external parameter needs to be chosen. The mechanism of diffusion can be directly observed in the trajectory, and includes collective motion effects naturally. For $LiBH_4$ the same mechanism was observed as reported by Ikeshoji *et al.* (2011). Lithium atoms jump into an empty interstitial site and from there onto the nearest free lattice site. As this mechanism is expected to be significantly influenced or accelerated by the presence of Schottky defects, systems with artificially introduced Schottky defects should be studied; this could not be pursued in this work.

While the direction in which the induced ion jumps occur is certainly biased by the field, the details of the mechanism are not, for two reasons. One is that linear response theory predicts that, to linear order, all processes induced by an external perturbation map exactly onto their equilibrium counterpart; this is generally true for other types of responses induced by a perturbation such as heat flow or shear flow. A caveat applies to mass flow, because the opposing fluxes that occur in the colour-diffusion algorithm can lead to head-on collisions by particles which would not occur in equilibrium since colour is a fictitious property; however, the spurious events cancel out overall in such a way that Equation (6.47) relating the zero-field diffusion coefficient to the artificially induced colour-flux is exact. The second reason is that the probability of head-on collisions of oppositely colour-charged particles is proportional to the square of the overall hopping rate, which is proportional to the external field. As discussed above, hopping events remain relatively rare events in the linear regime and can be regarded as isolated events, such that the probability of a head-on collision tends towards zero. If ion jumps were so frequent that the positive and negatively charged ions were in motion at the same time most of the time, head-on collisions between oppositely charged particles could occur which do not occur in a real conductivity experiment and would represent an unrealistic trajectory event. Thus, in the weak field limit, the external field induces no spurious effects but only accelerates the same processes that are occurring in equilibrium (zero field) as well but less frequently; the external field in effect reduces the time between two successive events.

The computational cost is comparable to other accelerated MD schemes. Identification of the linear response domain requires a series of runs at varying field strengths; the results in this work can serve as a rough guideline for the choice of external field strengths to determine the linear response domain. Depending on the maximum acceptable external field, the run time required will incur a large cost to evaluate a precise average response. There is no difficulty applying this method with a different underlying molecular dynamics simulation method. For example, in some materials a classical force field has provided very good results for the description of the motion of atoms, and using tailored force fields for solids in combination with NEMD would substantially reduce the computational requirements and enable the study of a wide class of solid ion conductors by the NEMD method.

CHAPTER 7

Conclusions and outlook

"If you can't convince them, confuse them."

Harry S Truman, 33rd US president

Despite a decade of research into lightweight hydrogen storage systems, there has been no major new materials breakthrough. Indeed, the principal shortfall in almost all the systems that have been investigated is the issue of poor reversibility. Though many high-capacity storage materials are known with suitable thermodynamics, experimental reality shows that absorption/desorption reactions are governed by multiple pathways with kinetics that are extremely difficult to rationalise in an atomic model. A knowledge of the structures and properties of all the components of both the hydrogenated and dehydrogenated states of a hydrogen storage system is only the starting point in forming a microscopic understanding of decomposition reactions.

The theoretical and computational methods presented in Chapters 2 and 3 can offer detailed insight into the atomic structure and dynamics of the system under investigation that are inaccessible by direct experimental observation. However, all these computational models must be tested against reliable experimental evidence for their validity to be verified. This thesis has predominantly discussed aspects of atomic structure for which

computational methods are particularly well suited; in particular, in combination with experimental techniques, a complete picture of the structure and dynamics of $LiBH_4$ has emerged.

The properties of materials under difficult experimental conditions such as high pressure are particularly suited for computational study. In Chapter 4, the polymorphism of $Ca(BH_4)_2$ was investigated by means of density functional theory (DFT) computation. Based on an observed strong analogy between TiO_2 and $Ca(BH_4)_2$ at ambient pressure, the crystal structures of $Ca(BH_4)_2$ at high pressure were hypothesised to be analogous to the high-pressure phases of TiO_2 and three structures of $Ca(BH_4)_2$ were predicted that are similar to the baddeleyite, columbite and cotunnite structures of TiO_2. Thermodynamic stability was predicted from DFT calculations by computing the free energy at finite temperature on the basis of DFT energies and nuclear vibrational energies that are based on the harmonic approximation. The calculated pressure ranges for these predicted phases are lower than 10 GPa, except for the cotunnite structure which is not predicted to be structurally stable below 34 GPa. As already discussed by Filinchuk *et al.* (2008b), high-pressure polymorphism may be a method to destabilise hydrogen storage materials as the H-H interatomic distances between neighbouring BH_4 units are reduced. Decomposition and hydrogen release may be favoured by high-pressure structures. The challenge would be to be able to experimentally stabilise the high-pressure crystal structures under ambient conditions, for example by chemical substitution.

In Chapter 5, the crystal structure of $LiBH_4$ was comprehensively studied and the structural controversies associated with the high temperature superionic phase have been resolved. The transition from the low-temperature phase to the high-temperature phase is order-disorder in nature, but experiments and simulations heretofore have failed to provide a consistent picture of this disorder. Molecular dynamics (MD) studies of this material were therefore performed to develop a model of this structure that accommodates both experimental and theoretical findings. The MD technique is an extremely powerful technique for the study of dynamical disorder as the atomic motion is simulated directly by numerical integration of their equations of motion at any temperature and without any

symmetry constraints. From the MD results the pair distribution functions and vibrational spectra were calculated and compared with published experimental equivalents; the good agreement found shows that simulation by MD indeed takes into account the dynamical disorder properly. Once the general validity of the molecular dynamics model was established, it remained to form a crystallographic description of the observed disorder. This model was then used as the input to structural refinement of neutron powder diffraction data and the good fit validated this model. Equilibrium MD simulations in combination with neutron scattering of X-ray diffraction data is an effective symbiosis of methods for structural studies that should become standard; no other computational technique would have been able to obtain the level of detail of information as described in Chapter 5.

Chapter 6 took the aspect of simulating dynamical disorder a step further and developed a novel, robust methodology for the analysis of superionic conductivity in the high-temperature phase of $LiBH_4$ to complete the characterisation of all aspects of the atomic dynamics in this material. The MD technique should by design be suitable to simulate ionic diffusion. However, vibrational and diffusional time scales in $LiBH_4$ span several orders of magnitude and thus a new methodological development was necessary to enable the study of lithium diffusion that occurs microscopically on what is (currently) a computationally intractable time scale. The colour diffusion algorithm, a nonequilibrium molecular dynamics (NEMD) method introduced by Evans *et al.* (1983) for the study of fluids, was adapted and applied to the diffusion of lithium ions in a solid for the first time. It was shown that the method can be used to obtain quantitative results for self-diffusion coefficients that are substantially more accurate than previous MD approaches for studying diffusion. It was also demonstrated that diffusion pathways could be discovered directly by this NEMD technique, opening up a great potential for further studies with this method in a wide range of solid systems that contain diffusing species.

7.1 Future work

A few directions for research based on the findings and developments in Chapters 4–6, which have had to be left unexplored by this thesis for reasons of time constraints, shall now be listed.

The crystal structure prediction based on the analogy between isoelectronic metal oxides and borohydrides could be extended to $Mg(BH_4)_2$, another attractive candidate hydrogen storage material due to its high weight capacity and isoelectronic equivalent of SiO_2. Similar to $Ca(BH_4)_2$, structural transitions under compression of $Mg(BH_4)_2$ have been observed (George *et al.*, 2009b), but no crystal structures could be determined from the available experimental data. However, the very large unit cell of ambient-pressure $Mg(BH_4)_2$ polymorphs makes computational studies of this material considerably more computationally intensive than the presented study of $Ca(BH_4)_2$ (Voss *et al.*, 2009).

Molecular dynamics, and in particular the nonequilibrium molecular dynamics method presented in Chapter 6, in our view, offers the greatest potential for future research projects in materials modelling in general and for the modelling of energy materials in particular. Many experimental solid state investigation techniques produce data that can be directly modelled by equilibrium MD, as was shown in Chapter 5. Not only hydrogen storage materials, but especially fuel cell and battery components are determined by dynamical processes, and ionic diffusion in particular, and these processes are suitable for study by NEMD. The study presented in Chapter 6 is the first established evidence that atom mobility in solids can be effectively modelled by NEMD; this opens up a wide range of potential further studies across many areas of condensed matter science and is particularly applicable for energy materials research where energy flow is often a result of atomic diffusion.

One of the first future aspects of NEMD that should be explored is the performance of classical force fields instead of DFT force calculations. MD studies on ionic solids using parametrised force fields have been undertaken before, and because of the substantially reduced computational requirements for classical MD simulations, more computations can

be performed and longer time scales and slower processes probed. For example, Islam *et al.* (2005) studied the defect structure and lithium diffusion in $LiFePO_4$ by equilibrium MD using a parametrised potential that is based on the core-shell model for polarisable ions and includes a two-body interaction potential between ions of the Buckingham potential type, and a three-body bond angle potential. As NEMD is a technique that requires a large number of long runs for most studies, the substantial reduction in computational requirements would be worth the effort of developing a tailored force field for the study of a specific system. The disadvantage with parametrised force fields is their limited transferability, that is a force field developed for one compound might not be applicable for simulations of a different compound; furthermore, it is difficult to adequately parametrise subtle effects arising from electron correlation in certain systems. Nevertheless, the computational efficiency would allow further tests to be conducted. These include the influence of the system size on both the observed diffusion mechanism and the diffusion coefficient; the temperature dependence of diffusion kinetics; diffusion pathways in systems with vacancies. Unfortunately, these topics were outside the scope and time and resource limitations for this thesis. Before carrying out such series of tests, the performance of the parametrised NEMD simulations must be compared with a reference *ab initio* NEMD run. The *ab initio* NEMD results presented in this thesis could serve as a starting point and a benchmark to set up NEMD simulations with a parametrised force field for $LiBH_4$: results must be compared to both equilibrium MD results from Chapter 5 and NEMD results from Chapter 6. Since classical force field methods use a fraction of the computational cost of *ab initio* methods, a wide variety of systems and conditions could be explored in this way.

A second technical aspect of NEMD that is worth exploring is the thermostat algorithm. A partial Gaussian thermostat as presented here worked in the specific circumstances, but might not be the most appropriate algorithm in other systems, for example in the presence of multiple mobile species. Inclusion of the streaming velocity in the thermostat could be developed via smooth particle methods (see, for example, Hoover, 2006). Furthermore, since NEMD is not constrained to the use of the Gaussian isokinetic thermostat, the method might be extended for the widely used Nosé-Hoover thermostat. Changes

in the thermostat would almost certainly necessitate further modifications to an existing MD package as the velocity-Verlet algorithm—used in most current MD packages—is unsuitable for integrating general equations of motion. In NEMD, the Gear predictor-corrector scheme is usually used (Gear, 1971); description of the implementation of this versatile integrator for NEMD simulations is presented in detail by Evans and Morriss (1984).

The NEMD method can also be used to study other dynamic processes in solids; in particular, NEMD has the potential to be a very useful technique for mechanism discovery because NEMD produces realistic trajectories. Trajectories might be analysed for correlations in BH_4 rotations as lithium diffuses through the lattice under the action of the external field. Alternatively, simulations for mechanism discovery could be devised by defining external fields and appropriate corresponding colour charges. For example, an external field that induces molecular rotation of BH_4 units could be defined to study the effects of molecular rotation on the mobility of lithium ions. This would be an *ad hoc* study, as for most such schemes a meaningful linear response cannot necessarily be defined.

Finally, existing NEMD algorithms for fluid dynamics could be extended and applied to solid state systems. One relatively straightforward NEMD algorithm to implement would be the thermal conductivity algorithm (Evans, 1982). The thermal conductivity of a material is a significant property of almost every material in an engineering context; in hydrogen storage, for example, extraction of the heat generated in the hydrogenation reaction is an important engineering problem that must be solved for the practical implementation of any material in a hydrogen fuel-cell car.

Bibliography

Alder, BJ and Wainwright, TE. "Phase Transition for a Hard Sphere System." *Journal of Chemical Physics*, **27(5)**, 1957, page 1208.

Andersen, HC. "Molecular dynamics simulations at constant pressure and/or temperature." *Journal of Chemical Physics*, **72(4)**, 1980, page 2384.

Ashurst, WT and Hoover, WG. "Argon Shear Viscosity via a Lennard-Jones Potential with Equilibrium and Nonequilibrium Molecular Dynamics." *Physical Review Letters*, **31(4)**, 1973, pages 206–208.

Austin, BM; Zubarev, DY; and Lester Jr., WA. "Quantum Monte Carlo and related approaches." *Chemical Reviews*, **112(1)**, 2012, pages 263–88.

Baitalow, F. "Thermal decomposition of B-N-H compounds investigated by using combined thermoanalytical methods." *Thermochimica Acta*, **391(1-2)**, 2002, pages 159–168.

Baldi, A; Gonzalez-Silveira, M; Palmisano, V; Dam, B; and Griessen, R. "Destabilization of the Mg-H System through Elastic Constraints." *Physical Review Letters*, **102(22)**, 2009, page 226102.

Barkhordarian, G; Klassen, T; Dornheim, M; and Bormann, R. "Unexpected kinetic effect of MgB_2 in reactive hydride composites containing complex borohydrides." *Journal of Alloys and Compounds*, **440(1-2)**, 2007, pages L18–L21.

Baur, WH. "Atomabstände und Bindungswinkel im Brookit, TiO_2." *Acta Crystallographica*, **14(3)**, 1961, pages 214–216.

Birch, F. "Finite Elastic Strain of Cubic Crystals." *Physical Review*, **71(11)**, 1947, pages 809–824.

Bird, PH and Churchill, MR. "The crystal structure of zirconium(IV) borohydride (at -160°C)." *Chemical Communications*, **(8)**, 1967, page 403.

Bogdanovic, B and Schwickardi, M. "Ti-doped alkali metal aluminium hydrides as potential novel reversible hydrogen storage materials." *Journal of Alloys and Compounds*, **253-254(1-2)**, 1997, pages 1–9.

Born, M and Oppenheimer, R. "Zur Quantentheorie der Molekeln." *Annalen der Physik*, **84(20)**, 1927, pages 457–484.

Bösenberg, U; Doppiu, S; Mosegaard, L; Barkhordarian, G; Eigen, N; Borgschulte, A; Jensen, T; Cerenius, Y; Gutfleisch, O; and Klassen, T. "Hydrogen sorption properties of MgH_2-$LiBH_4$ composites." *Acta Materialia*, **55(11)**, 2007, pages 3951–3958.

Boulfelfel, SE; Seifert, G; and Leoni, S. "Atomistic investigation of Li^+ diffusion pathways in the olivine $LiFePO_4$ cathode material." *Journal of Materials Chemistry*, **21(41)**, 2011, page 16365.

Brewer, GD. "Aviation usage of liquid hydrogen fuel—prospects and problems." *International Journal of Hydrogen Energy*, **1**, 1976, pages 65–88.

Buchter, F; Łodziana, Z; Mauron, P; Remhof, A; Friedrichs, O; Borgschulte, A; Züttel, A; Sheptyakov, D; Strässle, T; and Ramirez-Cuesta, AJ. "Dynamical properties and temperature induced molecular disordering of $LiBH_4$ and $LiBD_4$." *Physical Review B*, **78(9)**, 2008a, page 94302.

Buchter, F; Łodziana, Z; Remhof, A; Friedrichs, O; Borgschulte, A; Mauron, P; Züttel, A; Sheptyakov, D; Barkhordarian, G; Bormann, R; Chłopek, K; Fichtner, M; Sørby, MH; Riktor, MD; Hauback, BC; and Orimo, SI. "Structure of $Ca(BD_4)_2$ β-phase from combined neutron and synchrotron X-ray powder diffraction data and density functional calculations." *Journal of Physical Chemistry B*, **112(27)**, 2008b, pages 8042–8.

Buchter, F; Łodziana, Z; Remhof, A; Friedrichs, O; Borgschulte, A; Mauron, P; Züttel, A; Sheptyakov, D; Palatinus, L; Chłopek, K; Fichtner, M; Barkhordarian, G; Bormann, R; and Hauback, BC. "Structure of the Orthorhombic γ-Phase and Phase Transitions of $Ca(BD_4)_2$." *Journal of Physical Chemistry C*, **113(39)**, 2009, pages 17223–17230.

Callear, SK; Nickels, EA; Jones, MO; Matsuo, M; Orimo, SI; Edwards, PP; and David, WIF. "Order and disorder in lithium tetrahydroborate." *Journal of Materials Science*, **46(2)**, 2010, pages 566–569.

Ceriotti, M; Cereda, S; Montalenti, F; Miglio, L; and Bernasconi, M. "Ab initio study of the diffusion and decomposition pathways of SiH_x species on Si(100)." *Physical Review B*, **79(16)**, 2009, page 165437.

Chang, TM and Dang, LX. "On rotational dynamics of an NH_4^+ ion in water." *Journal of Chemical Physics*, **118(19)**, 2003, page 8813.

Chater, PA; David, WIF; and Anderson, PA. "Synthesis and structure of the new complex hydride $Li_2BH_4NH_2$." *Chemical Communications*, **(45)**, 2007, pages 4770–2.

Chater, PA; David, WIF; Johnson, SR; Edwards, PP; and Anderson, PA. "Synthesis and crystal structure of $Li_4BH_4(NH_2)_3$." *Chemical Communications*, **(23)**, 2006, pages 2439–41.

Chen, P; Xiong, Z; Luo, J; Lin, J; and Tan, KL. "Interaction of hydrogen with metal nitrides and imides." *Nature*, **420(6913)**, 2002, pages 302–4.

Chłopek, K; Frommen, C; Léon, A; Zabara, O; and Fichtner, M. "Synthesis and properties of magnesium tetrahydroborate, $Mg(BH_4)_2$." *Journal of Materials Chemistry*, **17(33)**, 2007, page 3496.

Churchard, AJ; Banach, E; Borgschulte, A; Caputo, R; Chen, JC; Clary, D; Fijalkowski, KJ; Geerlings, H; Genova, RV; Grochala, W; Jaron, T; Juanes-Marcos, JC; Kasemo, B; Kroes, GJ; Ljubic, I; Naujoks, N; Nørskov, JK; Olsen, RA; Pendolino, F; Remhof, A; Romanszki, L; Tekin, A; Vegge, T; Zäch, M; and Züttel, A. "A multifaceted approach to hydrogen storage." *Physical Chemistry Chemical Physics*, **13(38)**, 2011, pages 16955–72.

Ciccotti, G and Tenenbaum, A. "Canonical Ensemble and Nonequilibrium States by Molecular Dynamics." *Journal of Statistical Physics*, **23(6)**, 1980, pages 767–772.

Clark, SJ; Segall, MD; Pickard, CJ; Hasnip, PJ; Probert, MIJ; Refson, K; and Payne, MC. "First principles methods using CASTEP." *Zeitschrift für Kristallographie*, **220**, 2005, pages 567–570.

de Groot, SR and Mazur, P. *Non-equilibrium thermodynamics*. Dover Publications, New York, 1984.

Dove, MT. "An introduction to the use of neutron scattering methods in mineral sciences." *European Journal of Mineralogy*, **14(2)**, 2002, pages 203–224.

Dubrovinsky, LS; Dubrovinskaia, NA; Swamy, V; Muscat, J; Harrison, NM; Ahuja, R; Holm, B; and Johansson, B. "The hardest known oxide." *Nature*, **410**, 2001, pages 653–4.

Einstein, A. "Über die von der molekularkinetischen Theorie der Wärme geforderte Bewegung von in ruhenden Flüssigkeiten suspendierten Teilchen." *Annalen der Physik*, **322(8)**, 1905, pages 549–560.

Euler, L. "Nova Methodvs Corporvm Rigidorvm Determinandi." *Novi Commentarii Academiae Scientiarvm Imperialis Petropolitanae*, **20**, 1776, pages 208–238.

Evans, DJ. "The frequency dependent shear viscosity of methane." *Molecular Physics*, **37(6)**, 1979, pages 1745–1754.

Evans, DJ. "Homogeneous NEMD algorithm for thermal conductivity—application of non-canonical linear response theory." *Physics Letters A*, **91(9)**, 1982, pages 457–460.

Evans, DJ; Hoover, WG; Failor, BH; Moran, B; and Ladd, AJC. "Nonequilibrium molecular dynamics via Gauss's principle of least constraint." *Physical Review A*, **28(2)**, 1983, page 1016.

Evans, DJ and Morriss, G. "Non-Newtonian Molecular Dynamics." *Computer Physics Reports*, **1**, 1984, pages 297–343.

Evans, DJ and Morriss, G. *Statistical Mechanics of Nonequilibrium Liquids*. Cambridge University Press, Cambridge, 2008.

Farrell, DE; Shin, D; and Wolverton, C. "First-principles molecular dynamics study of the structure and dynamic behavior of liquid $Li_4BN_3H_{10}$." *Physical Review B*, **80(22)**, 2009, page 224201.

Filinchuk, YE; Cerny, R; and Hagemann, H. "Insight into $Mg(BH_4)_2$ with Synchrotron X-ray Diffraction: Structure Revision, Crystal Chemistry, and Anomalous Thermal Expansion." *Chemistry of Materials*, **21(5)**, 2009a, pages 925–933.

Filinchuk, YE; Chernyshov, D; and Cerny, R. "Lightest Borohydride Probed by Synchrotron X-ray Diffraction: Experiment Calls for a New Theoretical Revision." *Journal of Physical Chemistry C*, **112(28)**, 2008a, pages 10579–10584.

Filinchuk, YE; Chernyshov, D; Nevidomskyy, A; and Dmitriev, V. "High-pressure polymorphism as a step towards destabilization of $LiBH_4$." *Angewandte Chemie (International ed in English)*, **47(3)**, 2008b, pages 529–32.

Filinchuk, YE; Rönnebro, E; and Chandra, D. "Crystal structures and phase transformations in $Ca(BH_4)_2$." *Acta Materialia*, **57(3)**, 2009b, pages 732–738.

Frisch, MJ; Trucks, GW; Schlegel, HB; Scuseria, GE; Robb, MA; Cheeseman, JR; Montgomery Jr., JA; Kudin, KN; Burant, JC; Millam, JM; Iyengar, SS; Tomasi, J; Barone, V; Mennucci, B; Cossi, M; Scalmani, G; Rega, N; Petersson, GA; Nakatsuji, H; Hada, M; Ehara, M; Toyota, K; Fukuda, R; Hasegawa, J; Ishida, M; Nakajima, T; Honda, Y; Kitao, O; Nakai, H; Klene, M; Li, X; Knox, JE; Hratchian, HP; Cross, JB; Adamo, C; Jaramillo, J; Gomperts, R; Stratmann, RE; Yazyev, O; Austin, AJ; Cammi, R; Pomelli, C; Ochterski, JW; Ayala, PY; Morokuma, K; Voth, GA; Salvador, P; Dannenberg, JJ; Zakrzewski, VG; Dapprich, S; Daniels, AD; Strain, MC; Farkas, O; Malick, DK; Rabuck, AD; Raghavachari, K; Foresman, JB; Ortiz, JV; Cui, Q; Baboul, AG; Clifford, S; Cioslowski, J; Stefanov, BB; Liu, G; Liashenko, A; Piskorz, P; Komaromi, I; Martin, RL; Fox, DJ; Keith, T; Al-Laham, MA; Peng, CY; Nanayakkara, A; Challacombe, M; Gill, PMW; Johnson, B; Chen, W; Wong, MW; Gonzalez, C; and Pople, JA. "Gaussian03 Revision B.05.", 2003.

Gauß, KF. "Über ein neues allgemeines Grundgesetz der Mechanik." *Journal für die reine und angewandte Mathematik*, **4**, 1826, pages 232–235.

Gear, WC. *Numerical Initial Value Problems in Ordinary Differential Equations*. Prentice Hall, London, 1971.

George, L; Drozd, V; Saxena, SK; Bardaji, EG; and Fichtner, M. "High-Pressure Investigation on Calcium Borohydride." *Journal of Physical Chemistry C*, **113(33)**, 2009a, pages 15087–15090.

George, L; Drozd, V; Saxena, SK; Bardaji, EG; and Fichtner, M. "Structural Phase Transitions of $Mg(BH_4)_2$ under Pressure." *Journal of Physical Chemistry C*, **113(1)**, 2009b, pages 486–492.

Gerlach, W. "Die Gitterstruktur der Erdalkalioxyde." *Zeitschrift für Physik*, **9(1)**, 1922, pages 184–192.

Goedecker, S; Teter, M; and Hutter, J. "Separable dual-space Gaussian pseudopotentials." *Physical Review B*, **54(3)**, 1996, pages 1703–1710.

Gomes, S; Hagemann, H; and Yvon, K. "Lithium boro-hydride $LiBH_4$ II. Raman spectroscopy." *Journal of Alloys and Compounds*, **346(1-2)**, 2002, pages 206–210.

Grochala, W and Edwards, PP. "Thermal decomposition of the non-interstitial hydrides for the storage and production of hydrogen." *Chemical Reviews*, **104(3)**, 2004, pages 1283–316.

Gunaydin, H; Houk, KN; and Ozolins, V. "Vacancy-mediated dehydrogenation of sodium alanate." *Proceedings of the National Academy of Sciences of the United States of America*, **105(10)**, 2008, pages 3673–7.

Haas, P; Tran, F; and Blaha, P. "Calculation of the lattice constant of solids with semilocal functionals." *Physical Review B*, **79(8)**, 2009, page 085104.

Haas, P; Tran, F; Blaha, P; da Silva, AJR; Odashima, MM; and Capelle, K. "Systematic investigation of a family of gradient-dependent functionals for solids." *Physical Review B*, **81(12)**, 2010, page 125136.

Hagemann, H; Gomes, S; Renaudin, G; and Yvon, K. "Raman studies of reorientation motions of $[BH4]^-$ anions in alkali borohydrides." *Journal of Alloys and Compounds*, **363(1-2)**, 2004, pages 129–132.

Hamann, D; Schlüter, M; and Chiang, C. "Norm-Conserving Pseudopotentials." *Physical Review Letters*, **43(20)**, 1979, pages 1494–1497.

Hamilton, WR. "On a New Species of Imaginary Quantities, Connected with the Theory of Quaternions." *Proceedings of the Royal Irish Academy*, **2**, 1844, pages 424–434.

Hamilton, WR. "Theory of Quaternions." *Proceedings of the Royal Irish Academy*, **3**, 1847, pages 1–16.

Harris, PM and Meibohm, EP. "The Crystal Structure of Lithium Borohydride $LiBH_4$." *Journal of the American Chemical Society*, **69**, 1947, pages 1231–1232.

Hartman, MR; Rush, JJ; Udovic, TJ; Bowman, RC; and Hwang, SJ. "Structure and vibrational dynamics of isotopically labeled lithium borohydride using neutron diffraction and spectroscopy." *Journal of Solid State Chemistry*, **180(4)**, 2007, pages 1298–1305.

Heffelfinger, GS and Swol, FV. "Diffusion in Lennard-Jones fluids using dual control volume grand canonical molecular dynamics simulation (DCV-GCMD)." *Journal of Chemical Physics*, **100(10)**, 1994, page 7548.

Hempelmann, R. *Quasielastic Neutron Scattering and Solid State Diffusion.* Oxford University Press, Oxford, 2000.

Hill, TL. *An Introduction to Statistical Thermodynamics.* Dover Publications, New York, 1986.

Hohenberg, P and Kohn, W. "Inhomogeneous Electron Gas." *Physical Review*, **136(3B)**, 1964, pages B864–B871.

Hoover, WG. "Canonical dynamics: Equilibrium phase-space distributions." *Physical Review A*, **31(3)**, 1985, pages 1695–1697.

Hoover, WG. "Molecular Dynamics." volume 258 of *Lecture Notes in Physics*. Springer-Verlag, Berlin/Heidelberg, 1986.

Hoover, WG. *Smooth Particle Applied Mechanics. The State of the Art.* Advanced series in nonlinear dynamics. World Scientific, Singapore, 2006.

Howard, CJ; Sabine, TM; and Dickson, F. "Structural and thermal parameters for rutile and anatase." *Acta crystallographica Section B, Structural science*, **47(4)**, 1991, pages 462–468.

Hummelshøj, JS; Landis, DD; Voss, J; Jiang, T; Tekin, A; Bork, N; Dulak, M; Mortensen, JJ; Adamska, L; Andersin, J; Baran, JD; Barmparis, GD; Bell, F; Bezanilla, AL; Bjork, J; Björketun, ME; Bleken, F; Buchter, F; Bürkle, M; Burton, PD; Buus, BB; Calborean, A; Calle-Vallejo, F; Casolo, S; Chandler, BD; Chi, DH; Czekaj, I; Datta, S; Datye, A; DeLaRiva, A; Despoja, V; Dobrin, S; Engelund, M; Ferrighi, L; Frondelius, P; Fu, Q; Fuentes, A; Fürst, J; García-Fuente, A; Gavnholt, J; Goeke, R; Gudmundsdottir, S; Hammond, KD; Hansen, HA; Hibbitts, D; Hobi, E; Howalt, JG; Hruby, SL; Huth, A; Isaeva, L; Jelic, J; Jensen, IJT; Kacprzak, KA; Kelkkanen, A; Kelsey, D; Kesanakurthi, DS; Kleis, J; Klüpfel, PJ; Konstantinov, I; Korytar, R; Koskinen, P; Krishna, C; Kunkes, E; Larsen, AH; Lastra, JMG; Lin, H; Lopez-Acevedo, O; Mantega, M; Martínez, JI; Mesa, IN; Mowbray, DJ; Mýrdal, JSG; Natanzon, Y; Nistor, A; Olsen, T; Park, H; Pedroza, LS; Petzold, V; Plaisance, C; Rasmussen, JA; Ren, H; Rizzi, M; Ronco, AS; Rostgaard, C; Saadi, S; Salguero, LA; Santos, EJG; Schoenhalz, AL; Shen, J; Smedemand, M; Stausholm-Møller, OJ; Stibius, M; Strange, M; Su, HB; Temel, B; Toftelund, A; Tripkovic, V; Vanin, M; Viswanathan, V; Vojvodic, A; Wang, S; Wellendorff, J; Thygesen, KS; Rossmeisl, J; Bligaard, T; Jacobsen, KW; Nørskov, JK; and Vegge, T. "Density functional theory based screening of ternary alkali-transition metal borohydrides: a computational material design project." *Journal of Chemical Physics*, **131(1)**, 2009, page 014101.

Ikeshoji, T; Tsuchida, E; Ikeda, K; Matsuo, M; Li, Hw; Kawazoe, Y; and Orimo, SI. "Diffuse and doubly split atom occupation in hexagonal $LiBH_4$." *Applied Physics Letters*, **95(22)**, 2009, page 221901.

Ikeshoji, T; Tsuchida, E; Morishita, T; Ikeda, K; Matsuo, M; Kawazoe, Y; and Orimo, SI. "Fast-ionic conductivity of Li^+ in $LiBH_4$." *Physical Review B*, **83(14)**, 2011, page 144301.

Islam, MS; Driscoll, DJ; Fisher, CAJ; and Slater, PR. "Atomic-Scale Investigation of Defects, Dopants, and Lithium Transport in the $LiFePO_4$ Olivine-Type Battery Material." *Chemistry of Materials*, **17(20)**, 2005, pages 5085–5092.

Johnson, SR; David, WIF; Royse, DM; Sommariva, M; Tang, CY; Fabbiani, FPA; Jones, MO; and Edwards, PP. "The monoammoniate of lithium borohydride, $Li(NH_3)BH_4$: an

effective ammonia storage compound." *Chemistry, an Asian journal*, **4(6)**, 2009, pages 849–54.

Kang, JK; Kim, SY; Han, YS; Muller, RP; and Goddard, WA. "A candidate $LiBH_4$ for hydrogen storage: Crystal structures and reaction mechanisms of intermediate phases." *Applied Physics Letters*, **87(11)**, 2005, page 111904.

Kearsley, SK. "On the orthogonal transformation used for structural comparisons." *Acta crystallographica Section A, Foundations of crystallography*, **45(2)**, 1989, pages 208–210.

Keen, DA. "A comparison of various commonly used correlation functions for describing total scattering." *Journal of Applied Crystallography*, **34(2)**, 2001, pages 172–177.

Kim, J; Jin, S; Shim, JH; and Cho, YW. "Thermal decomposition behavior of calcium borohydride $Ca(BH_4)_2$." *Journal of Alloys and Compounds*, **461(1-2)**, 2008, pages L20–L22.

Kleinhesselink, D and Wolfsberg, M. "The evaluation of power spectra in molecular dynamics simulations of anharmonic solids and surfaces." *Surface Science*, **262(1-2)**, 1992, pages 189–207.

Kleinman, L and Bylander, D. "Efficacious Form for Model Pseudopotentials." *Physical Review Letters*, **48(20)**, 1982, pages 1425–1428.

Kohn, W and Sham, LJ. "Self-Consistent Equations Including Exchange and Correlation Effects." *Physical Review*, **140(4A)**, 1965, pages A1133–A1138.

Kojima, Y and Kawai, Y. "IR characterizations of lithium imide and amide." *Journal of Alloys and Compounds*, **395(1-2)**, 2005, pages 236–239.

Laio, A and Gervasio, FL. "Metadynamics: a method to simulate rare events and reconstruct the free energy in biophysics, chemistry and material science." *Reports on Progress in Physics*, **71(12)**, 2008, page 126601.

Laio, A and Parrinello, M. "Escaping free-energy minima." *Proceedings of the National Academy of Sciences of the United States of America*, **99(20)**, 2002, pages 12562–12566.

Liu, A; Xie, S; Dabiran-Zohoory, S; and Song, Y. "High-Pressure Structures and Transformations of Calcium Borohydride Probed by Combined Raman and Infrared Spectroscopies." *Journal of Physical Chemistry C*, **114(26)**, 2010, pages 11635–11642.

Łodziana, Z and Vegge, T. "Structural Stability of Complex Hydrides: $LiBH_4$ Revisited." *Physical Review Letters*, **93(14)**, 2004, page 145501.

Łodziana, Z and Vegge, T. "Łodziana and Vegge reply." *Physical Review Letters*, **97**, 2006, page 119602.

Maginn, EJ; Bell, AT; and Theodorou, DN. "Transport diffusivity of methane in silicalite from equilibrium and nonequilibrium simulations." *Journal of Physical Chemistry*, **97(16)**, 1993, pages 4173–4181.

Majzoub, EH and Ozolins, V. "Prototype electrostatic ground state approach to predicting crystal structures of ionic compounds: Application to hydrogen storage materials." *Physical Review B*, **77(10)**, 2008, page 104115.

Majzoub, EH and Rönnebro, E. "Crystal Structures of Calcium Borohydride: Theory and Experiment." *Journal of Physical Chemistry C*, **113(8)**, 2009, pages 3352–3358.

Marchetti, C. "On hydrogen and energy systems." *International Journal of Hydrogen Energy*, **1(1)**, 1976, pages 3–10.

Maronsson, JB; Jónsson, H; and Vegge, T. "A method for finding the ridge between saddle points applied to rare event rate estimates." *Physical Chemistry Chemical Physics*, **14(8)**, 2012, page 2884.

Marsaglia, G. "Choosing a point from the surface of a sphere." *The Annals of Mathematical Statistics*, **43**, 1972, pages 645–646.

Martelli, P; Remhof, A; Borgschulte, A; Ackermann, R; Strässle, T; Embs, JP; Ernst, M; Matsuo, M; Orimo, SI; and Züttel, A. "Rotational motion in $LiBH_4$/LiI solid solutions." *Journal of Physical Chemistry A*, **115(21)**, 2011, pages 5329–34.

Martelli, P; Remhof, A; Borgschulte, A; Mauron, P; Wallacher, D; Kemner, E; Russina, M; Pendolino, F; and Züttel, A. "BH_4^- self-diffusion in liquid $LiBH_4$." *Journal of Physical Chemistry A*, **114(37)**, 2010, pages 10117–21.

Martin, RM. *Electronic Structure. Basic Theory and Practical Methods.* Cambridge University Press, 2004.

Martyna, GJ; Klein, ML; and Tuckerman, M. "Nosé-Hoover chains: The canonical ensemble via continuous dynamics." *Journal of Chemical Physics*, **97(4)**, 1992, page 2635.

Martyna, GJ; Tobias, DJ; and Klein, ML. "Constant pressure molecular dynamics algorithms." *Journal of Chemical Physics*, **101(5)**, 1994, page 4177.

Matsuo, M; Nakamori, Y; Orimo, SI; Maekawa, H; and Takamura, H. "Lithium superionic conduction in lithium borohydride accompanied by structural transition." *Applied Physics Letters*, **91(22)**, 2007, page 224103.

Matsuo, M; Remhof, A; Martelli, P; Caputo, R; Ernst, M; Miura, Y; Sato, T; Oguchi, H; Maekawa, H; Takamura, H; Borgschulte, A; Züttel, A; and Orimo, SI. "Complex hydrides with $(BH_4)^-$ and $(NH_2)^-$ anions as new lithium fast-ion conductors." *Journal of the American Chemical Society*, **131(45)**, 2009, pages 16389–91.

Miwa, K; Aoki, M; Noritake, T; Ohba, N; Nakamori, Y; Towata, SI; Züttel, A; and Orimo, SI. "Thermodynamical stability of calcium borohydride $Ca(BH_4)_2$." *Physical Review B*, **74(15)**, 2006, page 155122.

Miwa, K; Ohba, N; Towata, SI; Nakamori, Y; and Orimo, SI. "First-principles study on lithium borohydride $LiBH_4$." *Physical Review B*, **69(24)**, 2004, page 245120.

Miyazaki, R; Karahashi, T; Kumatani, N; Noda, Y; Ando, M; Takamura, H; Matsuo, M; Orimo, SI; and Maekawa, H. "Room temperature lithium fast-ion conduction and phase relationship of LiI stabilized $LiBH_4$." *Solid State Ionics*, **192(1)**, 2011, pages 143–147.

Morriss, G and Evans, DJ. "Isothermal response theory." *Molecular Physics*, **54(3)**, 1985, pages 629–636.

Murnaghan, FD. "The compressibility of media under extreme pressures." *Proceedings of the national academy of sciences of the United States of America*, **30(9)**, 1944, page 244.

Nakamori, Y; Miwa, K; Ninomiya, A; Li, HW; Ohba, N; Towata, SI; Züttel, A; and Orimo, SI. "Correlation between thermodynamical stabilities of metal borohydrides and cation electronegativites: First-principles calculations and experiments." *Physical Review B*, **74(4)**, 2006, page 45126.

Neumann, MA. "Tailor-made force fields for crystal-structure prediction." *Journal of Physical Chemistry B*, **112(32)**, 2008, pages 9810–29.

Noritake, T; Aoki, M; Matsumoto, M; Miwa, K; Towata, SI; Li, HW; and Orimo, SI. "Crystal structure and charge density analysis of $Ca(BH_4)_2$." *Journal of Alloys and Compounds*, **491(1-2)**, 2010, pages 57–62.

Nosé, S. "A molecular dynamics method for simulations in the canonical ensemble." *Molecular Physics*, **52(2)**, 1984a, pages 255–268.

Nosé, S. "A unified formulation of the constant temperature molecular dynamics methods." *Journal of Chemical Physics*, **81(1)**, 1984b, page 511.

Ozolins, V; Majzoub, EH; and Wolverton, C. "First-principles prediction of thermodynamically reversible hydrogen storage reactions in the Li-Mg-Ca-B-H system." *Journal of the American Chemical Society*, **131(1)**, 2009, pages 230–7.

Pawley, G and Dove, MT. "Quaternion-based reorientation conditions for molecular dynamics analyses." *Molecular Physics*, **55(5)**, 1985, pages 1147–1157.

Payne, MC; Arias, TA; and Joannopoulos, JD. "Iterative minimization techniques for ab initio total-energy calculations: molecular dynamics and conjugate gradients." *Reviews of Modern Physics*, **64(4)**, 1992, pages 1045–1097.

Perdew, JP; Burke, K; and Ernzerhof, M. "Generalized Gradient Approximation Made Simple." *Physical Review Letters*, **77(18)**, 1996, pages 3865–3868.

Pickard, CJ and Needs, RJ. "Structures at high pressure from random searching." *Physica Status Solidi B*, **246(3)**, 2009, pages 536–540.

Rappe, A; Rabe, K; Kaxiras, E; and Joannopoulos, JD. "Optimized pseudopotentials." *Physical Review B*, **41(2)**, 1990, pages 1227–1230.

Refson, K; Tulip, PR; and Clark, SJ. "Variational density-functional perturbation theory for dielectrics and lattice dynamics." *Physical Review B*, **73(15)**, 2006, page 155114.

Remhof, A; Łodziana, Z; Martelli, P; Friedrichs, O; Züttel, A; Skripov, AV; Embs, JP; and Strässle, T. "Rotational motion of BH_4 units in MBH_4 (M=Li, Na, K) from quasielastic neutron scattering and density functional calculations." *Physical Review B*, **81(21)**, 2010, page 214304.

Rifkin, J. *The Hydrogen Economy: the creation of the worldwide energy and the redistribution of power on earth.* Jeremy P. Tarther/Penguin, New York, 2002.

Riktor, MD; Sørby, MH; Chłopek, K; Fichtner, M; Buchter, F; Züttel, A; and Hauback, BC. "In situ synchrotron diffraction studies of phase transitions and thermal decomposition of $Mg(BH_4)_2$ and $Ca(BH_4)_2$." *Journal of Materials Chemistry*, **17(47)**, 2007, page 4939.

Rönnebro, E. "Development of group II borohydrides as hydrogen storage materials." *Current Opinion in Solid State and Materials Science*, **15**, 2011, pages 44–51.

Rönnebro, E and Majzoub, EH. "Calcium borohydride for hydrogen storage: catalysis and reversibility." *Journal of Physical Chemistry B*, **111(42)**, 2007, pages 12045–7.

Rugh, H. "Dynamical Approach to Temperature." *Physical Review Letters*, **78(5)**, 1997, pages 772–774.

Sato, T; Miwa, K; Nakamori, Y; Ohoyama, K; Li, HW; Noritake, T; Aoki, M; Towata, SI; and Orimo, SI. "Experimental and computational studies on solvent-free rare-earth metal borohydrides $R(BH_4)_3$ (R=Y, Dy, and Gd)." *Physical Review B*, **77(10)**, 2008, page 104114.

Schlapbach, L and Züttel, A. "Hydrogen-storage materials for mobile applications." *Nature*, **414(6861)**, 2001, pages 353–8.

Simons, PY and Dachille, F. "The structure of TiO_2 II, a high-pressure phase of TiO_2." *Acta Crystallographica*, **23(2)**, 1967, pages 334–336.

Skripov, AV; Soloninin, AV; Filinchuk, YE; and Chernyshov, D. "Nuclear Magnetic Resonance Study of the Rotational Motion and the Phase Transition in $LiBH_4$." *Journal of Physical Chemistry C*, 2008, pages 18701–18705.

Soulié, J; Renaudin, G; Cerny, R; and Yvon, K. "Lithium boro-hydride $LiBH_4$ I. Crystal structure." *Journal of Alloys and Compounds*, **346(1-2)**, 2002, pages 200–205.

Staubitz, A; Robertson, APM; and Manners, I. "Ammonia-borane and related compounds as dihydrogen sources." *Chemical Reviews*, **110(7)**, 2010, pages 4079–124.

Sutherland, W. "A Dynamical Theory of Diffusion for Non-Electrolytes and the Molecular mass of Albumin." *Philosophical Magazine*, **9(6)**, 1905, pages 781 – 785.

Tekin, A; Caputo, R; and Züttel, A. "First-Principles Determination of the Ground-State Structure of $LiBH_4$." *Physical Review Letters*, **104(21)**, 2010, page 215501.

Tolman, RC. *The Principles of Statistical Mechanics.* Oxford University Press, London, 1938.

Tsuchida, E. "Ab initio mass tensor molecular dynamics." *Journal of Chemical Physics*, **134(4)**, 2011, page 044112.

Vajeeston, P; Ravindran, P; and Fjellvåg, H. "A new series of high hydrogen content hydrogen-storage materials—A theoretical prediction." *Journal of Alloys and Compounds*, **446-447**, 2007, pages 44–47.

Vanderbilt, D. "Soft self-consistent pseudopotentials in a generalized eigenvalue formalism." *Physical Review B*, **41(11)**, 1990, pages 7892–7895.

VandeVondele, J and Hutter, J. "Gaussian basis sets for accurate calculations on molecular systems in gas and condensed phases." *Journal of Chemical Physics*, **127(11)**, 2007, page 114105.

VandeVondele, J; Krack, M; Mohamed, F; Parrinello, M; Chassaing, T; and Hutter, J. "QUICKSTEP: Fast and accurate density functional calculations using a mixed Gaussian and plane waves approach." *Computer Physics Communications*, **167(2)**, 2005, pages 103–128.

Voss, J; Hummelshøj, JS; Łodziana, Z; and Vegge, T. "Structural stability and decomposition of $Mg(BH_4)_2$ isomorphs—an ab initio free energy study." *Journal of Physics: Condensed Matter*, **21(1)**, 2009, page 012203.

Voter, A. "Hyperdynamics: Accelerated Molecular Dynamics of Infrequent Events." *Physical Review Letters*, **78(20)**, 1997, pages 3908–3911.

Williams, SR and Evans, DJ. "Linear Response Domain in Glassy Systems." *Physical Review Letters*, **96(1)**, 2006, page 015701.

Winsche, WE; Hoffman, KC; and Salzano, FJ. "Hydrogen: Its Future Role in the Nation's Energy Economy." *Science*, **180(4093)**, 1973, pages 1325–32.

Wolverton, C; Siegel, DJ; Akbarzadeh, AR; and Ozolins, V. "Discovery of novel hydrogen storage materials: an atomic scale computational approach." *Journal of Physics: Condensed Matter*, **20(6)**, 2008, page 64228.

Xiong, Z; Yong, CK; Wu, G; Chen, P; Shaw, WJ; Karkamkar, A; Autrey, T; Jones, MO; Johnson, SR; Edwards, PP; and David, WIF. "High-capacity hydrogen storage in lithium and sodium amidoboranes." *Nature materials*, **7(2)**, 2008, pages 138–41.

Zarkevich, N and Johnson, D. "Predicting Enthalpies of Molecular Substances: Application to $LiBH_4$." *Physical Review Letters*, **100(4)**, 2008, page 040602.

Zhang, Y; Majzoub, EH; Ozolins, V; and Wolverton, C. "Theoretical prediction of different decomposition paths for $Ca(BH_4)_2$ and $Mg(BH_4)_2$." *Physical Review B*, **82(17)**, 2010, page 174107.

Zupan, A; Blaha, P; Schwarz, K; and Perdew, JP. "Pressure-induced phase transitions in solid Si, SiO_2, and Fe: Performance of local-spin-density and generalized-gradient-approximation density functionals." *Physical Review B*, **58(17)**, 1998, pages 11266–11272.

Züttel, A; Rentsch, S; Fischer, P; Wenger, P; Sudan, P; Mauron, P; and Emmenegger, C. "Hydrogen storage properties of $LiBH_4$." *Journal of Alloys and Compounds*, **356-357**, 2003, pages 515–520.

APPENDIX A

Publications arising from this thesis

- Aeberhard, PC; Refson, K; Edwards, PP; and David, WIF. "High-pressure crystal structure prediction of calcium borohydride using density functional theory." *Physical Review B*, **83(17)**, 2011, page 174102.
- Aeberhard, PC; Williams, SR; Evans, DJ; Refson, K; and David, WIF. "Ab initio Nonequilibrium Molecular Dynamics in the Solid Superionic Conductor $LiBH_4$." *Physical Review Letters*, **108(9)**, 2012, page 095901.